The Pennsylvania State University
The Graduate School
College of Engineering

SIMULATION, ANALYSIS, AND MITIGATION OF VORTEX ROPE FORMATION IN THE DRAFT TUBE OF HYDRAULIC TURBINES

A Dissertation in
Mechanical Engineering
by
Hosein Foroutan

© 2015 Hosein Foroutan

Submitted in Partial Fulfillment
of the Requirements
for the Degree of

Doctor of Philosophy

May 2015

The dissertation of Hosein Foroutan was reviewed and approved* by the following:

Savas Yavuzkurt
Professor of Mechanical Engineering
Dissertation Advisor, Chair of Committee

John M. Cimbala
Professor of Mechanical Engineering

Gita Talmage
Professor of Mechanical Engineering

Eric G. Paterson
Professor of Marine Propulsion
Head of the Department of Aerospace and Ocean Engineering
Virginia Polytechnic Institute and State University
Special Member

Cengiz Camci
Professor of Aerospace Engineering

Karen Thole
Professor of Mechanical Engineering
Head of the Department of Mechanical and Nuclear Engineering

*Signatures are on file in the Graduate School.

Abstract

Flow in the draft tube of a hydraulic turbine operating under off-design conditions is very complex. The instability of the swirling flow may lead to the formation of a helical precessing vortex called the “vortex rope”. The vortex rope causes efficiency reduction, severe pressure fluctuation, and even structural vibration.

The primary objectives of the present study are to model and analyze the vortex rope formation using high fidelity numerical simulations. In particular, this work aims to understand the fundamental physical processes governing the formation of the vortex rope, and to investigate the capability of turbulence models to simulate this complex flow. Furthermore, mitigation of the vortex rope formation is addressed. Specifically, a vortex rope control technique, which includes injection of water from the runner crown tip to the inlet of the draft tube, is numerically studied.

A systematic approach is considered in this study starting from the simplest and advancing towards the most complicated test case. First, steady simulations are carried out for axisymmetric and three-dimensional grids in a simplified axisymmetric geometry. It is shown that steady simulations with Reynolds-averaged Navier-Stokes (RANS) models cannot resolve the vortex rope, and give identical symmetric results for both the axisymmetric and three-dimensional flow geometries. These RANS simulations underpredict the axial velocity by at least 14%, and turbulent kinetic energy (TKE) by at least 40%, near the center of the draft tube even quite close to the design condition. Moving farther from the design point, models fail in giving the correct levels of the axial velocity in the draft tube. This is attributed to the underprediction of TKE production and diffusion near the center of the draft tube where the vortex rope forms. Hence, a new RANS model taking into account the extra production and diffusion of TKE due to vortex rope formation is developed, which can successfully predict the mean flow velocity with as much as 37% improvements in comparison with the realizable k-ε model.

Then, unsteady simulations are performed, where it is concluded that Unsteady RANS (URANS) models cannot capture the self-induced unsteadiness of the vortex rope, but instead give steady solutions. The hybrid URANS/large eddy simulation (LES) models are proposed to be used in unsteady simulations of the vortex rope. Specifically, a new hybrid URANS/LES model in the framework of partially-averaged Navier-Stokes (PANS) modeling is developed. This new model is one of the main contributions of the present study. The newly developed PANS model is used in unsteady numerical simulations of two turbulent swirling flows containing vortex rope formation and breakdown, namely swirling flow through an abrupt expansion and the flow in the FLINDT draft tube, a model-scale draft tube of a Francis turbine. The present PANS model accurately predicts time-averaged and root-mean-square (rms) velocities in the case of the abrupt expansion, while it is shown to be superior to the delayed detached eddy simulation (DDES) and shear stress transport (SST) k-ω models. Predictions of the reattachment length using the present model shows 14% and 23% improvements compared to the DDES and the SST k-ω models, respectively. For the case of the FLINDT draft tube, four test cases covering a wide range of operating conditions from 70% to 110% of the flow rate at the best efficiency point (BEP) are considered, and numerical results of PANS simulations are compared with those from RANS/URANS simulations and experimental data. It is shown that RANS and PANS both can predict the flow behavior close to the BEP operating condition. However, RANS results deviate considerably from the experimental data as the operating condition moves away from the BEP. The pressure recovery factor predicted by the RANS model shows more than 13% and 58% overprediction when the flow rate decreases to 91% and 70% of the flow rate at BEP respectively. Predictions can be improved dramatically using the present unsteady PANS simulations. Specifically, the pressure recovery factor is predicted by less than 4% and 6% deviation for these two operating conditions. Furthermore, transient features of the flow that cannot be resolved using RANS/URANS simulations, e.g., vortex rope formation and precession, is well captured using PANS simulations. The frequency of the vortex rope precession, which causes severe fluctuations and vibrations, is well predicted by only about 2.7% deviation from the experimental data.

Finally, the physical mechanism behind the formation of the vortex rope is analyzed, and it is confirmed that the development of the vortex rope is associated with formation of a stagnant region at the center of the draft tube. Based on this observation, a vortex rope elimination method consisting of water jet injection to the draft tube is introduced and numerically assessed. It is shown that a small fraction of water (a few percent of the total flow rate) centrally injected to the inlet of the draft tube can eliminate the stagnant region and mitigate the formation of the vortex rope. This results in improvement of the draft tube performance and reduction of hydraulic losses. Specifically in the case of the simplified FLINDT draft tube, the loss coefficient can be reduced by as much as 50% and 14% when the turbine operates with 91% and 70% of the BEP flow rate, respectively. In addition, reduction (by about 1/3 in the case with 70% of BEP flow rate) of strong pressure fluctuations leads to more reliable operation of the turbine.

Table of Contents

List of Figures viii

List of Tables xii

List of Symbols xiii

Acknowledgments xvi

Chapter 1
Introduction 1
1.1 Hydropower 2
1.1.1 Hydropower's Place as an Energy Source 2
1.1.2 Principles of Hydroturbines 4
1.2 Flow in the Draft Tube of a Francis Turbine 8
1.3 Previous Studies on Vortex Rope in Draft Tubes 12
1.3.1 Analytical and Experimental Studies 12
1.3.2 Numerical Studies 14
1.4 Present Study 16
1.4.1 Scientific Motivation 16
1.4.2 Industrial Motivation 16
1.4.3 Dissertation Focus Areas and Objectives 19

Chapter 2
General Computational Methodology 20
2.1 Governing Equations 20
2.1.1 The Navier-Stokes Equations 21
2.1.2 The Reynolds-Averaged Navier-Stokes Equations: The RANS Approach 22
2.1.3 The Filtered Navier-Stokes Equations: The LES Approach 23
2.1.4 The Hybrid RANS/LES Approach 25

2.2 Turbulence Closure Models 27
    2.2.1 The RANS Models 29
        2.2.1.1 The k-ε Model 29
        2.2.1.2 The Realizable k-ε Model 30
        2.2.1.3 The k-ω Model 30
        2.2.1.4 The Shear Stress Transport (SST) k-ω Model 31
        2.2.1.5 Near-Wall Treatment in RANS Models 32
    2.2.2 The Unsteady RANS Models 33
    2.2.3 The Hybrid RANS/LES Models 33
        2.2.3.1 The Detached Eddy Simulation (DES) Model 34
        2.2.3.2 The Delayed Detached Eddy Simulation (DDES) Model 36
2.3 Discretization and Numerical Solution 37
2.4 Flow Solvers 39
    2.4.1 ANSYS-FLUENT CFD Code 39
    2.4.2 OpenFOAM CFD Code 40
2.5 Computational Grid 42

Chapter 3
Description of the Test Case: The FLINDT Draft Tube **44**
3.1 The Model Francis Turbine 45
3.2 Measurements 46
3.3 Draft Tube Geometry 48
3.4 Investigated Operating Conditions in this Study 50
3.5 Summary 55

Chapter 4
Simulations of the Flow in the Simplified FLINDT Draft Tube **56**
4.1 The Simplified Draft Tube 56
4.2 Steady Axisymmetric Simulations 58
4.3 Steady 3D Simulations 62
4.4 Unsteady 3D Simulations 65
4.5 The Vortex Rope Frequency 71
4.6 Development of an Axisymmetric Model for Draft Tube Flow at Partial Load 76
    4.6.1 Investigations of RANS Turbulence Models 77
    4.6.2 Model Development and Results 81
4.7 Summary 91

Chapter 5
Development of a New Partially- Averaged Navier-Stokes Model **92**
5.1 Introduction 92
5.2 Model Formulation 93
5.3 Validation Test Case: Swirling Flow Through an Abrupt Expansion . . 103

5.3.1 Test Case Description and Numerical Methodology 103
5.3.2 Results and Discussion 106
5.4 Summary 112

Chapter 6
Simulations of the Flow in the Complete FLINDT Draft Tube 114
6.1 The Complete FLINDT Draft Tube 114
6.2 Results and Discussion 118
6.2.1 Global Parameters 118
6.2.2 Mean Velocity and Wall Pressure Distributions 120
6.2.3 Unsteady Flow Field and Vortex Rope 125
6.2.4 Pressure Fluctuations 130
6.3 Summary 136

Chapter 7
Mitigation of the Vortex Rope Formation 137
7.1 Introduction 137
7.2 Methodology and Approach 140
7.3 Results and Discussion 144
7.3.1 Steady Axisymmetric Simulations 144
7.3.2 Unsteady 3D Simulations 148
7.4 Summary 151

Chapter 8
Summary and Conclusions 153
8.1 Highlights 153
8.2 Summary 154
8.3 Recommendations for Future Studies 159

Appendix A
Videos 161
A.1 Vortex Rope Formation Inside the FLINDT Draft Tube 161
A.2 Mitigation of the Vortex Rope by Water Jet Injection 162

Appendix B
Publications Related to this Dissertation 163

Bibliography 165

List of Figures

1.1 World net electricity generation by energy source (2010-2040) 2
1.2 Renewable energy share of global electricity production (2012) 3
1.3 Regional distribution of the total hydroelectricity production capacity (2012) 3
1.4 Hydroturbines application range 6
1.5 Installation of a Francis turbine at Grand Coulee dam's third powerplant 7
1.6 Vertical cross section of a hydropower plant 8
1.7 Francis turbine components 9
1.8 Sample hill chart of a Francis turbine 9
1.9 Components of an elbow draft tube 10
1.10 Velocity triangles at runner exit 10
1.11 Vortex rope formation in a draft tube at part-load and full-load conditions 11
1.12 Vortex rope in the draft tube of a model Francis turbine 17
1.13 Head losses of individual components of a hydropower plant 18

2.1 Filtered functions $\hat{\phi}_i$ and $\hat{\hat{\phi}}_i$ obtained from spatial filtering of $\phi_i(x)$ using (a) narrow box filter and (b) wide box filter 24
2.2 Some of the configurations of the zonal RANS/LES coupling 28
2.3 Overview of the content of a case in OpenFOAM 41
2.4 Configuration of blocks for generating the computational grid and a sample mesh 43

3.1 The FLINDT Francis turbine model 45
3.2 Components of the Francis turbine model investigated in the FLINDT project 46
3.3 Side and top views of the FLINDT draft tube 46
3.4 Change in the FLINDT draft tube cross-section area 47
3.5 Vortex rope formation inside the FLINDT draft tube 47
3.6 Measurements in the FLINDT draft tube cone 48
3.7 Pressure taps for unsteady wall pressure measurements 49
3.8 Experimental setup for PIV measurements 49
3.9 The LDA paths for the flow survey in the draft tube cone 50
3.10 Three-dimensional view of the regenerated FLINDT draft tube 51

3.11 Side view of the regenerated FLINDT draft tube 52
3.12 Investigated operating points on the machine hill chart 53
3.13 Characteristics of the studied operating points 54
3.14 Velocity components measured in the draft tube cone 55

4.1 FLINDT draft tube and its 2D and 3D simplified geometries 57
4.2 Streamline patterns for the steady axisymmetric simulation of flow in the simplified draft tube 59
4.3 Profiles of axial velocity, circumferential velocity, and turbulent kinetic energy in the simplified draft tube for case C, comparison of results of various turbulence closure models 63
4.4 Profiles of axial and circumferential velocity in the simplified draft tube for case D, comparison of results of various turbulence closure models . 64
4.5 Profiles of axial velocity for case C and case D in the simplified draft tube, comparison of axisymmetric and three-dimensional simulations 66
4.6 Isopressure surfaces in the draft tube for an instance in time, comparison of results using three different unsteady turbulence closure approaches . 67
4.7 Vortex rope visualized by isopressure surfaces in comparison with experimental visualizations 68
4.8 Pressure fluctuation in the simplified draft tube and its normalized frequency spectra 69
4.9 Isopressure surface (dark) representing vortex rope and isovelocity surface (light) representing the stagnant region for an instance in time 70
4.10 The change in the wicket gate momentum parameter with wicket gate opening angle 74
4.11 The change in the frequency parameter with the swirl number 75
4.12 Investigated sections in the simplified draft tube 77
4.13 Radial distributions of the turbulent kinetic energy production in the simplified draft tube 79
4.14 Locations of the peaks in TKE production in the simplified draft tube . 80
4.15 Locations of the vortex core in the draft tube, comparison between PIV measurements, 2D axisymmetric predictions, and 3D unsteady simulations 81
4.16 Radial distributions of the TKE production in the draft tube, comparison between DES and RANS simulations 82
4.17 Distributions of the turbulent kinetic energy (TKE) in the simplified draft tube 83
4.18 Extraction of the rope diameter by image processing in a PIV study . . 85
4.19 vortex rope diameter ℓ_c as a function of normalized streamwise distance from the draft tube inlet 86
4.20 Profiles of axial velocity and turbulent kinetic energy in the simplified draft tube for case C, comparison of the present model and the realizable k-ε turbulence model 88

4.21 Profiles of axial velocity and turbulent kinetic energy in the simplified draft tube for case C, comparison of the present model and the realizable k-ε turbulence model 89
4.22 Radial distributions of the normalized TKE budgets in the draft tube . 90
4.23 Near-wall distributions of the normalized TKE budgets in the draft tube 91

5.1 Turbulence energy spectrum 99
5.2 Variations of the f_k parameter with respect to Λ/Δ 102
5.3 Computational domain and coordinate system for the abrupt expansion 104
5.4 Velocity profiles at the inlet section of the abrupt expansion test case . . 105
5.5 Details of the computational grid in the case of the abrupt expansion . . 106
5.6 Instantaneous axial velocity contours predicted by URANS (SST k-ω), DDES, and present PANS model 107
5.7 Vortex breakdown in the pipe with sudden expansion 108
5.8 Radial distributions of axial mean velocity, axial rms velocity, tangential mean velocity, and tangential rms velocity downstream of the expansion; comparison of experimental data, present PANS model, DDES model, and SST k-ω model 110
5.9 Radial distributions of axial mean velocity, axial rms velocity, tangential mean velocity, and tangential rms velocity downstream of the expansion; comparison of experimental data, and present PANS model and DDES model both with main and fine grids 111
5.10 Radial distributions of the unresolved-to-total ratio of turbulent kinetic energy f_k in the pipe 112
5.11 Radial distributions of axial mean velocity, axial rms velocity, tangential mean velocity, and tangential rms velocity downstream of the expansion; comparison of experimental data and PANS model using Eq. (5.34) and Eq. (5.22) for f_k 113

6.1 Side view of the FLINDT draft tube showing the investigated sections and points where unsteady pressure is monitored in this study 115
6.2 Velocity profiles at the inlet section of the computational domain for the complete FLINDT draft tube 116
6.3 Three-dimensional view of the complete FLINDT draft tube showing the components of a draft tube, and “right” and “left” channels 119
6.4 Radial distributions of time-averaged axial and circumferential velocity on section S2 for case A 122
6.5 Radial distributions of time-averaged axial and circumferential velocity on section S2 for case B 123
6.6 Radial distributions of time-averaged axial and circumferential velocity on section S2 for case C 123
6.7 Radial distributions of time-averaged axial and circumferential velocity on sections S1 and S2 for case D 124

6.8 Locations of pressure transducers at four sections in the draft tube where wall pressure is measured in experiments 125
6.9 Distributions of wall pressure in the draft tube at four sections; comparison of experimental data, the present PANS model, and the k-ε RANS model 127
6.10 Contours of instantaneous and time-averaged axial velocity in the draft tube obtained by PANS simulations 128
6.11 Contours of instantaneous pressure and axial velocity, and mean axial velocity in the draft tube at three arbitrary instances of time obtained using the PANS simulations for case D 130
6.12 Vortex rope visualized by the isopressure surfaces at three instants of time 131
6.13 Wall pressure fluctuations and their normalized frequency spectra obtained from the present PANS simulations 132
6.14 Distributions of wall pressure fluctuation amplitude in the draft tube at section S2 133
6.15 Wall pressure fluctuations monitored on eight points in the draft tube obtained by PANS unsteady simulations 134
6.16 Crack in concrete at the draft tube door for a hydroturbine operated for extended period of time at partial-load operating conditions 135
6.17 The root-mean-square of wall pressure fluctuations in the draft tube for the eight monitored points in Fig. 6.15 135

7.1 Computational domain for the simplified draft tube used in investigations of the vortex rope control technique 141
7.2 Water jet injection from the runner crown cone into the draft tube . . . 142
7.3 Axial velocity profiles at the inlet section to the draft tube for case C and case D, effect of jet injection 145
7.4 Streamline patterns for the steady axisymmetric simulation of flow in the simplified draft tube, effect of water jet injection 146
7.5 Losses in the draft tube for (a) case C and (b) case D as a function of the jet radius 149
7.6 Contours of instantaneous axial velocity showing the stagnant region and vortex rope with and without water jet injection 150
7.7 Time evolution of the controlled draft tube flow by water jet injection showing the reduction and elimination of the vortex rope 151
7.8 Unsteady pressure on the draft tube wall for case D, effect of water jet injection 152

List of Tables

3.1 Dimensions of the FLINDT draft tube shown in Fig. 3.11 (All dimensions are in mm). 50
3.2 Characteristics of investigated operating conditions. 51

4.1 Draft tube performance parameters calculated between inlet section and a section 1 m downstream (Sec. A in Fig. 4.1). 61

5.1 Reattachment length z_r/h. 108

6.1 Pressure recovery coefficient χ in the draft tube (deviations from experimental data are given in the parentheses). 120
6.2 Flow portion (percentage of the total flow rate) through the "left" channel (see Fig. 6.3 for the definition of "left" and "right" channels). 121
6.3 The percentage difference (%) between wall pressure predictions of the k-ε RANS and the present PANS models, and the experimental data. . 126
6.4 Normalized vortex rope frequency f/f_{runner} (deviations from experimental data are given in the parentheses). 132

7.1 Draft tube performance parameters calculated between inlet section and a section 1 m downstream (Section A in Fig. 7.1). The effect of jet injection is studied by changing the jet radius. Maximum possible jet radius, i.e., the runner crown tip radius, is 34 mm. 147

List of Symbols

A	Area
C_p	Normalized pressure fluctuation amplitude
$C_{1\varepsilon}, C_{2\varepsilon}, C_{3\varepsilon}, C_\mu$	Turbulence model constants
D	Diameter
E	Mechanical energy
f	Frequency
f_k	Unresolved-to-total ratio of turbulent kinetic energy
f_ε	Unresolved-to-total ratio of turbulence dissipation rate
H	Turbine head
k	Turbulent kinetic energy
l, ℓ	Characteristic length scale
P	Turbulence production
p	Pressure
Q	Volume flow rate
R	Radius
r	Radial coordinate
S	Swirl number
S_{ij}	Strain rate tensor
$\bar{u}_i$	Reynolds-averaged velocity

$\hat{u}_i$	Filtered velocity
u_i'	Fluctuating velocity
U, V, W	Velocity components
V_r, V_θ, V_z	Velocity components in cylindrical coordinates
x_i, x, y, z	Coordinates
y^+	Dimensionless wall distance

Greek Symbols

α, β, β^*	Turbulence model constants
Δ	Grid length scale
ε	Dissipation rate of turbulent kinetic energy
θ	Tangential coordinate
κ	Wave number
Λ	Turbulence length scale
ν_s	Turbine specific speed
ν_t	Eddy viscosity
ν_u	PANS eddy viscosity
ρ	Density
$\sigma_k, \sigma_\varepsilon, \sigma^*$	Turbulence model constants
φ	Flow rate (discharge) coefficient
ψ	Head (energy) coefficient
ω	Angular velocity or specific dissipation (in the k-ω model)

Subscripts

c	Coherent
u	Unresolved
r	Resolved

ref	Reference

Abbreviations

BEP	Best Efficiency Point
CFD	Computational Fluid Dynamics
DES	Detached Eddy Simulation
DDES	Delayed Detached Eddy Simulation
DNS	Direct Numerical Simulation
EVM	Eddy Viscosity Model
EXP	Experimental
LDV	Laser Doppler Velocimetry
LES	Large Eddy Simulation
PANS	Partially-Averaged NavierStokes
PIV	Particle Image Velocimetry
RANS	Reynolds-Averaged Navier-Stokes
RSM	Reynolds Stress Model
SAS	Scale-Adaptive Simulation
SST	Shear Stress Transport
TKE	Turbulent Kinetic Energy
URANS	Unsteady RANS

Acknowledgments

The writing of this dissertation would not have been possible without the guidance, support, encouragement, and assistance of a number of individuals. I would like to express my deepest gratitude to my advisor, Prof. Savas Yavuzkurt, for his guidance, caring, and providing me with an excellent atmosphere for performing research. He has not only guided me to become a competent researcher, but has been an exemplar of kindness and consideration. In addition, I am grateful to my colleagues in the Penn State Hydropower Research Program, especially Prof. John M. Cimbala for very helpful feedback and suggestions throughout my work.

The work presented herein was funded in part by the Office of Energy Efficiency and Renewable Energy (EERE), U.S. Department of Energy, under Award Numbers DE-EE0002667 (the DOE/PSU Graduate Student Fellowship Program for Hydropower Research) and DE-EE0002668 (The HRF Fellowship), and the Hydro Research Foundation. I had the privilege of being a member of the Penn State Hydropower Group and a Hydro Research Foundation Fellow, where I was involved in various hydro research projects. I would like to appreciate this opportunity to become familiar with a wide range of hydropower and renewable energy challenges and issues.

Finally, this work was only possible with the love, inspiration, and encouragement of my wonderful wife, Bahareh, who has been standing beside me throughout my career and writing this dissertation. I thank my parents for their faith in me, and their dedication and many years of support.

Chapter 1

Introduction

“Water is the driver of nature.” - Leonardo da Vinci

Water has always been an essential resource for mankind. It is vital for the basic needs of food production, sanitation and health, and is increasingly substantial for sustainable development. In the course of human history, water has been inextricably linked to energy. This energy has been exploited for centuries. Ancient Greeks used water wheels, placed in a river, for grinding wheat into flour more than 2,000 years ago. In the late 19th century, the invention of the electrical generator produced a new way to exploit energy from the flowing water. By using water turbines together with generators, a reliable source of electricity was created. This source of electricity which extracts the energy from the flowing water is called hydroelectric power or hydropower.

Hydropower relies on the water cycle. Solar energy evaporates water on the surface of the earth (oceans and rivers) and draws it upward as water vapor. This water vapor condenses into clouds and falls back onto the surface as precipitation. As gravity drives the water, moving it from higher to lower elevations, energy can be extracted and used to generate electricity. Finally, the water flows through rivers back into the oceans, where it can evaporate and begin the cycle over again. Hydropower, therefore, is a renewable energy source as long as the water cycle continues.

1.1 Hydropower

1.1.1 Hydropower's Place as an Energy Source

The demand for electricity is constantly increasing because of demographic growth and development prospects. Worldwide projections predict that the net electricity generation will increase from 20.2 trillion kilo watt-hours in 2010 to 39.0 trillion kilo watt-hours in 2040 [1]. Figure 1.1 shows the evolution of the predicted sources of electricity generation from 2010 until 2040.

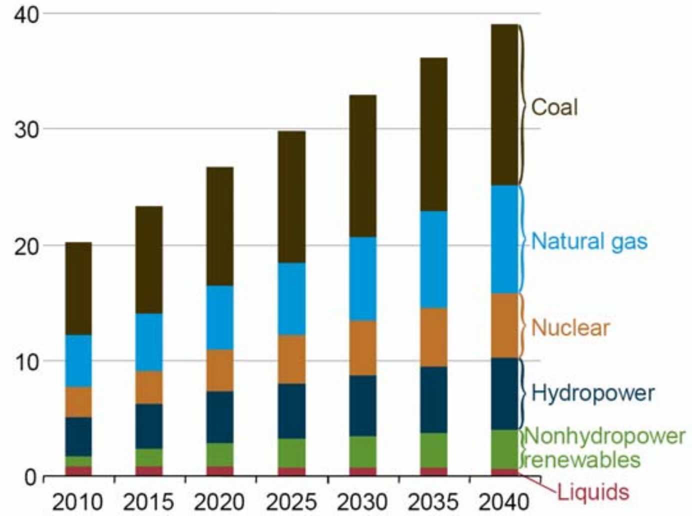

Figure 1.1: World net electricity generation by energy source, 2010-2040 (trillion kilo watt-hours). Source: U.S. Energy Information Administration [1].

The use of renewable resources is seen as a key element in energy policy, as is reducing emissions from carbon sources and decoupling energy costs from oil prices. In 2012, the share of renewable resources in electricity production was around 21.7%, with hydropower being the leading renewable energy source as shown in Fig. 1.2.

Hydropower presents the advantage of avoiding emissions of gases in spite of other environmental impacts on the fauna, flora, and sediments. The social impacts are, on the one hand, detrimental because of population displacements and land transformation, but on the other hand positive as hydropower offers the possibility to mitigate flooding, enabling better fluvial navigation and irrigation, and providing employment. Moreover, the drawbacks related to hydropower production can be mitigated by taking appropriate counter-measures at the early stages of the projects.

Hydropower is currently being utilized in 150 countries with around 27,000 generating

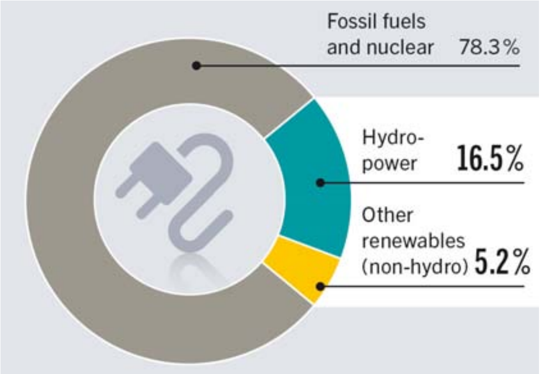

Figure 1.2: Renewable energy share of global electricity production, 2012. Source: REN21 [2].

units. In 2012, hydropower production covered 16.5% of the world electricity needs with a total installed capacity estimated to be around 990 GW [2]. The regional distribution of the total production capacity is illustrated in Fig. 1.3 with about 23% of the installed capacity in Europe, 35% in Asia Pacific, 19% in North America, 20% in South America, and the remaining 3% shared between Africa and the Middle East.

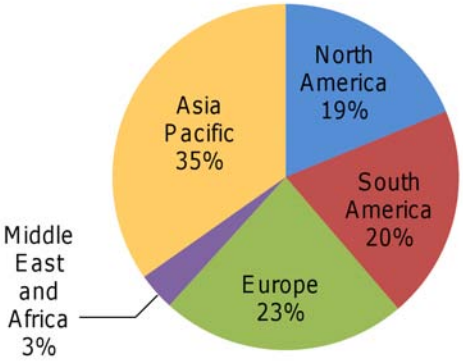

Figure 1.3: Regional distribution of the total hydroelectricity production capacity, 2012. Data source: British Petroleum [3].

However, the currently installed capacity represents only 39.7% of the economically exploitable and 22.2% of the technically exploitable resources [4]. Therefore, hydropower still has a high potential for growth. Regarding the development of hydroelectric production, it can be decomposed into four main areas

- Exploitation of new hydropower resources: the main contribution is expected to come from the completion of hydro facilities in Asia.
- Refurbishment of existing power plants: a gain of efficiency of old electromechanical

equipment can represent a significant increase in the production capacity. This is mainly the case in Europe and North America for facilities that are around 50 years old.

- Rehabilitation of old power plants: older facilities in Europe and North America are subject to full re-equipment considering also new constructions in order to increase drastically the capacity of a power plant.
- Small hydro: This is related to rural areas where electrification can be achieved through small-hydro with reduced environmental impacts.

One aspect of development of the hydropower market is the increasing need for power plants able to stabilize the global power network by allowing quick set point changes. The increase of renewable energy resources such as wind power, whose availability cannot be ensured, will represent a source of disturbance for the power grid. Therefore, hydropower plants are considered as the solution to restore grid stability by allowing hydraulic machines, especially Francis turbines, to quickly change operating points over a large range of heads and power in order to cover the variation in the electrical demand. New technologies like variable speed generators also provide an additional degree of freedom for reducing time response of power plants and offering flexibility to power management.

Modern hydropower has to face new challenges related to completely different exploitation strategies leading to an increase of the solicitation of the entire machine. Thus, hydraulic machines are increasingly subject to off-design operation, startup and shutdown sequences, and quick set point changes. In such off-design operating conditions, dynamic behavior of different components in the hydraulic system must be understood and controlled to ensure the reliability and the safety of energy production for the power grid. This requires developing appropriate experimental and numerical tools and methods for a better understanding and thus a more accurate prediction of operating conditions of hydropower plants.

1.1.2 Principles of Hydroturbines

The role of a hydroturbine (also known as a hydraulic turbine or a water turbine) is to convert hydraulic power $\dot{W}_{\text{hydraulic}}$ into useful mechanical power $\dot{W}_{\text{mechanical}}$ with the highest possible hydraulic efficiency, which is given by

$$\eta = \frac{\dot{W}_{\text{mechanical}}}{\dot{W}_{\text{hydraulic}}} = \frac{T\omega}{\rho g Q H} \tag{1.1}$$

where T is the torque extracted by the machine, ω is the angular velocity of the machine, ρ is the fluid (water) density, Q is the volume flow rate, and H is the hydraulic head.

According to the hydrology and the exploitation strategy of a given hydraulic project, the nominal head and flow rate are determined for a power plant. Then, depending on the number of machines and their rotational speed, which is related to the grid frequency and the number of poles in the generator, the type of hydroturbine can be chosen. Figure 1.4 shows the domain of application of the different types of hydroturbines as function of the nominal net head Hn (meters of water) and the nominal discharge Q (m^3/s) of the machine. Typically, for high, medium, and low head, Pelton, Francis, and Kaplan turbines are respectively chosen (see Fig. 1.4). However, the final decision on the type of turbine is also based on the construction and maintenance costs and the flexibility of operation.

Because of its reliability, high efficiency, and wide operating range, the Francis turbine is widely used in hydropower plants. Francis turbines are the most common hydroturbine in use today [6]. They cover a head range from 20 to 700 meters and an output power range from a few kilowatts up to one gigawatt. Some of the world's well-known hydropower plants that use Francis turbines are Three Gorges in China with 22,400 MW (32 × 700 MW), Itaipu on the border between Brazil and Paraguay with 14,000 MW (20 × 700 MW), Grand Coulee in the United States with 6,809 MW, and Hoover Dam in the United States with 2,074 MW [7]. Figure 1.5 shows the installation of a Francis turbine at Grand Coulee dam's third powerplant in 1974.

Figure 1.6 shows a simplified view of a hydropower plant employing a Francis turbine. A Francis turbine is a mixed-flow machine where flow enters radially and exits axially (c.f., Kaplan or propeller turbine which is an axial-flow machine where flow enters and exits axially). A Francis turbine is composed of five main components: spiral casing, stay vanes, guide vanes (wicket gates), runner, and draft tube, as shown in Fig 1.7. The stored water behind a dam reaches the spiral casing through the penstock. The spiral shape of the casing permits the conversion of the flow direction from axial to radial and balances flow distribution in the stay vane channels. The guide vanes distribute and control the incoming flow angular momentum to the runner. This distributor mechanism consists of a large number of guide vanes (e.g., 20 as in Fig. 1.7) around the circumference, which are simultaneously adjustable. The opening angle of the guide vanes controls the flow

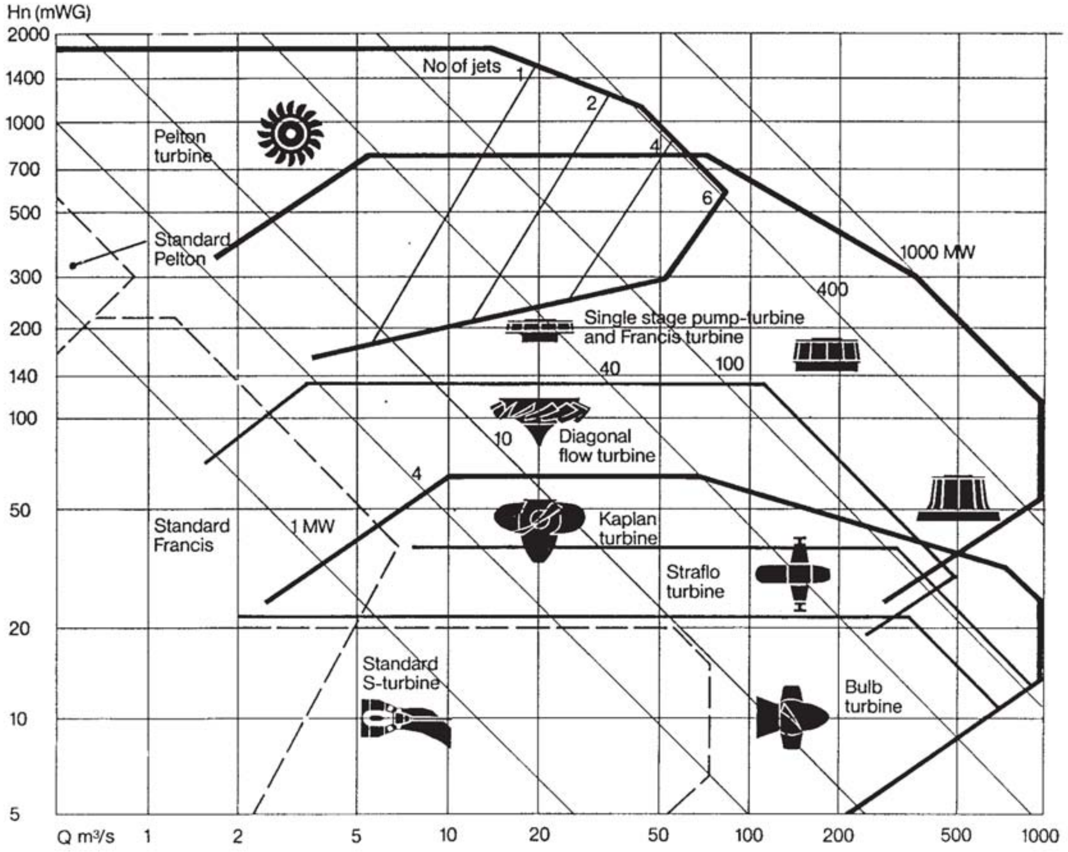

Figure 1.4: Typical application range for various turbines, given as a function of nominal net head (Hn) and flow rate (Q). Source: Franc et al. [5].

rate through the runner. The runner is made up of several fixed curved blades (see also Fig. 1.5). The curved shape of the blade induces the necessary pressure difference on the two sides of the blade that causes the rotational motion. The axis of the runner is coupled to the generator, which converts the rotational motion into electric power. The water flows through the turbine, then through the draft tube, and finally to the tail race downstream of the draft tube exit.

Head, flow rate, and angular velocity determine the flow conditions of a Francis turbine. The characteristics of the machine are represented on a φ vs. ψ hill chart (obtained from dimensional analysis) for a given angular velocity (see Fig. 1.8). The dimensionless coefficients of the head ψ and of the flow rate φ allow comparison with other machines of different dimensions and rotational speeds and are defined as [10]

Head (energy) coefficient

$$\psi = \frac{2gH}{\omega^2 R^2} \tag{1.2}$$

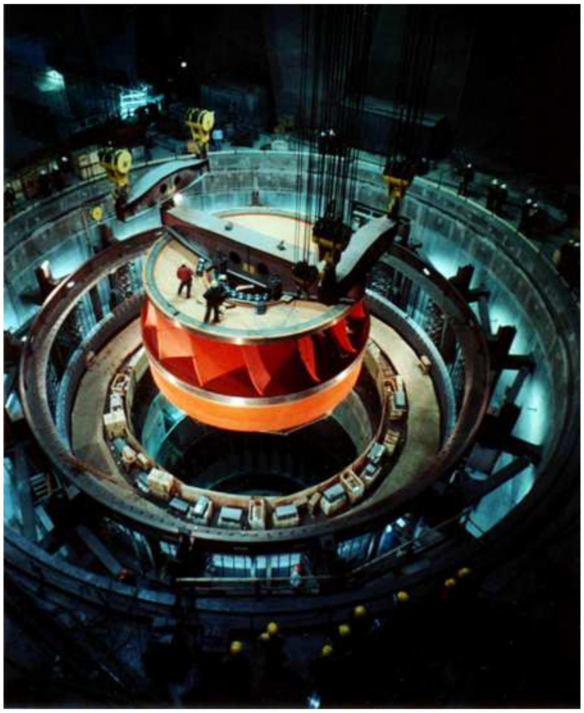

Figure 1.5: Installation of a Francis turbine at Grand Coulee dam's third powerplant (December, 1974). Source: U.S. Bureau of Reclamation photo archives.

Flow rate (discharge) coefficient

$$\varphi = \frac{Q}{\pi \omega R^3} \tag{1.3}$$

Here H is the turbine head, Q is the turbine flow rate, ω is the runner angular velocity, and R is the runner radius. The specific speed ν_s is a non-dimensional parameter based on the best efficiency point (nominal discharge, head and rotational speed) of the machine and defines the main characteristics of the runner design. The specific speed of the machine is defined as follows [10]

$$\nu_s = \omega \frac{(Q/\pi)^{1/2}}{(2gH)^{3/4}} = \frac{\varphi^{1/2}}{\psi^{3/4}} \tag{1.4}$$

Depending on the specific speed, Francis turbines are divided into three types: low- ($\nu_s \leq 0.35$), medium-, and high-speed ($\nu_s \geq 0.6$). For high specific speed machines the draft tube is the most critical component with respect to losses [11].

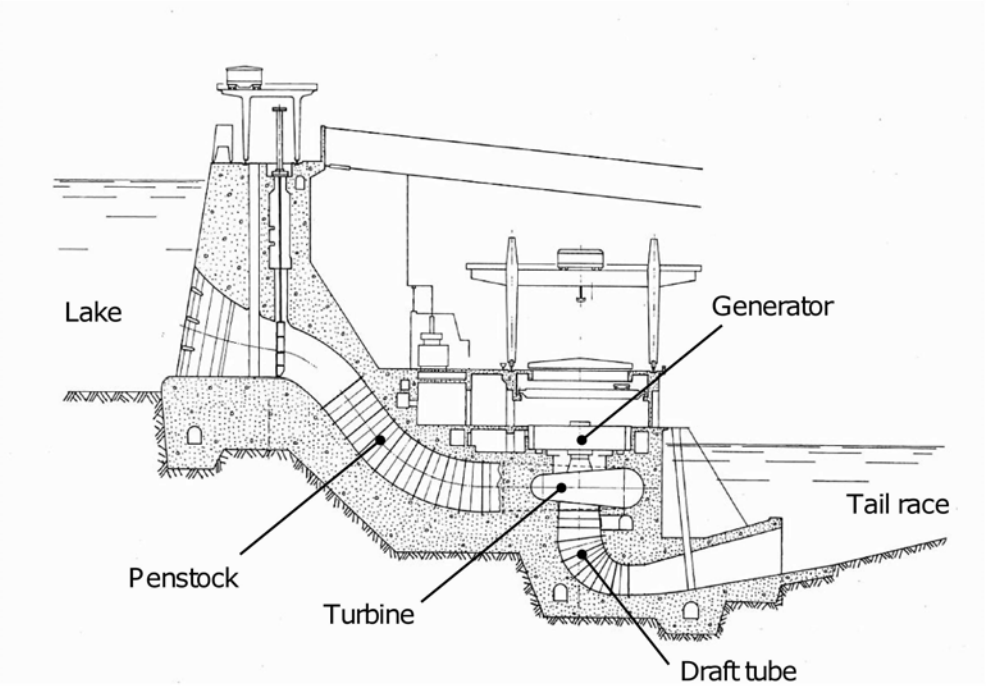

Figure 1.6: Vertical cross section of a hydropower plant. Modified from Henry [8].

1.2 Flow in the Draft Tube of a Francis Turbine

As discussed in the previous section, the draft tube is the last component of a Francis turbine connecting the flow exiting from the runner to the tail-water region. The main goal of a Francis turbine draft tube is to decelerate the flow exiting the runner, thereby converting the excess of kinetic energy into static head. The draft tube increases the efficiency of the plant at the best efficiency point (BEP) and makes it possible to locate the turbine above the tail-water. In practice, the hydraulic performance of a draft tube is quantified by the pressure recovery coefficient given by the following [12]

$$\chi \equiv \frac{\left(\frac{p}{\rho} + gz\right)_{\text{outlet}} - \left(\frac{p}{\rho} + gz\right)_{\text{inlet}}}{\frac{Q^2}{2A_{\text{inlet}}^2}\left[1 - \left(\frac{A_{\text{inlet}}}{A_{\text{outlet}}}\right)^2\right]} \tag{1.5}$$

The numerator in Eq. 1.5 is the difference in potential energy and the denominator is the difference in kinetic energy from inlet to outlet of the draft tube. For an ideal

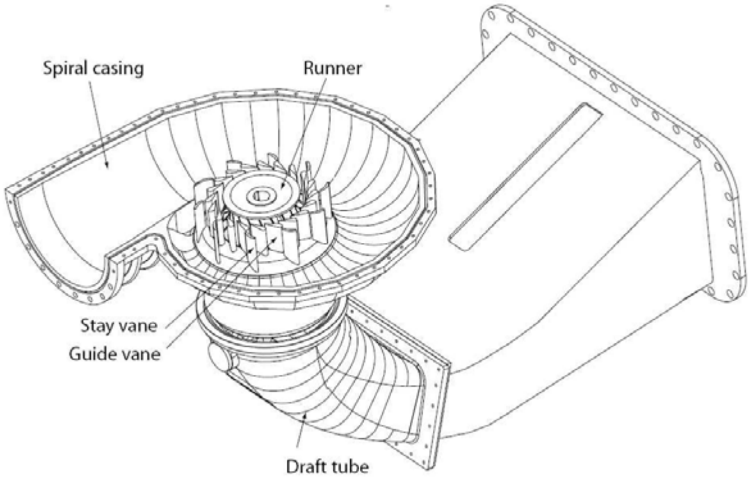

Figure 1.7: Francis turbine components. Source: Zobeiri [9]

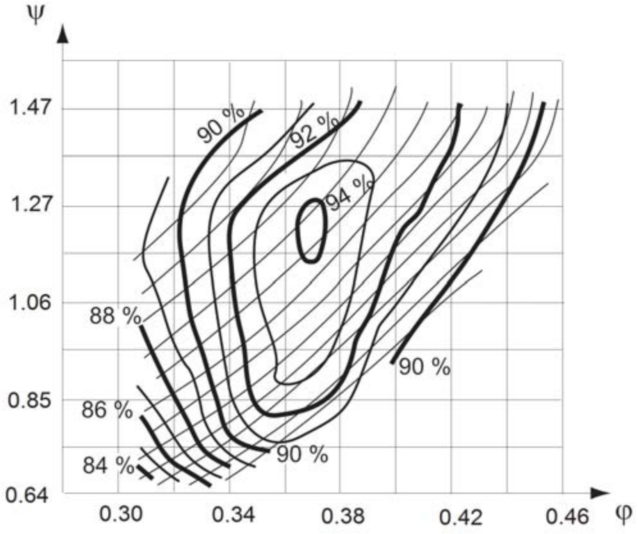

Figure 1.8: Sample hill chart of a Francis turbine, where isocontours of efficiency (thick lines) are plotted as a function of head coefficient and flow rate coefficient. Thin lines represent constant wicket gate opening angles. Source: Mauri [11]

draft tube with no losses the pressure recovery factor is equal to one. However, in practice, losses including friction, flow separation, and flow blockage result in lower pressure recoveries.

For constructional reasons most plants have elbow-type draft tubes and often one or two piers are included. As depicted in Fig. 1.9, this type of draft tube can be decomposed into three parts: the inlet cone, the elbow part, and the last straight divergent diffuser.

Most of the pressure recovery occurs in the draft tube inlet cone [12]. Modern hydraulic turbines have compact elbow draft tubes, with a rather short cone. As a result, the draft tube hydrodynamics is very complex due to the combination of swirling flow deceleration with flow direction and cross-section shape/area changes.

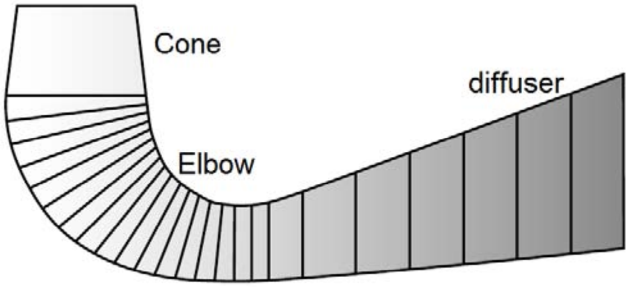

Figure 1.9: Components of an elbow draft tube

Theoretically, the flow leaving the runner and ingested by the draft tube is almost purely axial at the best efficiency point (see Fig. 1.10(b) where $V_t = 0$ and $V = V_a$). However, in practice, to prevent flow separation from the draft tube wall and to minimize hydraulic losses associated with kinetic energy-to-static pressure conversion in the draft tube, a certain level of residual swirl is provided at the runner outlet. This swirling flow at the draft tube inlet is tuned for optimal performance at the best efficiency operating point. However, the swirl ingested by the draft tube departs significantly from the best configuration as the turbine discharge varies, and hydroturbines, especially Francis turbines, operating at off-design conditions often have a high residual swirl at the draft tube inlet.

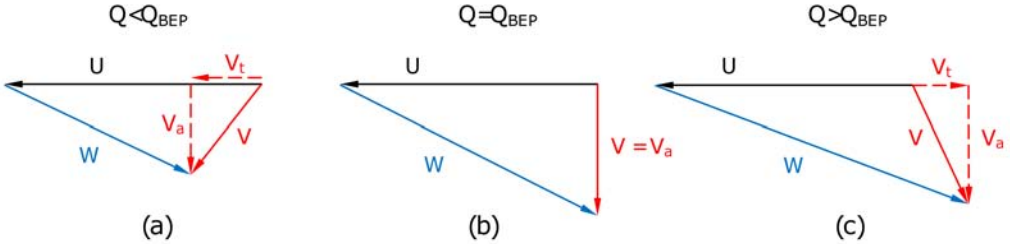

Figure 1.10: Velocity triangles at runner exit for (a) part-load, (b) best efficiency point, and (c) full-load. U is the runner velocity, W is the relative velocity, and V is the absolute velocity leaving the runner and ingested by the draft tube, with V_a and V_t being axial and circumferential (swirl) components.

The instability of decelerated swirling flow in the draft tube may lead to efficiency reduction and severe pressure fluctuations. These pressure fluctuations become more dangerous if their corresponding frequency approaches the natural frequency of the power plant structures. This can result in vibration of the whole installation [13]. In general, vibration and pounding noise, periodic variations in power output (power swing), vertical movement of the runner, and penstock vibrations are all attributed to the draft tube flow instabilities [14].

Depending on the operating conditions, two forms of the flow instability can be observed (Fig. 1.11). At part-load conditions, for which the flow rate is lower than the one at the BEP, the flow has a positive absolute circumferential velocity in the same sense as the runner revolution (see Fig. 1.10(a) where V_t and U are in the same direction). In this case a helical precessing vortex called the "vortex rope" develops in the draft tube with the frequency of precession of about 0.2-0.4 of the runner's rotation frequency [13]. At full-load conditions corresponding to a higher flow rate than that of the BEP, the absolute circumferential velocity is negative inducing a swirling flow rotating in the opposite direction of the runner (see Fig. 1.10(c) where V_t and U are in opposite direction). In this case, the vortex rope takes a nearly axisymmetric shape, sometimes called the "torch". In both cases, cavitation may occur in the vortex core.

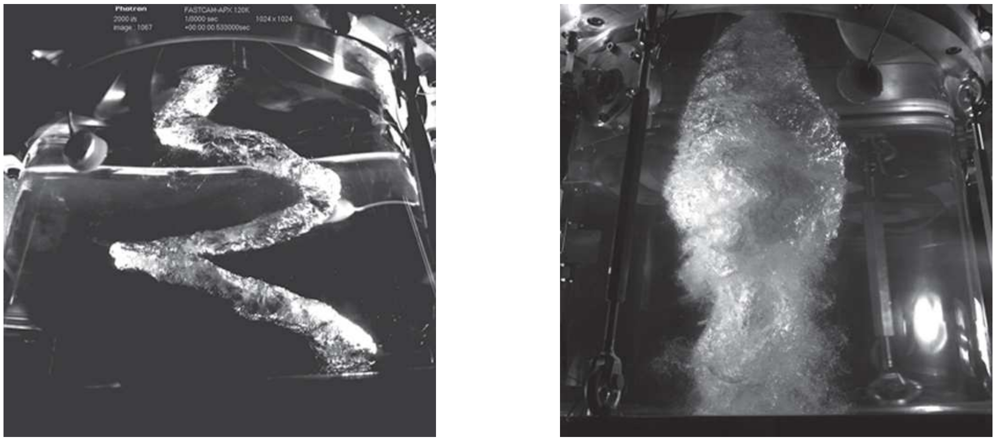
(a) part-load

(b) full-load

Figure 1.11: Vortex rope formation in a draft tube at (a) part-load, and (b) full-load condition. In the latter case, it is also called the "cavitation torch". Source: Alligné [10].

The physical mechanism of vortex rope formation relies on "vortex breakdown". Vortex breakdown [15] can be defined as a sudden change of the flow structure. At a critical swirl level, a steady quasi-cylindrical flow can nearly instantly transform to a highly unsteady, asymmetric, recirculating flow. Experimental visualizations of vortex breakdown in pipes at low Reynolds numbers [16] show that the initial flow structure of a vortex breakdown often resembles a bubble. In bubble-like vortex breakdown a free stagnation point forms. The outer part of the flow is accelerated, while the inner part of the flow starts to recirculate in the region just downstream of the stagnation point. The bubble-like vortex breakdown is very unstable and its life is usually very short. The bubble structure eventually transforms to a highly unsteady flow. Usually, as in the case of the draft tube, the vortex breakdown changes to a helical vortex structure that rotates around the axis of the draft tube cone, as well as spins around its own axis. This phenomenon is what is known as the vortex rope.

1.3 Previous Studies on Vortex Rope in Draft Tubes

Experimental, numerical, and analytical investigations have been carried out for more than fifty years to understand and to predict the vortex rope formation. In this section, the state of the art is divided into two parts. The first one deals with the analytical and experimental studies of the flow in the draft tube, and the second one recounts the numerical investigations that aim to predict and simulate the vortex rope formation in the draft tube.

1.3.1 Analytical and Experimental Studies

The first analytical and experimental investigations were focused on understanding the development of swirling flow in circular tubes with constant diameter. Swirl number, defined as the ratio between the circumferential and the axial momentums, has been shown to have large effects on the flow field. Increasing the swirl level, a recirculating region acting as a blockage is induced, called the vortex breakdown. Harvey [17] was the first to visualize this phenomenon experimentally with an air swirling flow in a straight pipe. Depending on different combinations of Reynolds number and swirl number, different types of vortex breakdown may appear as observed by Sarpkaya [16]. Cassidy and Falvey [18] focused on the helical form of the vortex breakdown. They set up an experimental apparatus to study its occurrence and to measure wall pressure fluctuations related to the vortex core precession. Since then many experimental investigations on the vortex breakdown phenomenon have been carried out [19, 20]. Moreover, many theories and explanations of the vortex rope formation and vortex breakdown have been developed by different researchers. Some of them, including Ref. [21], assume that this phenomenon is based on the concept of a critical state related to the wave phenomena, analogous to the hydraulic jump in open-channel flow, whereas others [22] think that a better analogy is between vortex breakdown and boundary layer separation. (It is shown in this study that the vortex rope is associated with the shear layer at the interface of the recirculating region near the centerline of the draft tube and swirling outer flow; more details are given in Chapter 4.)

Later, the previous knowledge on the vortex breakdown has been applied to the draft tube flow in Francis turbines [23]. The helical cavitating vortex rope in Francis turbines is assumed to be a manifestation of the vortex breakdown phenomenon. Susan-Resiga et al. [24] analytically demonstrated the unstable nature of the flow in the draft tube. They have shown that the swirling flow at the outlet of the runner can be accurately decomposed into a sum of three distinct vortices. Kuibin et al. [25] derived a mathematical model that can recover averaged axial and circumferential velocity profiles, as well as the vortex rope geometry, precessing frequency, and the level of pressure fluctuations at the wall. They stated that this model would be useful in the early stages of the runner design. Susan-Resiga et al. [26] introduced a mathematical model for computing the axial and circumferential velocity profiles of the swirling flow exiting the runner within the full operating range. Their model can be used for the early optimization stages of the runner design.

In order to understand and analyze the flow pattern in the draft tube of Francis turbines, many experimental investigations have been carried out. Nishi et al. [27, 28] measured wall pressure fluctuations in an elbow draft tube for different flow regimes. They focused on the regime where a stagnant region in the center of the draft tube was surrounded by a rotating helical vortex rope. The influence of the cavitation number on the amplitude of pressure pulsations and on the vortex precession frequency was pointed out. The practical importance of the vortex rope in a Francis turbine and its potential harmful effects led to the FLINDT (FLow INvestigation in a Draft Tube) research project [29]. The main objective of this project was to understand the physics of the flow within the elbow draft tube of a Francis turbine. Accordingly, an extensive experimental database was built up. In this framework, Arpe et al. [30] performed extensive unsteady wall pressure measurements of the rotating vortex rope for different operating points in thirteen cross sections of the draft tube. Advanced flow measurements such as Laser Doppler Anemometry (LDA) and Particle Image Velocimetry (PIV) were also used for understanding the flow pattern in this project. Ciocan et al. [31] measured velocity profiles at the draft tube inlet by LDA, and afterwards Iliescu et al. [32] extended the velocity field measurements to the whole draft tube cone using PIV. The synchronization of the PIV measurements with vortex rope visualization allowed quantification of both the periodic velocity components and the rope shape. A recent review of analytical and experimental studies on vortex rope formation in draft tubes was performed by Nishi and Liu [33].

1.3.2 Numerical Studies

In parallel to the experimental and analytical studies, a considerable number of numerical investigations were attempted and results were compared to experimental data. The progress of the numerical techniques in the prediction of the turbine characteristics for the operating ranges in the vicinity of the best efficiency point (BEP) ensures a good accuracy. One of the new challenges for the numerical simulation is to predict off-design operating regimes where the vortex rope appears in the draft tube.

Several previous draft tube flow predictions have been carried out employing the Reynolds-Averaged Navier-Stokes (RANS) equations with various turbulence closure models. In the framework of the FLINDT project, Mauri [11] performed steady numerical simulations to obtain the averaged flow pattern under various conditions. Miyagawa et al. [34] reported an unsteady simulation of flow in an elbow draft tube for a Francis pump-turbine. The purpose was to analyze the effect of the velocity profile at the runner outlet on the flow instability in the draft tube. They observed the same vortex behavior in numerical simulations and experiments by qualitative comparisons. Sick et al. [35] performed a numerical simulation of a draft tube vortex in a medium specific speed pump-turbine. The computational domain included the runner and the draft tube in order to capture the unsteady pressure field, caused by the draft tube vortex, on the runner. The flow field was simulated by solving the RANS equations with the Reynolds Stress Model (RSM) as the turbulence closure model. The comparison with experimental data showed an overestimation of the vortex frequency but good agreement for the pressure fluctuation amplitude. Unsteady RANS simulations and experimental measurements were carried out and compared by Ciocan et al. [36]. They utilized a two-equation standard k-ε turbulence model in ANSYS-CFX 5.6 and a relatively coarse mesh for computations. Vortex global quantities, i.e., pressure fluctuation amplitude and vortex frequencies were predicted with 3% and 13% error respectively while the mean axial velocity was underestimated near the centerline. Zhang et al. [37] investigated the physical characteristics and control strategy of the unsteady vortical flow in a Francis turbine draft tube, based on the URANS simulation of the "sole draft tube flow" under part-load conditions. The computation was conducted using the commercial CFD code FLUENT 6.1.22 and the renormalization group (RNG) k-ε turbulence model with logarithmic wall functions. No comparison with experimental data, however, was reported. Steady and unsteady computations of flow in an elbow draft tube were performed by Vu et al. [38] in order to predict draft tube losses over the complete range of turbine operation. The two-equation k-ε turbulence model was used in two flow solvers, ANSYS-CFX 12.1 and OpenFOAM-1.5dev. They stated that the choice of turbulent inlet boundary conditions is important even close to the best efficiency operating point. It was also observed that as the operating conditions move away from the best efficiency point, the performance of the k-ε turbulence model tends to deteriorate, particularly for part-load operating conditions.

Relatively less work has been done on studying the performance of turbulence models for hydraulic machinery applications. Turbulence modeling studies can be categorized in two areas. The first area is the evaluation of different RANS turbulence closure models in predicting time-averaged turbulent flow. One such work has been done by Yaras and Grosvenor [39] who tested several turbulence models to establish the prediction accuracy with respect to strongly swirling confined flow. They concluded that predictions were rather poor with all models (the two-layer k-ε model of Rodi, the two-equation shear stress transport (SST) model of Menter, and the one-equation eddy-viscosity model of Spalart and Allmaras) significantly overestimating radial diffusive transport. Among these models, the SST model yielded the worst predictions. Ware [40] investigated three turbulence models for draft tube simulations, and concluded that the RNG k-ε model has significant problems properly predicting the flow, while k-ε and RSM models give quite comparable results which are in acceptable agreement with experimental data. The second area of turbulence modeling studies are those related to the investigation of more complex turbulence models including large eddy simulation (LES) and hybrid RANS/LES models in draft tube simulations. The main objective in this area is to study the models' capability of predicting detailed unsteady, turbulent features of the flow. The first attempt to numerically simulate the unsteady flow in a draft tube using LES was done by Skotak [41]. In spite of a quite coarse grid, a vortex rope was simulated that agrees qualitatively with the rotating rope observed in experiment. Ruprecht et al. [42] developed an extended k-ε model based on the very large eddy simulation (VLES) approach and applied it to the unsteady simulation of flow in a draft tube. They showed that unsteady features of the flow (e.g., pressure amplitudes and vortex rope size) are better predicted with this model compared to using the standard k-ε model in which the flow becomes stationary due to too much damping. The frequency of pressure fluctuations is well predicted in their simulations but amplitudes are underestimated. Various hybrid RANS/LES models have been used for unsteady swirling flow and draft tube simulations including the detached eddy simulation (DES) [43], the filtered SST k-ω model [44], and the scale-adaptive simulation (SAS) [45, 46]. Most of these models have shown relative improvement over the URANS models. However, detailed evaluation and investigation of these models for various operating conditions of the hydroturbine are seldom addressed.

1.4 Present Study

1.4.1 Scientific Motivation

The flow in the draft tube of a hydroturbine operating at off-design conditions is a complex hydrodynamic phenomenon (see Fig. 1.12). It is characterized by highly unsteady large scale vortices, regions with high shear and intense turbulence production, and recirculation regions. The complexity follows from the swirling flow entering the draft tube, the wake of the crown cone, the draft tube flow streamline curvature, change in cross-sectional shape, and adverse pressure gradients. Each of these characteristics is known to be difficult to predict with numerical computations. A clear comparison with detailed measurements, which would allow an estimation of the influence of modeling parameters, is necessary. Various forms of unsteadiness characterize the flow of hydraulic turbines. In the draft tube, particularly for part-load operating conditions, strong flow fluctuations are observed. The application of the traditional, two-equation turbulence models for the simulation of unsteady flows is questionable, and the limitations are still not well defined. The conventional closure models have been derived for and calibrated by reference to simple, steady flows near walls and then used in unsteady free shear layer flows. Therefore, the likelihood of traditional closure models being an adequate framework decreases with increasing the complexity of the flow and the frequency of the coherent structures. Therefore, applications of more complex models, such as hybrid RANS/LES models, as well as improving the currently used models, are challenges that need to be addressed.

1.4.2 Industrial Motivation

As discussed in Sec. 1.1, hydropower is the largest source of renewable electricity generation. High peak operating efficiencies (above 95%), storage capability, and fast response

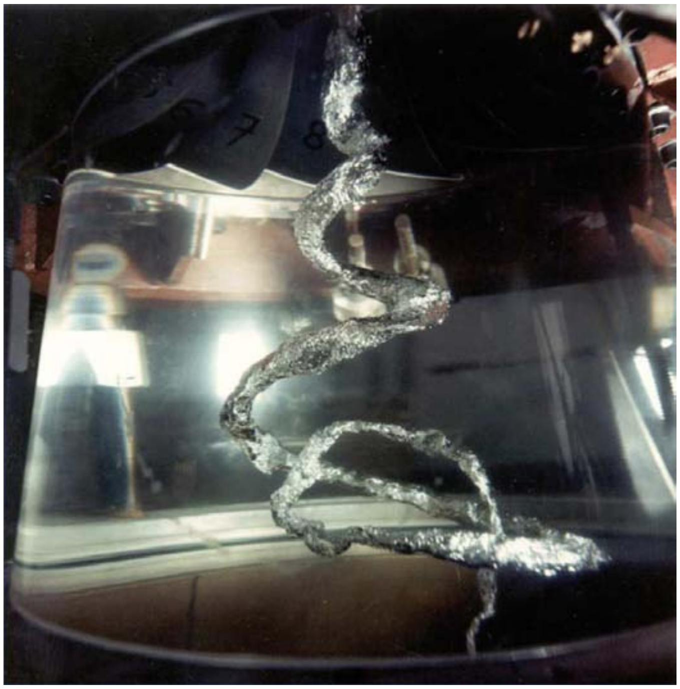

Figure 1.12: Flow in the draft tube of a model Francis turbine showing the development of a cavitating unsteady vortex rope. Source: Brennen [47].

make hydropower an ideal form of power generation. However, the variable energy demand and load following require hydroturbines to be operated over an extended range of conditions, quite far from their design point (the BEP).

One of the main components of a hydroturbine where unwanted flow phenomena appear under off-design conditions is the draft tube. As shown in Fig. 1.13, the draft tube displays an abrupt increase in hydraulic losses as the operating regime departs from the BEP, while other components (e.g., stay vanes, guide vanes, and runner) have rather modest variations with the operating regime [48]. Therefore, it is admitted that for modern Francis turbines the shape of the performance chart (hill chart) is dictated by the losses in the draft tube [26]. It must be recognized that efficiency improvements of only a few tenths of a percent generate substantially increased profits and save water which is limited nowadays.

Additionally, most of the hydropower plants were designed several decades ago. This gives rise to the potential for changing their design in order to improve the efficiency and associated power output as well as greater operating stability. Usually the runner and guide vanes are the focus of the refurbishment process and the spiral casing and the draft tube are seldom redesigned due to constructional costs. However, undesirable

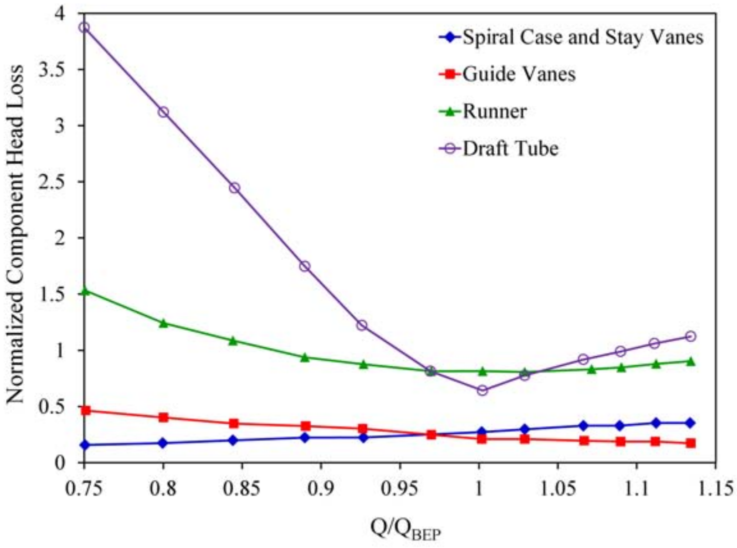

Figure 1.13: Head losses of individual components of a hydropower plant normalized by the runner head loss at the best efficiency point. Data source: Vu et al. [48].

flow behavior occurs when the runner and the draft tube are not matched. This can result in flow instability and can reduce the optimal operating range of the machine[1]. Understanding of the physics of the flow in the draft tube allows engineers to avoid undesirable phenomena such as pressure fluctuations, flow blockage (draft tube surge), and other dangerous instabilities when redesigning the runner. The knowledge gained can be applied to improve the output of existing hydropower plants, adding significantly to the power generation capacity.

Finally, in addition to the direct environmental benefits of renewable energy, draft tube studies have indirect benefits: a better understanding of the flow characteristics within the draft tube allows better control of the mixing process in this component, e.g., for the air admission purposes, which is of prime importance for the local river life.

---

[1] One such problem, described by Falvey [49], was associated with the Fremont Canyon Power Plant in Wyoming. Vibrations and noise due to the draft tube vortex were so severe that operation was prohibited. Eventually, it was found that the exit area of the runner was too small. The trailing edge of each runner blade was trimmed to increase the exit area, which considerably reduced the severity of the vibration and noise.

1.4.3 Dissertation Focus Areas and Objectives

Given the adverse effects (severe pressure fluctuations, structural vibrations, flow instabilities, and efficiency drop) that vortex rope can have on the operation of a hydropower plant, analysis and investigation of the vortex rope formation as well as control or elimination of its effects are necessary for improving hydroelectric plant efficiency over a wide range of operating conditions, and preventing structural vibrations. Furthermore, detailed features of the vortex rope formation are shown to be difficult to predict with numerical computations. These computations are still widely based on the traditional RANS turbulence models due to ease of use and lower computational expenses. The limitations of such turbulence models, however, are not well known, particularly for the prediction of complex, three-dimensional, time-dependent flows. On the other hand, the use of more complex models, such as hybrid RANS/LES simulations, in hydroturbine applications is not well documented.

The main objectives of the present study are, therefore, the high fidelity numerical simulation, physical understanding, analysis, and mitigation of the vortex rope formation, with the emphasis being on the investigation of turbulence models in predicting this complex flow. Therefore, attention is focused in particular on off-design operating conditions of the hydroturbine where considerable flow instability, efficiency loss, and structural vibrations due to the vortex rope formation have been reported. Complex hydrodynamic phenomena associated with these losses and unsteady pressure fluctuations are studied in detail. In particular, this work aims to understand the fundamental processes governing the formation of the vortex rope, and to study and define the predictive capability of the models and to develop/modify turbulence models for better prediction of vortex rope behavior. Additionally, a method for mitigation of the vortex rope formation is numerically investigated and its effects on the draft tube performance and pressure fluctuations are studied. Therefore, this study is of interest both from a theoretical and an application perspective.

Chapter 2

General Computational Methodology

"Mechanics is the paradise of the mathematical sciences, because by means of it one comes to the fruits of mathematics." - Leonardo da Vinci

This chapter is devoted to a brief discussion of the numerical methodology in this study. The governing equations representing the dynamics of the turbulent flow and methods for numerically solving these equations are discussed first. Since one of the primary objectives of this study is to investigate various turbulence models, a wide range of models is then considered and discussed. Finally, computational techniques including the discretization and the grid generation are presented. Further details of the numerical setup for each test case are given in the associated chapter.

2.1 Governing Equations

Most of the flows in nature and in industry are turbulent. In these flows an irregular fluctuation (mixing and vortical motion) is superimposed on the main stream. The fluctuating turbulent motions contribute significantly to the transport of mass and momentum, and hence have a determining influence on the velocity field. The governing equations of turbulent flows are the conservation laws of mass, momentum, and energy. In engineering applications, many hydraulic flows can be considered incompressible. Also, the flow in the present application can be considered isothermal, and the fluid is assumed to be Newtonian. An incompressible and isothermal flow has constant viscosity. This flow can be described by the velocity and pressure fields. The system of conservation laws (mass and linear momentum) is known as the Navier-Stokes equations.

2.1.1 The Navier-Stokes Equations

The formulation of the equations governing the fluid flow is ascribed to the French engineer/physicist Claude-Louis Navier (1785-1836) and the English mathematician/physicist George Gabriel Stokes (1819-1903). This section introduces the Navier-Stokes equations and continuity.

For an incompressible flow where the density is constant following any fluid particle, the continuity equation can be simplified to

$$\frac{\partial u_i}{\partial x_i} = 0 \tag{2.1}$$

The momentum equation is merely Newton's second law formulated for a fluid particle. For an incompressible flow of a Newtonian fluid in a stationary frame of reference, it can be written as

$$\begin{aligned} \rho\frac{\partial u_i}{\partial t} + \rho u_j \frac{\partial u_i}{\partial x_j} &= -\frac{\partial p}{\partial x_i} + \frac{\partial \tau_{ij}}{\partial x_j} + \rho g_i \\ &= -\frac{\partial p}{\partial x_i} + \frac{\partial}{\partial x_j}\left[\mu\left(\frac{\partial u_i}{\partial x_j} + \frac{\partial u_j}{\partial x_i}\right)\right] + \rho g_i \end{aligned} \tag{2.2}$$

The most important property of a Newtonian fluid is that the shear stress tensor τ_{ij} is a linear function of the strain rate tensor, i.e., $\tau_{ij} = \mu\left(\frac{\partial u_i}{\partial x_j} + \frac{\partial u_j}{\partial x_i}\right) = 2\mu S_{ij}$. The Newtonian assumption is valid for water and air at standard temperature as considered in this study. The gravitational body force ρg_i is usually integrated and included in the pressure term.

The Navier-Stokes equations belong to the class of non-linear partial differential equations. The solution to the equations is the local velocity vector $u_i(x_i, t)$ and pressure $p(x_i, t)$. However, it is not straightforward to find a solution to the Navier-Stokes equations for turbulent flows. Turbulent fluid motion is highly random and consists of many eddies with different length and time scales. Due to these complexities, turbulent motions are extremely difficult to describe and to predict. The principal difficulty in computing and modeling turbulent flows resides in the dominance of non-linear effects and the continuous and wide spectrum of observed scales. In the direct numerical simulation (DNS) approach, no extra model is applied so that motions of all sizes have to be resolved numerically by a grid which is sufficiently fine. Hence, the computational requirements increase rapidly with Reynolds number. The storage capacity and speed of present-day computers are still not sufficient to allow a DNS solution for a practically relevant turbulent flow. Hence, for many applications DNS, which is of great value for theoretical investigations and model testing, is unaffordable. An alternative approach is to average or filter the governing equations and to solve for the averaged/filtered velocity and pressure fields. By averaging or filtering the Navier-Stokes equations, flow characteristics of some of the length scales of the flow need not be computed (instead they are modeled, depending on which type of modeling is used), and in general a much larger (coarser) grid spacing can be used.

2.1.2 The Reynolds-Averaged Navier-Stokes Equations: The RANS Approach

The RANS equations are based on the Reynolds decomposition, which reads

$$\phi_i = \bar{\phi}_i + \phi_i' \tag{2.3}$$

where $\bar{\phi}_i$ is an ensemble-averaged quantity and ϕ_i' is a fluctuation from the ensemble average. The ensemble average can be expressed as

$$\bar{\phi}_i = \lim_{N \to \infty} \frac{1}{N} \sum_{i=1}^{N} \phi_i \tag{2.4}$$

The ensemble average is a tool that separates stochastic turbulent fluctuations from the resolved flow. The ensemble average of a stochastic fluctuation equals zero by definition, i.e., $\bar{\phi}_i' = 0$, and hence, $\bar{\bar{\phi}}_i = \bar{\phi}_i$.

The RANS equations can be derived by replacing the arbitrary quantity ϕ_i in the Reynolds decomposition by velocity and pressure, and then implementing the decomposed variables in Eqs. (2.1) and (2.2), which yields

$$\frac{\partial \bar{u}_i}{\partial x_i} = 0 \tag{2.5}$$

$$\rho \frac{\partial \bar{u}_i}{\partial t} + \rho \bar{u}_j \frac{\partial \bar{u}_i}{\partial x_j} = -\frac{\partial \bar{p}}{\partial x_i} + \frac{\partial}{\partial x_j}\left[\mu\left(\frac{\partial \bar{u}_i}{\partial x_j} + \frac{\partial \bar{u}_j}{\partial x_i}\right) - \tau_{ij}^{\mathrm{RANS}}\right] \tag{2.6}$$

These equations are known as the Reynolds-averaged Navier-Stokes (RANS) equations and they can be solved for the averaged velocity and pressure fields. However, an unknown term $\tau_{ij}^{\mathrm{RANS}}$ results from averaging, and now appears in Eq. (2.6). This term, known as the Reynolds stress tensor $\tau_{ij}^{\mathrm{RANS}} = \rho\overline{u_i' u_j'}$ introduces six unknown quantities which must be modeled in order to close the system of equations. This is called the "turbulence closure problem".

2.1.3 The Filtered Navier-Stokes Equations: The LES Approach

Another way of averaging is to filter the equations. A filtering operation converts the governing equations into a large eddy simulation (LES) form. A filtered quantity, in the fluid domain D, can be written as [50]

$$\hat{\phi}_i(\boldsymbol{x}, t) = \int_D G(\boldsymbol{x} - \boldsymbol{x'}, \Delta)\phi_i(\boldsymbol{x'}, t)\, d\boldsymbol{x'} \tag{2.7}$$

where Δ is the filter width (related to the computational mesh size[1]) and G is a filter function for which

$$\int_D G(\boldsymbol{x} - \boldsymbol{x'}, \Delta)\, d\boldsymbol{x'} = 1 \tag{2.8}$$

The filter G determines the scale of the resolved eddies in the flow by filtering out any eddies with scales smaller than the filter width. Figure 2.1 illustrates the effect and importance of the filter width. If the filter is too large, some details of the actual flow can be lost, while a proper filter size can capture important dynamics of the actual flow. Furthermore, it should be noted that unlike a Reynolds-averaged quantity, for a filtered quantity in general $\hat{\hat{\phi}}_i \neq \hat{\phi}_i$, as shown in Fig. 2.1. This is because the filtered value of the fluctuating quantity is not zero anymore, and there is a correlation between the filtered and fluctuating quantities [51].

The 3D box filter, provided implicitly in the finite-volume discretization, is commonly used in computational fluid dynamics solvers [52, 53]. Using this filtering operation, a filtered variable can be written as

$$\hat{\phi}_i(\boldsymbol{x}, t) = \frac{1}{\delta V}\int_{\delta V} \phi_i(\boldsymbol{x'}, t)\, d\boldsymbol{x'} \tag{2.9}$$

where δV is the local cell volume of the computational grid. Therefore, the filter width is determined by the computational grid size, and, hence, all eddies smaller than the computational spacing are filtered out.

By applying this filter to each term of Eqs. (2.1) and (2.2), the filtered Navier-Stokes equations are obtained, namely,

---

[1] Therefore, filtering is an operation in space.

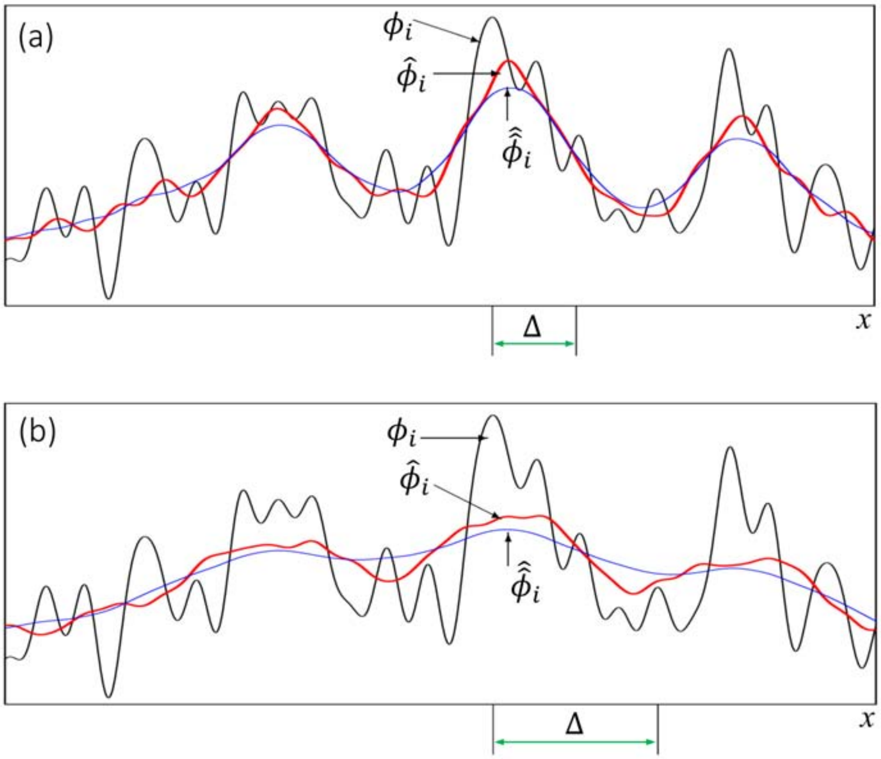

Figure 2.1: Filtered functions $\hat{\phi}_i$ and $\hat{\hat{\phi}}_i$ obtained from spatial filtering of $\phi_i(x)$ using (a) narrow box filter and (b) wide box filter.

$$\frac{\partial \hat{u}_i}{\partial x_i} = 0 \tag{2.10}$$

$$\rho \frac{\partial \hat{u}_i}{\partial t} + \rho \hat{u}_j \frac{\partial \hat{u}_i}{\partial x_j} = -\frac{\partial \hat{p}}{\partial x_i} + \frac{\partial}{\partial x_j}\left[\mu \left(\frac{\partial \hat{u}_i}{\partial x_j} + \frac{\partial \hat{u}_j}{\partial x_i}\right) - \tau_{ij}^{\mathrm{SGS}}\right] \tag{2.11}$$

Here, the last term is called the subgrid scale stress tensor τ_{ij}^{SGS} which needs to be modeled. This term appears as a result of filtering and can be expressed as

$$\tau_{ij}^{\mathrm{SGS}} = \rho\left(\widehat{u_i u_j} - \hat{u}_i \hat{u}_j\right) \tag{2.12}$$

The different LES variants are based on the filtering techniques and the modeling of the subgrid scale stress tensor.

2.1.4 The Hybrid RANS/LES Approach

As shown in Secs. 2.1.2 and 2.1.3, the Reynolds-averaged and filtered Navier-Stokes equations, Eqs. (2.6) and (2.11), are identical with the exception of the form of the unknown stress tensor, $\tau_{ij}^{\mathrm{RANS}}$ or τ_{ij}^{SGS}. The obvious similarity is further enhanced by the usage of the eddy viscosity concept for most subgrid scale (SGS) models and that the employed models are commonly derived from RANS counterparts. If any eddy viscosity model is used to close any of the systems of equations, there is no mathematical difference between the two and merely a conceptual difference remains. As a consequence, not only do the governing equations exhibit a structural similarity, but so also do many of the turbulence models.

A RANS model depends on physical quantities describing the entirety of the turbulent fluctuations. For example in two-equation models, in general,

$$\tau_{ij}^{\mathrm{RANS}} = f\left(\frac{\partial \bar{u}_i}{\partial x_j}, k, l, C\right) \tag{2.13}$$

where C is a model constant, and k and l are the turbulent kinetic energy and length scale respectively. On the other hand, LES based on the Smagorinsky model [54] uses a relation like

$$\tau_{ij}^{\mathrm{SGS}} = f\left(\frac{\partial \hat{u}_i}{\partial x_j}, \Delta, C\right) \tag{2.14}$$

where Δ is a length scale related to the numerical grid, e.g., $\Delta = (\Delta_x \Delta_y \Delta_z)^{1/3}$. Therefore, it can be concluded that a model qualifies as an LES model if it explicitly involves the size of the computational grid; and RANS models, in contrast, depend only on physical quantities, including geometric features like the wall distance.

In the LES approach, the large, energy carrying, dynamically important, and flow-dependent eddies are solved directly, leaving only the smallest scales of turbulence with very low energy and supposedly universal behavior (assumed isotropic) to be modeled. The application of LES has been particularly successful in non-equilibrium flows in free shear layers, and in massively separated flows in which the accurate simulation of regions near the wall is not of primary importance [55]. However, one of the major obstacles to the use of LES in complex industrial flows with high Reynolds numbers, such as the flow in a draft tube, is the modeling of the near-wall region [56, 50]. The dynamics of the flow near the wall are strongly anisotropic even at small scales and turbulence production in this region is associated with an upscale energy cascade (energy transfer from smaller eddies near the wall, where turbulence production is maximum, to larger eddies away from the wall) that is largely dominant over the commonly assumed downscale energy cascade (energy transfer from larger to smaller eddies which eventually results in dissipation of the turbulent kinetic energy), presenting elsewhere. Also, the large eddies that must be captured on the computational grid to perform an accurate LES shrink in size and are not isotropic as one approaches the wall, leading to excessive computational costs [55]. In fact the small eddies are not isotropic near a wall either. Current LES modeling approaches require that either the near-wall region be adequately resolved (using a DNS-like grid near the wall which makes it inapplicable for industrial flows), or that an LES wall-model (for example a two-layer model [57] or a dynamic wall model [58]) be used, which to date has not provided accurate results in relatively complex flows [59, 60] (See Ref. [50] for further details).

Contrary to LES, the weakness in the RANS simulations is that the resolved large scale unsteady motions are often damped out by the turbulence model. The near-wall modeling, on the other hand, is often quite accurate since all these models are developed and calibrated for near-wall flows.

The hybrid RANS/LES methods aim at combining the best of RANS and LES turbulence models. Full realization of the potential of the hybrid RANS/LES approach requires that LES be used in regions of the flow to capture the physics the RANS model cannot, and RANS be used everywhere else for computational efficiency. The transition between LES and RANS solutions can be continuous or discontinuous in space, leading to two main classes of hybrid RANS/LES methods, namely “global” and “zonal” hybrid RANS/LES approaches [61].

The global hybrid methods rely on a single set of model equations, and a continuous treatment of the flow variables at the RANS/LES interface. They switch automatically from one method to another based on the physical and numerical (grid size) scales of the problem. Most global hybrid RANS/LES models are a merging between a RANS-type eddy viscosity model (see Sec. 2.2.1 for more details) and an LES-type subgrid viscosity model. Since these turbulent viscosities have different built-in characteristic scales, switching from one definition to another or interpolating between the two values is equivalent to switching from one effective filter to another. The switching between the built-in scales of the model for the unresolved scales are performed locally in space. The global hybrid RANS/LES methods can, therefore, be interpreted as multiresolution methods, in which the resolution in terms of wave number is increased in regions with low eddy viscosity levels and decreased in regions with high viscosity levels. For example, the decrease of the eddy viscosity in the separated regions far away from the wall allows eddies to develop rapidly. The switch from RANS to LES mode in the global hybrid methods does not imply an instantaneous change in the resolution level. Therefore, these methods introduce a "grey area" in which the solution is neither "pure RANS" nor "pure LES". Accordingly, global hybrid RANS/LES models are also known as "weak RANS/LES coupling" methods since there is no mechanism to transfer the modeled turbulence energy into resolved turbulence energy. This may be problematic in situations where upstream turbulence plays a significant role, as well as in cases with transition and separation not triggered by the geometry.

The zonal hybrid methods are based on a discontinuous treatment of the RANS/LES interface. In this approach, two regions of "pure RANS" and "pure LES" are predefined in the flow in which classical RANS and LES models are utilized respectively. Therefore, the problem of the gray area may be alleviated. The difficulty, however, is that information must be exchanged at the RANS/LES domain interface. Thus, these methods are known as "strong RANS/LES coupling" methods. The coupling between RANS and LES solutions is challenging since RANS solution does not provide any turbulent fluctuations that can be used to feed to the LES solution. In many cases, additional modeling which includes further assumptions on local length scales, time scales, and energy distribution are required. The RANS/LES interface can be in various forms as shown in Fig. 2.2. In the wall-modeled LES (WMLES) [62], the inner part of the boundary layer is treated using a RANS model and the rest of the flow is solved using LES (see Fig. 2.2(a)). Another common configuration for the RANS/LES interface is when an LES region is located downstream of a RANS region (see Fig. 2.2(b)). Usually in this case, synthetic turbulent structures have to be generated to match statistical characteristics provided by the RANS solution [63]. Finally, the most general problem concerns the case where a local LES simulation is embedded into a global RANS simulation [57] as shown in Fig. 2.2(c).

2.2 Turbulence Closure Models

Any averaging or filtering procedure of non-linear equations gives rise to additional unknowns whose influence on the mean flow has to be approximated. As shown in the previous section, for the case of the Navier-Stokes equations, the additional unknowns turn out to be correlations of fluctuating velocities. The unknowns originate from the

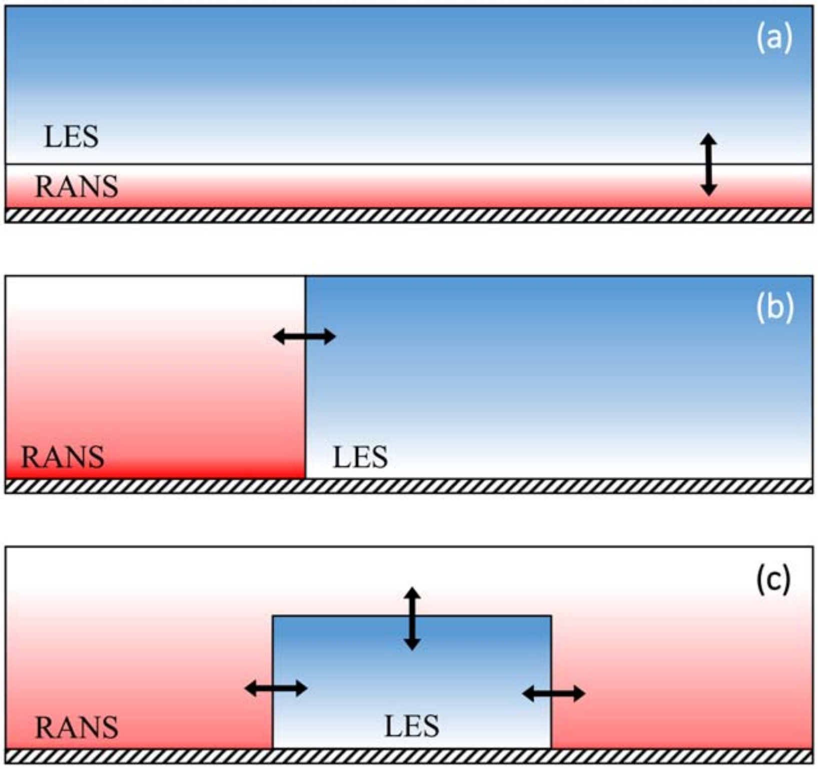

Figure 2.2: Some of the configurations of the zonal RANS/LES coupling: (a) wall-modeled LES (WMLES), (b) LES region downstream of the RANS region, and (c) embedded LES.

non-linear advection terms and must accordingly be regarded as turbulent momentum flux. However, they are usually referred to as the Reynolds stresses/subgrid scale stresses because they are parts of a second-order tensor. Providing proper models for these additional unknowns is called "turbulence closure" or "turbulence modeling". The larger the fraction of modeled scales of the flow, the lesser is the requirement on the grid resolution. The required grid therefore depends on the choice of turbulence model. Most often it is the other way around, i.e., that the resolution or computational time is the limiting factor and determines which approach to turbulence modeling is most suitable for a specific case. There is thus a wide spectrum of complexity of turbulence models. It should be noted, however, that because a turbulence model is merely a "model", it has a limited range of applicability and will always cause modeling errors of some magnitude. This section is devoted to briefly introduce turbulence models that are used in this research study. Further details on these models can be found in [64, 65, 66].

2.2.1 The RANS Models

The basic class of turbulence models, eddy viscosity models (EVM), is based on the assumption that the Reynolds stress tensor can be expressed in terms of the mean rate of strain in the same way as the viscous stress for a Newtonian isotropic fluid, except that the coefficient of molecular viscosity is replaced by the eddy viscosity. According to the first EVM proposed by Boussinesq, the Reynolds stresses are proportional to the mean velocity gradients as [67]

$$-\frac{\tau_{ij}^{\mathrm{RANS}}}{\rho} = -\overline{u_i' u_j'} = \nu_t \left(\frac{\partial \bar{u}_i}{\partial x_j} + \frac{\partial \bar{u}_j}{\partial x_i} \right) - \frac{2}{3} k \delta_{ij} \tag{2.15}$$

where ν_t is the turbulent eddy viscosity, k is the turbulent kinetic energy, and δ_{ij} is the Kronecker delta. The eddy viscosity is not a fluid property as is the molecular viscosity, but a flow property that depends strongly on the state of turbulence.

This approach is computationally very convenient since the same algorithm and computational code can be used for both laminar and turbulent transport phenomena without having to make many modifications. The problem of closure remains, however, except that now it is reduced to defining the eddy viscosity coefficient ν_t. Different turbulence models are developed in order to model this coefficient

2.2.1.1 The k-ε Model

The k-ε model is one of the most prominent turbulence models. It has been implemented in most general purpose CFD codes and it is now considered as an industrial standard model. For general purpose simulations, the k-ε model offers a good compromise in terms of simulation time, accuracy, and robustness. Transport equations for turbulent kinetic energy k and its dissipation rate ε are solved in this model, and the eddy viscosity is specified as [64]

$$\nu_t = C_\mu \frac{k^2}{\varepsilon} \tag{2.16}$$

The model uses the following transport equations for turbulent kinetic energy and turbulence dissipation rate [64]

$$\frac{\partial k}{\partial t} + \bar{u}_j \frac{\partial k}{\partial x_j} = \frac{\partial}{\partial x_j} \left[\left(\nu + \frac{\nu_t}{\sigma_k} \right) \frac{\partial k}{\partial x_j} \right] + P - \varepsilon \tag{2.17}$$

$$\frac{\partial \varepsilon}{\partial t} + \bar{u}_j \frac{\partial \varepsilon}{\partial x_j} = \frac{\partial}{\partial x_j}\left[\left(\nu + \frac{\nu_t}{\sigma_\varepsilon}\right)\frac{\partial \varepsilon}{\partial x_j}\right] + C_{1\varepsilon}\frac{P\varepsilon}{k} - C_{2\varepsilon}\frac{\varepsilon^2}{k} \tag{2.18}$$

where P is the turbulent kinetic energy production term which is

$$P = -\overline{u_i' u_j'}\frac{\partial \bar{u}_i}{\partial x_j} = \nu_t\left(\frac{\partial \bar{u}_i}{\partial x_j} + \frac{\partial \bar{u}_j}{\partial x_i}\right)\frac{\partial \bar{u}_i}{\partial x_j} \tag{2.19}$$

The five constants in this model are [64]

$$\sigma_k = 1.0 \qquad , \qquad \sigma_\varepsilon = 1.3$$

$$C_{1\varepsilon} = 1.44 \qquad , \qquad C_{2\varepsilon} = 1.92 \qquad , \qquad C_\mu = 0.09$$

2.2.1.2 The Realizable k-ε Model

The realizable k-ε model is similar to the standard k-ε model except that it places special constraints on the Reynolds stresses such that it would be consistent with the physics of the turbulent flow, such as positivity of normal stresses ($\overline{u_i' u_i'} > 0$) and Schwarz inequality for shear stresses ($\overline{u_i' u_j'}^2 \leq \overline{u_i'^2 u_j'^2}$) [68]. This model is a physically realizable model, i.e., it does not let the normal Reynolds stresses become negative. Turbulent viscosity is modeled similarly to the standard k-ε model (Eq. (2.16)), however C_μ is not constant as in standard k-ε but is a function of strain rate and rotation rate tensors [68].

2.2.1.3 The k-ω Model

The k-ω model is also a two-equation turbulence model. It is based on transport equations for the turbulent kinetic energy k and for the specific dissipation rate ω (rate of dissipation per unit of turbulence kinetic energy, often called turbulent frequency[2]). In the original k-ω model [69] the eddy viscosity is expressed by

$$\nu_t = \frac{k}{\omega} \tag{2.20}$$

Transport equations for k and ω are as follows [69]

$$\frac{\partial k}{\partial t} + \bar{u}_j \frac{\partial k}{\partial x_j} = \frac{\partial}{\partial x_j}\left[(\nu + \sigma^* \nu_t)\frac{\partial k}{\partial x_j}\right] + P - \beta^* k\omega \tag{2.21}$$

---

[2] $\omega = \varepsilon/(C_\mu k)$

$$\frac{\partial \omega}{\partial t} + \bar{u}_j \frac{\partial \omega}{\partial x_j} = \frac{\partial}{\partial x_j}\left[(\nu + \sigma \nu_t)\frac{\partial \omega}{\partial x_j}\right] + \alpha \frac{P\omega}{k} - \beta \omega^2 \tag{2.22}$$

where [69]

$$\sigma = \frac{1}{2} \qquad , \qquad \sigma^* = \frac{1}{2}$$

$$\alpha = \frac{5}{9} \qquad , \qquad \beta = \frac{3}{40} \qquad , \qquad \beta^* = \frac{9}{100}$$

Various other versions of the k-ω model are proposed later with several modifications including extra terms and coefficients [64, 65].

2.2.1.4 The Shear Stress Transport (SST) k-ω Model

The shear stress transport model is a blending between the k-ω model near the surface and the k-ε model in the outer region, which is developed by Menter [70]. The combination of the two models has been accomplished using a blending function. By multiplying the k-ω model equations by function F_1 and the transformed k-ε model equations by $1 - F_1$, the SST k-ω model equations can be written as follows

$$\frac{\partial k}{\partial t} + \bar{u}_j \frac{\partial k}{\partial x_j} = \frac{\partial}{\partial x_j}\left[\left(\nu + \frac{\nu_t}{\sigma_{k3}}\right)\frac{\partial k}{\partial x_j}\right] + P - \beta^* k \omega \tag{2.23}$$

$$\frac{\partial \omega}{\partial t} + \bar{u}_j \frac{\partial \omega}{\partial x_j} = \frac{\partial}{\partial x_j}\left[\left(\nu + \frac{\nu_t}{\sigma_{\omega 3}}\right)\frac{\partial \omega}{\partial x_j}\right] + \alpha_3 \frac{P\omega}{k} - \beta_3 \omega^2 + (1 - F_1)\frac{2}{\omega \sigma_{\omega 2}}\frac{\partial k}{\partial x_j}\frac{\partial \omega}{\partial x_j} \tag{2.24}$$

All closure coefficients in these equations are expressed in terms of the blending function

$$C_{SST} = F_1 C_{k-\omega} + (1 - F_1) C_{k-\varepsilon} \tag{2.25}$$

The proper transport behavior can be obtained by a limiter added to the formulation of eddy viscosity [70]

$$\nu_t = \frac{k}{\max(\omega, F_2 S)} \tag{2.26}$$

F_2 is a blending function which restricts the limiter to the wall boundary layer, as the underlying assumptions are not valid for free shear flows. S is the magnitude of the strain rate. Both F_1 and F_2 are represented by tangent hyperbolic functions of several flow variables including k, ω, and their spatial derivatives (see Ref. [70, 65] for details of the formulation).

2.2.1.5 Near-Wall Treatment in RANS Models

In general, the areas of the flow domain where high gradients occur are of high interest. In the case of a turbulent wall-bounded flow, the solution variables have large gradients near the wall, and the momentum and other scalar transport occur most vigorously. Therefore, accurate modeling of the near-wall region determines successful predictions of the flow.

The k-ε models, the Reynolds stress model (RSM), and the large eddy simulation (LES) model (so called high-Reynolds number models) are primarily valid for the turbulent core flow, i.e., the region far away from any wall. In comparison, the k-ω models are designed to be applicable throughout the boundary layer (low-Reynolds number models). Therefore, in the case of high-Reynolds number models, consideration needs to be given as to how to make them suitable in the near-wall region.

There are two approaches commonly used in modeling the near-wall region. First, the near-wall region (viscous sublayer and buffer layer) is modeled using semi-empirical formulas called “wall functions” [71], instead of actually solving the flow using computational grids. By using wall functions it is assumed that the flow is “well-behaved” near the wall and follows a generic and predictable behavior. Another method is so called “near-wall modeling” which focuses on the modification of turbulence models to make them enable to resolve the near-wall region all the way to the wall. Generally, several damping functions are used to decrease the level of turbulence in the viscosity-affected near-wall region. This results in “low-Reynolds number” versions of the above-mentioned models, for example low-Reynolds number k-ε models [72]. The two-layer zonal model [73] is another near-wall modeling method. In this model, the flow field is completely calculated all the way to the viscous sublayer (similar to the low-Reynolds number models). In the viscosity-affected near-wall region (the “layer” close to the wall) the momentum and turbulent kinetic energy transport equations are solved, however, the turbulent viscosity ν_t is obtained by an algebraic equation [73]. The demarcation of the two layers is determined by the turbulent Reynolds number $Re_y = y\sqrt{k}/\nu$, where y is the wall-normal distance and k is the turbulent kinetic energy. The viscosity-affected inner layer is defined as the region where $Re_y < 200$ [73].

It should be noted that there is a close relationship between the near-wall treatment approach and the computational grid requirements as different methods exhibit very different requirements on the wall normal distance of the first grid point, and any violation of these leads to a drastic degeneration in the solution quality[3]. This places a very high level of importance on the design of the numerical grid.

2.2.2 The Unsteady RANS Models

It has become common to name Reynolds averaged Navier-Stokes modeling as URANS (Unsteady RANS) whenever the solution is time-dependent (including changes of quantities with time). The approach is then to apply an existing RANS model with time derivatives with the purpose of resolving some of the unsteady features of the flow without recalibration of model coefficients. In the URANS approach the Reynolds decomposition, discussed in Sec. 2.1.2, is considered to be time-averaging over a time interval T. This averaging time T has to be larger than the characteristic time scale of turbulence τ and smaller than the characteristic time θ for the time evolution of the mean properties. In fact, in URANS modeling, the non-turbulent unsteadiness is resolved in the mean flow while all the turbulent fluctuations are still modeled by the RANS model. Therefore, the URANS approach can be successfully used in cases where the flow is forced to be unsteady by an external force (e.g., an unsteady boundary condition). The inherent assumption is that the flow field can be characterized by a separation of time scale between the unsteadiness of the mean field and turbulence. This will be discussed further in Sec. 4.4.

2.2.3 The Hybrid RANS/LES Models

As discussed in Sec. 2.1.4, the hybrid RANS/LES models have been developed as a coupling between LES and RANS to reduce computational cost for making LES affordable in a wider range of complex industrial applications. The development of hybrid models has received increasing attention among turbulence modeling experts, CFD code developers, and industrial CFD engineers. Hybrid RANS/LES has become one of the main modeling frameworks for quantitatively accurate predictions of complex unsteady flows at high Reynolds numbers. A wide variety of hybrid RANS/LES models, e.g., detached eddy simulation (DES) [75], very large eddy simulation (VLES) [50], extra-large eddy simulation (XLES) [76], partially-integrated transport model (PITM) [77], partially-averaged Navier-Stokes (PANS) [78], and scale-adaptive simulation (SAS) [79], have been developed and used in simulations of several industrial and academic flow test cases (see Ref. [56, 61] for a comprehensive review). In the present study two hybrid RANS/LES models, namely DES and PANS are used. The rest of this section is devoted to the DES model. The PANS model will be discussed in detail in Chapter 5.

---

[3] For example, an underprediction of the skin friction coefficient of up to a factor of five has been reported for airfoil flows when inappropriate wall treatment is applied [74].

2.2.3.1 The Detached Eddy Simulation (DES) Model

The most common type of hybrid RANS/LES models is detached eddy simulation (DES). The approach was given the name detached eddy simulation since it is meant to resolve the "detached" large eddies far from any boundary in an LES-like manner whereas small structures "attached" to the wall would be modeled in a RANS mode. As defined by Travin et al. [80] *"a Detached-Eddy Simulation is a three-dimensional unsteady numerical solution using a single turbulence model, which functions as a sub-grid-scale model in regions where the grid density is fine enough for a large-eddy simulation, and as a Reynolds-averaged model in regions where it is not."* Based on this definition, the implementation of the DES is quite simple. It is based on using the same background RANS model with different length scales (RANS and subgrid ones respectively) depending on the local grid resolution. Exactly this simplicity combined with impressive results obtained in the first uses of DES for complex aerodynamic applications [81] and positive experience have motivated further development. The DES proposed by Spalart et al. [82] is historically the first approach of such a type. They combined the Spalart-Allmaras RANS model with its subgrid scale counterpart by means of a limiter defined as [82]

$$l_{DES} = \min\left(d_w, C_{DES}\Delta\right) \tag{2.27}$$

where l_{DES} is the model length scale, d_w is the distance to the wall involved in the destructive term of the Spalart-Allmaras model, C_{DES} is the only additional empirical model constant, and Δ is defined as the largest local grid-spacing

$$\Delta = \max\left(\Delta_x, \Delta_y, \Delta_z\right) \tag{2.28}$$

Substitution of the length scale (Eq. (2.27)) in place of the distance to the wall in the eddy-viscosity transport equation of the Spalart-Allmaras model directly results in the DES model of Spalart et al. [82], which performs as the background RANS model in the attached boundary layer near the wall ($d_w < C_{DES}\Delta$) and as an SGS model with implicit filter $C_{DES}\Delta$ in the flow regions away from the wall ($d_w > C_{DES}\Delta$).

A more general definition of the DES limiter (Eq. (2.27)), compatible with any RANS model, given by Travin et al. [80] reads as

$$l_{DES} = \min\left(l_{RANS}, l_{LES}\right) \tag{2.29}$$

where l_{RANS} is the RANS length scale explicitly or implicitly involved in any RANS model. For example, for the k-ε model this length scale is defined as $l_{RANS} = k^{3/2}/\varepsilon$, and for the k-ω model $l_{RANS} = k^{1/2}/(C_\mu \omega)$. The $l_{LES} = C_{DES}\Delta$ is the LES length scale. Based on this definition a wide range of DES versions based on RANS models ranging from one- and two-equation linear eddy viscosity models [83] to algebraic Reynolds stress models [84] have been developed. Many of these models are summarized in [66, 84]. As of today, no strong evidence of noticeable DES model-sensitivity for the wall bounded flows are known [66]. This is naturally considered as an essential advantage of DES. Nonetheless, its versions based on different RANS models are still of interest. One reason for this is that some of these versions still may provide higher accuracy, especially when accurate prediction of the separation point (where flow becomes detached) is of crucial importance. Furthermore, some researchers prefer to use the DES versions based exactly on those models which are used in the RANS context. In the present study, the three following versions of the DES model are used.

- The Spalart-Allmaras Based DES Model

The formulation for this version which is based on the original DES of Spalart et al. [82] is given by Eq. (2.27). The empirical constant C_{DES} has the value of 0.65.

- The Realizable k-ε Based DES Model

This DES model is similar to the realizable k-ε model discussed in Sec. 2.2.1.2 , with the exception of the dissipation term in the k equation (Eq. (2.17)). In the DES model, the realizable k-ε RANS dissipation term (originally ε) is modified such that [85]

$$\varepsilon_{DES} = \frac{k^{3/2}}{l_{DES}} \tag{2.30}$$

where l_{DES} is given by Eq. (2.29) with $l_{RANS} = k^{3/2}/\varepsilon$ and $l_{LES} = C_{DES}\Delta$. In this version C_{DES} has a value of 0.61 and Δ is defined by Eq. (2.28). It can be seen that for the case of $l_{DES} = l_{RANS}$, the original dissipation term ε is retrieved.

- The SST k-ω Based DES Model

The dissipation term of the turbulent kinetic energy in the SST k-ω model (originally $\varepsilon = \beta^* k\omega$ in Eq. (2.23)) is modified for the DES turbulence model as described in [83] to become

$$\varepsilon_{DES} = \beta^* k\omega F_{DES} \tag{2.31}$$

where F_{DES} is expressed as

$$F_{DES} = \max\left(\frac{l_{RANS}}{C_{DES}\Delta}, 1\right) \tag{2.32}$$

here, C_{DES} is equal to 0.61 and Δ is defined in Eq. (2.28). The turbulent length scale is defined by the RANS simulation

$$l_{RANS} = \frac{k^{1/2}}{\beta^* \omega} \tag{2.33}$$

2.2.3.2 The Delayed Detached Eddy Simulation (DDES) Model

The DES formulation in Eqs. (2.29) and (2.28) is based on the assumption that the wall-parallel grid spacing near the wall exceeds the boundary layer thickness. Only then will the interface where

$$l_{RANS} = l_{LES} = C_{DES}\Delta$$

be located outside of the boundary layer as required. In the case of an ambiguous grid definition, however, the DES limiter may activate the LES mode inside the boundary layer, where the grid is not fine enough to sustain resolved turbulence. In this case, DES exhibits an incorrect behavior inside the boundary layer including underprediction of the skin friction coefficient[4] and even premature separation[5] [66].

Therefore, a modification of the DES formulation attempting to avoid nonphysical behavior in attached boundary layers was proposed by Spalart et al. [86]. In this formulation, which aims to preserve the RANS mode throughout the boundary layer, the model length scale is modified to be [86]

$$l_{DDES} = l_{RANS} - f_d \max\left(0, l_{RANS} - C_{DES}\Delta\right) \tag{2.34}$$

---

[4] Known as modeled stress depletion (MSD).

[5] Known as grid induced separation (GIS).

with

$$f_d = 1 - \tanh\left[(8r_d)^3\right] \tag{2.35}$$

$$r_d = \frac{2\left(\nu_t + \nu\right)}{\kappa^2 d_w^2 S} \tag{2.36}$$

where κ is the von kármán constant, d_w is the distance to the nearest wall, and S is the strain rate magnitude.

The hyperbolic tangent blending function f_d is tuned such that the earliest onset of LES mode occurs just outside the boundary layer [86]. f_d=0 inside a turbulent boundary layer, blending smoothly to f_d=1 outside of the boundary layer. Intended to prevent DES from a too early switch to LES mode, the modified version is called delayed detached eddy simulation (DDES).

2.3 Discretization and Numerical Solution

Computational fluid dynamics (CFD) is an important tool for studying fluid flows of various kinds. The relative low cost and availability of detailed data sets make CFD of special interest. CFD solvers usually use a finite-volume-based technique to convert a general scalar transport equation to an algebraic equation that can be solved numerically. In the finite-volume method the computational domain is divided into a large number of control volumes. The general transport equation of a scalar quantity ϕ can be written as

$$\frac{\partial \phi}{\partial t} = \nabla.\left(\mathbf{V}\phi\right) = \nabla.\left(\Gamma \nabla \phi\right) + S_\phi \tag{2.37}$$

with $\mathbf{V}$ being the velocity vector, Γ the coefficient of diffusivity, and S_ϕ a source term. Integrating this equation over each control volume (CV) and time interval Δt, and using the Gauss divergence theorem, we may write

$$\int_t^{t+\Delta t}\left[\int\limits_{CV}\frac{\partial \phi}{\partial t}dV + \int\limits_{CS}\phi\mathbf{V}.\mathbf{n}dA\right]dt = \int_t^{t+\Delta t}\left[\int\limits_{CV}\Gamma\nabla\phi.\mathbf{n}dA + \int\limits_{CV}S_\phi dV\right]dt \tag{2.38}$$

where $\mathbf{n}$ is an outward pointing, normal vector of the boundary of the control volume (control surface CS). The first term on the left-hand side represents the rate of change of the fluid property ϕ in the control volume and the second term represents the net transport rate of property ϕ out of the volume due to advection. The first term on the right-hand side is the net rate of transport of property ϕ into the control volume due to diffusion and the last term on the right-hand side is the net rate of increase of ϕ due to sources inside the control volume.

In order to solve Eq. (2.38) numerically, the various terms need to be discretized. Discretization transforms the underlying partial differential equations into a set of algebraic equations that can be solved computationally. Depending on the physics of the term being discretized, the discretization can be performed in different ways, resulting in different "discretization schemes". These schemes are actually the ways to interpolate the information that is transported between the cells, and the order of each discretization scheme is a measure of its numerical efficiency and accuracy. The diffusion term in Eq. (2.38) is discretized using the second-order central-differencing scheme [87].

For the discretization of the advection term, however, various schemes are used depending on the transport equation being solved. In the RANS simulations, the advection term in transport equations of momentum and turbulence quantities (e.g., k and ε) is discretized using the second-order upwind scheme. The pure central-differencing scheme is the ideal choice for LES and hybrid RANS/LES simulations due to the low level of numerical diffusion. It, however, results in numerical instabilities and some nonphysical oscillations added to the solution [88]. Therefore, hybrid RANS/LES simulations are performed using a bounded central-differencing scheme [89] for the momentum equation, while a second-order upwind scheme is used for turbulence quantities. The bounded central-differencing scheme, which blends the central differencing and second-order upwind schemes as well as forces the convection boundedness criterion [90], is shown to be competitive in terms of minimizing the numerical errors [91, 92].

For unsteady simulations, the governing equations must be discretized not only in space but also in time. Temporal discretization involves the integration of every term in the differential equations over a time step Δt (see Eq. (2.38)). In this study, a second-order implicit differencing scheme is used, whereby values of a scalar ϕ at each new time step $t + 1$ are determined from the values at the previous two time steps t and $t - 1$ according to

$$\left.\frac{\partial \phi}{\partial t}\right|_{t+1} = \frac{1}{2\Delta t}\left(3\phi^{t+1} - 4\phi^{t} + \phi^{t-1}\right) \tag{2.39}$$

This implicit equation should be solved iteratively at each time step. It is unconditionally stable independent of the time step size. The attention should be paid, however, to adjust the time step Δt such that a satisfactory temporal resolution of transient flow phenomena is achieved.

As there is no explicit pressure equation included in the calculations, special treatments are needed to couple the pressure and the velocity fields. The common approach, also used in this study, is so called the "segregated" solution where equations are solved sequentially rather than simultaneously. The procedure in this study is based on the SIMPLE algorithm which obtains the pressure field by solving a pressure correction equation iteratively. The pressure correction equation is derived based on the combination of the continuity and momentum equations. Therefore, it ensures that mass and momentum are conserved within the computational domain. When applied to unsteady flow problems, the SIMPLE algorithm enables the simulation to advance at large time steps, however, several sub-iterations are required within each time step to obtain a converged solution. The details of formulations for the pressure-velocity coupling algorithms, such as SIMPLE, SIMPLEC, and PISO are well covered in Ref. [88].

2.4 Flow Solvers

Numerical simulations in the present study are performed using two CFD codes, namely ANSYS-FLUENT [52] and OpenFOAM [53].

2.4.1 ANSYS-FLUENT CFD Code

ANSYS-FLUENT, a commercial CFD solver, provides comprehensive modeling capabilities for a wide range of compressible and incompressible, laminar and turbulent fluid flow problems. Steady or transient analyses can be performed with this code. ANSYS-FLUENT contains the broad physical modeling capabilities needed to model flow, turbulence, heat transfer, and reactions for industrial applications [52]. Several turbulence models are implemented in ANSYS-FLUENT making it a proper choice for the present simulations.

Two numerical approaches are available in ANSYS-FLUENT: density-based solver and pressure-based solver. In both methods the velocity field is obtained from the momentum transport equation. In the density-based approach, the continuity equation is used to obtain the density field while the pressure field is determined from the equation of state [85]. On the other hand, in the pressure-based approach, the pressure field is extracted by solving a pressure or pressure correction equation which is obtained by manipulating the continuity and momentum equations as discussed in Sec. 2.3. Based on the physics of the current problem the pressure-based solver is used. Since the governing equations are nonlinear and coupled, the solution process involves iterations wherein the entire set of governing equations is solved repeatedly until the solution converges, i.e., the solution residuals become smaller than a predefined threshold.

The source code is not available for ANSYS-FLUENT; therefore, any customization in boundary conditions, fluid properties, turbulence models, solvers, etc. should be performed via user-defined functions (UDF) [93]. A UDF is a routine (programmed by the user) written in C programming language which can be dynamically linked with the solver and addresses a wide range of applications. However, it is not possible to address every application using UDFs. Not all solution variables and models can be accessed by UDFs. This makes the flexibility to changes of ANSYS-FLUENT limited, particularly for new model development.

2.4.2 OpenFOAM CFD Code

OpenFOAM (Open Field Operation And Manipulation) is an open source, free CFD code that has the advantage of being open for changes and development. The users can contribute with new ideas and help with extending the software features. OpenFOAM consists of C++ libraries, which foremost are used to create applications. These applications consist of solvers and utilities. The solvers are used for solving continuum mechanics problems, and the utilities are mostly used to manipulate data in various forms. The main advantage of OpenFOAM is the ease of creating/customizing solvers and utilities. To be able to make this happen, the programming language needs to have properties such as inheritance, template classes, virtual functions, and operator overloading which are available in C++ programming language.

The solvers and utilities are controlled through the use of dictionaries. These are files where specifications of the applications are accessed and controlled. Specifications such as discretization schemes, simulation time steps, divergence schemes, turbulence models, pressure corrector settings, and linear solver settings are all controlled and accessed through these sets of dictionaries. OpenFOAM uses a common structure to set up a problem. An overview of the three subdirectories which are necessary to create a case in OpenFOAM is given in Fig. 2.3. When the solver is running, it initiates the computations with the values given in a directory named `0`, as in time `0`. Then it prints the quantity fields in time directories, with a time interval specified in a dictionary called `controlDict` located in subdirectory `system`. Two other files in the system subdirectory are `fvSolution` and `fvSchemes` which include information on solver settings (tolerances, under-relaxation factors, etc.) and numerical schemes, respectively. Information about computational grid, turbulence model, and material properties are given in subdirectory `constant`. When the simulations are done, results can be post-processed through software such as Paraview, Gnuplot, or Tecplot.

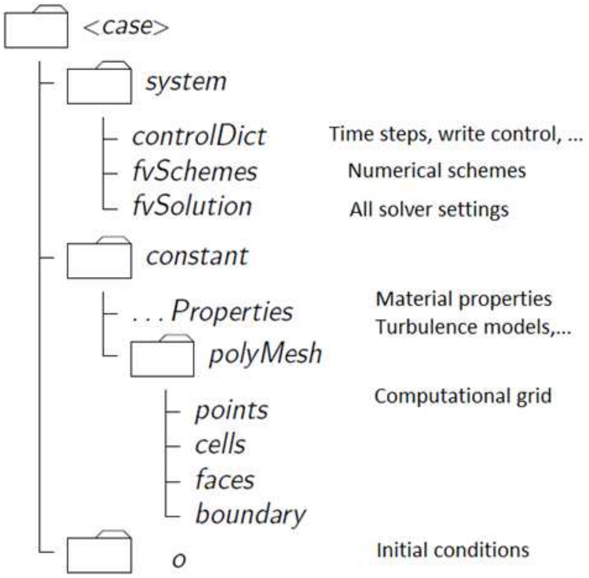
<case>
system
controlDict
Time steps, write control, ...
fvSchemes
Numerical schemes
fvSolution
All solver settings
constant
. . . Properties
Material properties
Turbulence models,...
polyMesh
points
Computational grid
cells
faces
boundary
o
Initial conditions

Figure 2.3: Overview of the content of a case in OpenFOAM.

OpenFOAM has a prospect to be widely used in CFD simulations of various fluid flow problems since it is free and open-source. In fact, particular attention is paid recently to the application of OpenFOAM in hydroturbine flow simulations [94, 95]. Nevertheless, its learning curve is quite steep, and a comprehensive, detailed user's manual is still unavailable. Therefore, a user is very much dependent on the community forum pages (e.g., `http://www.cfd-online.com/Forums` and `http://www.openfoamwiki.net`), the Extend project repositories (`http://sourceforge.net/projects/openfoam-extend`), and inter-colleague discussions. The author would like to acknowledge the help received from all the above-mentioned sources.

2.5 Computational Grid

In any CFD solver, the discretized system of equations must be solved iteratively on a spatial domain consisting of discrete grid points. The design of this computational grid is very important, having a strong impact on the accuracy and stability of the solution. In general, regions with strong gradient in the flow variables such as boundary layers or shear layers must be resolved using a sufficient number of grid points. Furthermore, some geometrical constraints may dictate the shape of computational cells resulting in sharp internal angles or high aspect ratios which can cause instabilities or errors in the numerical solution.

Using hybrid RANS/LES models, as it is done throughout this work, compounds the difficulty in grid generation. These models incorporate both RANS and LES treatments in the same field, therefore, the computation grid should satisfy further detailed criteria. Grid convergence in LES is more subtle than grid convergence in RANS because in LES the variables are filtered using a grid-dependent filter (see Sec. 2.1.3).

Considering these complexities in generation of a computational grid for hybrid RANS/LES simulations, special attention is paid in this study in building the grids. Specifically, all the computational grids used in this study are generated based on the guideline provided by Spalart [96] who is one of the pioneers in hybrid RANS/LES simulations. According to this guideline, the requirements for the regions of the domain where RANS treatment is expected to be active (e.g., boundary layers) are the same as for a full-domain RANS simulation. For low Reynolds-number RANS models or those with a two-layer zonal model for wall treatment (see Sec. 2.2.1.5), the requirement would be that the first grid point should be located at $y^+ \approx 2$ or less, and the stretching ratio $\Delta y_{i+1}/\Delta y_i$ should be around 1.25 or less in the log layer [96]. In the directions parallel to the wall, RANS practice would also be appropriate and the grid spacing is usually determined based on the steepness of variations of the geometry. At least 10 grid points would be used to discretize the outer region of the boundary layer where RANS modeling is still active. Regions where LES treatment is expected to be active (e.g., near the center of the draft tube) can be divided into the “focus region”, which is the region where turbulence must be well resolved and a high resolution grid should be used, and the “departure region” where lower grid resolution can be used. Obviously, a smooth transition between these two regions is required. As an ideal choice for hexahedral cells, computational grid cells should be as close as possible to the cubic shape in the “focus region”. This can be justified considering the definition of the grid length scale, e.g., in Eq. (2.28) [96]. There is no unique choice for the size of the grid in the “focus region”, however, a gross figure is provided by Spalart [96] discussing several flow problems.

In the present study, these detailed considerations become practically possible by writing a script for the grid generation. A script in `m4` language is written in order to parametrize the `blockMeshDict` dictionary file which is used by OpenFOAM to build the computational grid. Using this method, a detailed control over the generated mesh and the possibility of parametric study on different grids become possible. The current script can be modified easily to generate grids for circular geometries such as pipes, nozzles, diffusers, sudden compression/expansion sections, and geometries including combinations of these. The grid for the simplified draft tube in Chapter 4, and the abrupt expansion in Chapter 5 are both generated using this script. The resultant mesh can then be exported easily to both OpenFOAM and ANSYS-FLUENT.

Every circular cross section is divided into 13 blocks as shown in Fig. 2.4(a). Discretization is performed using an O-grid. The user should specify the size of each block, i.e., R_1 to R_5, as well as the number of grids for each side of the block in both radial and tangential directions. Furthermore, the stretching ratio of the grid points can be adjusted independently for each block. This is very helpful in a hybrid RANS/LES simulation where two different models (with two different grid requirements) are used in the same flow field. Figure 2.4(b) illustrates a computational grid generated using this method.

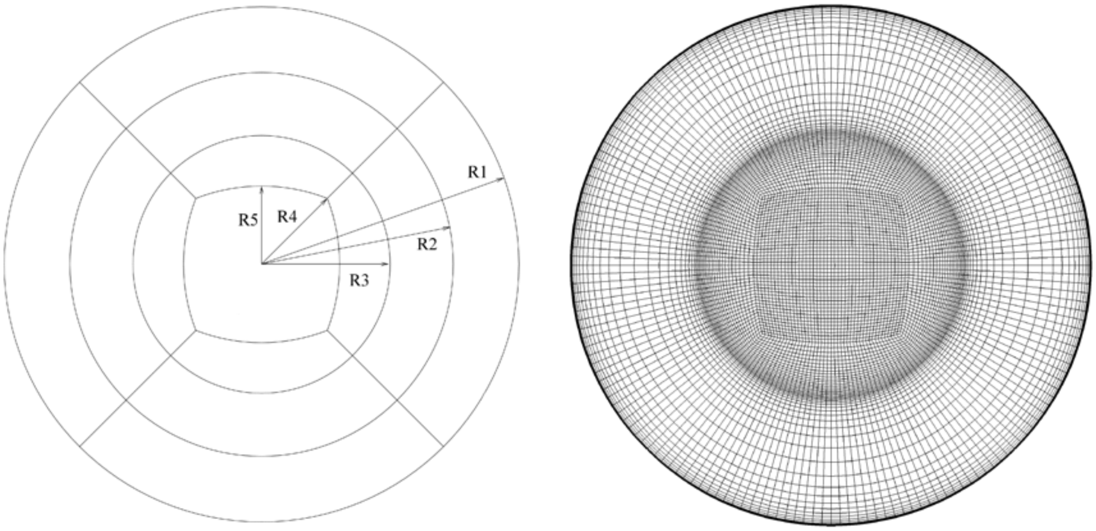

(a)

(b)

Figure 2.4: (a) Configuration of blocks for generating the computational grid and (b) a sample mesh.

Chapter 3

Description of the Test Case: The FLINDT Draft Tube

"Do what you can where you are with what you have." - Theodore Roosevelt

One of the challenges any CFD study of draft tube faces is the lack of a test case for which the geometry and boundary conditions, as well as detailed experimental data are available. These experimental data are needed for assessment and validation of numerical simulations. The measurements should include not only pressure fluctuations, but also profiles of velocity components as well as turbulent quantities. Among the several experimental studies reviewed for this study, those related to the FLINDT project [29] contain these details. The FLINDT (FLow INvestigation in Draft Tubes) research project was performed in the Laboratory for Hydraulic Machines (LHM) at the Swiss Federal Institute of Technology of Lausanne (École Polytechnique Fédérale de Lausanne - EPFL) in Lausanne, Switzerland. The project partners were the EPFL, Électricité de France, Alstom, General Electric Canada, Sulzer Hydro, Va Tech Voest Alpine MCE, and Voith Hydro. It aimed to "investigate the flow in hydraulic turbines draft tubes for a better understanding of the physics of these flows and to build up an extensive experimental data base describing a wide range of operating points which can provide a firm basis for the assessment of the CFD engineering practice in this component" [29]. Nevertheless, details of the draft tube geometry are not available in open literature and are limited to the project partners. Furthermore, all the data related to the draft tube's characteristics, various operating conditions, and measurements are not reported in one openly accessible, comprehensive document, rather they are distributed in several articles, theses, and reports. These were the main challenges in providing a reliable test case for the present numerical simulations. This chapter describes the FLINDT draft tube and summarizes some of the challenges the author faced in obtaining the required data.

3.1 The Model Francis Turbine

The FLINDT project's experiments were carried out on a scaled model (1:10) of an existing Francis turbine with specific speed of ν_s=0.56. The original power plant was built in 1926, but the runner was upgraded in the late 80s. In building the scale model within the FLINDT research project, the original draft tube was replaced by a specially designed elbow draft tube [29].

The turbine model (see Fig. 3.1 and Fig. 3.2) has a spiral case, stay ring of 10 stay vanes, a distributor made of 20 wicket gates (guide vanes), a 17-blade runner of 0.4 m outlet diameter (D in Fig. 3.2), and an elbow draft tube [29]. The draft tube geometry includes the conical part of 17° angle and about 0.32 m length followed by a 90° curved elbow and a rectangular section diffuser with a pier as shown in Fig. 3.3.

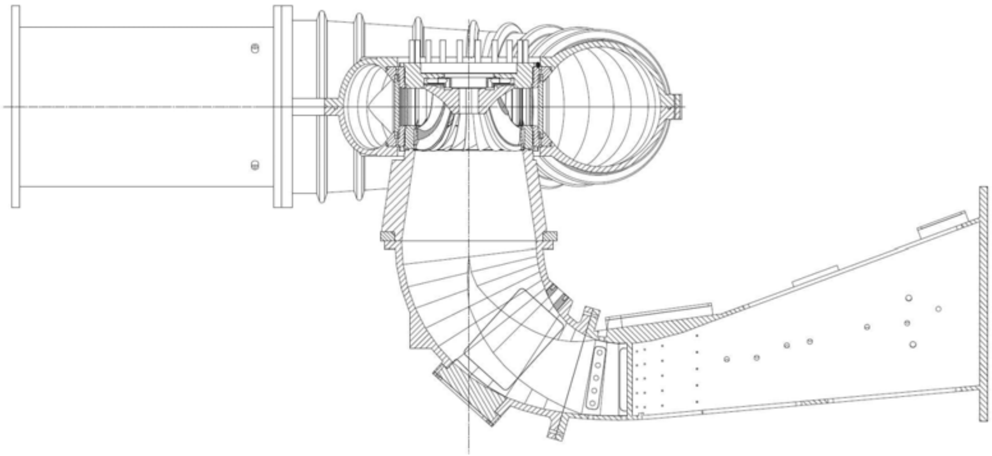

Figure 3.1: Cross section of the Francis turbine model investigated in the FLINDT project. Source: Nicolet [97].

Figure 3.4 shows the evolution of the draft tube cross-section area from inlet to outlet. The draft tube was equipped with a transparent cone (see Fig. 3.5), made with polymethyl methacrylate, for the observation purposes as well as optical measurements.

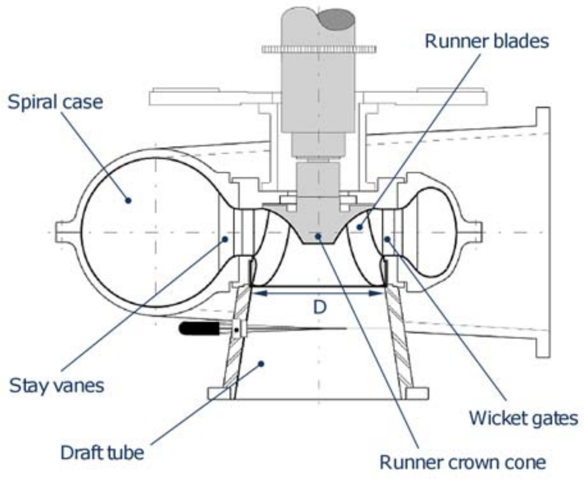
Runner blades
Spiral case
D
Stay vanes
Wicket gates
Draft tube
Runner crown cone

Figure 3.2: Components of the Francis turbine model investigated in the FLINDT project. Modified from Susan-Resiga et al. [24].

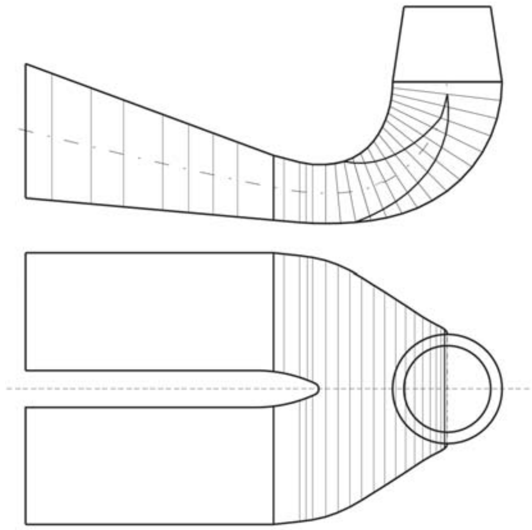

Figure 3.3: Side and top views of the FLINDT draft tube. Source: Susan-Resiga et al. [12].

3.2 Measurements

Three different measurement methods were used within the FLINDT research project, namely wall pressure measurements [30, 98], PIV [32, 99, 36], and LDA [31, 36] (see Fig. 3.6).

The unsteady wall pressure could be acquired simultaneously at up to 96 positions

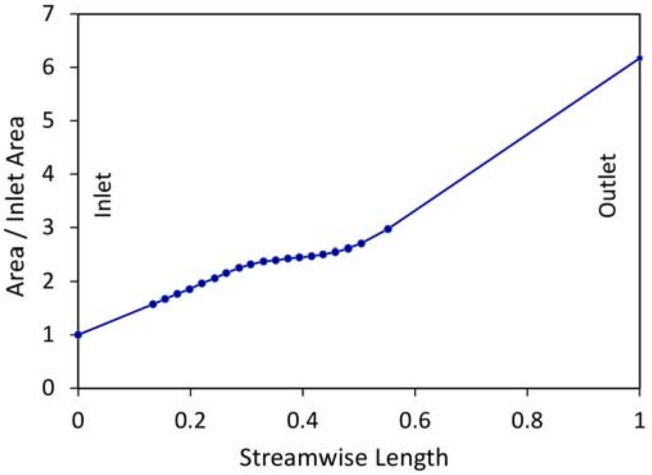

Figure 3.4: Change in the FLINDT draft tube cross-section area from inlet to outlet. Data Source: Mauri [11].

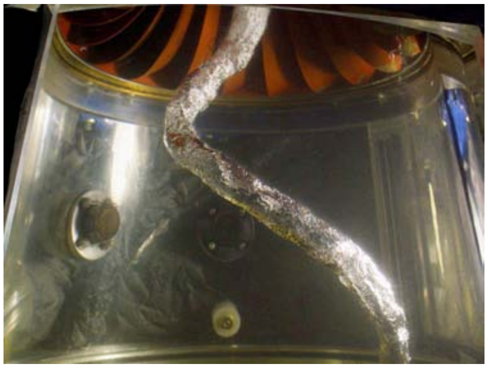

Figure 3.5: Vortex rope formation inside the FLINDT draft tube. The draft tube cone was transparent. Source: Iliescu et al. [32].

using piezoresistive pressure transducers (see Fig. 3.7). The measurement uncertainty in wall pressure was estimated to be less than 3% [30]. The three-dimensional instantaneous velocity field in the draft tube cone was investigated with a PIV system (see Fig. 3.8). The overall uncertainty of the 3-D PIV velocity fields was estimated to be 3% of the mean velocity value [32]. The LDA system with a non-orthogonal optical arrangement consisting of four optical access windows (see Fig. 3.9) was used to measure three components of the velocity vector and six components of the Reynolds stress tensor. The LDA measurements were performed in two survey sections in the draft tube cone (see

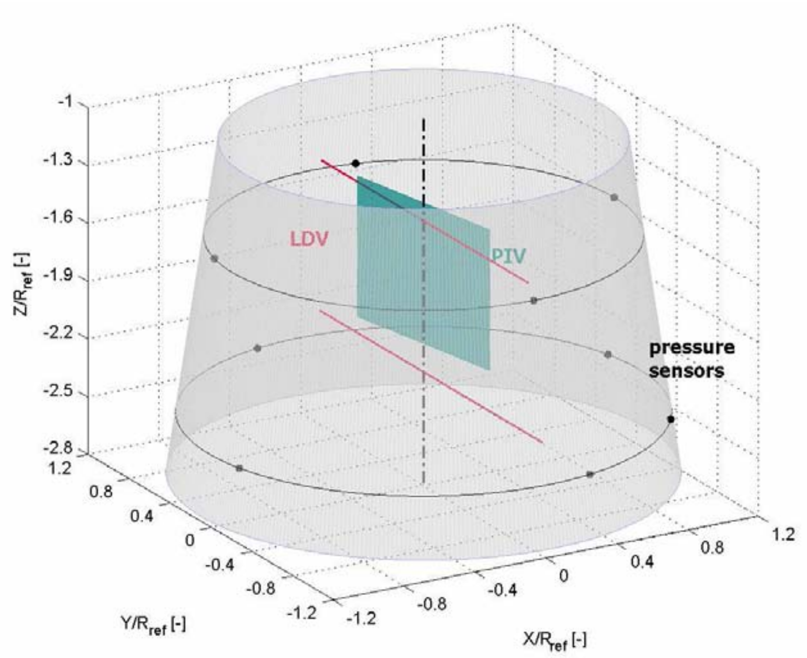

Figure 3.6: Various measurement techniques including wall pressure sensors, LDV, and PIV were used within the FLINDT project. Only nine pressure sensors (in two sections) are shown. R_{ref} is the runner radius (= 0.2 m). Source: Ciocan and Iliescu [99].

Fig. 3.6) located 84 mm and 242 mm downstream of the draft tube inlet respectively. The uncertainties of the laser measurements were estimated to be 2% for the velocity components and 3% for the Reynolds stress components [36, 11].

3.3 Draft Tube Geometry

As discussed above, the exact geometry of the draft tube is not available in open literature. Therefore, the simplified FLINDT draft tube is investigated by some researchers [12, 100, 101]. In this study, a simplified draft tube is studied first with results being presented in Chapter 4. Then, a comprehensive investigation of the previously published documents (theses, journal and conference papers, and reports) within the FLINDT project is performed, in order to build a complete database with details of the draft tube geometry (as much as possible) and available experimental data. Using this database the three-dimensional FLINDT draft tube geometry was rebuilt as shown in Fig. 3.10. To the best of author's knowledge, this is the first attempt at regenerating the FLINDT draft tube and making it available in open literature with all details required for a CFD simulation.

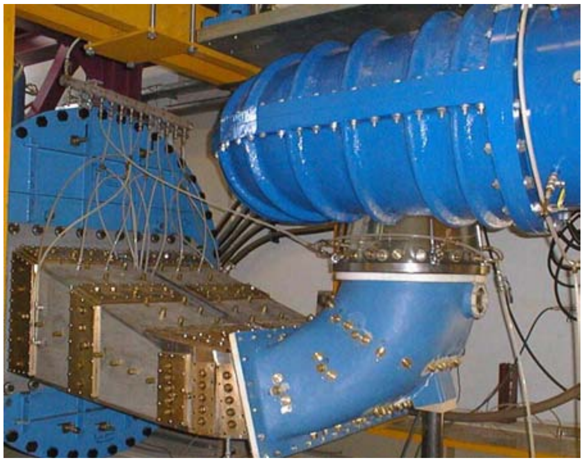

Figure 3.7: Pressure taps for unsteady wall pressure measurements. Source: Avellan [29].

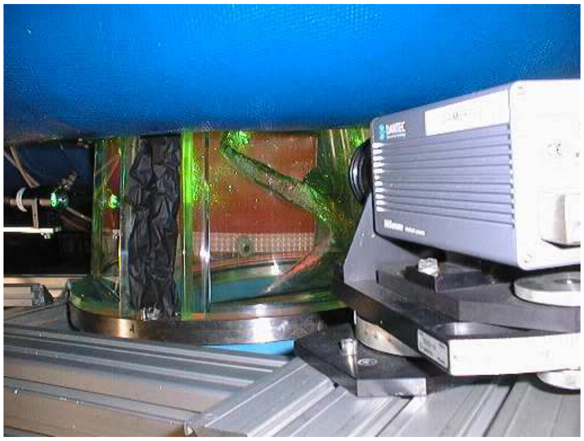

Figure 3.8: Experimental setup for PIV measurements. Source: Ciocan and Iliescu [99].

The regenerated draft tube geometry includes the runner crown cone, the draft tube cone, the 90° elbow, and the diffuser with a pier. Section S0 in Fig. 3.11 is located just downstream of the trailing edge of runner blades. Sections S1 and S2 are the locations within the draft tube cone where LDA measurements were performed in experimental studies (see Fig. 3.6). They are located 84 mm and 242 mm downstream of the runner outlet respectively. The static pressure was measured at the draft tube wall at sections S1 to S6 using pressure transducers [11, 98]. The dimensions in Fig. 3.11 are given in Table 3.1.

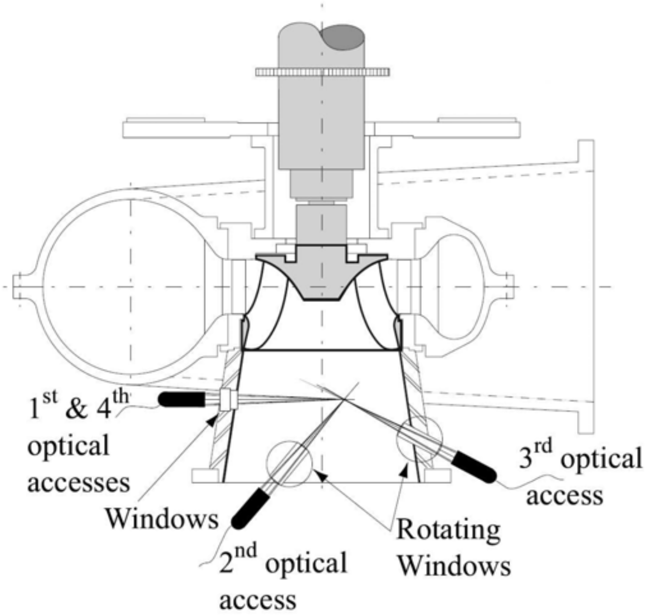

Figure 3.9: The LDA paths for the flow survey in the draft tube cone. Modified from Avellan [29].

Table 3.1: Dimensions of the FLINDT draft tube shown in Fig. 3.11 (All dimensions are in mm).

a	b	c	d	e
122	68	400	503	161
f	g	h	i	j
316	52	1060	1978	631

3.4 Investigated Operating Conditions in this Study

According to the objectives of this study, four cavitation-free operating points are selected covering a wide range (70% to 110% of the BEP flow rate) of operating conditions. Table 3.2 summarizes the characteristics of these four operating points. The points of interest are selected for the same head (energy) coefficient of $\psi = 1.18$ and different flow rate coefficients of $\varphi = 0.41$, 0.368, 0.34, and 0.26 corresponding to about 110%, 99%, 91%, and 70% of the flow rate at the BEP.

Figure 3.12 shows the locations of these four operating points on the machine hill chart. The pressure recovery factor in Fig. 3.12 is obtained by

$$\chi = \frac{p_6 - p_2}{\frac{1}{2}\rho\left(\frac{Q}{A_2}\right)^2} \tag{3.1}$$

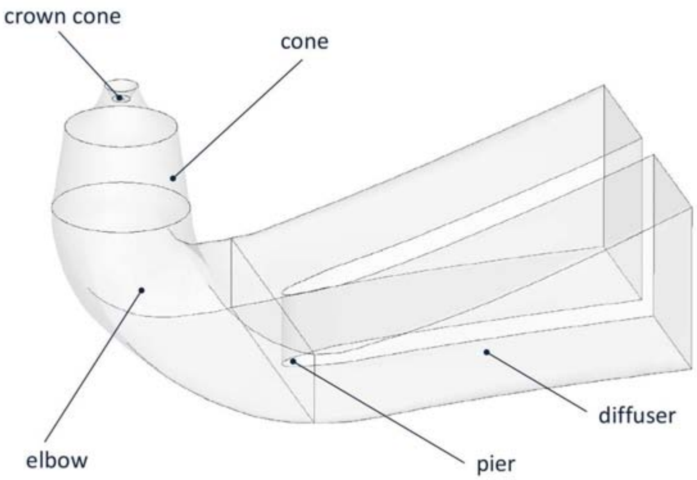

Figure 3.10: Three-dimensional view of the regenerated FLINDT draft tube.

Table 3.2: Characteristics of investigated operating conditions.

	Q/Q_{BEP}	ψ	φ	Guide Vane Opening [deg]
Case A	110%	1.18	0.41	27
Case B	99%	1.18	0.368	23
Case C	91%	1.18	0.34	21
Case D	70%	1.18	0.26	16

and calculated between section S2 and S6 in Fig. 3.11. Equation 3.1 is the simplified form of Eq. 1.5 where the elevation difference is not considered (due to the small size of the model) and the kinetic energy at the draft tube outlet is neglected compared to the kinetic energy at the draft tube inlet [29].

Figure 3.13 shows the pressure recovery factor and the machine efficiency for these four operating points. As expected, the maximum pressure recovery factor in the draft tube is associated with the best efficiency operating condition. As the flow rate deviates from the BEP condition, the pressure recovery factor decreases, especially under part-load conditions. Specifically, decreasing the flow rate by 30% results in about 85% reduction of pressure recovery factor in the draft tube (compare case D and case A).

Experimental studies were performed with two runner's rotational speeds of 500 and 1000 rpm for cases A to C, and with the rotational speed of 750 rpm for case

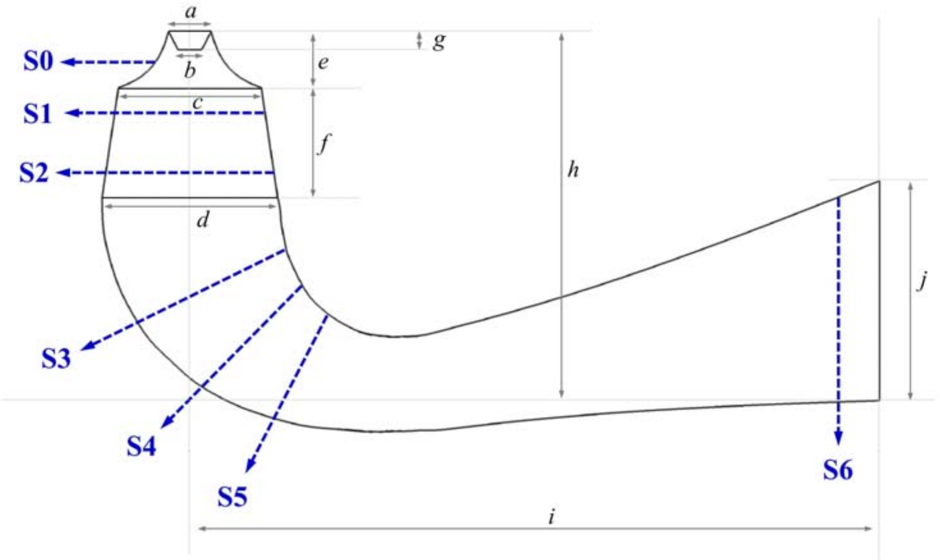

Figure 3.11: Side view of the regenerated FLINDT draft tube showing the investigated sections. See Table 3.1 for dimensions.

D [24, 98]. The corresponding Reynolds numbers, based on the runner's diameter (0.4 m) and angular velocity, are 4.2×10^6, 6.3×10^6, and 8.4×10^6 for 500, 750, and 1000 rpm respectively. No significant variation in the dimensionless velocity profiles (where velocity is made dimensionless by the *runner angular velocity* × *runner outlet radius*, and lengths are made dimensionless with respect to the *runner outlet radius*) was seen in the experiments by changing the runner's angular velocity (i.e., the Reynolds number) [24]. Moreover, the velocity profiles measured at the same discharge coefficient (φ) were not sensitive to energy coefficient (ψ) changes within the investigated range of 1.0 to 1.3 [24]. Therefore, it is concluded that the only relevant parameter for the operating points considered in this study is the turbine's discharge coefficient.

Figure 3.14 shows the dimensionless axial and circumferential velocity profiles for four cases of A to D measured at section S1. The evolution of the axial velocity component is characterized by increasing the low velocity region at the center of the draft tube as the turbine's flow rate decreases. This region forms due to the wake of the crown cone as well as the swirling nature of the flow tending to decrease the flow momentum near the center and to increase it near the wall. The circumferential velocity increases as the operating condition deviates from the BEP. This is due to the difference between the angular momentum provided by the wicket gates and the one extracted by the runner. However, the direction of the circumferential velocity (i.e., the direction of the swirl)

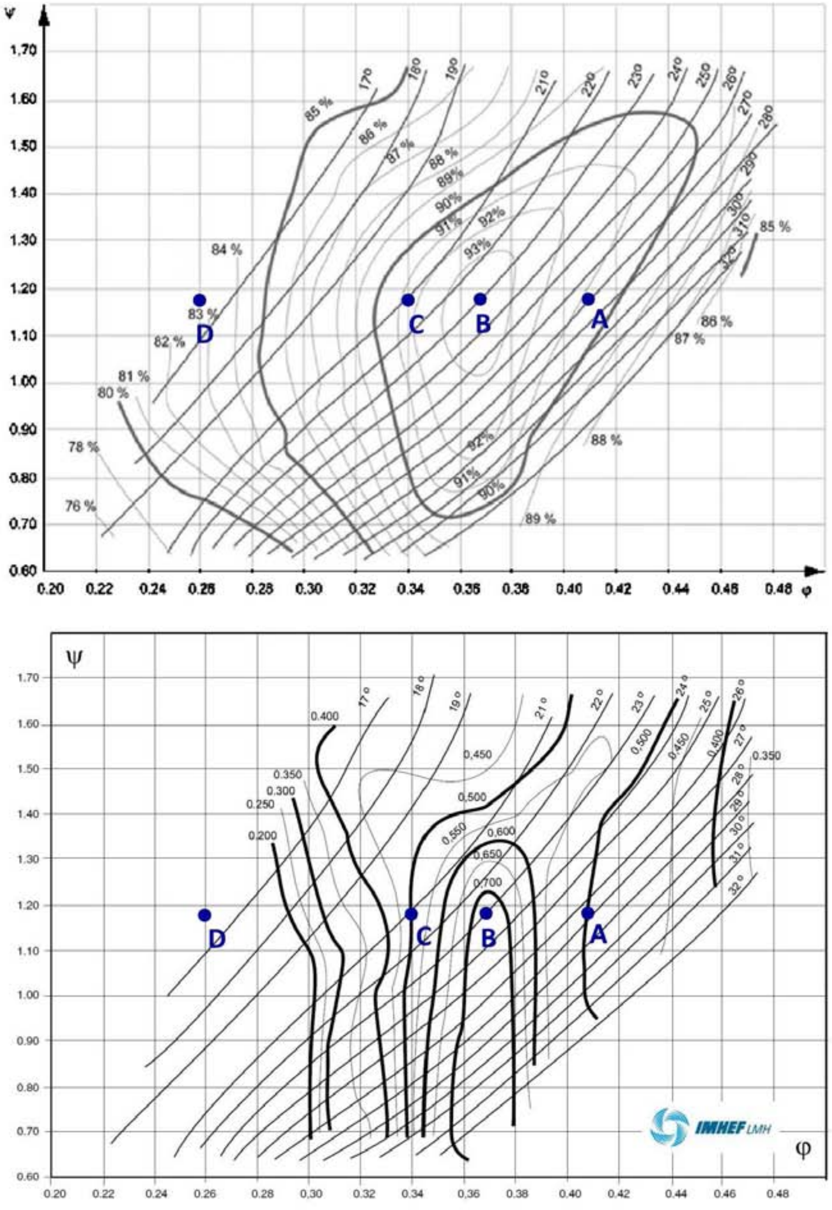

Figure 3.12: Operational hill chart for the FLINDT Francis turbine showing isocontours of machine efficiency (top) and draft tube pressure recovery factor (bottom). Operating points A-D are studied in the present work, which are of the same head and different flow rates. Modified from: Ciocan et al. [36] and Avellan [29].

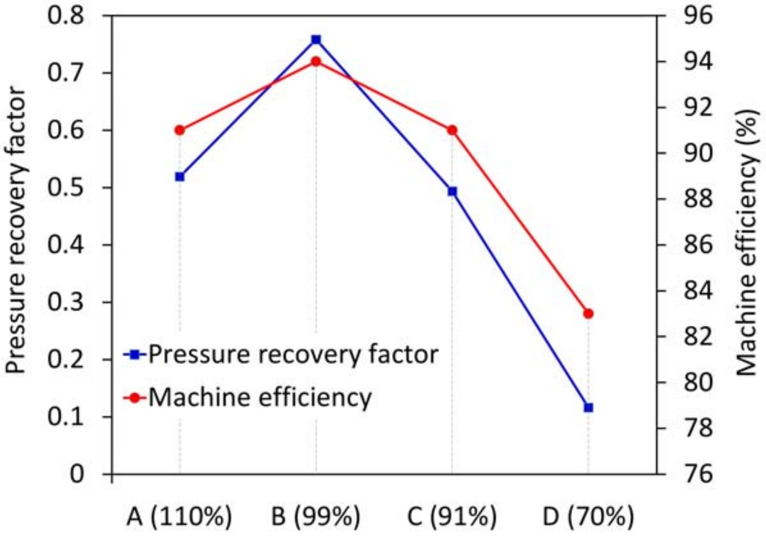

Figure 3.13: the draft tube pressure recovery factor and the machine efficiency for the studied operating points. For each point the value of Q/Q_{BEP} is given in parentheses.

is inverted for the operating point at the higher flow rate (i.e., case A). The detailed discussion on the direction of the swirl was given in section 1.2 around Fig. 1.10. The circumferential velocity is quite high in case D resulting in a high level of swirl at the inlet to the draft tube.

The swirl number is the ratio between the circumferential and the axial momentums, and is defined in this case at the inlet as [12]

$$S = \frac{\displaystyle\int_0^R UVr^2\,dr}{\displaystyle R\int_0^R U^2 r\,dr} \tag{3.2}$$

with R being the runner's radius, $R = D/2$, and V and U denoting the mean circumferential and axial velocities respectively. The inlet swirl number at the BEP is found to be about 0.22 while it increases dramatically as wicket gates are further closed (part-load operating conditions), namely to the value of 0.33 and 0.63 for cases C and D respectively.

By investigating the velocity profiles for these four points, with the same head and different flow rates, the wicket gates operation can be described. For a given head, as

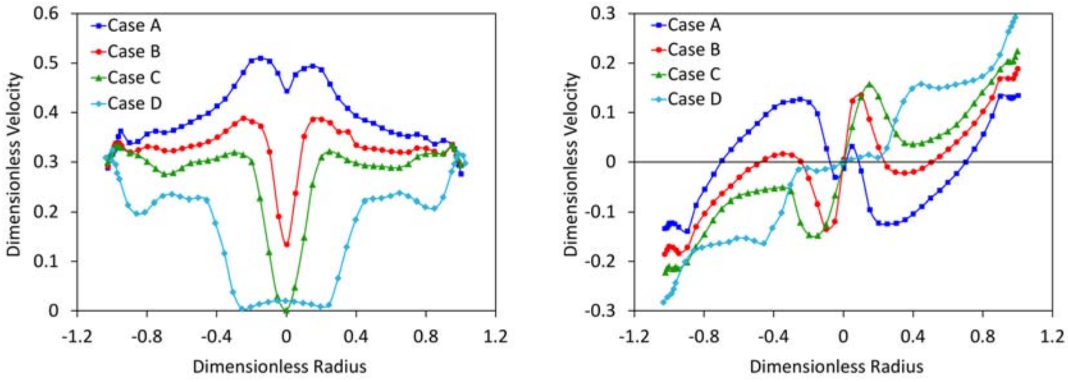

(a) axial velocity (b) circumferential velocity

Figure 3.14: Comparison between velocity components ingested by the draft tube under various operating conditions.

in this case, the flow rate through the turbine is adjustable by changing the opening angle of the wicket gates. Adjusting the wicket gate angle results in two phenomena simultaneously: changing the available flow area between the wicket gates, and modifying the angle of attack by which water interacts with the runner blades. The former results in changing the streamwise velocity through the runner and the draft tube, and the latter ultimately changes the flow angle discharged from the runner and ingested by the draft tube.

3.5 Summary

The draft tube of a model Francis turbine investigated in the FLINDT project [29] is chosen for numerical studies in this work. The main reason for choosing this test case was the availability of accurate and detailed measured data for several operating conditions. The primary challenge, however, was that the geometry of the draft tube is not available in open literature. Therefore, combining data from several documents [12, 10, 11, 24, 29, 30, 31, 32, 36, 98, 99, 101], the geometry of the FLINDT draft tube is obtained. Within the present research study, the simplified FLINDT draft tube is investigated first with results being presented in Chapter 4. Then, the complete elbow draft tube is numerically investigated in Chapter 6.

Chapter 4

Simulations of the Flow in the Simplified FLINDT Draft Tube

"Everything should be made as simple as possible... but not simpler." - Albert Einstein

4.1 The Simplified Draft Tube

As discussed in Chapter 3, the exact geometry of the FLINDT draft tube is not available in the open literature. Therefore, a simplified geometry (Fig. 4.1) based on the hydraulic diameter of the actual draft tube is built using the same approach used by Susan-Resiga et al. [12]. According to this approach the effect of cross section increase is discriminated from the changes in cross section shape and bending the mean flow path, and therefore, an axisymmetric straight diffuser is considered. In doing so, one practically focuses on the decelerated swirling flow and vortex rope formation in the draft tube cone which is indeed axisymmetric and hence is represented exactly using this model. The resulting geometry consists of a straight diffuser with a total divergence angle of 17 degrees (equal to the angle of the actual cone), followed by a long cylindrical section, as shown in Fig. 4.1.

For the simulations in this chapter the data measured at section S1 (see Fig. 3.6 and Fig. 3.14) are used as the inlet boundary conditions, therefore the computational domain starts 84 mm downstream of the actual draft tube inlet where the cone diameter is 0.425 m. All the computational results in Sec. 4.2 and Sec. 4.3 are plotted at the second measurement station, which is 158 mm downstream of the inlet section of the

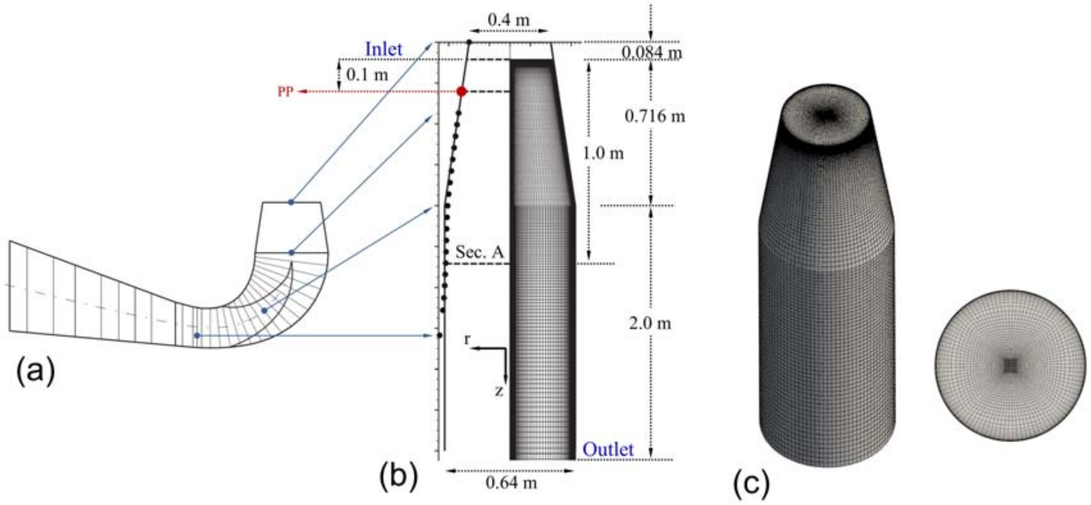

Figure 4.1: (a) FLINDT draft tube [29], (b) Simplified draft tube and 2D axisymmetric computational grid, and (c) 3D computational grid.

computational domain.

The 2D axisymmetric geometry corresponding to the meridian half-plane is discretized by 120,000 quadrilateral structured grids, while the 3D computational domain consists of 2,028,000 structured cells. In both cases the grids are refined near the wall as well as near the center of the draft tube as shown in Fig. 4.1(b) and Fig. 4.1(c). The grid is built such that the y^+ values of the grid points closest to the wall are of the order of unity. This is important [102] since all turbulence models utilized in this study are either low-Reynolds number models or are used within a two-layer zonal model for near wall treatments. Furthermore, refinement of the grid near the center of the draft tube is essential due to occurrence of large gradients. Grid sensitivity analysis in this study shows that nonrefined grids result in convergence problems and as high as 10% error in predictions.

At the inlet section, the radial profiles of axial and circumferential velocity components as well as turbulent kinetic energy are obtainable from the mean circumferentially averaged experimental data [24, 11, 36] by interpolation (see Fig. 3.14). Because of the relatively high uncertainty and low magnitude of the radial velocity component in measurements, a linear variation of this component is considered [11]. Turbulence dissipation rate is usually difficult to measure and thus is not available from experiments. Here, the inlet profiles for the dissipation rate are computed from the turbulent kinetic energy profiles as $\varepsilon = k^{3/2}/l$. The turbulence length scale $l = 0.01R$ (R is the runner radius) has been chosen according to previous studies [12] which are based on the analysis of LDV measurements. Profiles of the specific dissipation rate at the inlet are obtained from $\omega = k^{1/2}/(C_\mu l)$ with $C_\mu = 0.09$. No-slip conditions are applied at wall boundaries. At the outlet section the radial pressure equilibrium ($\partial p/\partial r = \rho V_\theta^2/r$) is applied, which is the reduced form of the radial momentum conservation equation. For the axisymmetric case, zero radial and circumferential velocities, as well as zero gradients for axial velocity, pressure, and turbulence quantities are applied at the centerline.

Two partial load operating points corresponding to case C (91% of the BEP flow rate) and case D (70% of the BEP flow rate) in Table 3.2 are selected for simulations in this chapter. Steady and unsteady numerical simulations are carried out for axisymmetric and three-dimensional grids. In steady simulations the objectives are to study the global parameters, mean flow fields and the abilities of various turbulence models in predicting mean flow quantities, whereas in unsteady simulations, transient features of the flow and vortex rope behavior and its effects are studied.

4.2 Steady Axisymmetric Simulations

Figure 4.2 shows the streamline patterns in the meridian half-plane obtained from steady axisymmetric simulations with the standard k-ε model for two cases (case C with 91% and case D with 70% of the BEP flow rate). Although the helical vortex rope is a three-dimensional, unsteady phenomenon, it can be inferred from the steady axisymmetric flow field considering the reverse flow region (recirculation bubble) visualized by the streamlines. This region is developed as a result of flow deceleration along the axis, and its size represents the vortex rope size and strength [27]. For case C the reverse flow region starts at the axial location of about 0.35 m and ends at about 0.85 m while for case D a considerably larger bubble starting from the inlet of the draft tube (z=0) and continuing up to z=0.85 m is seen. This large recirculation bubble blocks the flow path and reduces the pressure recovery in the draft tube.

The reduction in draft tube efficiency is investigated quantitatively considering the parameters evaluating the performance of the draft tube such as kinetic energy recovery coefficient, pressure recovery coefficient, and loss coefficient. The main purpose of a hydraulic turbine draft tube is to convert as much as possible the kinetic energy of the

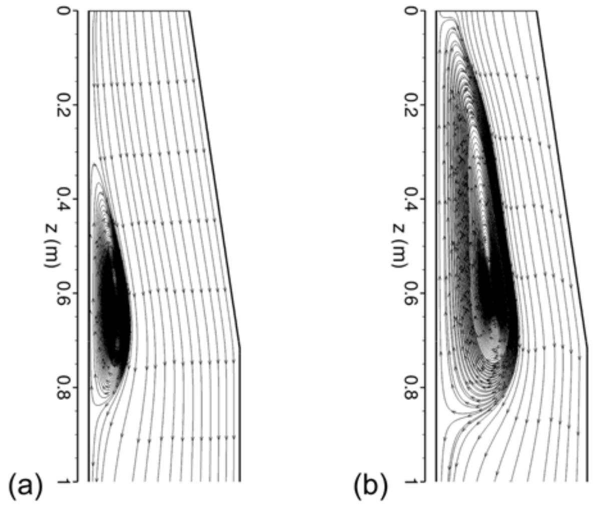

Figure 4.2: Streamline patterns for the steady axisymmetric simulation of flow in the simplified draft tube, (a) case C (91% of BEP flow rate), and (b) case D (70% of BEP flow rate).

flow leaving the runner into static pressure with minimum hydraulic losses. In order to analyze the kinetic energy-to-pressure transformation process the following integral quantities on a generic cross section $S(z)$ at the axial distance z from the inlet section are considered [103]

Flux of static pressure

$$\Pi(z) \equiv \int_{S(z)} p(r,z)\mathbf{V}.\mathbf{n}\, dA \tag{4.1}$$

Flux of kinetic energy

$$K(z) \equiv \int_{S(z)} \rho \frac{V^2(r,z)}{2}\mathbf{V}.\mathbf{n}\, dA \tag{4.2}$$

Flux of mechanical energy

$$E(z) \equiv \Pi(z) + K(z) \tag{4.3}$$

Kinetic energy recovery coefficient

$$C_{kr}(z) \equiv 1 - \frac{K(z)}{K(0)} \tag{4.4}$$

Pressure recovery coefficient

$$C_{pr}(z) \equiv \frac{\Pi(z) - \Pi(0)}{K(0)} \tag{4.5}$$

Kinetic energy-to-pressure conversion coefficient

$$C_{cr}(z) \equiv \frac{\Pi(z) - \Pi(0)}{K(0) - K(z)} = \frac{C_{pr}(z)}{C_{kr}(z)} \tag{4.6}$$

Loss coefficient

$$C_l(z) \equiv \frac{E(0) - E(z)}{K(0)} = C_{kr}(z) - C_{pr}(z) \tag{4.7}$$

For a loss-free flow the flux of mechanical energy E is constant. However, when hydraulic losses are present, E decreases monotonically with axial direction, i.e., for increasing z in this case (note z=0 is the draft tube inlet with z increasing towards downstream). These losses are normalized by the flux of kinetic energy at the draft tube inlet and represented by the loss coefficient C_l (Eq. 4.7). Furthermore, the performance of the draft tube can be evaluated using the kinetic energy-to-pressure (dynamic-to-static pressure) conversion coefficient C_{cr} (Eq. 4.6) which quantifies the transformation of the kinetic energy to static pressure within the draft tube. Obviously, higher C_{cr} and lower C_l are always desired for a draft tube. Table 4.1 shows these parameters calculated for the present simplified draft tube between inlet and a section 1 m downstream (Sec. A in Fig. 4.1). It is seen that the kinetic energy and pressure recovery coefficients are reduced by about 5% and 46% respectively by decreasing the flow rate from 91% of the BEP (case C) to 70% of the BEP (case D). Reduction of the kinetic energy recovery coefficient shows that the flow has relatively more kinetic energy at the draft tube outlet which will be wasted. This is due to the fact that the flow is blocked by the stagnant region near the center and forced to accelerate elsewhere as a result of conservation of mass principle. The main effect, however, is seen in the pressure recovery factor where considerably less kinetic energy is transformed into static pressure and the rest is dissipated by friction in the draft tube. This results in 43% reduction in the kinetic energy-to-pressure conversion coefficient in case D, while the loss coefficient associated with this case is 5 times larger than the one associated with case C. The sudden increase in the draft tube losses in part-load conditions has also been reported in previous studies [48]. Overall, this high level of losses in the draft tube results in considerable reduction of power plant total efficiency.

Table 4.1: Draft tube performance parameters calculated between inlet section and a section 1 m downstream (Sec. A in Fig. 4.1).

	Case C	Case D
Q/Q_{BEP}	91%	70%
C_{kr}	0.7114	0.6747
C_{pr}	0.6465	0.3481
C_{cr}	0.9088	0.5159
C_l	0.0649	0.3266

In order to investigate the capability and limitation of RANS models, simulations are also performed using the various turbulence models introduced in Chapter 2, and results are compared with the experimental data [11, 36] on a section located 158 mm downstream of the inlet. Figure 4.3 shows axial and circumferential velocity, and turbulent kinetic energy profiles for case C, obtained using three models, i.e., standard and realizable k-ε, and SST k-ω, in comparison with experimental data. As shown in Fig. 4.3(a), no considerable difference is seen in predictions away from the center of the draft tube, and all models show relatively good agreement with measured data. However, models underpredict the axial velocity near the centerline. Best agreement is seen in results of the SST k-ω model, still underpredicting the axial velocity by 14%. Predictions of the realizable k-ε model, on the other hand, show as much as 73% deviation from the data. It should be noted again that the uncertainties in measurements were estimated to be less than 2% [11, 36]. Interestingly, no improvement is seen by applying the realizable k-ε model instead of the standard k-ε model. Predictions of all models for the circumferential velocity are nearly the same, showing a relatively good agreement with data, namely 7% average deviation (see Fig. 4.3(b)). Turbulent kinetic energy (TKE) profiles are compared in Fig. 4.3(c). It is equally important to correctly predict TKE since it is directly used to calculate the eddy viscosity in the momentum equation, and therefore affects the velocity and pressure fields. Again, acceptable results (within 10% of data) are obtained away from the center, while results near the centerline region (-0.05 m $\leq r \leq 0.05$ m) are quite poor with at least 40% underpredictions together with a non-physical local minimum in the TKE profiles at the centerline. It appears that RANS models do not capture the correct production and diffusion of TKE near the center of the flow (see Sec. 4.6 for more details). This class of models has been developed for and calibrated by use of data from simple, steady flows near walls. Therefore, they are insufficient for predicting strong free shear-layers as in the case of the part-load draft tube flow where a strong vortex is present. This underprediction of TKE is the reason for underestimation of the axial velocity as seen in Fig. 4.3(a) since in the simulations the diffusion of momentum to the centerline is lower than expected in real life as evidenced by the experimental data. This is caused by low TKE values obtained in simulations as compared to the data.

The deviation between simulation results and data becomes larger as turbine's discharge decreases (farther away from the BEP). As shown in Fig. 4.4(a), all models completely fail in correctly predicting the level of the axial velocity near the centerline for case D. All models predict a large backflow region, and as a result, overpredict the level of the velocity outside of the shear flow region, while no reverse flow is observed within experimental data. It explains that in this case the flow is much more complicated due to higher level of swirl, larger stagnant region, and stronger shear layer, and RANS models cannot handle these complicated flow phenomena. Model predictions for the circumferential velocity component also deteriorate as one compares case C (Fig. 4.3(b)) and case D (Fig. 4.4(b)); Results show as much as 47% difference with data for case D. No experimental data for turbulent kinetic energy are found in the literature for case D, however, simulations predict a large local minimum near the centerline (not shown here) which is expected not to be seen in the experiment.

Based on these results, it is concluded that the traditional two-equation RANS models cannot correctly predict the turbulent kinetic energy and thus the axial velocity near the center of the draft tube, where the low-velocity inner region interacts with outer flow and the vortex rope forms. The precessing vortex rope enhances the mixing and turbulence production and diffusion that cannot be modeled using these turbulence models in the RANS framework. Further discussions on this issue and a possible solution are given in Sec. 4.6.

4.3 Steady 3D Simulations

Results of the three-dimensional steady simulations are presented in this section. The objectives are to compare steady 3D and 2D axisymmetric simulations, and to examine if a steady 2D axisymmetric solution (as presented in Sec. 4.2) is adequate in these cases. Furthermore, simulations are carried out using two CFD codes, namely OpenFOAM [53] and ANSYS-FLUENT [52]. As discussed in Sec. 2.4.2, OpenFOAM is an open-source library designed for development of multi-dimensional modeling codes. It includes numerous C++ classes for development of customized numerical solvers and pre-/postprocessing

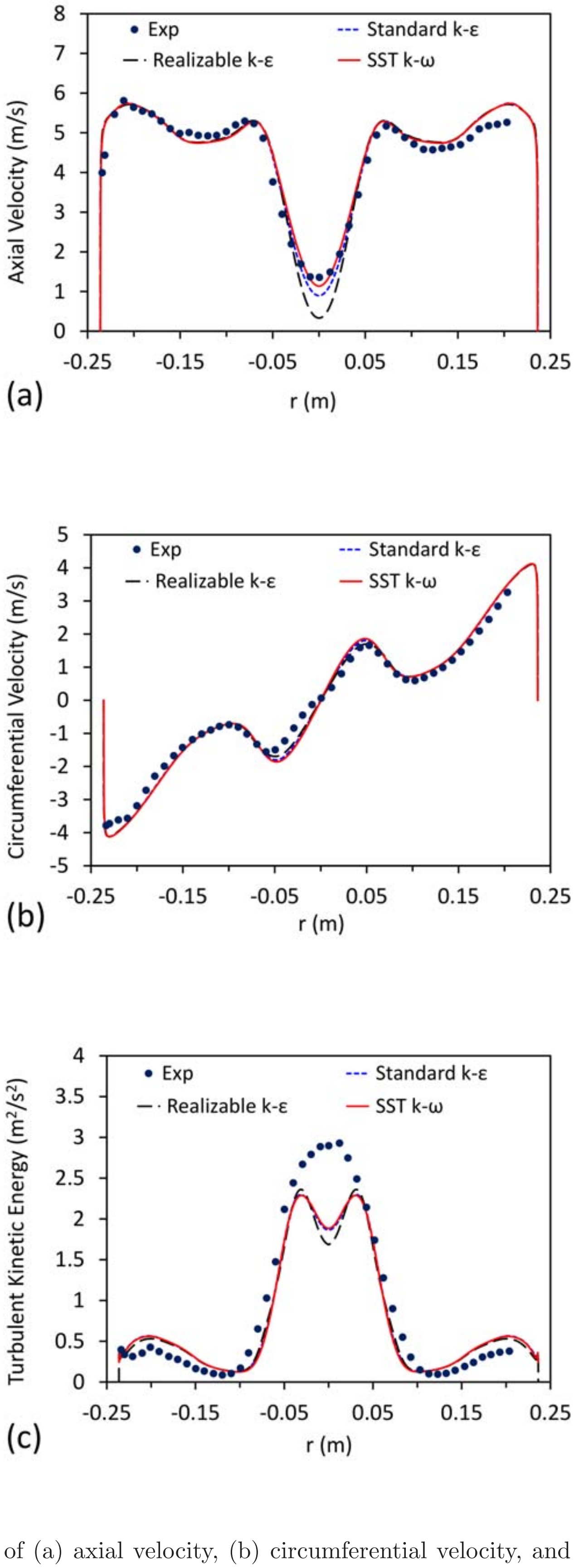

Figure 4.3: Profiles of (a) axial velocity, (b) circumferential velocity, and (c) turbulent kinetic energy in the simplified draft tube for case C, comparison of results of various turbulence closure models.

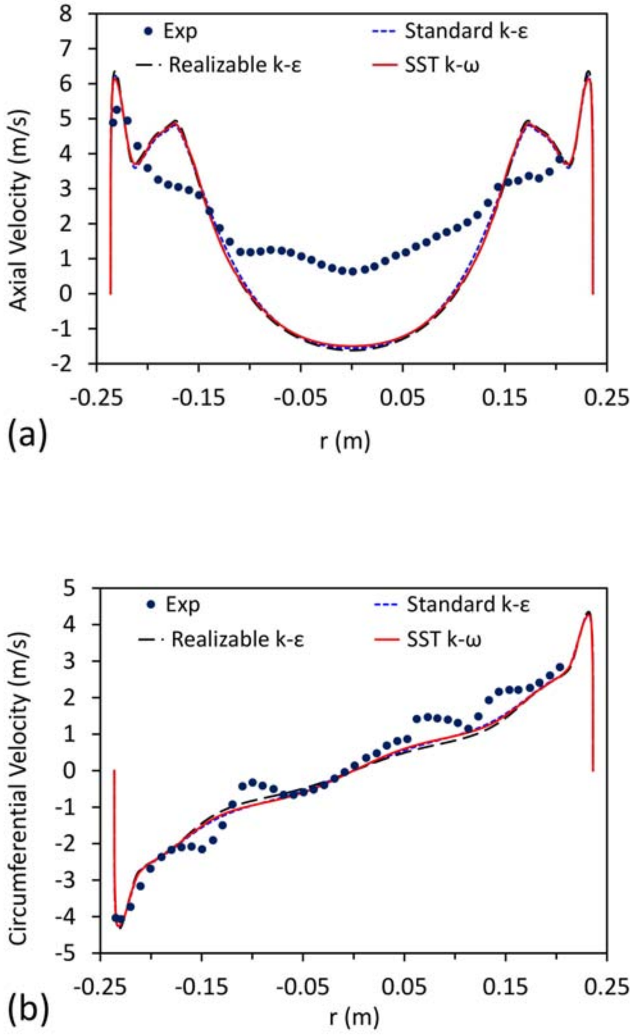

Figure 4.4: Profiles of (a) axial velocity, and (b) circumferential velocity in the simplified draft tube for case D, comparison of results of various turbulence closure models.

utilities for the solution of continuum mechanics problems, including CFD. The users can easily make changes to and develop the software features. Therefore, OpenFOAM has a prospect to be widely used in CFD simulations. However, it is required to validate its results against a commonly-used commercial CFD code such as ANSYS-FLUENT. Steady simulations are carried out on the 3D grid (Fig. 4.1(c)) utilizing the same boundary conditions, numerical schemes, and turbulence models in OpenFOAM 1.7 [53] and ANSYS-FLUENT 13.0 [52]. Since no significant improvement is seen in the previous 2D axisymmetric simulations applying more complicated turbulence models, the baseline standard k-ε turbulence model is chosen for the steady 3D simulations. Figure 4.5(a) and 4.5(b) show the axial velocity profiles for case C and case D respectively in comparison with experimental data. It is seen that OpenFOAM and ANSYS-FLUENT give nearly identical results in both cases. Also, axial velocity profiles obtained from steady 3D simulations and those obtained from 2D axisymmetric simulations almost coincide, both showing underpredictions. Therefore, it is concluded that steady RANS modeling with symmetric boundary conditions cannot generate asymmetric results for this type of flow.

4.4 Unsteady 3D Simulations

Unsteady simulations are carried out in order to model the vortex rope formation in the draft tube. The standard k-ε and the SST k-ω turbulence models are used within the URANS approach, and the detached eddy simulation (DES) is used as a hybrid URANS/LES model. Steady, symmetric inlet boundary conditions, as discussed in Sec. 4.1, are applied and unsteady simulations are initialized by their corresponding steady solutions. The time step size is taken corresponding to one degree rotation of the runner which is known to be sufficient for hydroturbine applications [36, 9]. For each time step, the solution is considered to be converged when residuals drop to 10^{-9} or maximum 30 subiterations achieved. Unsteady simulations are performed for 40,000 iterations corresponding to about 110 revolutions of the runner on a 4-CPU Linux cluster. Each time step takes 18.6 seconds using the standard k-ε model and 21.6 seconds using the DES model.

Figure 4.6 compares the results of URANS and DES simulations. Isopressure surfaces representing the vortex rope are depicted for an instance in time. For the sake of consistency, the isosurfaces of static pressure equal to -18,000 Pa (gauge pressure) are displayed in all cases. It can be seen that URANS models cannot capture the self-induced unsteadiness of the vortex rope and give steady symmetric results (similar to RANS) due to steady symmetric boundary conditions. In order to further explain this insufficiency, it is required to identify different categories of unsteady flows. The first category consists of flows with large time scale unsteadiness where a distinguished scale separation exists between the unsteadiness of the mean flow and turbulence. A generic example may be problems that involve fluctuating boundary conditions. URANS models can be successfully used in this category where the flow is forced to be unsteady because of

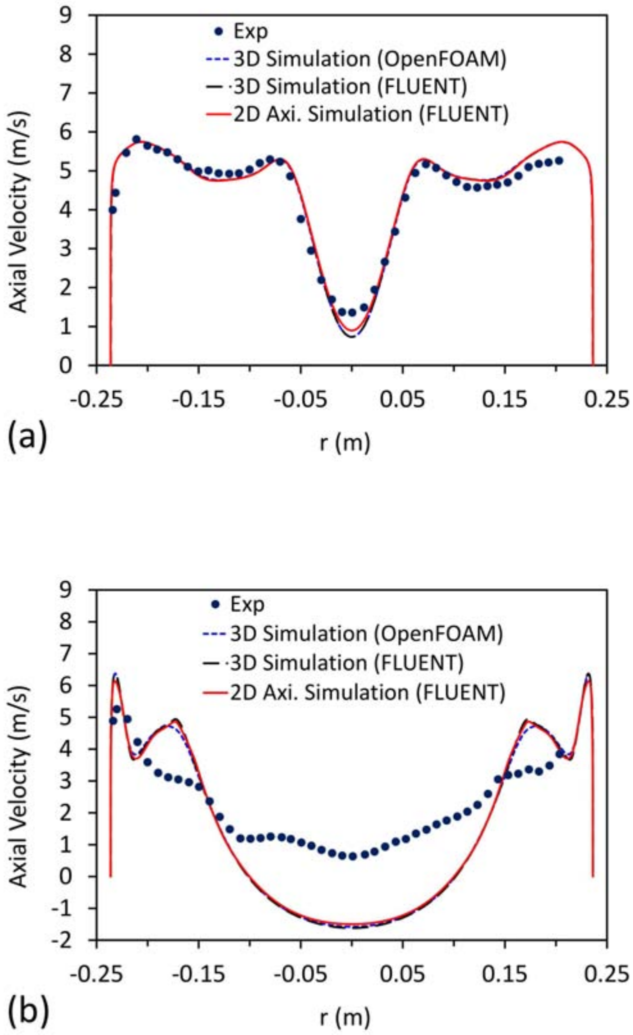

Figure 4.5: Profiles of axial velocity for (a) case C, and (b) case D in the simplified draft tube, comparison of axisymmetric and three-dimensional simulations.

unsteady boundary conditions. The second category includes flows with small time scale unsteadiness where the scale of the unsteady structures is near that of turbulence. This type of flow usually contains energetic eddies and strong instabilities which overwhelm the turbulence inherited from the upstream boundary conditions. In this category, it is difficult to distinguish between the unsteadiness and turbulent fluctuations; hence, it is quite challenging to correctly model the flow behavior. The present problem is an example of the second category, where small time scale, self-induced unsteadiness presents within the flow. This type of unsteadiness is a form of the Kelvin-Helmholtz instability and is due to the roll-up and breakdown of the shear layer at the interface of the central region with lower velocity (due to the wake of the crown cone) and swirling, high-velocity region farther away. The URANS approach does not differentiate between this small time scale unsteadiness of the vortex rope and turbulent fluctuations and hence averages away all the unsteadiness of the flow resulting in steady solutions. Applying the DES model, when the vortex rope unsteadiness is resolved in an LES manner, detailed unsteady features of the flow can be captured sufficiently, resulting in a nonsymmetric precessing vortex rope as shown in Fig. 4.6.

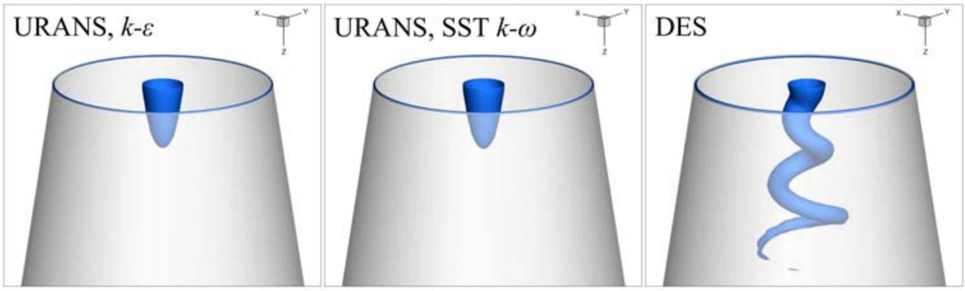

Figure 4.6: Isopressure surfaces in the draft tube for an instance in time, comparison of results using three different unsteady turbulence closure approaches.

Based on these results, the DES turbulence model is chosen for further unsteady simulations. Figure 4.7 compares the vortex rope resulting from these simulations with experimental visualizations for both case C and D. The vortex rope developed in case D is considerably larger both in diameter and length. As seen in this figure, the helical vortex has a short wavelength and a small diameter near the best efficiency region and its length and diameter increase as the flow rate is decreased. The overall shape of the vortex rope agrees well with the experimental visualizations [104] for both operating conditions as shown in Fig. 4.7. It should be noted that experiments were performed for different cases (with and without cavitation) [36, 104]. Here, numerical results are compared quantitatively with experimental data for a noncavitating case, while the shape of the vortex rope is compared qualitatively with the case with cavitation, since no experimental visualization was performed for the noncavitating case. However, regardless of the cavitation number, the vortex rope can be formed and can affect the performance of the draft tube.

As discussed in Chapter 1, formation of the vortex rope is associated with pressure

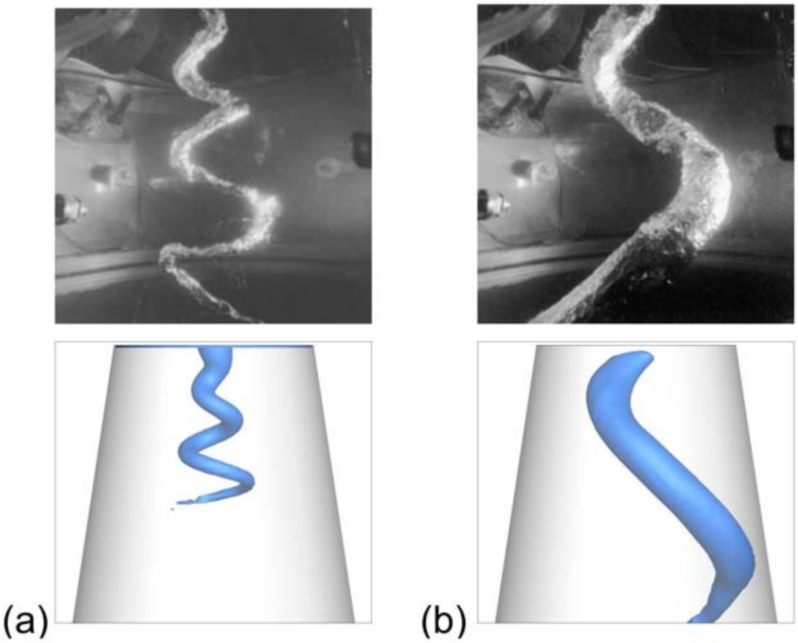

Figure 4.7: Vortex rope visualized by isopressure surfaces for (a) case C (91% of the BEP flow rate), and (b) case D (70% of the BEP flow rate) in comparison with experimental visualizations [104].

fluctuations in the draft tube. Figure 4.8 shows the evolution of wall pressure with time in the draft tube cone for point PP in Fig. 4.1(b), 0.1 m downstream of the inlet section, during unsteady simulations of case D. It takes about 2 seconds (corresponding to 12,000 iterations and 33 rotations of the runner) to reach the periodic unsteady (quasi-steady) state. Simulations are performed for more than 4 seconds (24,000 iterations) after this point to make sure that a well-converged solution is obtained.

Pressure fluctuations due to the vortex rope have large amplitude, as high as twice the local mean pressure value, and low frequency as shown in Fig. 4.8(a). The dominant frequency of the pressure fluctuations can be obtained by performing a fast Fourier transform (FFT) on the results (time to frequency transformation). Figure 4.8(b) shows the normalized frequency spectrum obtained from present simulations. The vortex rope frequency is found to be about 0.318 of the runner rotation frequency. This is in good agreement with the value of 0.3 obtained from experimental studies [36] (only 6% error). It should be noted that the effect of a 90-degree elbow is mainly to increase the amplitude of the pressure fluctuations due to interaction between the vortex core and secondary

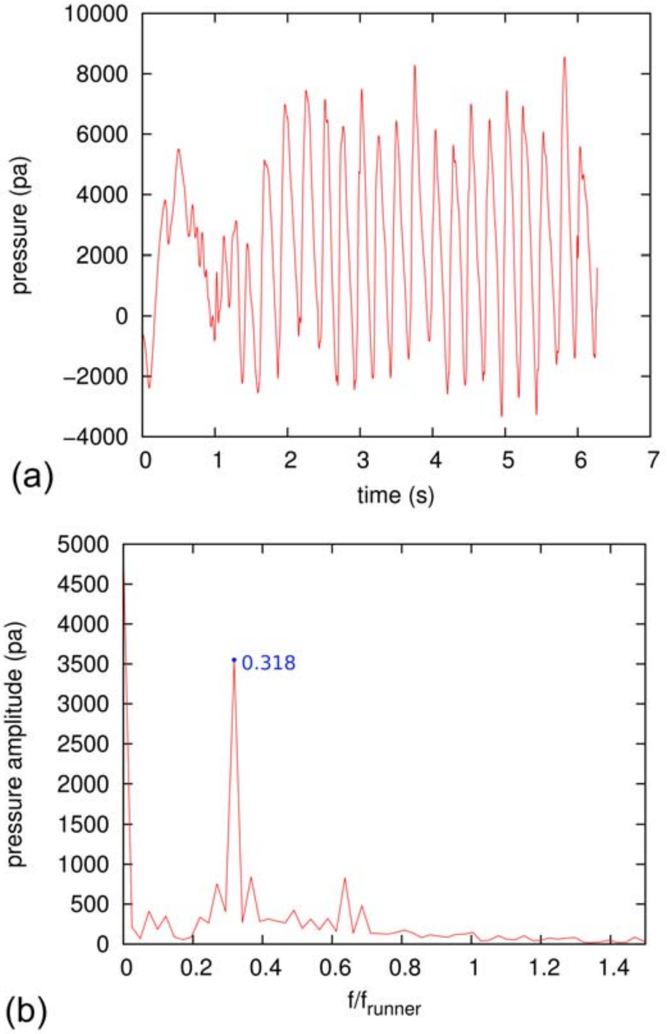

Figure 4.8: (a) Wall pressure fluctuations in the simplified draft tube for point PP in Fig. 4.1(b), and (b) their normalized frequency spectra showing the frequency of the vortex rope precession.

flows; however, resonance phenomena and frequency of fluctuations remain unchanged since the excitation source is still generated as explained in Ref. [33]. Therefore, only the frequency (and not amplitude) of the fluctuations is compared with data here.

The physics behind the formation of a vortex rope is analyzed in this study. It is confirmed in the present simulations that the development of the vortex rope is associated with formation of a stagnant region at the center of the draft tube. The flow is stopped or even reversed in this region. This is mainly due to the wake behind the crown cone as well as the swirl, which tends to decrease flow momentum near the centerline and increase it near the wall. Figure 4.9 shows formation of the vortex rope in the draft tube cone obtained from unsteady simulations with DES. Instantaneous isopressure surfaces (dark) representing the vortex rope and isoaxial velocity (U=0) representing the stagnant region (light) are shown in this figure. The stagnant region was represented in steady simulations by the recirculation bubble. It can be seen that the rope forms at the interface between this stagnant region and highly swirling outer flow. In fact, the vortex rope is wrapped around the low-velocity inner region. The physical mechanism of vortex rope formation can be related to the Kelvin-Helmholtz instability which occurs when a velocity gradient is present within a continuous fluid. The shear layer at the interface of two flows with different velocities may roll up resulting in formation of vortices spinning with high angular velocity. Pressure drops within these vortices according to the radial momentum conservation, which may result in cavitation as seen in many experiments related to draft tube flow [32, 36, 104]. Based on these results possible controlling mechanisms for the prevention of vortex rope formation can be introduced, which is based on the elimination of the stagnant and reversed flow region. This is investigated in Chapter 7.

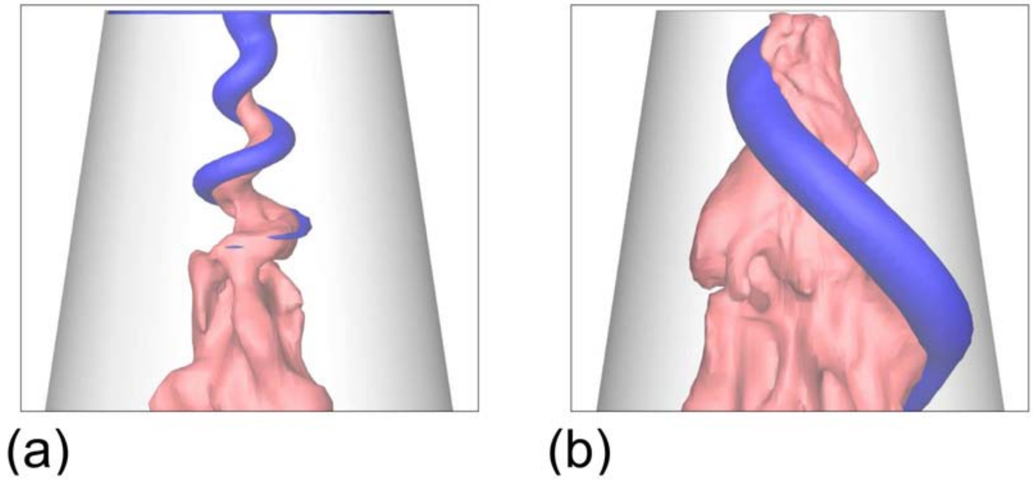

Figure 4.9: Isopressure surface (dark) representing vortex rope and isovelocity surface (light) representing the stagnant region for (a) case C and (b) case D for an instance in time.

4.5 The Vortex Rope Frequency

As shown in Sec. 4.4, the formation of the vortex rope in draft tubes results in strong pressure fluctuations. Two main parameters characterizing these fluctuations are their amplitude and frequency. The amplitude of the pressure fluctuation, usually quantified by the root-mean-square (rms) of the oscillation, defines the magnitude of the oscillatory force experienced by the power plant components due to the rotation of the vortex rope. Therefore, as it is obvious, higher-amplitude oscillations are more critical. The frequency of fluctuation, also known as the vortex rope frequency or the draft tube surge frequency, becomes important when it gets close to the natural frequency of the draft tube structure[1]. In this condition the pressure pulsation observed at different circumferential locations becomes approximately synchronous and shows a resonance-like behavior [105]. This is extremely harmful for a hydropower plant and is considered as a “forbidden” or “no-go” operating condition. Therefore, it is important to study the vortex rope frequency (Pressure fluctuation amplitude is studied in Chapter 6.).

The frequency of the vortex rope is generally known to be around 0.2-0.4 of the frequency of rotation of the runner. The earliest prediction of the vortex rope frequency was performed by Rheingans [106], who found the following relationship between the frequencies of the vortex rope f_v and the runner f_r

$$\frac{f_v}{f_r} \simeq \frac{1}{3.6} \simeq 0.278 \tag{4.8}$$

Later, Hosoi [107] developed the following empirical relation using model tests

$$\frac{f_v}{f_r} \simeq \frac{1}{2}\left(\frac{r_a}{R}\right)^2 \tag{4.9}$$

where r_a is the radius of the vortex core and R is the draft tube radius. Experiments [107] indicated that r_a/R varies between 0.7 and 0.8, therefore, Eq. (4.9) agrees with Eq. (4.8) of Rheingans [106].

Following Cassidy [108] and Falvey and Cassidy [109], a dimensional analysis can be performed to obtain a relation for the vortex rope frequency. The frequency f is considered to be a function of

- Fluid density $\rho\left\{ML^{-3}\right\}$

---

[1] More exactly speaking, the natural frequency of the draft tube structure together with the contained fluid which becomes critical when cavitation occurs and vapor forms in the flow. The cavitating vortex rope is out of the scope of this work.

- Fluid kinematic viscosity $\nu \left\{L^2T^{-1}\right\}$
- Draft tube inlet diameter $D\left\{L\right\}$
- Draft tube length $L\left\{L\right\}$
- Flow rate $Q\left\{L^3T^{-1}\right\}$
- Flow rate of the angular momentum $\Omega \equiv \displaystyle\int \rho\left(\vec{r}\times\vec{V}\right)\mathbf{V.n}\,dA\left\{ML^2T^{-2}\right\}$

in a functional relationship as

$$F\left(f,\rho,\nu,D,L,Q,\Omega\right)=0 \tag{4.10}$$

Considering f, Ω, ν, and L as independent variables which are related to ρ, D, and Q, one may perform a dimensional analysis to obtain four dimensionless groups

- $\Pi_1 = \left(\frac{fD^3}{Q}\right)$ The non-dimensional frequency of the vortex rope (The frequency parameter)
- $\Pi_2 = \left(\frac{\Omega D}{\rho Q^2}\right)$ The non-dimensional angular momentum of flow entering the draft tube (The swirl number S)
- $\Pi_3 = \left(\frac{Q}{\nu D}\right)$ The Reynolds number
- $\Pi_4 = \left(\frac{L}{D}\right)$ The draft tube length-to-diameter ratio

Therefore

$$\left(\frac{fD^3}{Q}\right)=g\left[\left(\frac{\Omega D}{\rho Q^2}\right),\left(\frac{Q}{\nu D}\right),\left(\frac{L}{D}\right)\right] \tag{4.11}$$

At large Reynolds numbers (typical in hydro applications) the viscous effects are negligible. Therefore, it can be assumed that the frequency is independent of the Reynolds number. Therefore, for a given draft tube with a fixed geometry (i.e., L/D =const.) the frequency of the vortex rope is a function of only the swirl number, i.e.,

$$\left(\frac{fD^3}{Q}\right)=g\left(\frac{\Omega D}{\rho Q^2}\right)=g(S) \tag{4.12}$$

The exact form of the function g is obtainable by performing extensive experiments for several inlet swirl numbers. It should be noted that g is unique for a specific draft tube shape.

In order to obtain a relation for the vortex rope-to-runner frequency ratio, the flow rate in the left-hand side of Eq. (4.12) is replaced by the discharge coefficient using Eq. (1.3). Furthermore, considering $R = D/2$ being the draft tube inlet radius (equal to the runner outlet radius) and $\omega = 2\pi f_r$ being the runner angular velocity, Eq. (4.12) can be written as

$$\frac{f_v}{f_r} = \frac{\pi^2}{4}\varphi g(S) \tag{4.13}$$

As discussed in Chapter 1, a hydroturbine typically has a constant head and rotational speed, and the flow rate is adjusted by the wicket gate opening which defines the operating point of the machine. Therefore, for a typical Francis turbine with a known head and rotational speed, the right-hand side of Eq. (4.13) is a function of only the wicket gate opening (WGO). Wicket gates add an angular momentum Ω_0 to the flow, part of which is extracted by the runner as the torque T. Therefore the angular momentum of the flow leaving the runner and entering the draft tube is

$$\Omega = \Omega_0 - T = \Omega_0 - \frac{P}{\omega} \tag{4.14}$$

where $P = \eta\rho g H$ is the runner mechanical power and ω is the angular velocity of the runner. Using Eq. (4.14), the dimensionless angular momentum parameter (the swirl number) can be written as

$$S = \frac{\Omega D}{\rho Q^2} = \frac{\Omega_0 D}{\rho Q^2} - \frac{PD}{\rho Q^2 \omega} \tag{4.15}$$

The first term on the right-hand side of Eq. (4.15) is called the wicket gate momentum parameter and can be related directly to the WGO. For example, it is shown [110] that

$$\frac{\Omega_0 D}{\rho Q^2} = 59\,(\mathrm{WGO})^{-1.18} \tag{4.16}$$

where WGO is the opening angle of the wicket gates in degrees, measured from 0 when fully closed. Figure 4.10 shows the value of the wicket gate momentum parameter as a function of the gate opening.

The second term on the right-hand side of Eq. (4.15) is the swirl extracted from the flow by the turbine runner. Using head and flow rate coefficients (Eq. (1.2) and (1.3) this term can be written as

$$\frac{PD}{\rho Q^2 \omega} = \frac{1}{\pi}\left(\frac{\psi}{\varphi}\right) \tag{4.17}$$

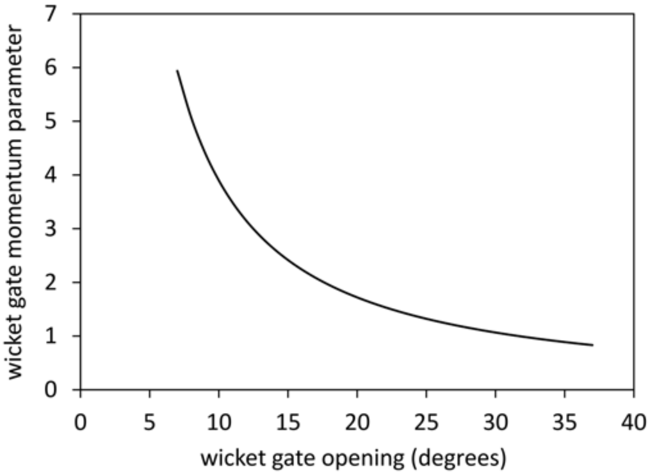

Figure 4.10: The change in the wicket gate momentum parameter $\frac{\Omega_0 D}{\rho Q^2}$ with wicket gate opening angle.Source: Wahl [110].

By substituting Eq. (4.16) and (4.17) in Eq. (4.13), another form for the vortex rope-to-runner frequency ratio is obtained

$$\frac{f_v}{f_r} = \left(\frac{\pi^2 \varphi}{4}\right) g\left[h(\mathrm{WGO}) - \frac{1}{\pi}\left(\frac{\psi}{\varphi}\right)\right] \tag{4.18}$$

where h is some function of WGO, for example, the right-hand side of Eq. (4.16). This form clearly shows that the ratio between the frequencies of the vortex rope and the runner is a function of only the WGO which defines the flow rate coefficient φ for a specific machine with fixed head ψ and rotational speed ω.

The simplest choice for the function g is a constant. This is inspired by the experimental measurements of Wahl [110] in a model (1:40) test of the 700 MW turbine installed at the Grand Coulee third power plant. As shown in Fig. 4.11, the frequency parameter is almost constant for swirl numbers less than one (remember that the swirl number in the FLINDT draft tube for case D with 70% of the BEP flow rate was 0.63.).

Figure 4.11 suggests the value of 0.5 for the frequency parameter, i.e.,

$$\left(\frac{fD^3}{Q}\right) = 0.5 \tag{4.19}$$

Hence, using Eq. (4.13), the relation for the vortex rope frequency is found to be

$$\frac{f_v}{f_r} = \left(\frac{\pi^2}{8}\right)\varphi \tag{4.20}$$

In the case of the FLINDT draft tube, for the operating point D with $\varphi = 0.26$, Eq. (4.20) gives the value of $f_v/f_r = 0.32$ which is in close agreement with the experimental value of 0.3. Furthermore, the linear increase of the vortex rope frequency with the discharge coefficient (suggested by Eq. (4.20)) is shown in Ref. [111].

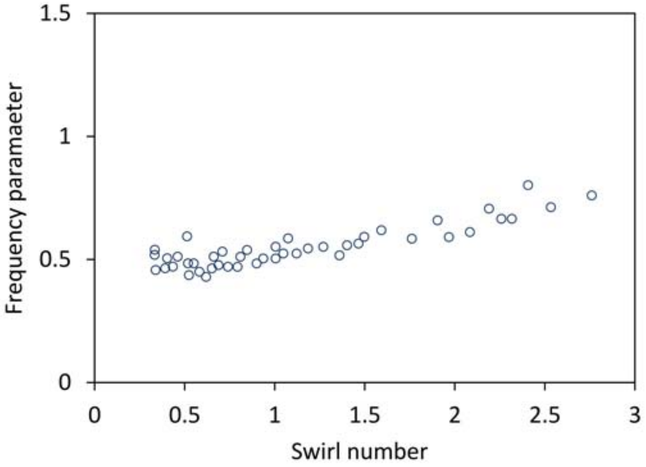

Figure 4.11: The change in the frequency parameter $\frac{fD^3}{Q}$ with the swirl number $\frac{\Omega D}{\rho Q^2}$. Data source: Wahl [110].

As stated above, a more comprehensive form of the function g can be obtained by performing extensive experimental or numerical studies. Furthermore, the effect of the draft tube shape on the surge frequency should be investigated. One such study was performed by Palde [14] who conducted extensive experiments using simplified models with air flow to correlate the draft tube shape and the draft tube surge characteristics. Palde stated that the draft tube shape has significant influence on the surging characteristics. However, it seems that this influence is more evident for the amplitude than for the frequency. In addition, the degree of divergence of the draft tube and the throat geometry were found to have more effect than the remaining downstream portion of the draft tube including the bend and the pier [14].

4.6 Development of an Axisymmetric Model for Draft Tube Flow at Partial Load

While agreeing with the fact that 3D unsteady simulations are necessary in predicting the behavior of the vortex rope in a draft tube operating under partial load, it should be noted that such computations are expensive in terms of both time and computing resources. As a result, more computationally tractable techniques are required for performance evaluation and design optimization purposes. These techniques would be useful, for example, in optimization of the shape of the runner blades in order to reduce the stagnant region extent, thus mitigating the vortex rope.

One such method is to analyze the draft tube flow at partial load by using an axisymmetric swirling flow model and steady simulations [101]. Obviously, the axisymmetric hypothesis is a major simplification having the main benefit of dramatically reducing the computational cost. On the other hand, it introduces important limitations as far as the three-dimensionality and unsteadiness are concerned. The inherent flow instability in the draft tube leads to a fully 3D unsteady flow field with precessing vortex rope when the Francis turbine is operated at partial discharge. As a result, the axisymmetry assumption is obviously violated. However, one can conjecture that an axisymmetric flow model can represent the circumferentially averaged three-dimensional unsteady flow. In other words, instead of circumferentially averaging the 3D unsteady computational results one can perform averaging on the governing equations in cylindrical coordinates, thus solving a 2D axisymmetric problem in a meridian half-plane [101, 112].

Nevertheless, one important issue to be addressed is the effect of neglecting the actual precessing vortex rope when computing directly the circumferentially averaged flow. As shown in the present numerical simulations (see the discussion around Fig. 4.3 and Fig. 4.4) and also previous studies [12, 101, 113], steady RANS turbulence models underpredict axial mean velocity and turbulent kinetic energy near the center of the draft tube. This is attributed mainly to the incapability of these models in predicting the mixing in the shear layer associated with the vortex rope. This strong shear layer forms at the interface between a stagnant region at the center of the draft tube and the outer flow. The stagnant region can be understood as the extent of the wake of the crown cone which is the average of the highly fluctuating flow field where the vortex rope wraps around. Susan-Resiga et al. [101] introduced a stagnant region model (SRM) which essentially enforces a unidirectional circumferentially averaged flow, by switching the axial and radial velocity directions and letting the swirl velocity equal to zero, whenever a negative (i.e., upstream oriented) axial velocity is detected. Although this model improved results in comparison to the original 2D simulations, it seems to be nonphysical and yet shows considerable deviations from the experimental data. In this section a new approach is considered, which is to develop a new RANS turbulence model in order to correctly predict the mean flow field in a draft tube operating under partial load using an axisymmetric model.

4.6.1 Investigations of RANS Turbulence Models

Steady RANS simulations of flow in the simplified draft tube performed in Sec. 4.2 showed underprediction of the axial velocity and turbulent kinetic energy near the center of the draft tube. The deviation from the experimental data increases considerably, moving farther from the best efficiency condition. Since no considerable improvement in predictions was seen applying different turbulence models, the two-equation standard k-ε turbulence model with two-layer zonal model for near wall treatment is chosen for development of the axisymmetric model in this section.

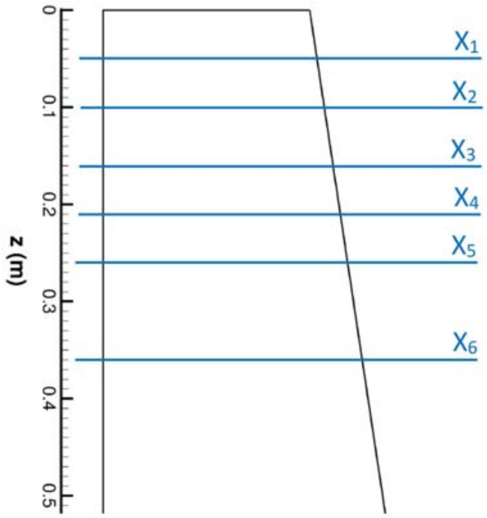

Figure 4.12: Investigated sections in the simplified draft tube.

In order to further investigate the flow field inside the draft tube, six cross sections (X_1 to X_6) are chosen as shown in Fig. 4.12. The streamwise (z) value associated with these cross sections are given in Fig. 4.12. Figure 4.13 shows the distributions of the turbulent kinetic energy (TKE) production on these six sections. Production of TKE can be written as

$$P = 2\nu_t S_{ij} S_{ij} = \nu_t \left(\frac{\partial \bar{u}_i}{\partial x_j} + \frac{\partial \bar{u}_j}{\partial x_i} \right) \frac{\partial \bar{u}_i}{\partial x_j} \tag{4.21}$$

Results are shown for two partial load cases, i.e., for case C and case D. Note that near-wall region ($R > 0.2$ m) is not shown in Fig. 4.13 in order to better present the results near the centerline ($R = 0$). Nevertheless, one can infer that P has a considerable peak near the wall due to high velocity gradients resulting in high TKE generation.

It can be seen that in both cases P has another peak near the center of the draft tube which moves farther from the centerline as the flow moves downstream. This maximum in TKE production shows the generation of turbulent kinetic energy near the centerline which can be attributed to the formation of a strong shear layer between stagnant region and the outer flow. Therefore, the location of the peak in TKE production may provide information about the location of the shear layer, i.e., the location of the boundary between stagnant region and outer flow. This is investigated in this study by locating the point of the maximum P value for each section and by plotting the radial distance of these points from centerline, as shown in Fig. 4.14. It is seen in Fig. 4.14 that a line can be fit through these data with very good precision. This line represents the location of the maximum TKE production due to the formation of the shear layer in the draft tube.

It was shown in Sec. 4.4 that the vortex rope is formed due to the role-up of this shear layer and wraps around a stagnant region in the draft tube. Therefore, the average location of the shear layer shown by the line in Fig. 4.14 represents the average location of the vortex core in the rope. This is validated by comparing with the experimental data of Ciocan and Iliescu [99] who used PIV to investigate the flow field in the draft tube cone and to locate the vortex core. They showed that the vortex rope wraps around a conical surface, and found the angle of inclination of this cone to be 17 degrees, twice the cone's inclination. The slope of the line fitted through maximum P points for case D (see Fig. 4.14(b)) is found to be 16.5 degrees which is in very good agreement with measurements of Ciocan and Iliescu [99]. This is better presented in Fig. 4.15 where the line of maximum TKE production obtained from steady axisymmetric simulations, PIV data of Ciocan and Iliescu [99], and 3D unsteady simulation results (details of these

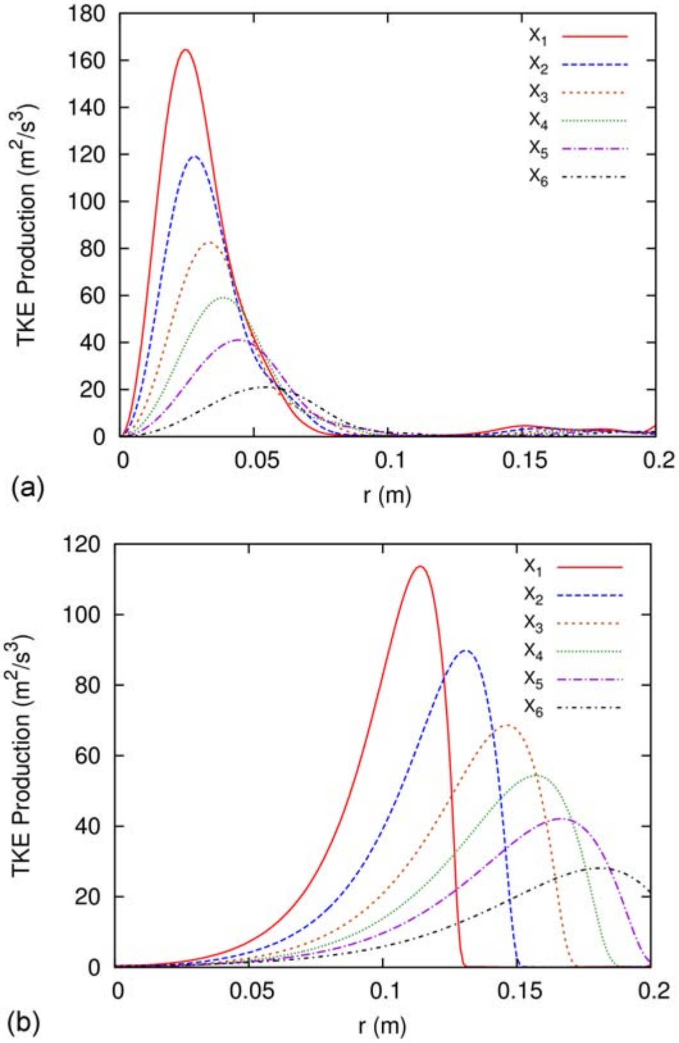

Figure 4.13: Radial distributions of the turbulent kinetic energy production at several streamwise sections for (a) case C, and (b) case D in the simplified draft tube.

simulations are given in Chapter 6) are shown together. It can be seen that there is a very good agreement between all three methods in locating the vortex core. Therefore, it is concluded that the line of the maximum TKE production obtained from steady axisymmetric simulations represents the surface of the cone (in 3D) where the vortex rope wraps around.

This is a very important finding, since it shows that although 2D axisymmetric simulations cannot model the vortex rope, they can give the average location of the boundary between the stagnant region and the outer swirling flow, i.e., the average location of the vortex rope in the conical part of the draft tube. Nevertheless, the level of

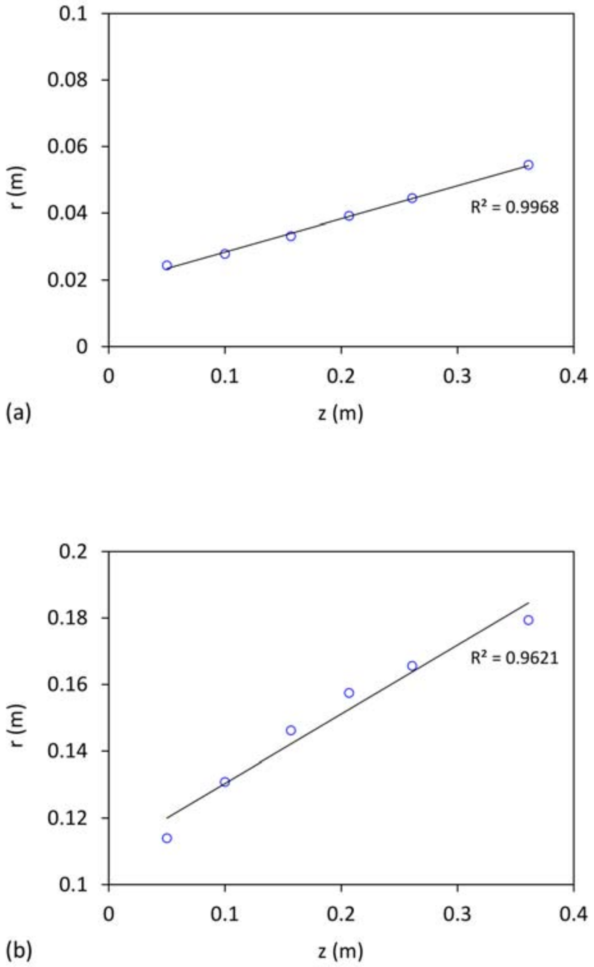

Figure 4.14: Locations of the peaks in TKE production P in the simplified draft tube for (a) case C, and (b) case D (also see Fig. 4.13). A line can be fit through these points with very good precision.

the TKE production may not be predicted correctly resulting in underprediction of TKE and axial velocity at the center of the draft tube as shown in Fig. 4.3 and Fig. 4.4. This is investigated by comparing the production obtained by the axisymmetric k-ε RANS simulations (Eq.(4.21)) with the one obtained by the 3D unsteady DES simulations. In the DES simulations, the production of TKE can be obtained by

$$P = -\overline{u_i u_j}\frac{\partial \bar{u}_j}{\partial x_i} \tag{4.22}$$

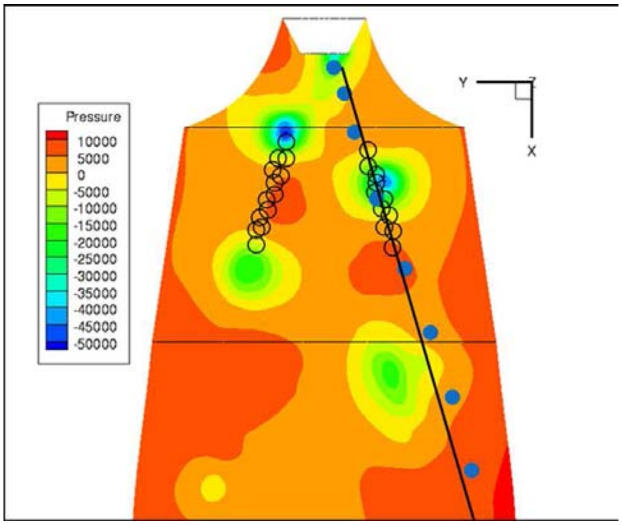

Figure 4.15: Locations of the vortex core in the draft tube, comparison between (○) PIV measurements of Ciocan and Iliescu [99], (●) 2D axisymmetric predictions and a line fitted through them, and contours of the instantaneous pressure (Pa) field in the background obtained from 3D unsteady simulations.

which is due to the interaction between resolved-scale velocity gradient ($\frac{\partial \bar{u}_j}{\partial x_i}$) and subfilter Reynolds stresses ($\overline{u_i u_j}$).

As depicted in Fig. 4.16, the level of the TKE production is underpredicted by RANS simulations comparing to the DES results, while the location of the maximum TKE production is well captured which is consistent with the previous observation.

Additionally, overprediction of the drop in TKE at the centerline (the difference between the level of TKE at the centerline and the peak associated with the shear layer) predicted by the RANS simulations (see Fig. 4.3(c)) indicates that the level of TKE diffusion is not correctly predicted either. Therefore, a modified model should deal with correcting the level of TKE production and diffusion within the shear layer and stagnant region in the draft tube.

4.6.2 Model Development and Results

It was argued in the previous section that steady RANS models underpredict the turbulent kinetic energy production and diffusion in regions of the flow where the vortex rope forms. This is summarized graphically in Fig. 4.17 where turbulent kinetic energy

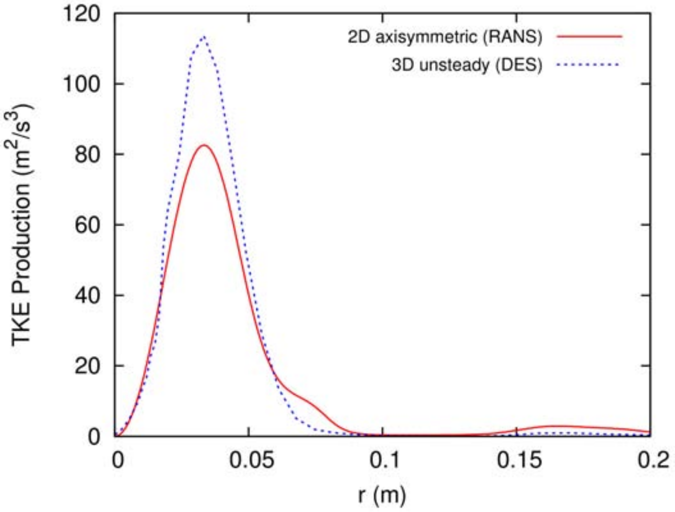

Figure 4.16: Radial distributions of the TKE production at section X_3 in the draft tube, comparison between DES and RANS simulations.

is plotted in the draft tube (same as Fig. 4.3(c)). It should be noted that this conclusion holds for both 2D axisymmetric and 3D steady RANS simulations since no difference is seen between results of these simulations (see Sec. 4.3). Nevertheless, the focus of the present section is on 2D axisymmetric modeling.

The goal of the present section is to take the effects of extra production and diffusion of TKE due to the vortex rope unsteadiness into account using a physical model. The extra production and diffusion can be physically understood as coherent or local turbulence production/diffusion as opposed to the mean production/diffusion. The Kelvin-Helmholtz instabilities associated with the formation of the vortex rope (see Sec. 4.4) locally generate turbulence as shown experimentally in other flow problems including a strong shear layer [114, 115, 116]. The shear layer instabilities yield a considerable kinetic energy transfer from the mean flow to the vortices in the region where the shear layer roll-up occurs. Scarano et al. [114] experimentally investigated the turbulent separated flow over a backward facing step and found a relationship between the coherent structures in the shear layer and the production of TKE. In their work, the dominant role of the coherent structures in the production of TKE is confirmed by the high values of coherent production compared with the corresponding mean production. Furthermore, they stated that regions with considerable TKE production correspond to the area where the occurrence of vortices is higher, which confirms the conclusion in Sec. 4.6.1.

Based on all these observations, a new steady RANS model for simulations of the

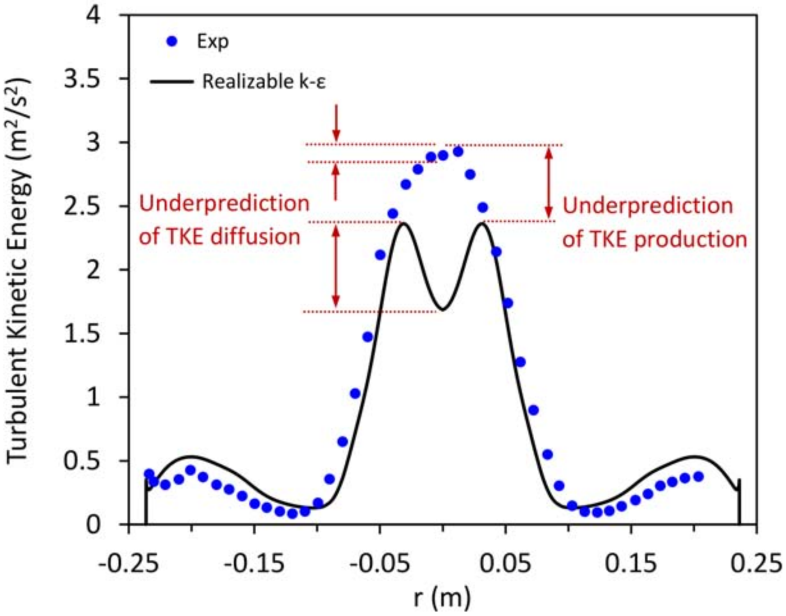

Figure 4.17: Distributions of the turbulent kinetic energy (TKE) in the simplified draft tube. The deviation between RANS predictions and experimental data is attributed to the underprediction of the TKE production and diffusion.

mean flow field in the draft tube cone is developed by modification of the TKE transport equation as follows

$$\bar{u}_i \frac{\partial k}{\partial x_i} = \frac{\partial}{\partial x_i}\left[\left(\nu + \frac{\nu_t}{\sigma_k}\right)\frac{\partial k}{\partial x_i}\right] + P - \varepsilon + P_c - D_c \tag{4.23}$$

where P_c and D_c are the coherent TKE production and diffusion due to the vortex rope respectively. Using the concept of the coherent eddy viscosity ν_c, these extra terms can be written as

$$P_c = \nu_c\left(\frac{\partial \bar{u}_i}{\partial x_j} + \frac{\partial \bar{u}_j}{\partial x_i}\right)\frac{\partial \bar{u}_i}{\partial x_j} \tag{4.24}$$

$$D_c = \frac{\partial}{\partial x_i}\left[\nu_c \frac{\partial k}{\partial x_i}\right] \tag{4.25}$$

Therefore, Eq. (4.23) can be written as

$$\bar{u}_i \frac{\partial k}{\partial x_i} = \frac{\partial}{\partial x_i}\left[\left(\nu + \frac{\nu_t}{\sigma_k} + \nu_c\right)\frac{\partial k}{\partial x_i}\right] + (\nu_t + \nu_c)\left(\frac{\partial \bar{u}_i}{\partial x_j} + \frac{\partial \bar{u}_j}{\partial x_i}\right)\frac{\partial \bar{u}_i}{\partial x_j} - \varepsilon \tag{4.26}$$

where the only unknown parameter is the coherent eddy viscosity ν_c. Considering the analogy with the eddy viscosity concept, this coherent eddy viscosity can be related to a length and a velocity scale as

$$\nu_c \propto \ell_c v_c \tag{4.27}$$

where ℓ_c and v_c are the length and velocity scales of the unsteady coherent structures forming within the shear layer in the draft tube. Note that Eq. (4.27) makes sense on dimensional grounds. The velocity scale v_c, itself, can be written as

$$v_c = \ell_c \Omega \tag{4.28}$$

where Ω represents the angular velocity of fluid particles in the vortices, therefore, it is chosen to be the vorticity magnitude

$$\Omega \equiv \sqrt{2\Omega_{ij}\Omega_{ij}} \tag{4.29}$$

where Ω_{ij} is the mean rate-of-rotation tensor

$$\Omega_{ij} = \frac{1}{2}\left(\frac{\partial \bar{u}_i}{\partial x_j} - \frac{\partial \bar{u}_j}{\partial x_i}\right) \tag{4.30}$$

Considering the simplest form, the coherent eddy viscosity can be written as

$$\nu_c = \ell_c^2 \Omega \tag{4.31}$$

The closure problem still exists, but now it has changed to finding the length scale ℓ_c. The length scale of the coherent structures in the vortex rope is related to the thickness of the shear layer, and can be seen as the vortex rope diameter. However, no general definition was found for the vortex rope diameter in the literature. There are attempts to extract the rope diameter by image processing [32], but they are limited to the cavitating vortex rope (see Fig. 4.18) using the volume of the vapor (which is a function of the cavitation number), and hence, cannot be used in general.

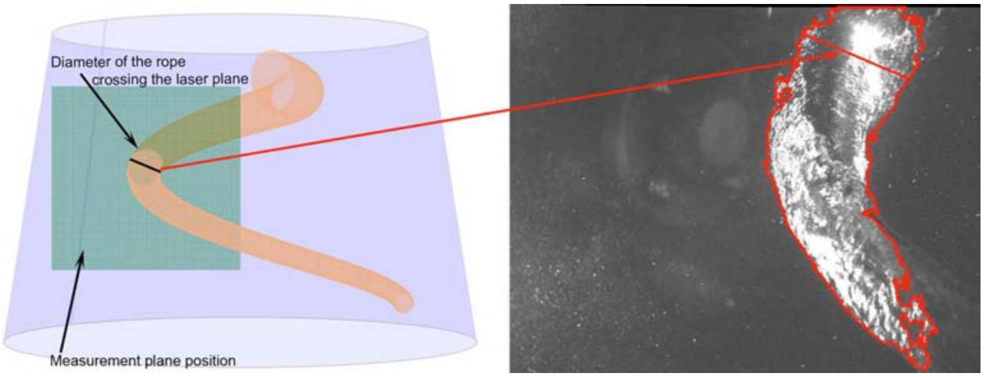

Figure 4.18: Extraction of the rope diameter by image processing in the PIV study of Iliescu et al. [32].

In this study, a new definition for the vortex rope diameter is presented. Further investigations of the unsteady 3D simulations presented in Sec. 4.4 revealed that the helicity has a local maximum at the vortex center, then drops, moving away from the vortex core. Helicity is a property of a moving fluid which represents the potential for helical flow. It provides insight into the vorticity aligned with the fluid stream. Mathematically, helicity for a fluid particle is defined by the dot product of the vorticity and the velocity vectors

$$H = \vec{\omega}.\vec{v} = \left(\nabla \times \vec{v}\right).\vec{v} \tag{4.32}$$

With this observation, the diameter of the vortex rope is defined as the distance from the vortex core by which the helicity drops by 90%. This is a general definition valid for both cavitating and non-cavitating cases. Using unsteady 3D simulations and this definition, the vortex rope diameter can be calculated directly. Figure 4.19 shows the values of the vortex diameter, i.e., the vortical structure length scale ℓ_c, normalized by the vortex core location (R_{vc} is the radial location of the vortex core) as a function of streamwise location z normalized by the draft tube inlet radius R_{ref}. The data in Fig. 4.19 present results for several different times, locations, and operating conditions. It can be seen that a curve can be fit through the data with an acceptable accuracy. This curve represents the average value of the length scale of the unsteady coherent structures forming within the shear layer in the draft tube. From this curve, the length scale ℓ_c is found to be

$$\ell_c = R_{vc} \exp\left(-0.6\frac{z}{R_{\text{ref}}}\right) \tag{4.33}$$

where R_{vc} is the radial distance of the vortex core from the draft tube centerline, z is the streamwise distance from the draft tube inlet, and R_{ref} is the draft tube inlet radius. The finding of Sec. 4.6.1 is very useful here because it was shown that although the vortex rope cannot be modeled by steady axisymmetric simulations, the location of the vortex core, i.e., R_{vc} is quite precisely defined by the location of maximum TKE production. Therefore, Eq. (4.33) can be used in steady axisymmetric simulations to find the length scale of vortical structures required by Eq. (4.31). Finally, the system of equations for the newly developed axisymmetric model is closed. The newly developed k-ε RANS model consists of Eq. (4.26) for the TKE transport where ν_c is obtained by Eq. (4.31), (4.29), and (4.33). The transport equation for the turbulent dissipation rate ε remains intact.

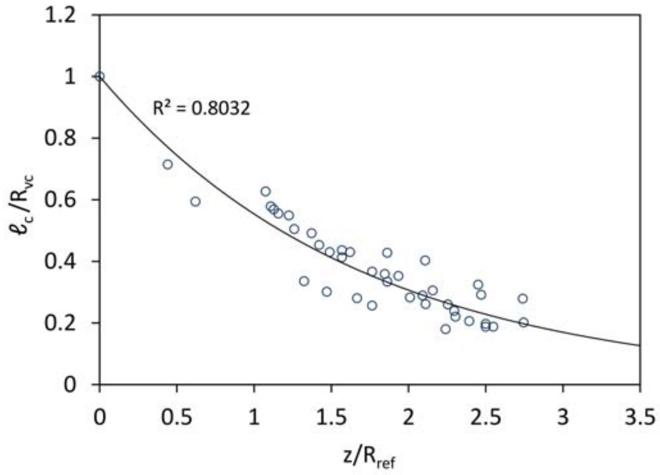

Figure 4.19: vortex rope diameter ℓ_c normalized by the vortex core location R_{vc} as a function of normalized (by the draft tube inlet radius R_{ref}) streamwise distance from the draft tube inlet. An exponential line can be fit through these points with good precision (see Eq. (4.33)).

Steady axisymmetric simulations are performed for the simplified draft tube introduced in Sec. 4.1 using the newly developed model combined with a two-layer zonal model for near wall treatment. All the details of the simulation setup is the same as in Sec. 4.1 and Sec 4.2. Simulations are performed for two partial load cases, i.e., case C and case D (see Table 3.2).

Figure 4.20 shows the profiles of axial velocity and turbulent kinetic energy in the draft tube for case C corresponding to 91% of the BEP flow rate. Results are shown at section S2 in the draft tube (see Fig. 3.11). It is seen that the present modified model overcomes the underprediction of the axial velocity and turbulent kinetic energy near the centerline of the draft tube, and a very good agreement is obtained with experimental data. Specifically, both the level of the TKE and its behavior at the center of the draft tube is modified (as much as 37% improvement at the centerline). Therefore, it is believed that the new model is able to capture the physics of the vortex rope formation in an average sense. Figure 4.21 shows the same results for case D with 70% of the BEP flow rate. Again, results for the axial velocity are considerably improved in comparison to the realizable k-ε model predictions. The new model better predicts the level of the axial velocity at the center of the draft tube, as well as it shows considerable improvement in prediction of the shear flow region. No experimental data for TKE are available for case D, therefore, only simulations results are presented. It should be noted that all model coefficients and constants are kept unchanged in predicting case C and D.

In order to further investigate the model, the turbulent kinetic energy budgets are considered. The transport equation for turbulent kinetic energy for a steady flow in the simplified draft tube can be written as

$$\frac{\partial k}{\partial t} = -\frac{\partial}{\partial x_i}\left(k\bar{u}_i\right) + D + P - \varepsilon = 0 \tag{4.34}$$

where D, P, and ε are the total TKE diffusion (transport), total TKE production, and total TKE dissipation. In the present model, P and D include both the effect of mean and coherent production and diffusion respectively, i.e.,

$$P = (\nu_t + \nu_c)\left(\frac{\partial \bar{u}_i}{\partial x_j} + \frac{\partial \bar{u}_j}{\partial x_i}\right)\frac{\partial \bar{u}_i}{\partial x_j} \tag{4.35}$$

$$D = \frac{\partial}{\partial x_i}\left[\left(\nu + \frac{\nu_t}{\sigma_k} + \nu_c\right)\frac{\partial k}{\partial x_i}\right] \tag{4.36}$$

whereas in a tradition RANS model, P and D only represent the mean production and diffusion of the turbulent kinetic energy ($\nu_c = 0$).

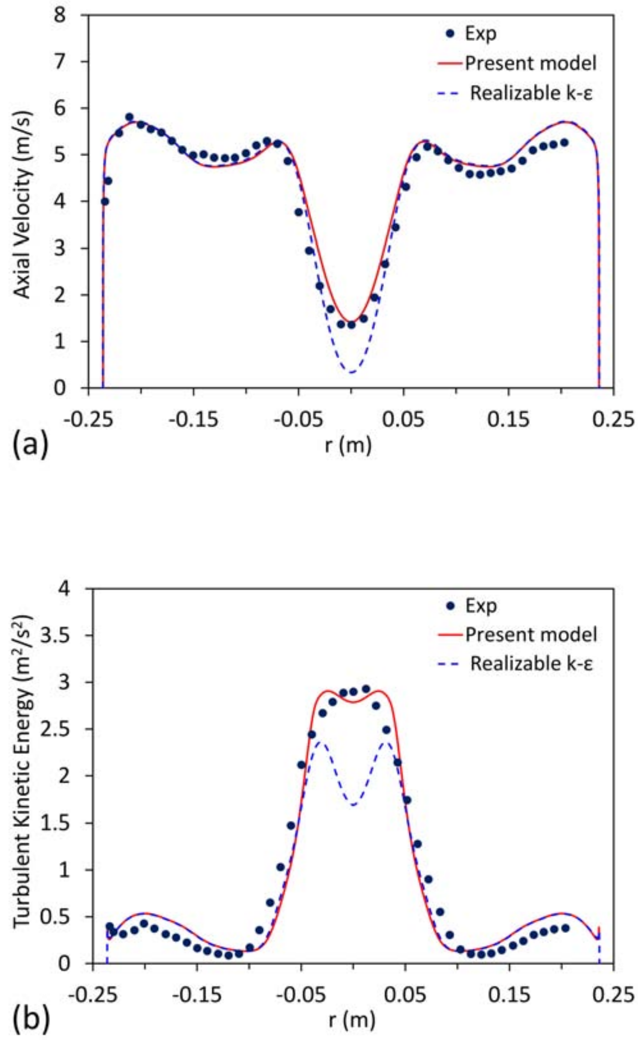

Figure 4.20: Profiles of (a) axial velocity and (b) turbulent kinetic energy in the simplified draft tube for case C, comparison of the present model and the realizable k-ε turbulence model.

Figure 4.22 shows radial distributions of the normalized TKE budgets at section S2 in the draft tube. The terms in the TKE transport equation are normalized by the draft tube inlet velocity (V_{ref}) and radius (R_{ref}). Results of the standard k-ε model and the present modified model are plotted in Fig. 4.22(a) and 4.22(b) respectively. In both simulations, the dominant term around the shear layer ($r \simeq 0.035$ m) is the TKE production which is in balance with the TKE dissipation. At the centerline, however, the production becomes zero and mainly diffusion and dissipation are in balance. Comparing

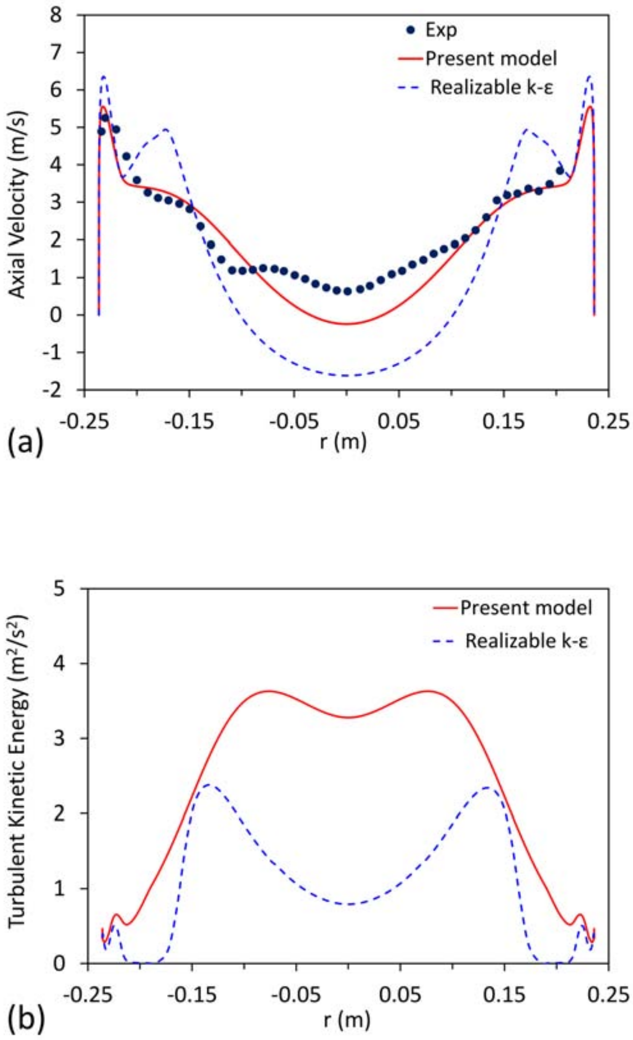

Figure 4.21: Profiles of (a) axial velocity and (b) turbulent kinetic energy in the simplified draft tube for case C, comparison of the present model and the realizable k-ε turbulence model.

Fig. 4.22(a) and 4.22(b), it is clearly seen that the level of TKE production and diffusion is predicted higher using the newly developed model, resulting in the improvements seen in Fig. 4.20 and Fig. 4.21. Specifically, the newly developed model predicts 31% and 46% more TKE production and diffusion right at the shear layer.

In both cases, the "imbalance" budget (also known as the residual) is the net difference between four TKE budgets. In both cases, the imbalance budget is quite negligible showing that the TKE transport equation is being solved with negligible numerical error.

It should be noted that in Fig. 4.22 the near wall region is not shown to better present the TKE budgets near the centerline. As one can imagine, the near-wall region is associated with very high levels of production and dissipation due to high velocity gradients. The TKE budgets for the near-wall region are similar for both cases of standard *k*-ε and the modified model, and are shown in Fig. 4.23 in wall coordinates.

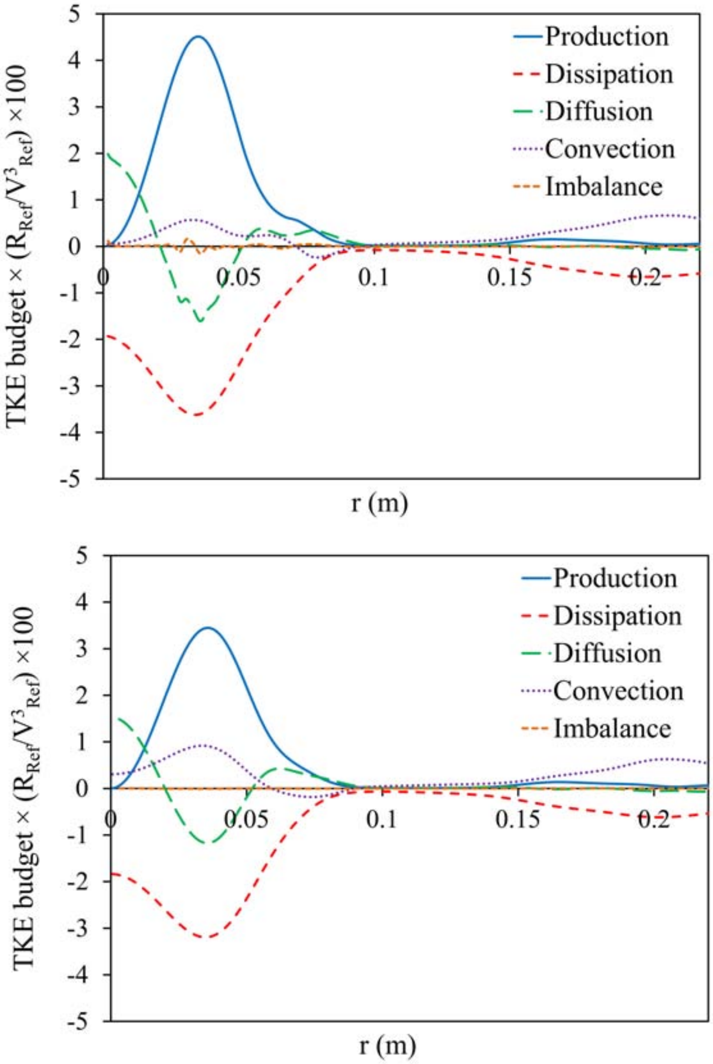

Figure 4.22: Radial distributions of the normalized TKE budgets (see Eq.(4.34)) in the draft tube for (top) the present model and (bottom) its baseline model (The *k*-ε model).

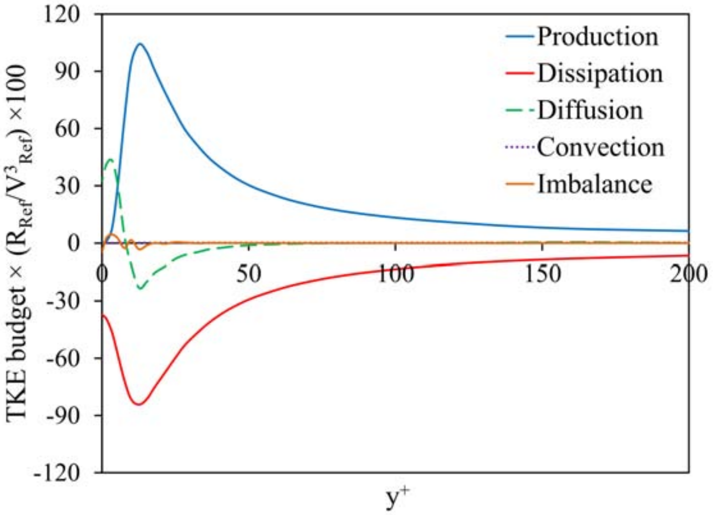

Figure 4.23: Near-wall distributions of the normalized TKE budgets in the draft tube.

4.7 Summary

The flow in the simplified FLINDT draft tube is studied in this chapter. Although not including the effect of the change in cross section shape and the bending of the flow path, this model can give very useful insights into the flow field inside the draft tube. Specifically, the initial conical part of the draft tube where the vortex rope starts to form is represented precisely. One of the main conclusions of this chapter is that the RANS simulations cannot correctly predict the flow in the draft tube when the turbine is operating under partial load and the vortex rope forms inside the draft tube. Attempts are made in this chapter to improve these models to give a better prediction of the mean flow. Nevertheless, hybrid RANS/LES models should be used when unsteady features of the flow are of interest. The next chapter addresses this issue.

Chapter 5

Development of a New Partially-Averaged Navier-Stokes Model

"What you seek is seeking you." - Rumi

5.1 Introduction

It is shown in Chapter 4 that the simulation of swirling flow even in a simplified draft tube is a challenging task, and accurate numerical calculations of the flow parameters require a careful choice of turbulence closure method. In fact, a review of the literature reveals that, in general, RANS turbulence models show inadequate performance in modeling highly swirling flows. This has been investigated and shown to be true for a wide range of RANS models including the standard k-ε [117], RNG k-ε [118], SST k-ω [39], algebraic Reynolds stress model (ASM) [119], and Reynolds stress model (RSM) [120]. Furthermore, there is a great challenge in accurately predicting the unsteady features of the flow, coherent structures, and turbulence statistics for a swirling flow with vortex breakdown (as in the case of the draft tube) using unsteady version of RANS (URANS) models, since these models tend to damp out the unsteadiness of the flow [42]. The time scale of unsteadiness of the vortex breakdown is close to that of turbulent fluctuations of energy carrying eddies, and therefore, this small scale unsteadiness is averaged off by the URANS approach.

In the unsteady simulation framework, LES is a candidate for studying turbulent swirling flows [121]. However, one of the major obstacles to the use of LES in complex confined industrial flows, such as swirling flow in cyclones and draft tubes, is the modeling of the near-wall region [122] (see Chapter 2 for more details). Current LES modeling approaches require that either the near-wall region be adequately resolved (using a DNS-like grid near the wall which makes it inapplicable for industrial flows), or that an LES wall-model (for example a two-layer model [57] or a dynamic wall model [58]) be used, which to date has not provided accurate results in relatively complex flows [59, 60].

An alternative solution is to use hybrid URANS/LES models. Due to their relative simplicity and robustness, these models have become one of the main modeling frameworks for quantitatively accurate prediction of complex unsteady flows at high Reynolds numbers. Various hybrid URANS/LES models have been used for unsteady draft tube flow simulations including very large eddy simulation (VLES) [42], detached eddy simulation (DES) [43], and scale-adaptive simulation (SAS) [45]. Most of these models have shown relative improvement over the URANS models. However, detailed evaluation and investigation of these models for various operating conditions of the hydroturbines are seldom addressed.

The partially-averaged Navier-Stokes (PANS) model was developed by Girimaji [78] as a continuous approach for hybrid URANS/LES simulations with seamless coupling between the URANS and LES regions. It is a bridging closure model that can be used with any level of grid resolution between RANS and direct numerical simulation (DNS) [78]. The PANS model has been successfully used in several turbulent separated flow problems, including flow past square [123] and circular [124] cylinders, flow over a backward facing step [125], flow around a simplified vehicle model [126], and flow around a rudimentary landing gear [127]. Nevertheless, it has been seldom applied in simulation of turbulent confined flows. Specifically, to date, no previous report is found in the literature on the development and application of the PANS model in simulation of turbulent confined swirling flows. This chapter presents the details of the development of a new PANS model, and its application in simulation of a benchmark test case, namely a swirling flow through an abrupt expansion.

5.2 Model Formulation

The partially-averaged Navier-Stokes (PANS) [78] method is a bridging model between RANS and DNS. Bridging models [128] aim to provide the best possible closure at any given level of computational grid size, and improve accuracy when increasing the resolution. They can be seen as an LES model with a cut-off wavenumber that can go continuously to zero, to become a RANS model. Therefore, bridging models including PANS are of particular interest in moderate grids where the cut-off is in the wavenumber range between RANS and LES. In these conditions PANS can provide better results than RANS, since it resolves part of the flow, while RANS models the whole flow. The PANS is advantageous in comparison with LES, since the grid does not need to be fine enough to fulfill the requirement of LES, therefore less number of grid points and less computational resources would be needed. Furthermore, in PANS modeling, a RANS turbulence model is used for the near-wall region which would be much more effective than a simple subgrid scale model as used in LES simulations. The seamless, continuous nature of the PANS model is a result of the so-called "partial averaging" concept, which corresponds to averaging (filtering) a portion of the fluctuating scales. The corresponding arbitrary explicit or implicit filter is linear and constant preserving, and commutes with temporal and spatial differentiation [78]. The partially-averaged Navier-Stokes equations for a turbulent incompressible flow are [78]

$$\frac{\partial \bar{u}_i}{\partial x_i} = 0 \tag{5.1}$$

$$\frac{\partial \bar{u}_i}{\partial t} + \frac{\partial (\bar{u}_i \bar{u}_j)}{\partial x_j} = -\frac{1}{\rho}\frac{\partial \bar{p}}{\partial x_i} + \frac{\partial}{\partial x_j}\left(\nu \frac{\partial \bar{u}_i}{\partial x_j} - \tau_{ij}\right) \tag{5.2}$$

where $\bar{u}_i$ and $\bar{p}$ are the partially-averaged velocity and pressure respectively. The sub-filter scale (SFS) stress tensor τ_{ij} results from the partial-averaging of non-linear terms and represents the effects of the unresolved motions on the resolved field. It is similar to the Reynolds stress tensor resulting from the Reynolds-averaging in RANS approach, or to the subgrid scale (SGS) stress tensor after the filtering in LES method. To close the system of PANS equations, as in RANS and LES, a model is needed for the SFS stress tensor τ_{ij} relating the unresolved field stress and the resolved flow field. Girimaji [78] proposed a generalized Boussinesq approximation for SFS stress tensor

$$\tau_{ij} = -2\nu_u \bar{S}_{ij} + \frac{2}{3}k_u \delta_{ij} \tag{5.3}$$

where $\bar{S}_{ij}$ is the resolved rate of strain tensor

$$\bar{S}_{ij} = \frac{1}{2}\left(\frac{\partial \bar{u}_i}{\partial x_j} + \frac{\partial \bar{u}_j}{\partial x_i}\right) \tag{5.4}$$

ν_u denotes the PANS eddy viscosity (eddy viscosity of unresolved scales) and can be obtained, as in RANS, by various turbulence closure models. In the original PANS model [78], the eddy viscosity of unresolved scales ν_u is formulated based on the turbulent kinetic energy k_u and turbulent dissipation rate ε_u of unresolved scales as follows

$$\nu_u = C_\mu \frac{k_u^2}{\varepsilon_u} \tag{5.5}$$

Therefore, in order to close the system of PANS equations, two transport equations for the unresolved turbulent kinetic energy k_u and its dissipation rate ε_u was derived by Girimaji [78]. He derived the evolution equation for k_u and ε_u by asking the following question: “If the RANS two-equation model represents the closure for the fully averaged kinetic energy and dissipation, what are the implied model equations for their partially averaged counterparts?” In order to answer this question, Girimaji [78] introduced two parameters f_k and f_ε, being the unresolved-to-total ratios of turbulent kinetic energy and turbulent dissipation rate respectively

$$f_k = \frac{k_u}{k} \tag{5.6}$$

$$f_\varepsilon = \frac{\varepsilon_u}{\varepsilon} \tag{5.7}$$

These parameters control the extent of averaging in PANS model. With $f_k = 1$, for example, all the turbulent kinetic energy of the flow field is unresolved (modeled) and the PANS model would render a RANS solution. On the other hand, setting $f_k = 0$ on a sufficiently fine grid results in resolving all the turbulent kinetic energy and giving a DNS solution asymptotically. With a value of f_k between 0 and 1, the PANS model resolves the turbulent structures partially and leaves the unresolved motions to be modeled.

In the PANS approach, the unresolved (partially-averaged) kinetic energy k_u and dissipation rate ε_u transport equations are obtained by substituting the total kinetic energy k and dissipation rate ε in a parent RANS model using Eq. (5.6) and (5.7) as shown in details by Girimaji [78] and Lakshmipathy and Girimaji [129]. Therefore, a PANS model can be derived from any parent RANS model based on the ratio between unresolved and total turbulence quantities. The original PANS model [78] was derived based on the standard k-ε model, while Lakshmipathy and Girimaji [129] suggested PANS equations based on the k-ω model. Later, a near-wall formulation of PANS was proposed by Basara et al. [130] in the form of the PANS k-ε-ζ-f model, and a low

Reynolds number variant of PANS was developed by Ma et al. [131] using the low-Reynolds number k-ε model of Abe et al. [132].

In the present research study, a new version of PANS model based on the extended k-ε turbulence model of Chen and Kim [133] is developed. Chen and Kim [133] proposed a modified k-ε model in which two different time scales are employed for calculating the rate of generation of ε. In their model, the rate of generation of ε is given by

$$C_{1\varepsilon}\frac{P\varepsilon}{k} + C_{3\varepsilon}\frac{P^2}{k} \tag{5.8}$$

The two time scales involved are the dissipation rate time scale k/ε and the production time scale k/P. Since P is based on the mean strain rates, this modification enables the ε equation to respond more strongly to changes in the mean strain. The new term (the one including $C_{3\varepsilon}$) may be viewed as the energy transfer rate from large to small scales controlled by the production time scale. The net effect of these changes is to increase ε when the mean strain is strong and to decrease it when the mean strain is weak. Chen and Kim [133] showed improved predictions of the flow field for several turbulent flows including plane and axisymmetric jets, turbulent boundary layers, flow over a backward facing step, and confined swirling flow.

Later, Monson et al. [134] developed a low-Reynolds version of the extended k-ε model of Chen and Kim [133] by combining this model with the low-Reynolds number k-ε model of Lam and Bremhorst [135]. The final form of the low-Reynolds number extended k-ε model of Chen and Kim [133] is as follows [134]

$$\frac{\partial k}{\partial t} + \bar{u}_j\frac{\partial k}{\partial x_j} = \frac{\partial}{\partial x_j}\left[\left(\nu + \frac{\nu_t}{\sigma_k}\right)\frac{\partial k}{\partial x_j}\right] + P - \varepsilon \tag{5.9}$$

$$\frac{\partial \varepsilon}{\partial t} + \bar{u}_j\frac{\partial \varepsilon}{\partial x_j} = \frac{\partial}{\partial x_j}\left[\left(\nu + \frac{\nu_t}{\sigma_\varepsilon}\right)\frac{\partial \varepsilon}{\partial x_j}\right] + C_{1\varepsilon}\tilde{f}_1\frac{P\varepsilon}{k} - C_{2\varepsilon}\tilde{f}_2\frac{\varepsilon^2}{k} + C_{3\varepsilon}\tilde{f}_3\frac{P^2}{k} \tag{5.10}$$

$$\nu_t = C_\mu \tilde{f}_\mu \frac{k^2}{\varepsilon} \tag{5.11}$$

where

$$\sigma_k = 0.75 \qquad , \qquad \sigma_\varepsilon = 1.15$$

$$C_{1\varepsilon} = 1.15 \quad , \quad C_{2\varepsilon} = 1.9 \quad , \quad C_{3\varepsilon} = 0.25$$

$$\tilde{f}_1 = \tilde{f}_3 = 1 + (0.05/\tilde{f}_\mu)^3 \quad , \quad \tilde{f}_2 = 1 - \exp(-Re_T^2) \tag{5.12}$$

$$\tilde{f}_\mu = (1 - \exp(-0.0165 Re_y))^2 \, . \, (1 + 20.5/Re_T)$$

$$Re_T = \frac{k^2}{\nu\varepsilon} \quad , \quad Re_y = \frac{\sqrt{k}y}{\nu}$$

Equations (5.9) to (5.11) are used as the parent RANS equations for development of the present PANS model. Derivation of the k_u and ε_u transport equations for the present PANS model is performed by multiplying the RANS equation for k (Eq. (5.9)) by f_k and for ε (Eq. (5.10)) by f_ε, as shown in detail in Girimaji [78]. Without repeating the details of the procedure, which can be found in Girimaji [78], Lakshmipathy and Girimaji [129], and Ma et al. [131], the final form of the present PANS model is given by

$$\frac{\partial k_u}{\partial t} + \bar{u}_j \frac{\partial k_u}{\partial x_j} = \frac{\partial}{\partial x_j}\left[\left(\nu + \frac{\nu_u}{\sigma_{ku}}\right)\frac{\partial k_u}{\partial x_j}\right] + P_u - \varepsilon_u \tag{5.13}$$

$$\frac{\partial \varepsilon_u}{\partial t} + \bar{u}_j \frac{\partial \varepsilon_u}{\partial x_j} = \frac{\partial}{\partial x_j}\left[\left(\nu + \frac{\nu_u}{\sigma_{\varepsilon u}}\right)\frac{\partial \varepsilon_u}{\partial x_j}\right] + C_1^* \frac{P_u \varepsilon_u}{k_u} - C_2^* \frac{\varepsilon_u^2}{k_u} + C_3^* \frac{P_u^2}{k_u} \tag{5.14}$$

where P_u is the production of unresolved turbulent kinetic energy, and can be written as

$$P_u = \nu_u \frac{\partial \bar{u}_i}{\partial x_j}\left(\frac{\partial \bar{u}_i}{\partial x_j} + \frac{\partial \bar{u}_j}{\partial x_i}\right) = f_k\left(P - \frac{\varepsilon_u}{f_\varepsilon}\right) + \varepsilon_u \tag{5.15}$$

All model coefficients in Eq. (5.13) and (5.14) are functions of the original RANS model coefficients [133], and f_k and f_ε parameters as follows

$$C_1^* = (C_{1\varepsilon}\tilde{f}_1 + 2C_{3\varepsilon}\tilde{f}_3) - 2C_{3\varepsilon}\tilde{f}_3 \frac{f_\varepsilon}{f_k} \tag{5.16}$$

$$C_2^* = (C_{1\varepsilon}\tilde{f}_1 + 2C_{3\varepsilon}\tilde{f}_3) + (C_{2\varepsilon}\tilde{f}_2 - C_{1\varepsilon}\tilde{f}_1 - C_{3\varepsilon}\tilde{f}_3)\frac{f_k}{f_\varepsilon} - C_{3\varepsilon}\tilde{f}_3 \frac{f_\varepsilon}{f_k} \tag{5.17}$$

$$C_3^* = C_{3\varepsilon}\tilde{f}_3 \frac{f_\varepsilon}{f_k} \tag{5.18}$$

$$\sigma_{ku} = \sigma_k \frac{f_k^2}{f_\varepsilon} \tag{5.19}$$

$$\sigma_{\varepsilon u} = \sigma_\varepsilon \frac{f_k^2}{f_\varepsilon} \tag{5.20}$$

The PANS eddy viscosity, which is used in Eq. (5.3), is defined by

$$\nu_u = C_\mu \tilde{f}_\mu \frac{k_u^2}{\varepsilon_u} \tag{5.21}$$

In order to close the present PANS system of equations, the unresolved-to-total ratios of turbulent kinetic energy f_k and turbulent dissipation rate f_ε are needed to be defined. The parameter f_ε plays an important role when the dissipative scales are resolved, which is most likely in a low Reynolds number flow. In a high Reynolds number flow, where there is a clear separation between energy-carrying and dissipative scales, the dissipative small scales are unlikely to be resolved, hence, $\varepsilon_u = \varepsilon$ and $f_\varepsilon = 1$ [130, 136].

In the early stages of PANS application, the unresolved-to-total ratio of turbulent kinetic energy f_k was prescribed as a constant [78, 123, 124]. As the assumption of constant f_k is not reasonable, Girimaji and Abdol-Hamid [136] proposed a formula for f_k to become a variable parameter that depends upon the grid size and turbulence length scale. They assumed that the smallest resolved length scale can be determined by the local dissipation and local eddy viscosity similar to the Kolmogorov scale. Requiring the grid size to be of the order of this "resolved-field Kolmogorov scale", Girimaji and Abdol-Hamid [136] derived the following formula for f_k

$$f_k = \frac{1}{\sqrt{C_\mu}} \left(\frac{\Delta}{\Lambda} \right)^{2/3} \tag{5.22}$$

where Δ is the smallest grid dimension, and $\Lambda = k^{3/2}/\varepsilon$ is the turbulence length scale [136]. Equation (5.22) has been widely used in PANS simulations by Basara et al. [137], Basara et al. [130], and Han et al. [126], however, they considered Δ to be the geometric-average grid cell dimension, i.e., $\Delta = (\Delta_x \Delta_y \Delta_z)^{1/3}$. This parameter f_k is implemented in the computational procedure as a dynamic parameter, changing at each point at the end of every time step, and then it is used as a fixed value at the same location during the next time step [137]. The formula in Eq. (5.22), however, does not guarantee that the f_k parameter remains bounded between 0 and 1 as required by Eq. (5.6). Specifically, for situations where $\Delta \sim \Lambda$, this equation, in this form, may give f_k values larger than 1. Furthermore, studying the turbulent channel and hump flow, Davidson [138] found, very recently, that the actual ratio of modeled to total turbulent kinetic energy k_u/k is much smaller than f_k from Eq. (5.22). The f_k obtained from Eq. (5.22) gives much too large a turbulent viscosity which kills all resolved turbulence [138].

In the present study, a new formulation for f_k is developed which overcomes these problems. Consider the turbulence energy spectrum $E(\kappa)$ and a cut-off wavenumber κ_c, as shown in Fig. 5.1. The cut-off wave number is the spectral filter size usually related to the grid size by $\kappa_c = \pi/\Delta$ [139], and it is assumed constant or slowly variable in the case of variable step size of the grid.

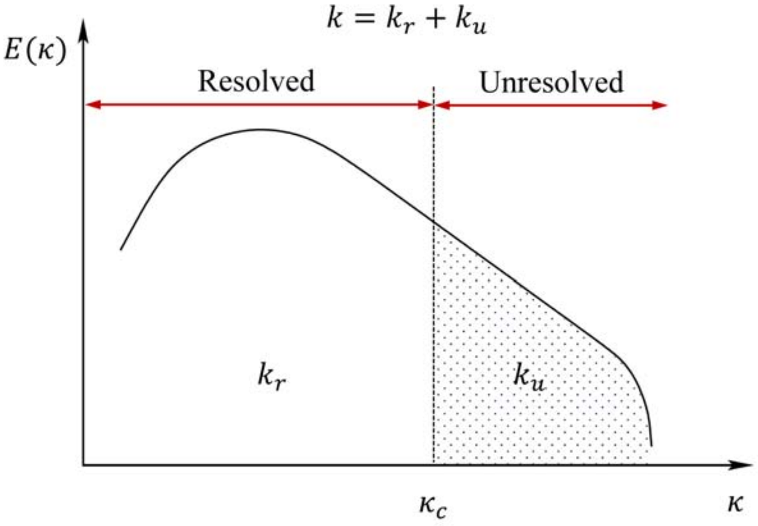

Figure 5.1: Turbulence energy spectrum showing resolved and unresolved parts of the turbulent kinetic energy.

The total turbulent kinetic energy k can be obtained as

$$k = \int_0^\infty E(\kappa) d\kappa \tag{5.23}$$

while the turbulent kinetic energy associated with the unresolved (modeled) scales (the shaded area in Fig. 5.1) is

$$k_u = \int_{\kappa_c}^\infty E(\kappa) d\kappa \tag{5.24}$$

Consequently, the unresolved-to-total ratio of turbulent kinetic energy, i.e., f_k can be written as

$$f_k = \frac{k_u}{k} = 1 - \frac{k_r}{k} = 1 - \frac{\int_0^{\kappa_c} E(\kappa) d\kappa}{\int_0^{\infty} E(\kappa) d\kappa} \tag{5.25}$$

Therefore, f_k can be analytically calculated using an energy spectrum equation. The energy spectrum at very low wavenumbers ($\kappa \to 0$) behaves as [140]

$$E(\kappa) \approx C_s \kappa^s \tag{5.26}$$

with C_s being a constant (the hypothesis of permanence of big eddies [140]). In the inertial range, on the other hand, the Kolmogorov spectrum has to be recovered

$$E(\kappa) \approx C_k \varepsilon^{2/3} \kappa^{-5/3} \tag{5.27}$$

In this study, a smooth approximation for the energy spectrum $E(\kappa)$ inspired from a von Kármán like spectrum [141] is used

$$E(\kappa) = C_k \varepsilon^{2/3} \kappa^s \left[\left(\frac{C_k \varepsilon^{2/3}}{C_s} \right)^{\frac{2}{5+3s}} + \kappa^{2/3} \right]^{-\frac{5+3s}{2}} \tag{5.28}$$

The use of this spectrum, Eq. (5.28), valid in the entire range of wavenumbers evolving from large to small eddies allows obtaining a more accurate result for the f_k than the one obtained by considering the Kolmogorov spectrum ($E(\kappa) = C_k \varepsilon^{2/3} \kappa^{-5/3}$) which is valid only in the inertial range. It is shown later that Eq. (5.22) for f_k implies the use of the Kolmogorov spectrum, which is not valid for the entire range of wavenumbers. This is specifically important when performing PANS simulations on coarse grids implying that the cut-off wavenumber may happen to be located before the inertial zone.

Integration of the spectrum over all wavenumbers gives the total turbulent kinetic energy

$$k = \int_0^{\infty} E(\kappa) d\kappa = \frac{1}{1+s} \left[C_s^{\frac{2}{3(1+s)}} C_k \varepsilon^{2/3} \right]^{\frac{3+3s}{5+3s}} \tag{5.29}$$

Using Eq. (5.29), the constant C_s can be written as

$$C_s = \left[\frac{\left(k(1+s)^{\frac{5+3s}{3+3s}} \right)}{C_k \varepsilon^{2/3}} \right]^{\frac{3+3s}{2}} \tag{5.30}$$

Now, the parameter f_k can be calculated as follows

$$\begin{aligned} f_k = \frac{k_u}{k} = 1 - \frac{k_r}{k} &= 1 - \frac{\int_0^{\kappa_c} E(\kappa) d\kappa}{k} \\ &= 1 - \frac{\int_0^{\kappa_c} C_k \varepsilon^{2/3} \kappa^s \left[\left(\frac{C_k \varepsilon^{2/3}}{C_s} \right)^{\frac{2}{5+3s}} + \kappa^{2/3} \right]^{-\frac{5+3s}{2}} d\kappa}{\frac{1}{1+s} \left[C_s^{\frac{2}{3(1+s)}} C_k \varepsilon^{2/3} \right]^{\frac{3+3s}{5+3s}}} \end{aligned} \tag{5.31}$$

Analytically calculating the integral in the numerator of Eq. (5.31), then substituting for C_s from Eq. (5.30) and simplifying yields

$$f_k = 1 - \left[\frac{\kappa_c^{2/3}}{\left(\frac{C_k \varepsilon^{2/3}}{k(1+s)} \right) + \kappa_c^{2/3}} \right]^{\frac{3}{2}(1+s)} \tag{5.32}$$

Defining $\Lambda = k^{3/2}/\varepsilon$ and $\Delta = \pi/\kappa_c$ as the turbulence and the grid length scales, the f_k parameter can be written as

$$f_k = 1 - \left[\frac{\left(\frac{\Lambda}{\Delta}\right)^{2/3}}{\left(\frac{C_k}{(1+s)\pi^{2/3}} \right) + \left(\frac{\Lambda}{\Delta}\right)^{2/3}} \right]^{\frac{3}{2}(1+s)} \tag{5.33}$$

Two constants, namely C_k and s need to be defined. For C_k, the Kolmogorov constant, a value of 1.5 is widely accepted [142].The question of permissible values for s, however, is a controversial one. A complete discussion about the choice of s can be found in Ref. [140]. The two most widely used values for s are 2 and 4 [140, 142], giving the following relations for f_k

$$f_k = 1 - \left[\frac{\left(\frac{\Lambda}{\Delta}\right)^{2/3}}{0.23 + \left(\frac{\Lambda}{\Delta}\right)^{2/3}} \right]^{4.5} \qquad (s = 2) \tag{5.34}$$

$$f_k = 1 - \left[\frac{\left(\frac{\Lambda}{\Delta}\right)^{2/3}}{0.14 + \left(\frac{\Lambda}{\Delta}\right)^{2/3}} \right]^{7.5} \qquad (s = 4) \tag{5.35}$$

In order to investigate the sensitivity of f_k to the choice of s, both relations are plotted against Λ/Δ in Fig. 5.2. It can be seen that the curves almost coincide, and the deviation between Eq. (5.34) and (5.35) for f_k is less than 3%. Therefore, Eq. (5.34) is chosen and presented as the final form for f_k.

For a coarse grid or very near the wall, where $\Lambda \ll \Delta$, $f_k \to 1$ (see Fig. 5.2) according

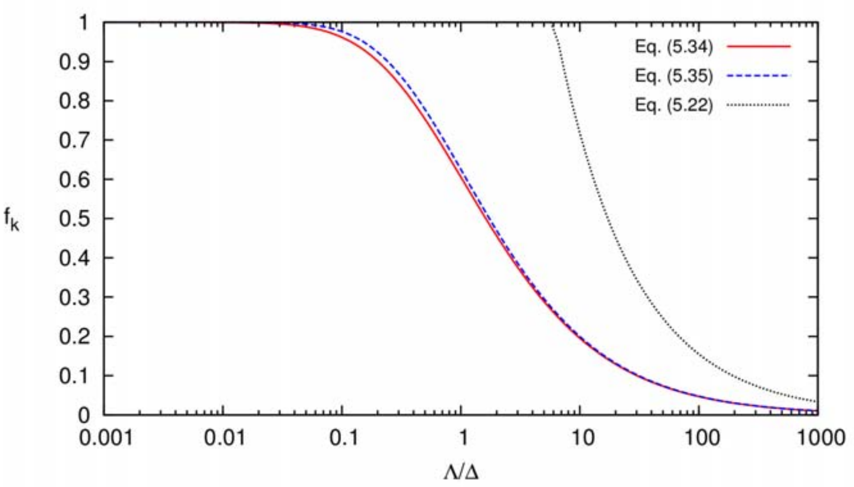

Figure 5.2: Variations of the f_k parameter with respect to Λ/Δ; comparison of Eq. (5.34), Eq. (5.35), and Eq. (5.22).

to Eq. (5.34), and the model is identical to a RANS approach with all scales being modeled. When the grid size is much smaller than the turbulence length scale, f_k decreases, and more and more of the turbulent kinetic energy can be resolved. The f_k value goes to zero asymptotically for $\Lambda/\Delta \to \infty$ as shown in Fig. 5.2. It is important to note that Eq. (5.34) guarantees that the f_k value remains between 0 and 1, a condition required by the definition of f_k, Eq. (5.6).

It is worth mentioning that if only the Kolmogorov energy spectrum (Eq. (5.27)) would be used to obtain the f_k parameter, the result reads as

$$f_k = \frac{k_u}{k} = \frac{\int_{\kappa_c}^{\infty} C_k \varepsilon^{2/3} \kappa^{-5/3} d\kappa}{k} = \frac{3}{2} C_k \frac{\varepsilon^{2/3}}{k} \kappa_c^{-2/3} \tag{5.36}$$

Using the above-mentioned definitions for the turbulence and the grid length scale, Δ and Λ, f_k can be written as

$$f_k = \frac{3}{2} C_k \left(\frac{1}{\pi}\right)^{2/3} \left(\frac{\Delta}{\Lambda}\right)^{2/3} \approx 1.05 \left(\frac{\Delta}{\Lambda}\right)^{2/3} \tag{5.37}$$

which is similar (but with a different constant coefficient) to the formula proposed by Girimaji and Abdol-Hamid [136] and Basara et al. [137] (Eq. (5.22)). As shown in Fig. 5.2, the f_k obtained from Eq. (5.22)) is considerably higher especially at lower Λ/Δ values. It reaches the value of one around $\Lambda/\Delta \simeq 6$, and gives even higher values for lower values of Λ/Δ.

As a summary, the present partially-averaged Navier-Stokes (PANS) model includes Eq. (5.1) and (5.2), where the PANS eddy viscosity is obtained by Eq. (5.21), solving two transport equations for unresolved turbulent kinetic energy Eq. (5.13), and unresolved dissipation rate Eq. (5.14). Two important parameters in Eq. (5.13) and (5.14), i.e., f_k and f_ε are obtained by Eq. (5.34) and $f_\varepsilon = 1$, respectively. In Eq. (5.34), $\Delta = (\Delta_x \Delta_y \Delta_z)^{1/3}$ is the grid length scale, and $\lambda = k^{3/2}/\varepsilon$ is the turbulence integral length scale. The total turbulent kinetic energy required to calculate the turbulence length scale is obtained in three steps. First, the total turbulent kinetic energy field is obtained from a preliminary steady RANS simulation. This RANS simulation requires a considerably smaller computational time, and is needed anyway to initialize transient simulations, since starting an unsteady simulation without any initialization often results in severe numerical instabilities. Second, the PANS simulations are performed for sufficiently long time in order to obtain preliminary statistics of k_u and k_r using the “frozen” RANS field for k. Finally, the last part of PANS simulations are performed in which the total turbulent kinetic energy is calculated ($k = k_u + k_r$) and updated on a regular basis.

5.3 Validation Test Case: Swirling Flow Through an Abrupt Expansion

5.3.1 Test Case Description and Numerical Methodology

The case of turbulent swirling flow through an abrupt expansion is chosen for validating the present model. It is a complex flow possessing various dynamic phenomena including vortex breakdown, recirculation, detachment and reattachment, and enhanced mixing. Therefore, correctly predicting the flow behavior is quite challenging and special considerations should be paid to choosing the turbulence closure model. Furthermore, the swirling flow through a sudden expansion is of industrial interest since it resembles the flow in several technical applications such as the gas turbine combustor.

The considered test case corresponds to the experimental study of Dellenback et al. [143], for which several numerical investigations, using different turbulence models, have been reported in the literature [121, 144, 44]. The experimental configuration consists of water flow at an axisymmetric expansion (with the expansion ratio D_2/D equal to 1.94) as shown in Fig. 5.3. The axial and circumferential components of time-averaged and root-mean-square (rms) velocity were measured by Dellenback et al. [143] at several cross-sections downstream of the sudden expansion. In addition, measurements were performed for two sections upstream of the expansion which can be used as the inflow boundary condition for the numerical simulations. Here, the inlet section of the computational domain is put at two diameters upstream of the expansion ($z/D = -2$) and the outlet boundary is place at $z/D = 10$. This computational domain is shown to be sufficient for this flow problem [144]. The swirl number defined as [143]

$$S = \frac{\int_0^R UVr^2dr}{R\int_0^R U^2rdr} \tag{5.38}$$

is approximately 0.6, with R being the inlet radius, $R = D/2$, and V and U denoting the time-averaged circumferential and axial velocities respectively. The Reynolds number based on the inlet diameter D and the bulk velocity is 30,000.

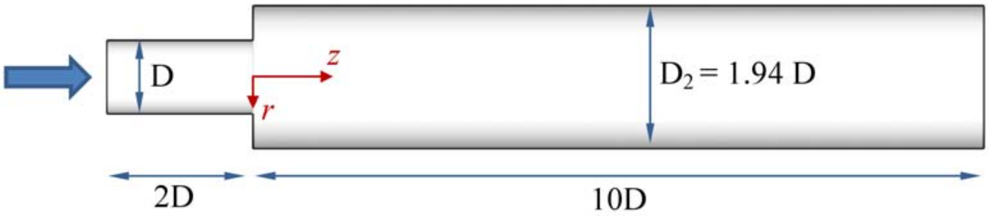

Figure 5.3: Computational domain and coordinate system for the abrupt expansion.

At the inlet section, the radial profiles of axial and circumferential velocity components are obtained from the measured data of Dellenback et al. [143] by interpolation. Figure 5.4 shows the velocity profiles applied at the inlet of the computational domain. The low axial velocity region near the center ($r/R = 0$) is formed due to the high circumferential velocity (swirl) transferring momentum away from the center. In this case, with a high level of swirl, the turbulence is mainly generated after the expansion, and regions of high turbulence production and shear layers created by the recirculating flow are basically independent of the inflow conditions. Therefore, the flow is almost independent of the initial turbulence conditions as shown in detail by Schlüter et al. [121]. Hence, no unsteadiness is added to the steady inlet conditions shown in Fig. 5.4. A constant uniform inlet turbulence intensity of 10% is estimated from measurements of Dellenback et al. [143]. No-slip conditions are applied at wall boundaries.

The main computational grid (with which all simulations are performed) consists of 1,660,384 hexahedral cells. The grid is refined in areas of large variable gradients, i.e., near-wall and centerline region, and near the expansion. The size of the grid is

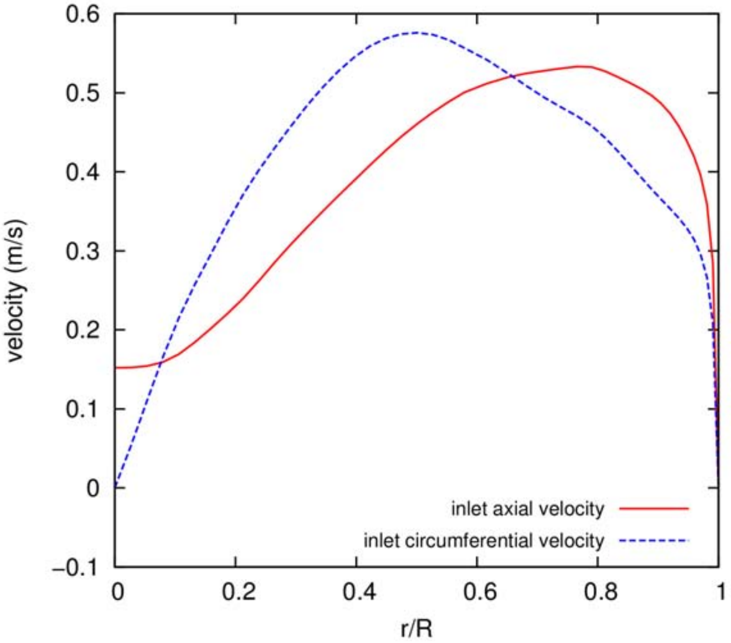

Figure 5.4: Velocity profiles at the inlet section of the abrupt expansion test case.

comparable to those used in previous LES and hybrid URANS/LES simulations of this test case [121, 144, 44]. Furthermore, attention is paid to make sure that this grid is within the range of the guidelines for hybrid URANS/LES grids [96] (see Sec. 2.5 for details). To examine the grid sensitivity of the present PANS model, simulations are also performed for a finer grid with 3,428,160 cells (results will be discussed later). The computational time on the finer grid is about 2.3 times the computational time of the main grid. The first cell center normal to the wall is placed at $y^+ \simeq 0.5$ everywhere in both grids. Figure 5.5 shows the mesh near the expansion section as well as a cross section downstream of the expansion section for both the main and the fine grids. The grid generation methodology was discussed in details in Sec. 2.5.

Unsteady simulations are carried out using the presently developed PANS model, as well as the delayed DES (DDES) [86], and the URANS (SST k-ω) [70] turbulence models. All unsteady simulations are initialized by a RANS steady solution. The dimensionless time-step size (normalized by the inlet diameter and the bulk velocity) is taken as 0.0044. The convergence criterion of the residuals for each time-step is set to three orders of magnitude drop or maximum 30 sub-iterations. Unsteady simulations are carried out for about 12 through-flow times (the time required by the mean flow to pass through the domain once), corresponding to about 32,000 time-steps.

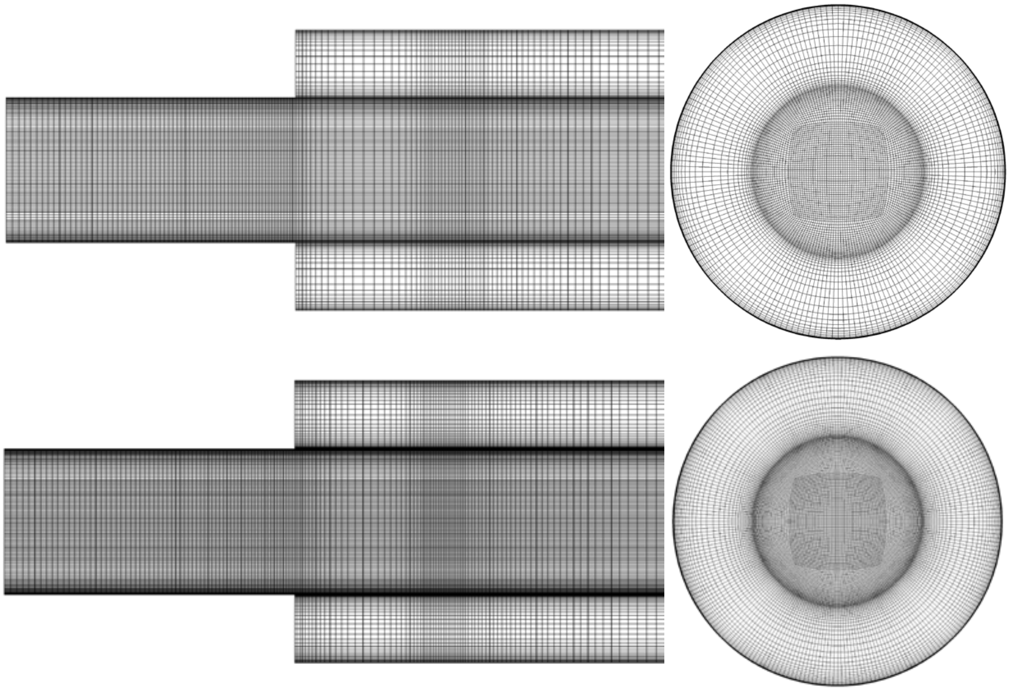

Figure 5.5: Details of the computational grid in the case of the abrupt expansion: the main grid (top), and the fine grid (bottom).

5.3.2 Results and Discussion

Figure 5.6 shows the instantaneous axial velocity contours on the meridian plane, obtained using various turbulence closure approaches, namely URANS, DDES, and present PANS models. The development of the reverse flow region at the center of the pipe, and the strong shear layer between this region and the main flow is clearly seen in all figures. However, as shown in Fig. 5.6(a), the SST k-ω URANS model cannot capture the self-induced unsteadiness of the vortex breakdown and gives steady symmetric results (similar to RANS) due to steady symmetric boundary conditions. A detailed discussion on this issue is given in Chapter 4. Applying hybrid URANS/LES models when the vortex breakdown unsteadiness is resolved in an LES manner, detailed unsteady features of the flow can be captured sufficiently resulting in non-symmetric unsteady results as shown in Fig. 5.6(b) for the DDES and in Fig. 5.6(c) for the PANS model.

A snapshot of the flow is presented in Fig 5.7. The three-dimensional vortical structures are visualized by the non-dimensional iso-surfaces of the Δ-criterion. The Δ-criterion was developed by Chong et al. [145] to identify the vortex. They proposed that a vortex core is a region with complex eigenvalues of velocity gradient tensor $\frac{\partial u_i}{\partial x_j}$.

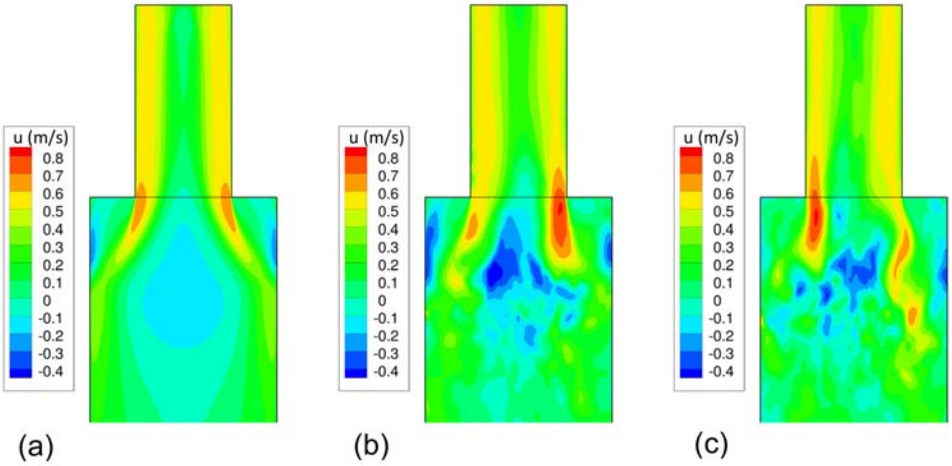

Figure 5.6: Instantaneous axial velocity contours predicted by (a) URANS (SST k-ω), (b) DDES, and (c) present PANS model.

As stated by Chong et al. [145], complex eigenvalues imply that the local streamline pattern is closed or spiral in a reference frame moving with the point. This physically can happen only if a vortex exists in the flow where fluid particles are rotating around the vortex axis. Complex eigenvalues will occur when

$$\Delta = \left(\frac{Q}{3}\right)^3 + \left(\frac{R}{2}\right)^2 > 0 \tag{5.39}$$

where $Q \equiv -\frac{1}{2}\frac{\partial u_i}{\partial x_j}\frac{\partial u_j}{\partial x_i}$ and $R \equiv \mathrm{Det}\left(\frac{\partial u_i}{\partial x_j}\right)$ are the invariants of $\frac{\partial u_i}{\partial x_j}$ [145].

It is seen in Fig. 5.7 that the flow is dominated by the precessing vortex core that rotates around the geometrical axis of symmetry and its subsequent breakdown to small coherent structures downstream of the expansion. Both the present PANS model and the DDES model simulate the vortex core and its breakdown; however, the present model is less dissipative and captures more detailed structures. This implies that the switch between RANS and LES is more efficient in the present model leading to resolving of more turbulent structures on the same grid.

Another important physical phenomenon in this flow is the separation and reattachment of the flow with respect to the wall of the expansion section. As the flow enters the wider section, it separates from the wall and a recirculating region is formed near the wall of the wider pipe (see Fig. 5.6). The flow reattaches to the wall at some distance downstream of the sudden expansion. This distance is called the reattachment length. Dellenback et al. [143] measured the reattachment length of the flow and obtained a

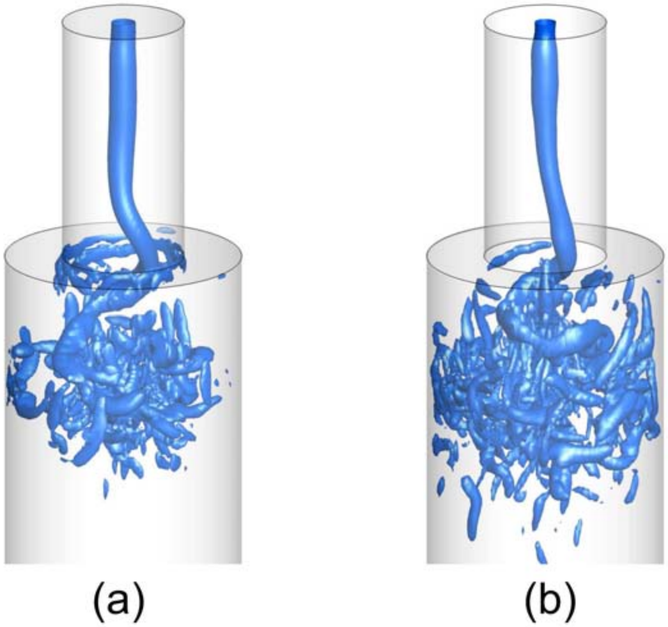

Figure 5.7: Vortex breakdown visualized by non-dimensional iso-surfaces of the Δ-criterion ($\Delta/\Delta_{max} = 10^{-6}$, where Δ_{max} is the maximum of Δ in the domain), obtained from (a) DDES and (b) present PANS model.

value of $z_r/h = 2.5$, where h is $\frac{1}{2}(D_2 - D)$. In this study, the reattachment length is obtained by calculating the skin friction coefficient. The reattachment length obtained from using the present PANS model is $z_r/h = 2.54$ which is in very good agreement with the experimental result (less than 2% deviation), while a reattachment length of $z_r/h = 2.90$ is obtained by using the DDES model and results in 16% deviation. The SST k-ω model underpredicts the reattachment length by 25%, giving a value of $z_r/h = 1.87$. Table 5.1 compares the reattachment length obtained using different turbulence models with experimental data.

Table 5.1: Reattachment length z_r/h.

Experiment [143]	PANS	DDES	SST k-ω
2.50	2.54	2.90	1.87

Figure 5.8 shows radial distributions of the mean (time-averaged) and rms axial and circumferential velocities on nine planes after the expansion, corresponding to the z/D values of 0.25 to 8.0. All time-averaged results are computed by temporal averaging of the results of 24,000 time-steps (with normalized time-step size of 0.0044) after setting

the simulations to run for an initial 8,000 time-steps (initial transient). Results obtained using the present model are compared to the experimental data of Dellenback et al. [143] as well as those obtained using the DDES and URANS (SST k-ω) models. It can be seen that the agreement between the predictions of the PANS model and experimental data is very good. The DDES model also gives quite good results; however, some deviations are seen around the reattachment point ($0.75 \leq z/D \leq 2.0$). Specifically, the axial velocity is overpredicted by DDES just upstream of the reattachment point ($z/D = 1.0$), resulting in a 16% overprediction of the reattachment length as discussed above. Using the present PANS model, an overall improvement is seen in results compared to the DDES predictions with as much as 51% and 28% improvements in predictions of the rms axial and circumferential velocities, respectively, near the centerline at $z/D = 1.0$. The SST k-ω URANS model gives poor results and the shear layer between the central reverse flow region and outer flow cannot be captured (see the mean axial velocity curves). Furthermore, the level of swirl cannot be predicted reasonably, resulting in underpredictions of the circumferential velocity as reported also by Gyllenram and Nilsson [44]. As discussed above, results of the SST k-ω model converge to a steady solution, hence, no rms velocity associated with this model is plotted in Fig. 5.8.

To investigate the sensitivity of the numerical solutions to the grid size, in addition to the main grid (with 1,660,384 cells) simulations are also carried out for a finer grid (with 3,428,160 cells), and results are shown in Fig. 5.9. Profiles of the mean and rms velocities obtained using PANS and DDES models on both grids are shown in Fig. 5.9 on four planes with z/D values of 0.5, 1.0, 3.0, and 6.0. Both PANS and DDES results can be slightly improved using a finer mesh, however, it can be seen that the grid dependence is not a major issue.

The evolution of the f_k parameter in PANS simulations is shown in Fig. 5.10 for three axial cross sections, one, two, and four diameters downstream of the expansion. At each section, three curves are compared, namely, the f_k parameter calculated using Eq. (5.34) (the present formula), the f_k parameter calculated using Eq. (5.22) (the previous formula), and the computed f_k parameter based on the calculated k_u and k using Eq. (5.6). It is seen that the present f_k parameter approaches 1 near the wall, resulting in a more RANS-like simulation for this region. Near the centerline f_k decreases, and the present PANS model resolves more turbulent motions in an LES manner. Also f_k has lower values at the section $z/D = 1.0$ where the vortex breaks down and the flow is very unsteady, therefore it needs to be resolved. Further downstream ($z/D = 4.0$) where the flow reattaches to the wall, f_k has higher values, although the model is still

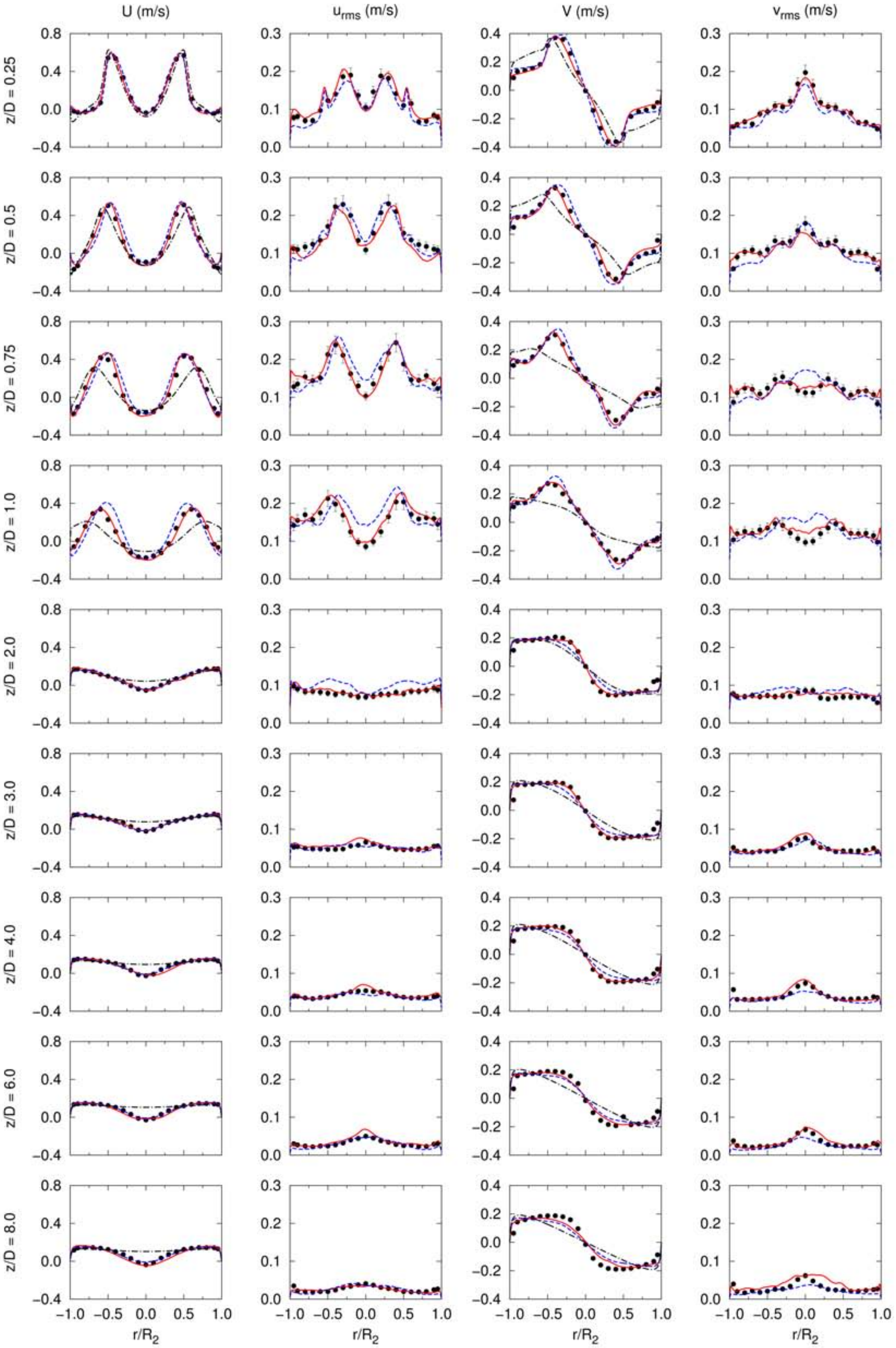

Figure 5.8: Radial distributions of axial mean velocity, axial rms velocity, tangential mean velocity, and tangential rms velocity downstream of the expansion; comparison of (●) experimental data [143], (——) present PANS model, (- - - -) DDES model, and (− · − · −) SST k-ω model.

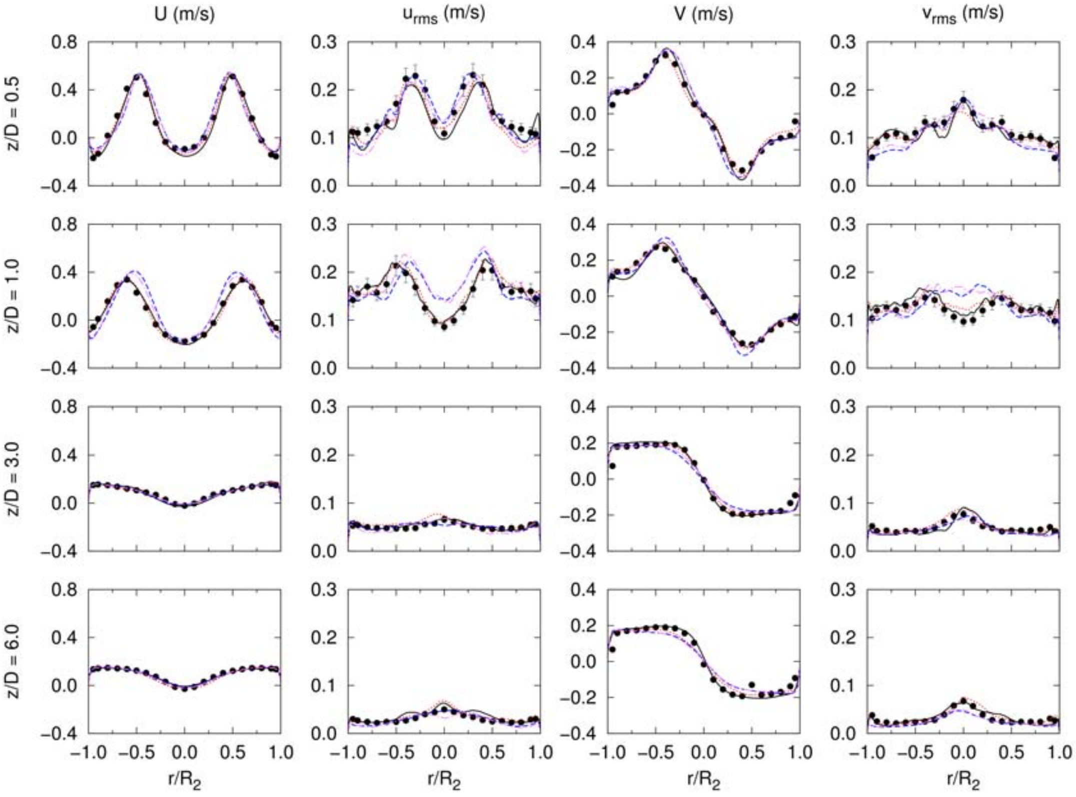

Figure 5.9: Radial distributions of axial mean velocity, axial rms velocity, tangential mean velocity, and tangential rms velocity downstream of the expansion; comparison of (●) experimental data [143], (·····) present PANS model with main grid, (———) present PANS model with fine grid, (- - - -) DDES model with main grid, and (–·–·–) DDES model with fine grid (main grid: 1,660,384 cells and fine grid: 3,428,160 cells).

in LES mode in most of the pipe, according to the Pope's criterion [142]. Furthermore, there is a good agreement between the present prescribed value of f_k (Eq. (5.34)) and the calculated value. It should be noted that the equality between the prescribed and computed values of f_k is exactly reached only in strict equilibrium flows; therefore, it is not surprising to see deviations between these two values in this complex flow. The previously used formula for f_k (Eq. (5.22)), however, shows considerable overprediction (also see Fig. 5.2). Higher values of f_k calculated by Eq. (5.22) result in predicting larger turbulent viscosities, damping more resolved turbulence, and showing slower change from RANS to LES, as also observed by Kubacki et al. [146] and Davidson [138]. Here, this effect is shown in Fig. 5.11 where predictions of PANS simulations using two different formulas for f_k, i.e., Eq. (5.22) and Eq. (5.34), are compared. All other parameters are kept unchanged. It is seen that predictions are improved using the present model, while the previous model tends to return to the RANS solution. Specifically at downstream sections ($z/D = 3.0$ and 6.0), the previous formulation considerably overpredicts the value of f_k resulting in underprediction of the rms velocities and returning the mean velocity values to the RANS predictions.

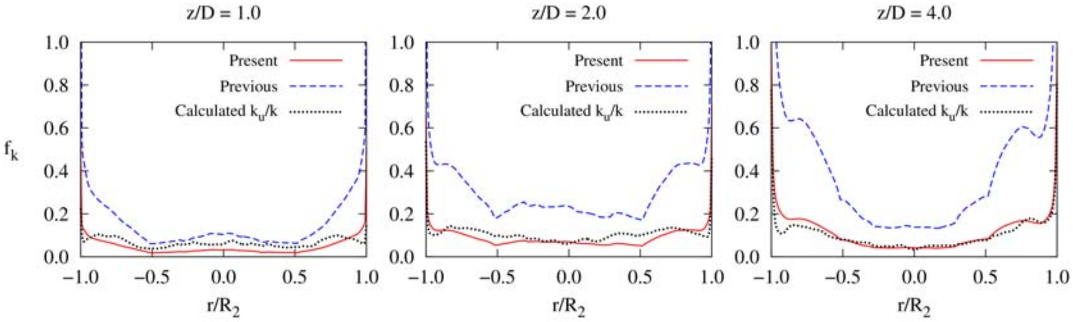

Figure 5.10: Radial distributions of the unresolved-to-total ratio of turbulent kinetic energy f_k in the pipe; comparison between prescribed (using Eq. (5.34) (Present) and Eq. (5.22) (Previous)) and calculated (k_u/k) values.

5.4 Summary

A new partially-averaged Navier-Stokes (PANS) turbulence model for predicting unsteady turbulent swirling flow with vortex breakdown is developed. The present model is formulated based on the extended k-ε turbulence model of Chen and Kim [133] by employing the PANS methodology. The main distinctive feature of the present model is to incorporate a newly developed relation for the unresolved-to-total turbulent kinetic energy ratio f_k, using partial integration of the complete turbulence energy spectrum. The new expression overcomes the problem of overestimated f_k and damped turbulent motions where the grid cut-off wave number is below the inertial range. It is clearly shown that the new formulation improves the predictions compared to the previously used expression for f_k. The present PANS model is validated by numerical simulations of a benchmark test case, namely swirling flow through an abrupt expansion. Results obtained using the present model are in very good agreement with experimental data, while improvements are seen comparing to the results of DDES and URANS (SST k-ω) models. Specifically, mean and rms axial and circumferential velocity profiles, as well as the reattachment length are accurately predicted for the validation test case. The application of the present PANS model in simulations of flow in the complete FLINDT draft tube is presented in Chapter 6.

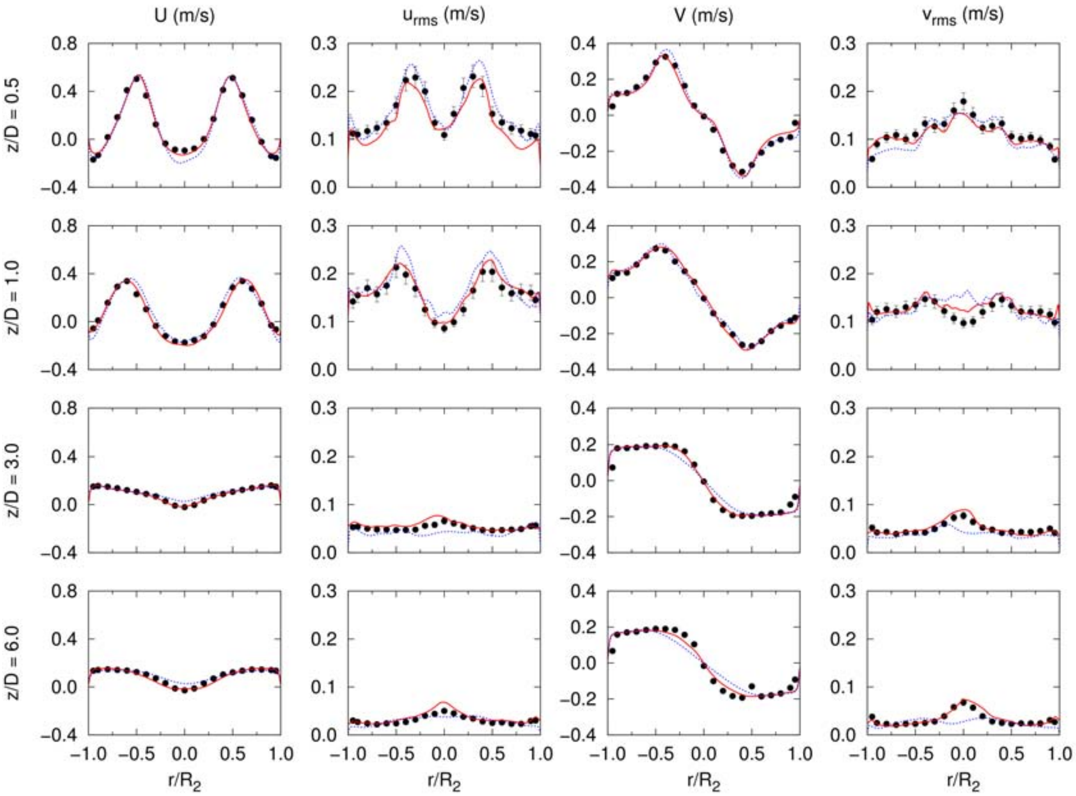

Figure 5.11: Radial distributions of axial mean velocity, axial rms velocity, tangential mean velocity, and tangential rms velocity downstream of the expansion; comparison of (●) experimental data [143], (———) PANS model using Eq. (5.34) (Present) for f_k, and (- - - -) PANS model using Eq. (5.22) (Previous) for f_k.

Chapter 6

Simulations of the Flow in the Complete FLINDT Draft Tube

"No one believes the CFD results except the one who performed the calculation, and everyone believes the experimental results except the one who performed the experiment."
- P. J. Roache, Computational Physicist

A new partially-averaged Navier-Stokes (PANS) model is developed in Chapter 5, which can be used in unsteady simulations of turbulent swirling flows. This chapter presents results obtained using this PANS model in simulations of flow in the complete FLINDT draft tube for various operating conditions. Therefore, the present chapter tries not only to validate the newly developed PANS model for a wide range of operating conditions, but also to discuss and compare physical phenomena occurring under each condition. In addition, the present PANS results are compared to the computational results obtained using RANS models and the capability/incapability of these models for various operating conditions are discussed.

6.1 The Complete FLINDT Draft Tube

The FLINDT draft tube was introduced in Chapter 3. It was discussed that the exact details of the draft tube geometry were not available in open literature, which was one of the challenges in the present research study. Therefore, a comprehensive investigation of the previously published articles within the FLINDT project is performed, in order to build a complete database on details of the draft tube geometry (as much as possible) and available experimental data. Using this database the three-dimensional FLINDT draft tube geometry was rebuilt. Thus, this study can provide a publicly available test case with all details required for a CFD simulation (see Sec. 3.3).

In the simulations of the complete draft tube presented in this chapter, all four cases discussed in Sec. 3.4 are considered, thereby a wide range of operating conditions is covered ranging from 110% (case A) to 70% (case D) of the BEP flow rate (see Table 3.2).

For case D, the circumferentially-averaged mean velocity components and turbulent quantities (k and ε) just downstream of the trailing edge of runner blades are available [147]. Therefore, the inlet section for this case is chosen to be the surface swept by the trailing edge of the runner (section S0 in Fig. 6.1). These data, however, are not available for cases A to C; hence, a downstream section in the draft tube cone (Section S1 in Fig. 6.1) is considered as the inlet section where the experimental data, including axial and circumferential velocity components and turbulent kinetic energy profiles, are available. Because of the relatively high uncertainty and low magnitude of the radial velocity component in measurements at section S1, a linear variation of this component is considered [11] at the inlet for cases A to C. As in the case of the simplified draft tube, the inlet profiles for the dissipation rate are computed from the turbulent kinetic energy profiles as $\varepsilon = k^{3/2}/l$ [12] for cases A to C, with the turbulence length scale being $l = 0.01R$ (R is the runner radius) [12].

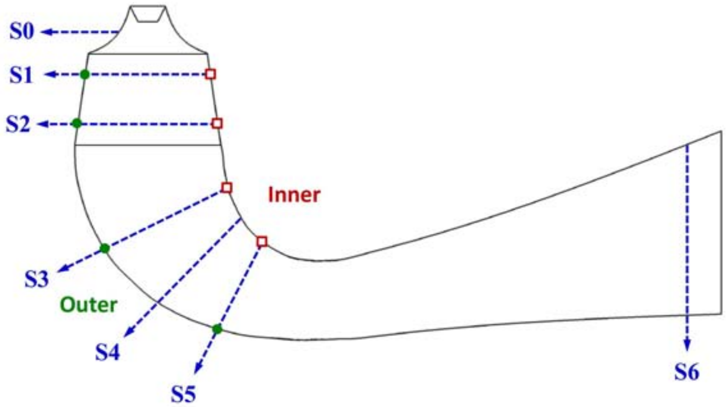

Figure 6.1: Side view of the FLINDT draft tube showing the investigated sections and points where unsteady pressure is monitored in this study.

Figure 6.2 illustrates profiles of velocity components applied at the inlet boundary, i.e., section S1 for cases A to C and section S0 for case D. The evolution of the axial velocity component at the inlet for cases A to C (Fig. 6.2(a)) is characterized by

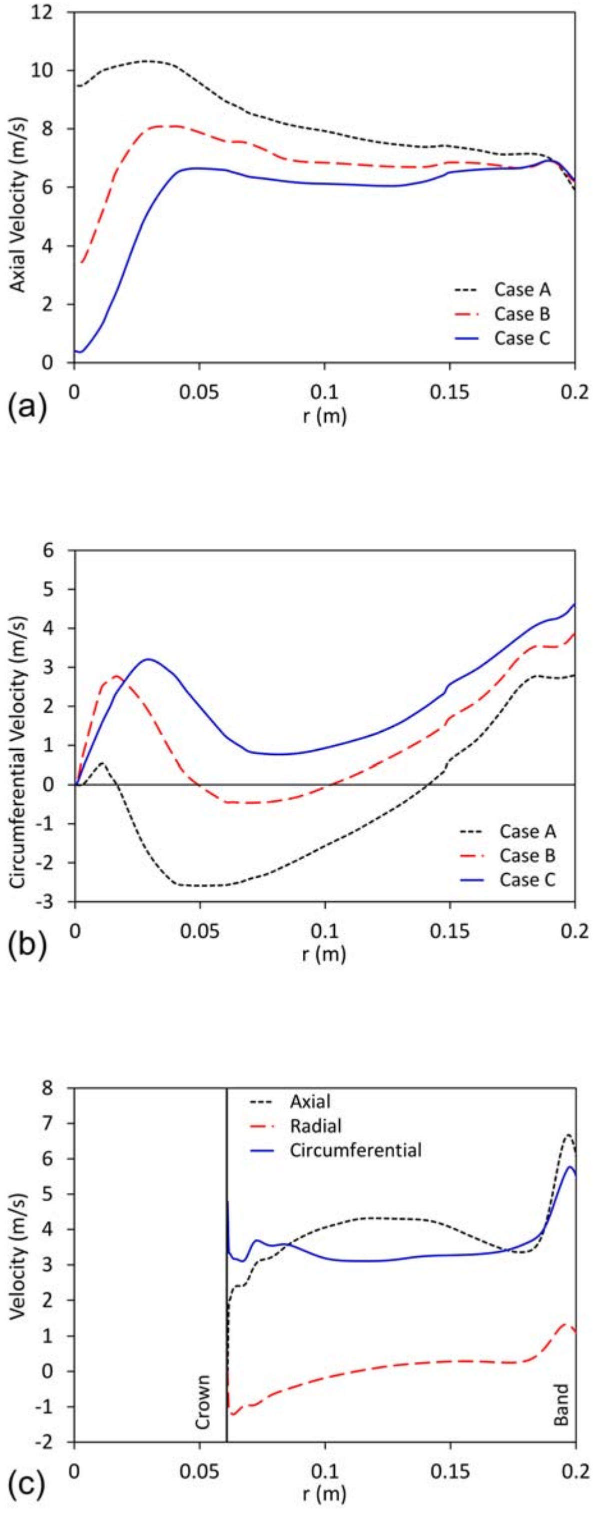

Figure 6.2: Velocity profiles at the inlet section of the computational domain (section S1 in Fig. 6.1 for cases A to C and section S0 in Fig. 6.1 for case D), (a) axial velocity profiles for cases A to C, (b) circumferential velocity profiles for cases A to C, (c) axial, radial, and circumferential velocity profiles for case D. Cases A to D correspond to 110%, 99%, 91%, and 70% of the flow rate at the BEP, respectively.

increasing the low velocity region at the center as turbine's flow rate decreases. Also, the circumferential velocity increases as the operating condition deviates from the BEP. However, the direction of the circumferential velocity (i.e., the direction of the swirl) is inverted for the operating points at the higher flow rates (Fig. 6.2(b)). This can be explained by considering the velocity triangles at the runner exit (see Sec. 1.2 for details). Figure 6.2(c) shows the axial, radial, and circumferential velocity profiles at section S0 (the inlet section for case D). The circumferential velocity is quite high in this case resulting in a high level of swirl (swirl number of 0.63) at the inlet to the draft tube. The increase in velocity components near the band (see Fig. 6.2(c)) in this case is related to the secondary flows in the blade channel at partial load with formation of inter-blade vortices [148].

In order to overcome back-flows at the outlet, which could introduce numerical instabilities, the outflow boundary is located farther downstream after the draft tube discharge. Nevertheless, it has been shown [149] that the outlet boundary plays a relatively less important role in this case. No-slip conditions are applied on all walls, while the crown cone is defined as a rotating wall with an angular velocity equal to that of the runner (for case D with S0 as the inlet section).

The main computational grid for cases A to C (where the computational domain starts from section S1) consists of 1,324,220 cells and for case D (where the computational domain starts from section S0) consists of 2,284,220 cells, which are quite moderate grid sizes. This, in fact, is one of the advantages of the PANS model where the requirement of the computational grid is not as rigid as for an LES model and a relatively coarser mesh can be used (see Chapter 5 for more details). The grid is refined in areas of large variable gradients, i.e., near-wall and centerline regions according to the guideline discussed in detail in Sec. 2.5. To make sure that a grid-independent solution is obtained, simulations are also performed for case A with a finer grid of 3,716,064 cells (results are discussed in Sec.6.2). The first cell center normal to the wall is placed at $y^+ \simeq 2$ everywhere in both grids.

The governing transport equations (Eq.(5.1), (5.2), (5.13), and (5.14)) are numerically solved using the finite volume method in ANSYS-FLUENT 14.0 [150], where the newly developed PANS model is implemented by means of a user-defined function (UDF). Unsteady PANS simulations are initialized by a k-ε RANS steady solution. The time-step size corresponds to one degree rotation of the runner (2.2×10^{-4} second) which is shown to be sufficient for hydroturbine applications [36, 45, 9][1]. The convergence criterion of the residuals for each time-step is set to 3 orders of magnitude drop or maximum 30 sub-iterations. In order to make sure that a quasi-steady condition is reached, unsteady simulations are continued for a very long time. Specifically, simulations are performed for 73,000 iterations corresponding to about 200 rotations of the runner, and about 37 through-flow time (the time required by the mean flow to pass through the domain once). All time-averaged parameters are computed by temporal averaging of the results of 60,000 time-steps (13.2 seconds of operation of the runner corresponding to 167 rotations) after setting the simulations to run for an initial 13,000 time-steps (2.86 seconds of operation of the runner corresponding to 36 rotations), i.e., initial transient. On average, each time-step takes about 27 seconds (48 seconds for case D) for the main grid and 82 seconds for the fine grid on a 16-processor Linux cluster. Simulations are performed on a high performance computing cluster within the Pennsylvania State University's Research Computing and Cyber-infrastructure (RCC) unit.

6.2 Results and Discussion

6.2.1 Global Parameters

Two global parameters are considered for overall evaluation of the present numerical simulations:

1. The pressure recovery coefficient defined as [11]

$$\chi \equiv \frac{p_6 - p_2}{\frac{1}{2}\rho\left(\frac{Q}{A_2}\right)^2} \tag{6.1}$$

and calculated between section S2 and S6 in Fig. 6.1. The pressure recovery coefficient quantifies the overall hydraulic performance of a turbine draft tube in converting the excess of kinetic energy at the runner outlet into static pressure as discussed in Sec.1.2.

2. The portion of the flow exiting the "left" channel (see Fig. 6.3 for the definition of "left" and "right").

Table 6.1 shows the draft tube pressure recovery coefficient obtained using the present simulations in comparison with the experimental data [98]. Numerical predictions of Mauri [11], who used the standard k-ε turbulence model, are also presented for compari-

---

[1] In fact, even larger time steps (up to three degrees of the runner revolution) are shown to be adequate, however, a smaller time step is used to make sure that details of the vortex rope structure is being resolved by the present model.

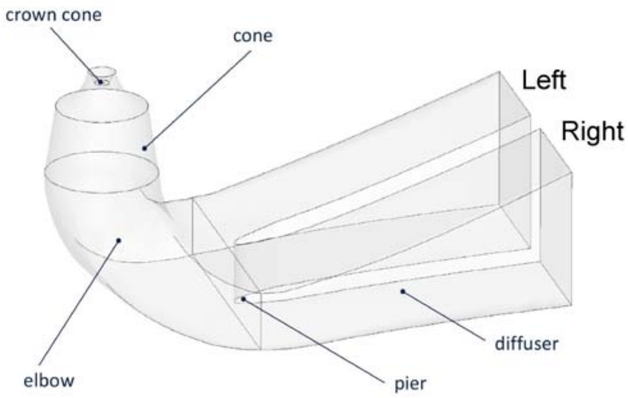

Figure 6.3: Three-dimensional view of the complete FLINDT draft tube showing the components of a draft tube, and “right” and “left” channels.

son (where available). It should be noted that in order to validate the present computational setup, RANS k-ε simulations are also performed and compared with predictions of Mauri [11] for cases A to C where a nearly perfect match is obtained.

As expected, the highest pressure recovery is achieved at the BEP, while the pressure recovery coefficient drops dramatically as conditions move away from the BEP. The k-ε RANS model gives good results at the BEP, i.e., 3.2% difference with experimental data. The draft tube flow at the BEP has very moderate level of swirl and is quite “well-behaved”. No strong flow instability or vortex rope exist in the flow; therefore, RANS closure models are able to give reasonable predictions. Even in case A, with 10% more flow rate than the BEP, the flow instability is not high enough to form the vortex rope and RANS simulations are able to predict the pressure recovery coefficient with only 3.7% deviation from the experimental data values. It should be noted, however, that in both cases A and B, predictions of the present PANS model are in very good agreement with experimental data (only 2.6% and 0.6% difference in case A and B respectively), while improvements are seen comparing to the k-ε RANS predictions. Nevertheless, as shown previously by [38], the clear drawback of the RANS model occurs under partial-load conditions, where the flow is highly unsteady and a strong helical vortex rope forms inside the draft tube. The RANS closure models are unable to predict the flow behavior in these conditions, while there still exists a good agreement between the predictions of the PANS model, which resolves important vortical structures of the flow, and experimental data. Specifically, deviation more than 13% is seen between experimental data and RANS simulations for case C, while PANS predictions show less than 4% deviation. For case D with 70% of the BEP flow rate, no pressure recovery calculation is found in [11], therefore, RANS simulations are performed which show more than 58% overprediction. The prediction of the present PANS simulations deviates by only 6% from experimental data for this case. Using the fine grid (with 3,716,064 cells), results of the present PANS model show a slight improvement and only 1.4% difference with experimental data is seen for case A. However, in view of the quite considerable increase in the computation time (more than three times), these simulations cannot be justified. Therefore, results obtained using the main grid (with 1,324,220 cells) are considered to be "grid-independent" within a reasonable error.

Table 6.1: Pressure recovery coefficient χ in the draft tube (deviations from experimental data are given in the parentheses).

	Q/Q_{BEP}	Exp. [11, 98]	PANS	RANS k-ε
Case A	110%	0.5192	0.5330 (2.6%)	0.5385 (3.7%)
Case B	99%	0.7584	0.7534 (0.6%)	0.7826 (3.2%)
Case C	91%	0.4937	0.5130 (3.9%)	0.5584 (13.1%)
Case D	70%	0.1161	0.1232 (6.0%)	0.1834 (58.1%)
Case A (fine mesh)	110%		0.5266 (1.4%)	

Table 6.2 presents the portion of the flow rate through the "left" channel, where the present PANS predictions are compared with experimental data as well as those obtained by the k-ε RANS simulations [11]. Again, a fairly good agreement is seen between present PANS predictions and experimental data, with PANS results for case A with the fine grid being in excellent agreement with data. Another interesting point is the uneven partition of the flow rate in the "left" and the "right" channels, which becomes more distinct at lower flow rates. It is seen that at 70% flow rate, only 20% of flow exits through the "right" channel. This is physically due to the interactions between swirling flow entering the draft tube and secondary flows due to the curvature of the draft tube elbow. A numerical test performed in this study indicates that reversing the swirl direction at inlet (i.e., reversing the runner's rotation direction) switches the portion of flow going through each channel.

6.2.2 Mean Velocity and Wall Pressure Distributions

Figures 6.4 to 6.7 shows the time-averaged axial and circumferential velocity components in the draft tube obtained from the present PANS simulations. For cases A to C, with

Table 6.2: Flow portion (percentage of the total flow rate) through the "left" channel (see Fig. 6.3 for the definition of "left" and "right" channels).

	Q/Q_{BEP}	Exp. [11, 98]	PANS	RANS k-ε
Case A	110%	62	63	66
Case B	99%	51	59	63
Case C	91%	73	74	72
Case D	70%	—	81	81
Case A (fine mesh)	110%		62	

section S1 as the inlet, results are plotted at section S2 (Fig. 6.4 to 6.6). Case D has the benefit of having the inlet at section S0, therefore, results can be plotted at two sections, i.e., S1 and S2 (Fig. 6.7). Results are compared to the experimental data [11, 36, 12] as well as those obtained from the k-ε RANS simulations. As shown by previous studies [42, 43] and discussed in Chapter 4, URANS models damped out the unsteadiness of the flow and give steady results. Hence, time-averaged k-ε URANS results found to be the same as the k-ε RANS steady results.

Comparing Fig. 6.4(a), 6.5(a), 6.6(a), 6.7(a), and 6.7(c) reveals that the axial velocity component is characterized by increasing the low velocity region (stagnant region) at the center of the draft tube as the turbine's flow rate decreases. Furthermore, comparing Fig. 6.7(a) and 6.7(c) shows that this region radially expands towards downstream in the draft tube. Comparing the circumferential velocity shows that the minimum swirl is associated with the BEP flow rate. Also, the swirl is damped moving downstream in the draft tube (compare Fig. 6.7(b) and 6.7(d)).

As shown in Fig. 6.4, both RANS and PANS models correctly predict the axial and circumferential velocities for case A. PANS, however, seems to capture more details of the circumferential component at the center of the draft tube. For case B (Fig. 6.5), the RANS k-ε model overpredicts the axial and circumferential velocities by as much as 19% and 35% respectively, while PANS predictions show excellent agreement with data. The deficiency of the RANS model, as also shown by Vu et al. [38], appears mainly for the partial load conditions. As illustrated in Fig. 6.6(a), RANS underpredicts the axial velocity by as much as 64% near the centerline. Predictions can be improved by about 47% using the PANS model, showing quite good agreement with experimental data. Predictions of both models for the circumferential velocity are nearly the same, showing a relatively good agreement with data, namely 7% average deviation (see Fig. 6.6(b)). The deviation between RANS simulation results and data becomes larger as the turbine's discharge decreases (farther away from the BEP). As shown in Fig. 6.7(a) and 6.7(c), the RANS k-ε model completely fails in correctly predicting the level of the axial velocity near the centerline for case D. It predicts a large backflow region, and as a result, overpredicts the level of the velocity outside of the shear flow region, while no reverse flow is observed within experimental data. This class of models has been developed for and calibrated by use of data from simple, steady flows. Therefore, they are insufficient for predicting strong, unstable shear layers as in the case of the partial load draft tube flow where a strong vortex is present. Predictions of the present PANS simulations show considerable improvements. The level of the axial velocity is well calculated in the shear layer, while better agreement is seen with experimental data near the centerline, although there still exists a notable underprediction. Based on these results, it is concluded that RANS models cannot correctly predict the flow behavior at partial load, where the low-velocity inner region interacts with outer flow and the vortex rope forms. The precessing vortex rope enhances the mixing and turbulence production and diffusion that cannot be modeled using the RANS turbulence models. Using the PANS turbulence model, the level of mixing and flow unsteadiness is better predicted and results are improved.

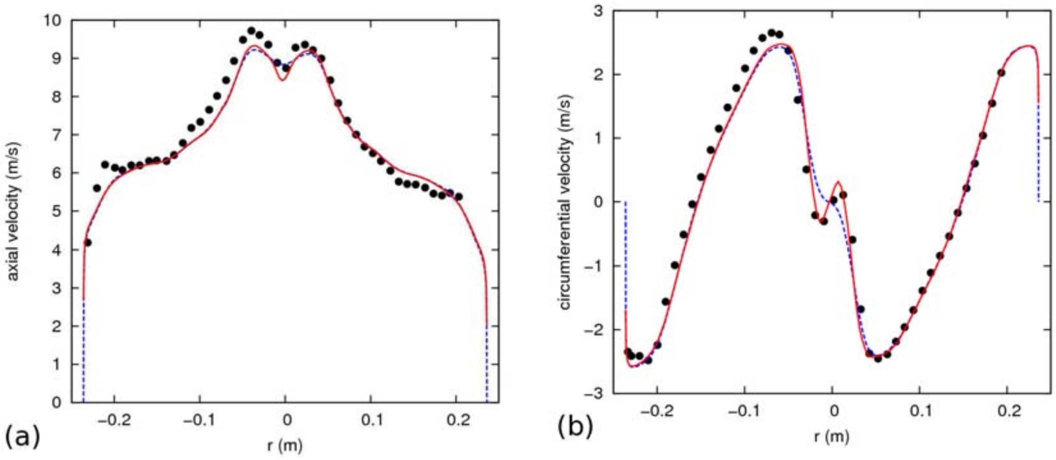

Figure 6.4: Radial distributions of time-averaged (a) axial and (b) circumferential velocity on section S2 for case A; comparison of (●) experimental data, (———) the present PANS model, and (- - - -) the k-ε RANS model.

The wall static pressure is shown at four sections (Sections S2 to S5 in Fig. 6.1 and Fig. 6.8) in Fig. 6.9 for three operating conditions, i.e., cases A to C. In the experimental measurements [98], several pressure transducers were located peripherally at each section. Figure 6.8 shows the top view of these four sections together with the pressure monitoring points. The “inner” and “outer” sides of the draft tube’s elbow are specified to help

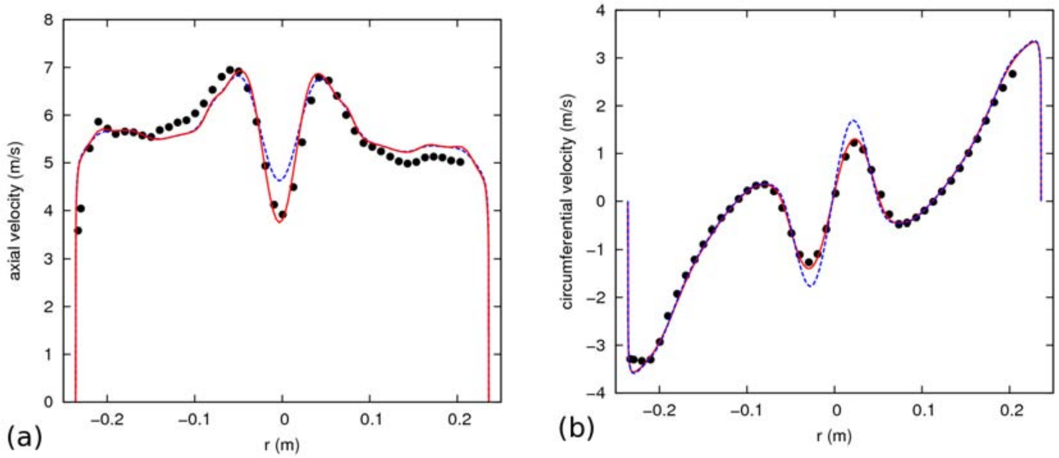

Figure 6.5: Radial distributions of time-averaged (a) axial and (b) circumferential velocity on section S2 for case B; comparison of (●) experimental data, (——) the present PANS model, and (- - - -) the k-ε RANS model.

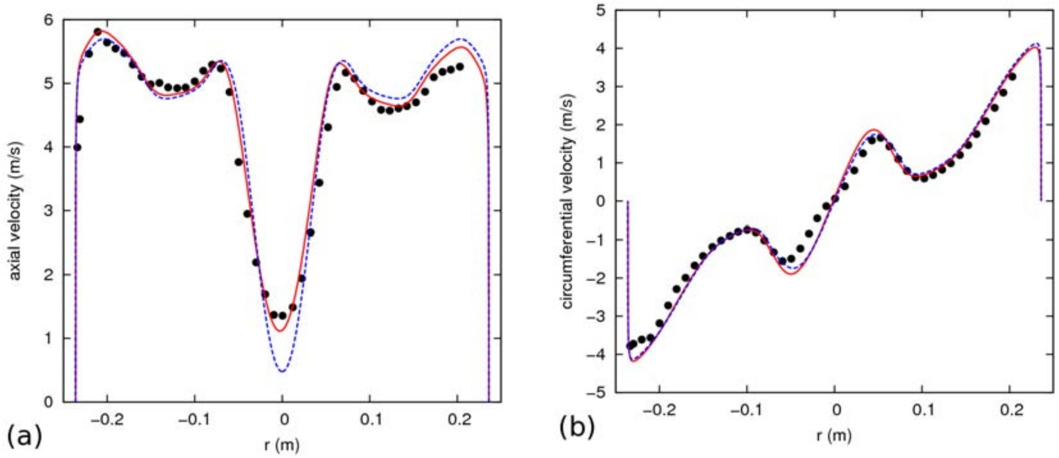

Figure 6.6: Radial distributions of time-averaged (a) axial and (b) circumferential velocity on section S2 for case C; comparison of (●) experimental data, (——) the present PANS model, and (- - - -) the k-ε RANS model.

understanding the directions in Fig. 6.8. As seen in Fig. 6.9, wall pressure is lower near the “inner” side of the elbow (e.g., P5 to P8 at section S3) and is higher near the “outer” side (e.g., P1, P2, P11, and P12 at section S3) for all operating conditions. This is expected due to the flow streamline curvature forced by the elbow. Results obtained from the PANS simulations are compared to the experimental data and the k-ε RANS results of Mauri [11]. The global trend of the experimental data is predicted fairly well by both models. Locally, however, the difference between RANS predictions and

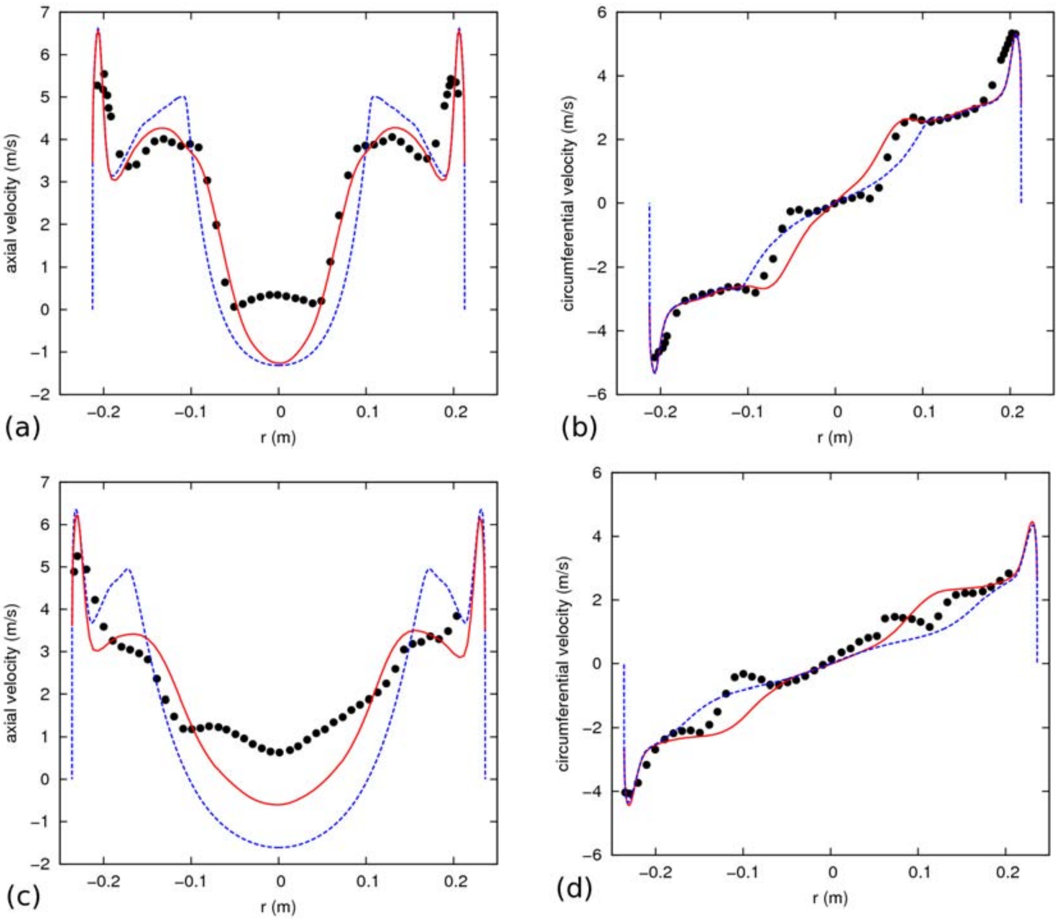

Figure 6.7: Radial distributions of time-averaged (a) axial velocity on section S1, (b) circumferential velocity on section S1, (c) axial velocity on section S2, and (d) circumferential velocity on section S2 for case D; comparison of (●) experimental data, (———) the present PANS model, and (- - - -) the k-ε RANS model.

experimental data reaches 90% of the measured value. The RANS calculations clearly overestimate the influence of elbow at the section S2, but the differences decrease in the following sections. Predictions are significantly improved by using the PANS model, specifically at the "outer" side of the elbow for section S2 (points P1, P2, P11, and P12), and the "inner" side of the elbow for section S3 and S4 (points P4 to P8).

In order to compare simulation results and experimental data more quantitatively, deviations between RANS and PANS predictions and the experimental data are calculated point by point and summarized in Table 6.3. For each case of A to C and each section of S2 to S5, the maximum and the average percentage difference between calculated results and experimental data is shown in Table 6.3. In case A, the difference between the k-ε

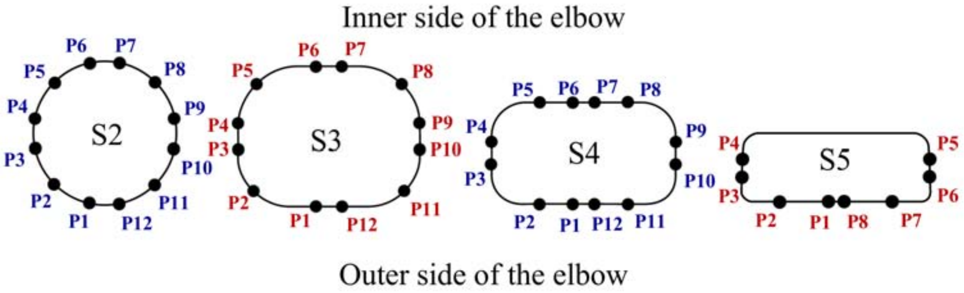

Figure 6.8: Locations of pressure transducers at four sections (see Fig. 6.1) in the draft tube where wall pressure is measured in experiments [11, 98].

RANS predictions and data can reach 49% (Section S4) with the average difference for the four sections being 15%. The average difference between PANS predictions and data is 9%, while improvements are seen for all sections. Similar results are seen for cases B and C with 7% and 8% improvements of predictions on average using the PANS model. Locally, a difference of 92% is seen between RANS results and data for case C while the maximum difference of PANS results and data never exceeds 30%.

6.2.3 Unsteady Flow Field and Vortex Rope

Using the present unsteady PANS simulations, transient features of the draft tube flow can be investigated. Figure 6.10 shows contours of instantaneous (for an arbitrary instance in time) and time-averaged axial velocity in the draft tube for all operating conditions. Contours are plotted in the symmetry plane, showing the draft tube cone and elbow up to the pier. The evolution of the axial velocity from over-load to partial-load can be clearly seen in Fig. 6.10. In case A, corresponding to 110% of the BEP flow rate, axial velocity is quite high especially at the center of the draft tube. By decreasing the flow rate towards cases B and C, a stagnant region starts to grow at the center of the draft tube (the dark region in Fig. 6.10). This stagnant region is the result of the wake of the crown cone as well as the swirling nature of the flow which tends to decrease the momentum near the center and increase it near the wall. In case B, corresponding to 99% of the BEP flow rate, the stagnant region is small and is limited to a very narrow region close to the centerline of the draft tube. However, as the flow rate further decreases, the stagnant region grows in size and expands in the draft tube. The shear layer forming between this stagnant region and the highly swirling outer flow becomes unstable and rolls up resulting in formation of a helical vortex which is known as the vortex rope.

Table 6.3: The percentage difference (%) between wall pressure predictions of the k-ε RANS and the present PANS models, and the experimental data.

	Case A				Case B				Case C			
	Maximum		Average		Maximum		Average		Maximum		Average	
	RANS	PANS	RANS	PANS	RANS	PANS	RANS	PANS	RANS	PANS	RANS	PANS
Section S2	38	22	21	10	35	11	18	5	39	19	18	8
Section S3	33	23	17	11	28	19	13	5	92	30	23	15
Section S4	49	17	15	8	22	19	10	7	36	26	15	6
Section S5	14	10	7	6	12	8	7	4	16	15	11	7
Four sections average	34	18	15	9	24	14	12	5	46	22	17	9

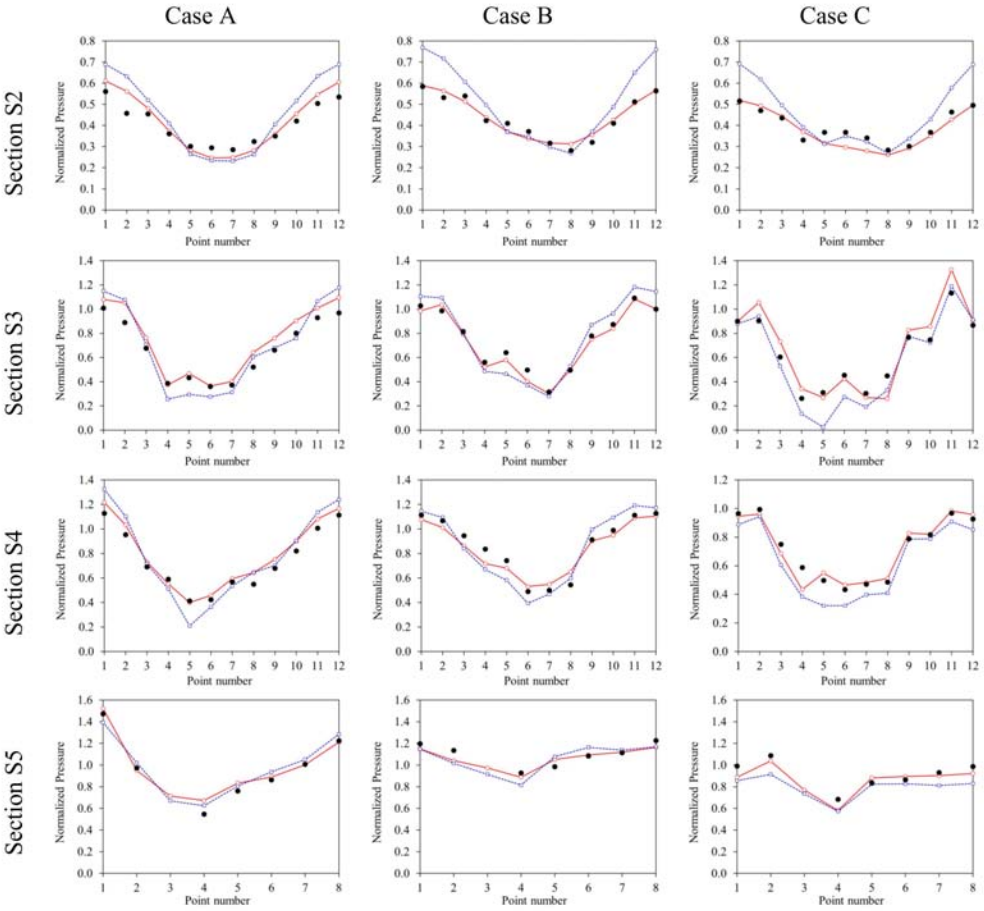

Figure 6.9: Distributions of wall pressure in the draft tube at four sections (see Fig. 6.1 and Fig. 6.8 for locations of these sections and the monitored points) for cases A to C; comparison of (●) experimental data, (———) the present PANS model, and (- - - -) the k-ε RANS model.

The vortex rope rotates around the vortex core as well as precesses around the draft tube centerline axis. As shown for case D, by further decreasing of the flow rate, a very strong precessing vortex rope forms in the draft tube. Contours of the time-averaged axial velocity in Fig. 6.10 show the mean extent of the stagnant region in the draft tube, which increases when decreasing the flow rate.

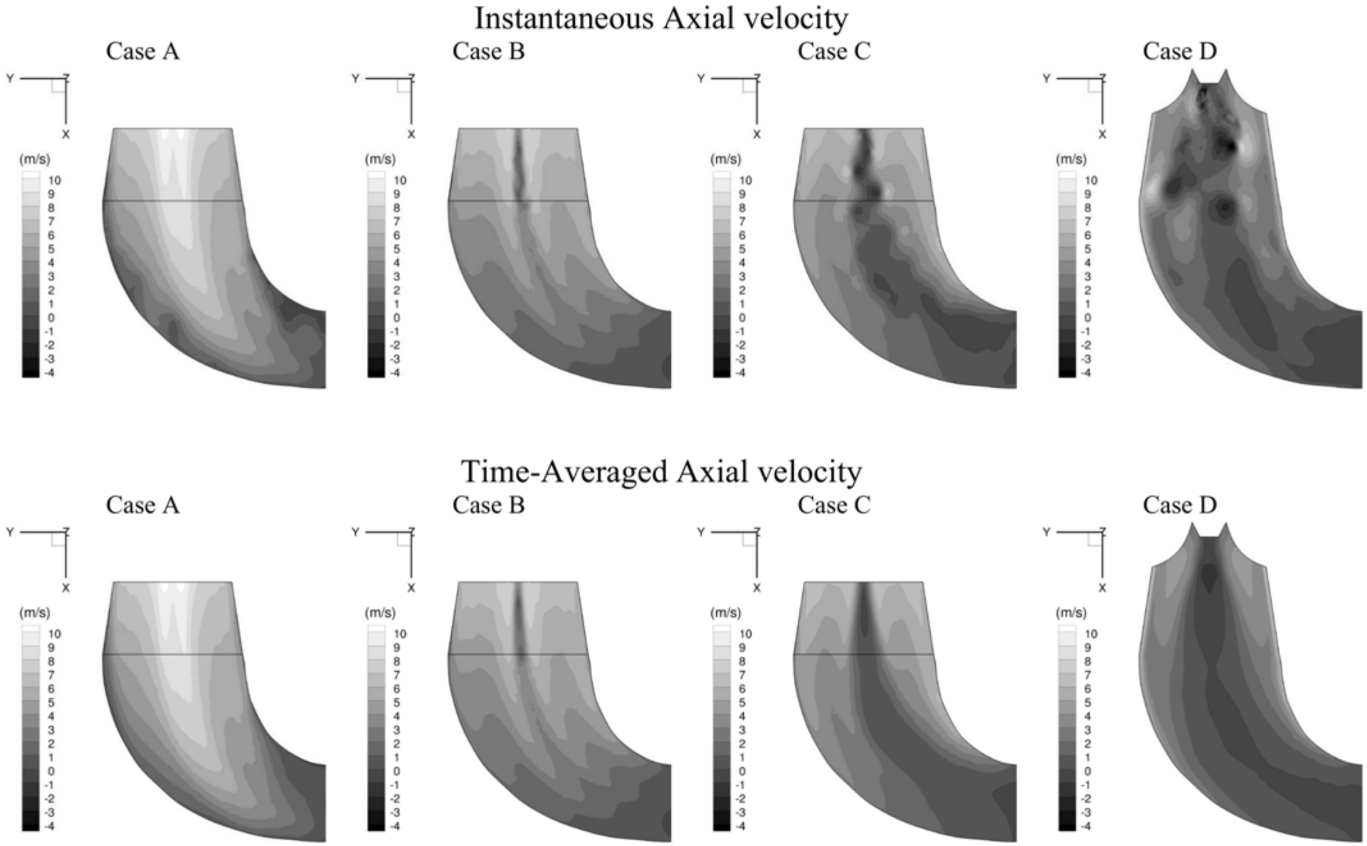

Figure 6.10: Contours of instantaneous (top row) and time-averaged (bottom row) axial velocity in the draft tube obtained by PANS simulations.

The details of the flow and pressure fields in the draft tube are illustrated in Fig. 6.11 for case D. Contours of instantaneous pressure and axial velocity for three arbitrary instances in time, as well as contours of the mean axial velocity in the draft tube are shown. In each figure, the average location of the vortex core in the draft tube cone obtained from linear curve fitting of PIV data of Ciocan and Iliescu [99] is shown using two black lines. In fact, these lines represent the 2D cross section of the conical surface around which vortex rope wraps (for a detailed discussion see Sec 4.6). Figure 6.11(a) shows low pressure discoid regions in the draft tube representing cross sections of the helical vortex rope. In a vortex, pressure tends to have a local minimum on the axis of a circulating flow when the centripetal force is balanced by the radial pressure gradient ($\partial p/\partial r = \rho V_\theta^2/r$). It can be seen that there is an overall good agreement between the locations of the vortex core predicted by the PANS simulations and those obtained from PIV measurements [99]. This also can be seen in Fig. 6.11(b) where instantaneous axial velocity contours are plotted at the same three time instants. Furthermore, Fig. 6.11(b) shows the strong shear layer which is the cause of the formation of the vortex rope. The direction of rotation of the vortex can be easily found out using Fig. 6.11(b) and considering the direction of the axial velocity at each shear layer. Note that in Fig. 6.11, downward is positive and upward (reverse flow) is negative. As discussed in Sec. 4.4, the vortex rope forms due to the roll-up of the shear layer at the interface between the low-velocity inner region created by the wake of the crown cone and highly swirling outer flow. This low-velocity inner region (stagnant region) is clearly shown in Fig. 6.11(c) by contours of the mean axial velocity. Again, it is interesting to note the agreement between the average locations of the vortex cores from PIV data (black lines) and the extent of the stagnant region predicted by the PANS simulations.

As shown in Fig. 6.12, the present PANS model captures a strong precessing vortex rope in the draft tube for case D. The helical vortex is visualized in Fig. 6.12 at three instants (corresponding to those shown in Fig. 6.11) by the isopressure surfaces corresponding to $p = -16,000$ Pa. The vortex rope has a very unsteady nature, and its shape can dramatically change over time. The tail of the vortex rope may impact the inner side of the elbow wall as seen in Fig. 6.12 at $t = 6.6$ s. This impact, called the "shock phenomenon", induces strong acoustic noise, pressure fluctuations, and even structural vibrations [151]. The unsteady pressure forces arising from this will be discussed in Sec. 6.2.4.

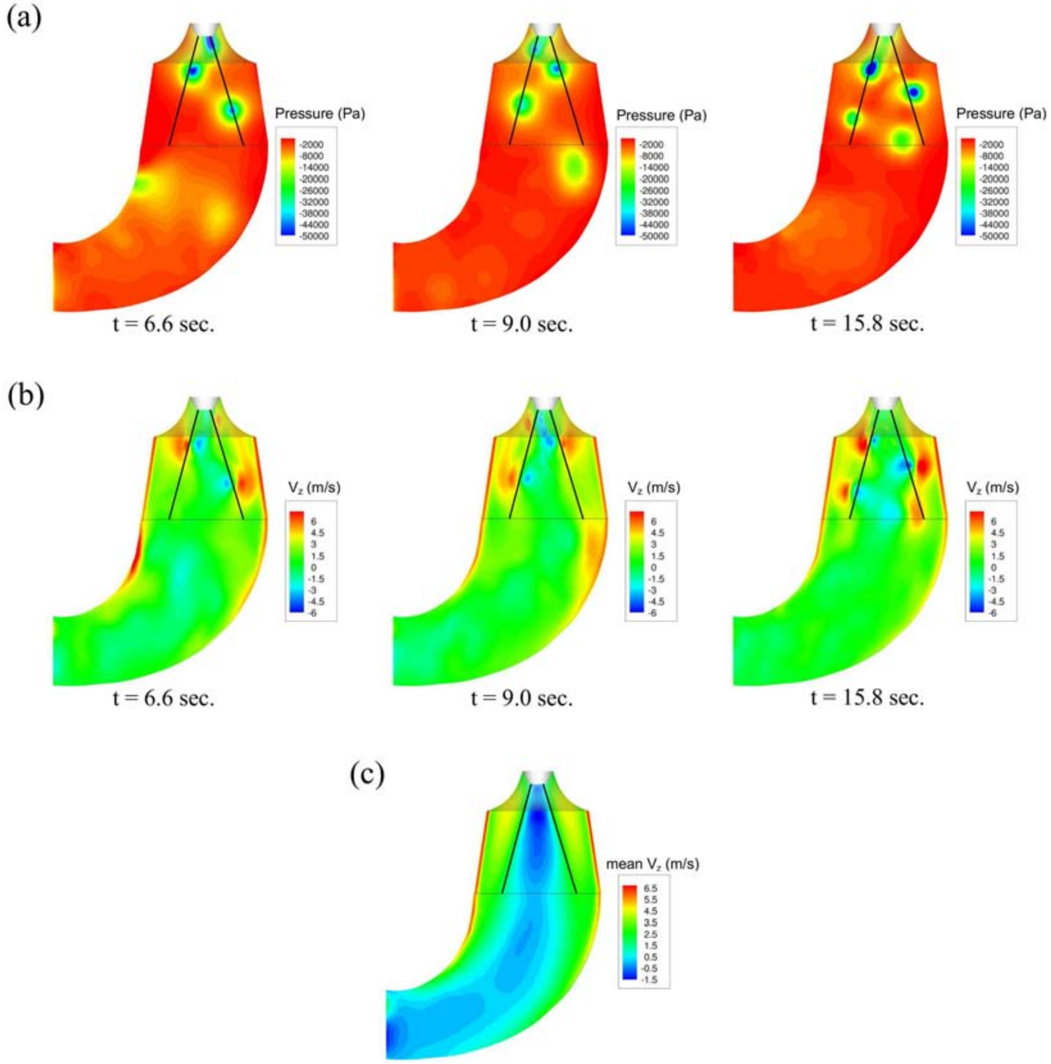

Figure 6.11: Contours of (a) instantaneous pressure, (b) instantaneous axial velocity, and (c) mean axial velocity in the draft tube at three arbitrary instances of time obtained using the PANS simulations for case D. The black lines show the location of the vortex core obtained from linear curve fitting of PIV data from Ciocan and Iliescu [99].

6.2.4 Pressure Fluctuations

Pressure fluctuations associated with formation of the vortex rope may result in severe structural vibrations and damage to hydropower plant components including runner, draft tube, and penstock. Here, to demonstrate fluctuations in the draft tube due to the formation of a strong vortex rope in case D, wall pressure is monitored on several points. Specifically, unsteady wall pressure is monitored for 12 points distributed along

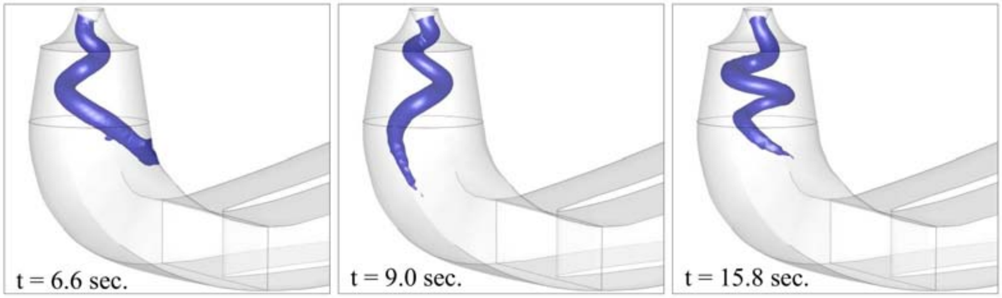

Figure 6.12: Vortex rope visualized by the isopressure surfaces at three instants of time.

the periphery of section S2 (see Fig. 6.8 and Fig. 6.1), located 0.24 m downstream of the draft tube inlet, as well as for eight points along the draft tube elbow (see Fig. 6.1). Figure 6.13(a) shows the evolution of wall pressure with time in the draft tube for point P9 on section S2 in Fig. 6.8 during unsteady PANS simulations. Results are shown for 6 s (about 27,000 iterations and 75 rotations of the runner) after letting the simulations run for an initial 4 seconds to make sure that a periodic unsteady (quasi-steady) state is reached. Pressure fluctuations due to the vortex rope have large amplitude ($p_{\mathrm{rms}} =$ 2423 Pa) and low frequency ($\sim$4 Hz) as shown in Fig. 6.13(a).

The dominant frequency of the pressure fluctuations can be obtained by performing a fast Fourier transform (FFT) on the results. Figure 6.13(b) shows the normalized frequency spectrum obtained from present PANS simulations. The vortex rope frequency is found to be 0.308 of the runner rotation frequency. This is in very good agreement with the value of 0.3 seen in experimental studies [36] (only 2.7% difference). Furthermore, results of the present PANS simulations give better predictions in comparison with the previous numerical studies of Ciocan et al. [36] who used the k-ε URANS model and Zobeiri [9] who used three turbulence models, namely the k-ε, the SST k-ω, and the scale adaptive simulation (SAS) models[2]. Table 6.4 shows the vortex rope frequency predicted by the present PANS simulations in comparison with the previous numerical simulations in the literature.

The amplitude of the pressure fluctuation, usually quantified by the root-mean-square (rms) of the oscillation, defines the magnitude of the oscillatory force experienced by the power plant components due to the rotation of the vortex rope. Therefore, it is equally important to study the pressure fluctuation amplitude associated with formation of the

---

[2] Both simulations in Ref. [9] and [36] include the runner as part of the solution, therefore, the unsteadiness in the draft tube is not only the result of the vortex rope self-induced instability, but also the result of the unsteady velocity exerted by the rotation of the runner.

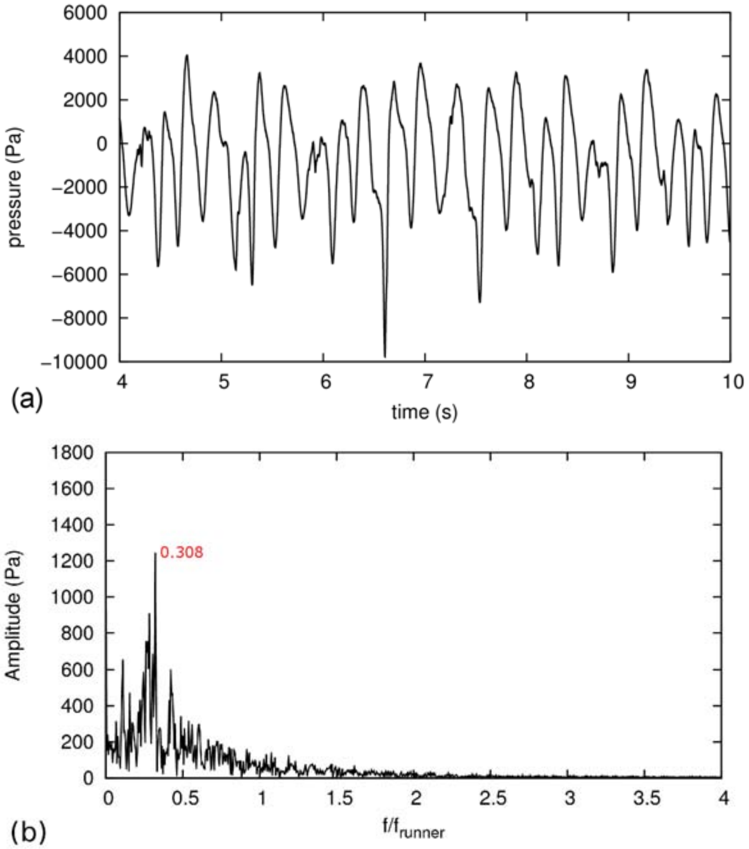

Figure 6.13: (a) Wall pressure fluctuations and (b) their normalized frequency spectra obtained from the present PANS simulations.

Table 6.4: Normalized vortex rope frequency f/f_{runner} (deviations from experimental data are given in the parentheses).

Experiment [36]	PANS	k-ε [36]	k-ε [9]	SST k-ω [9]	SAS [9]
0.3	0.308 (% 2.7)	0.339 (% 13)	0.346 (% 15.3)	0.344 (% 14.7)	0.315 (% 5.1)

vortex rope. The pressure fluctuation amplitudes, based on the root-mean-square of the pressure oscillations, are calculated for 12 points positioned at the periphery of section S2 (Fig. 6.8), and plotted in Fig. 6.14 in comparison with experimental data [9]. The normalized pressure fluctuation amplitude C_p in Fig. 6.14 is defined as

$$C_p = \frac{p_{\mathrm{rms}}}{\frac{1}{2}\rho V_{inlet}^2} \tag{6.2}$$

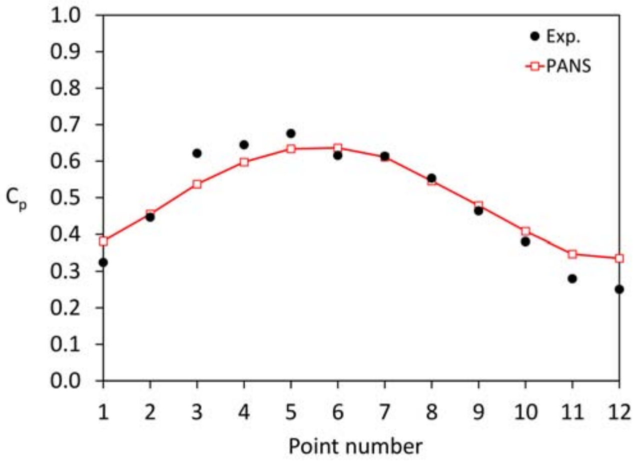

Figure 6.14: Distributions of wall pressure fluctuation amplitude in the draft tube at section S2; comparison of experimental data [9] and present PANS simulations.

where V_{inlet} is the average velocity at the draft tube inlet.

It can be seen that the predictions of the PANS simulations closely follow the experimental data. The highest amplitude was found to be associated with point P5 in the experiments which is predicted by only 6% difference by the present simulations. Nevertheless, some overpredictions are seen for points with lower amplitude. The distributions of the pressure fluctuation amplitude clearly show the displacement of the vortex center from the cone axis and the asymmetric nature of the flow even in the draft tube cone. Thus, pressure fluctuations are not evenly distributed in the draft tube and, therefore, it is important to detect regions in the draft tube with higher pressure fluctuation amplitudes. For this purpose, wall pressure is monitored at several points located farther downstream in the draft tube. Figure 6.15 shows the evolution of wall pressure with time for eight points along the draft tube elbow (marked with squares and circles in Fig. 6.1). The top row in Fig. 6.15 labeled “inner path” shows pressure fluctuations for four points on sections S1, S2, S3, and S5 located in the “inner” side of the draft tube elbow. The bottom row labeled with “outer path” shows pressure fluctuations at the same sections but located on the “outer” side of the elbow. These eight points are shown in Fig. 6.1 with four “inner” points marked with red squares and four “outer” points marked with green circles. Results are shown for about 12 seconds after letting the simulations run for an initial 4 seconds. It is seen that pressure fluctuations show similar behavior for the “inner” and the “outer” points at section S1, which is due to the symmetry of the draft tube cone. It should be noted that, as expected, pressure fluctuations for these two points show a 180 degree phase lag. However, this 180 degree phase difference is not perfect for the all instants due to the effect of the elbow, which can be felt even in the cone, as well as the vortex break-apart causing additional fluctuations. The peak-to-peak amplitude of pressure fluctuations can reach 4,000 Pa in this section. The asynchronous (with a 180 degree phase lag) nature of these fluctuations exerts severe oscillatory forces on the draft tube wall. The long-term operation under this condition may results in structural damage to the draft tube components [13] as shown in Fig. 6.16. In cases where the draft tube is hung below the turbine and is not integrated with the powerhouse structure, these forces may cause failure of the lateral supports that brace the draft tube to the powerhouse [152]. Moving farther downstream towards sections S2 and S3, pressure fluctuations show a very different behavior for the "inner" and "outer" points. Specifically, the "inner" side of the elbow demonstrates very severe pressure fluctuations with the peak-to-peak amplitude as high as 14,000 Pa. This is mainly due to the interactions between the vortex rope, the secondary flows, and the low pressure region in the "inner" side of the elbow. This is the region where the vortex rope may impact the draft tube wall causing the "shock phenomenon" [151] as shown in Fig. 6.12. The concrete erosion in the draft tube elbow [152] can be related to the strong forces exerted by these phenomena.

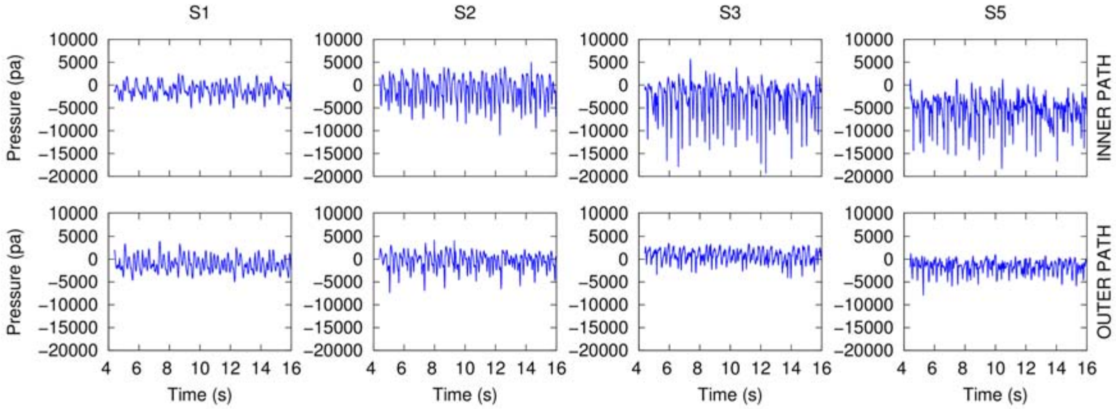

Figure 6.15: Wall pressure fluctuations monitored on eight points in the draft tube (four points on the "inner" side and four points on the "outer" side of the elbow) obtained by PANS unsteady simulations.

Figure 6.17 shows p_{rms} for the eight monitored points in Fig. 6.15. It is seen that p_{rms} in the inner side of the elbow increases to as much as 2.4 times the one in the cone (from 1,397 Pa to 3,343 Pa) and then decreases farther downstream to 2,800 Pa,

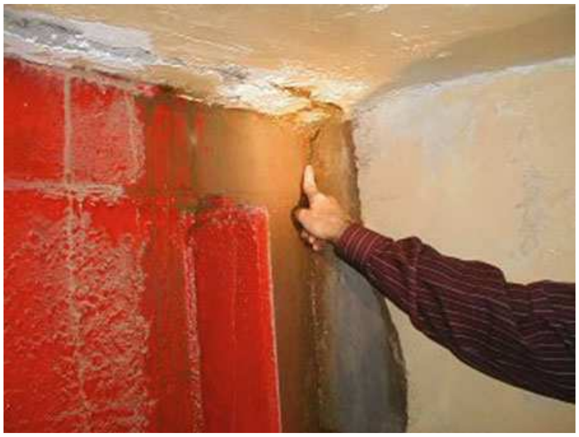

Figure 6.16: Crack in concrete at the draft tube door for a hydroturbine operated for extended period of time at partial-load operating conditions. Source: Dörfler et al. [13].

while the “outer path” shows a relatively consistent behavior in terms of changing p_{rms} (around 1,500 Pa). Therefore, it is concluded that for a draft tube of a hydroturbine operating under partial load, where a strong vortex rope forms in the draft tube, the most critical region where severe pressure fluctuations are felt is the inner side of the draft tube elbow.

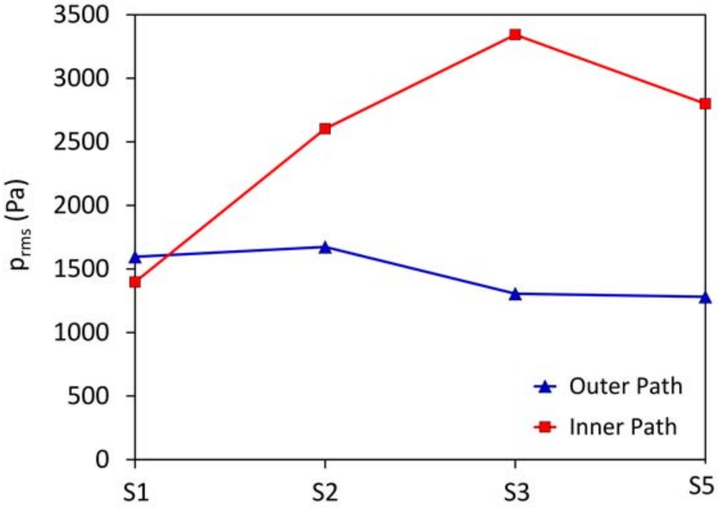

Figure 6.17: The root-mean-square of wall pressure fluctuations in the draft tube for the eight monitored points in Fig. 6.15.

6.3 Summary

Numerical simulations of the flow in the complete FLINDT draft tube are carried out in this chapter. The test case, the FLINDT draft tube, is reconstructed by compiling data from several published papers as discussed in Chapter 3. The PANS model developed in Chapter 5 is used as the turbulence closure model. Four operating conditions ranging from 70% to 110% of the BEP flow rate are considered, and several parameters including the pressure recovery coefficient, the mean velocity, and the wall pressure obtained from the present PANS simulations are compared with experimental data as well as those obtained from the RANS k-ε simulations. It is shown that RANS and PANS both can predict the flow behavior close to the BEP operating condition. However, RANS results deviate considerably from the experimental data as the operating condition moves away from the BEP. The pressure recovery factor predicted by the RANS k-ε model shows more than 13% overprediction for case C with 91% of BEP flow rate, while axial velocity is underpredicted by more than 64% near the centerline. In case D, with even lower flow rate (70% of BEP), the k-ε model fails substantially in predicting mean axial velocity while more than 58% difference is seen in prediction of the recovery factor. Predictions can be improved dramatically using the present unsteady PANS simulations. Specifically, the pressure recovery factor is predicted to less than 4% deviation and mean axial velocity is calculated to less than 17% difference with experimental data for case C. Even for case D, with a strong vortex rope forming in the draft tube and flow being very unstable, the pressure recovery factor is predicted to only 6% difference with data, while considerable improvement is seen in comparison to the RANS results, although still notable underprediction is seen near the center of the draft tube. Furthermore, details of the unsteady flow field, including the unstable shear layer and the stagnant region, and the precessing helical vortex rope are captured using the unsteady PANS simulations.

Chapter 7

Mitigation of the Vortex Rope Formation

"When you are studying any matter, or considering any philosophy, ask yourself only what are the facts, and what is the truth that the facts bear out. Never let yourself be diverted either by what you wish to believe, or what you think could have beneficent social effects if it were believed; but look only, and solely, at what are the facts."
- Bertrand Russell

7.1 Introduction

As discussed so far, the flow in the draft tube of a Francis turbine operating at partial load is characterized by severe flow instabilities and the presence of a helical vortex called the vortex rope. The self-induced flow instabilities and the vortex rope are responsible for many undesirable operating characteristics including efficiency reduction, noise, vibrations, variations in power output, vertical movement of the runner, and pressure pulsations in the penstock [13]. These undesirable phenomena may occur individually or in combination in hydroelectric plants. Therefore, control or elimination of the vortex rope is necessary for improving hydropower plant efficiency and preventing structural vibrations.

Different mechanisms have been proposed to control the draft tube vortex rope. Each of these methods usually introduces additional hydraulic losses and efficiency reduction. Furthermore, since there is not yet a general agreement on the main causes that lead to self-induced instabilities in a swirling flow, the practical solutions sometimes have mixed results. These solutions are nearly as numerous as the number of field problems, as each situation is unique. Bhan et al. [153] investigated several different cases of the draft tube surge and noted that, “in general, no single solution can be guaranteed to eliminate draft tube surge problems.”

Fins mounted on the draft tube wall have shown to be effective in reducing the amplitude of the pressure fluctuations in many cases [154]. The idea is to decrease the swirl in the draft tube cone. Nishi et al. [154] performed experimental investigations to clarify the effects of fins on draft tube surge by analyzing wall pressure fluctuations. It was shown that installation of fins to the draft tube wall can be useful to broaden the operating range of a Francis turbine. However, usage of fins beyond the limit of their applicability would be unfavorable due to their enhancement of instabilities. The disadvantages of fins are significant losses in efficiency, being subjected to cavitation erosion, and structural vibrations [155]. Flow splitters are the fins that extend far enough into the flow to touch each other [155]. They have similar applications and advantages/disadvantages as fins. Both these methods target the effects of the pressure fluctuations, rather than addressing the main cause.

Another approach used in controlling the draft tube vortex rope is to modify the runner crown cone. Modifications can be applied in the form of the cone extension [156], grooved runner cone [157], or combination of both [158]. These methods do not reduce efficiency significantly as in the case of fins, however, they may cause large lateral forces on the turbine shaft arising from pressure pulsations in the draft tube which act on the runner cone extension. Nevertheless, these solutions are obviously acceptable only for a narrow range of operating regimes. Outside this range, the non-adjustable geometrical corrections have adverse effects.

One of the most widely used methods to reduce the amplitude of the pressure fluctuations by the vortex rope is the admission of air into the runner or draft tube [159]. Air can be admitted in several locations including the spiral case, the annular chamber between the wicket gates and the runner, the draft tube wall, the runner band, the runner crown cone, or a snorkel attached to the runner cone [155, 159, 160, 161, 162]. Both the location and the quantity of air have significant effects on the efficiency of the unit. For high tailwater units, where the most severe pulsations occur [155], compressed air must be injected into the draft tube since the pressure below the runner is more than the atmospheric pressure. Therefore, the technical solution for the admission of air may be costly [163].

Susan-Resiga et al. [164] and Zhang et al. [37] stated the main requirements and guidelines for a successful vortex rope control technique. They are obtained by assessment of various previous methods for the draft tube surge [164], and analysis of the numerical solutions [37]. These guidelines can be summarized as follows

- The control should address the cause of the vortex rope formation, rather than just its effects such as pressure fluctuations and structural vibrations.
- The vortex rope should be controlled at the inlet of the draft tube.
- The method should focus on the stagnant region near the axis of the draft tube rather than the swirl near the wall.
- The method should not affect the efficiency of the machine when operating at or near the best efficiency point.
- The control technique should not result in considerable reduction in the machine efficiency.

Analysis of the vortex rope formation performed in Sec. 4.4 and 6.2.3 confirmed that the development of the vortex rope is associated with formation of a stagnant region at the center of the draft tube. The shear layer resulting from high velocity gradients between the wake or the stagnant region and highly swirling outer flow near the centerline of the draft tube results in formation of the precessing vortex rope. This also has been shown by previous experimental and numerical investigations [27, 37]. Therefore, it can be concluded that a successful control technique should focus on dealing with the stagnant flow region in the center of the draft tube. Adding an extension to the runner crown cone [156] is one of the methods developed based on this principle. It is a passive flow control by solid means, where the runner crown extension displaces a portion of the stagnant flow region in the draft tube. This control technique leads to a favorable effect. However, since the possible size of the crown cone is limited, it can only partially eliminate the strong pressure fluctuations. It also decreases the flow area, and thereby reduces the effect of the draft tube in recovering the pressure. In addition, since this is a passive control method, it is not possible to adjust it for different operating conditions. Alternative to solid means, one may introduce a fluid flow into the draft tube to counteract the stagnant (and reversed) flow there. The air admission through the runner crown tip is actually a weak form of this kind of control [159].

In this study a water jet injection is considered which should be far more effective due to high momentum flux values. Furthermore, the technical solution for producing the water jet at the crown tip (nose cone) takes advantage of the hollow turbine shaft and a high-pressure water supply from upstream of the turbine spiral case. Therefore, this method does not alter the geometry of the turbine water passage, and does not use any pumps, although for fine adjustments the use of a pump may be considered. This is a so-called active control technique, as it can be adjusted for different operating conditions. At the best efficiency point (BEP) or when machine is operating as a pump, the water jet can be completely shut off, and since there are no appendages inside the draft tube, the efficiency of the machine remains unchanged. This active control technique has been first introduced by Susan-Resiga et al. [164] (although it was inferred independently in this study by numerical simulations), and later experimentally investigated by Bosioc et al. [165] and Tănasă et al. [166]. The main idea is to increase the momentum of the stagnant flow in the centerline of the draft tube and to eliminate the high velocity gradients, which result in formation of the shear layer and helical vortex rope. This is investigated numerically in this chapter.

7.2 Methodology and Approach

In this section, the water jet injection technique for controlling the vortex rope is investigated for the case of the simplified draft tube introduced in chapter 4 (see Fig. 7.1). The operating points of interest are associated with case C and case D (see Table 3.2). They have the same head coefficient of ψ=1.18 and different flow rate coefficients (discharge coefficients) of φ=0.34 (case C) and 0.26 (case D), corresponding to 91% and 70% of the BEP flow rate respectively. The same geometry and grid as in chapter 4 are used. Again, both axisymmetric and three-dimensional grids are considered for a simplified, axisymmetric draft tube geometry. The 2D axisymmetric computational domain corresponding to the meridian half-plane is discretized by 120,000 structured grids, and the 3D computational domain consists of 2,028,000 structured cells. In both cases reduced-size grids are used near the wall and the center of the draft tube.

The effect of an injected water jet is taken into account by modifying the inlet velocity profiles. Since the present computational domain starts from a section downstream of the runner outlet where the jet is injected, as shown in Fig. 7.2, the velocity profiles induced at the inlet section by a jet issued from the runner crown cone located upstream should be estimated. It is assumed that no extra pump is used for injecting water and the control jet is supplied by a bypass line from upstream of the spiral case right after the penstock, through the turbine shaft, to a nozzle attached to the runner crown cone.

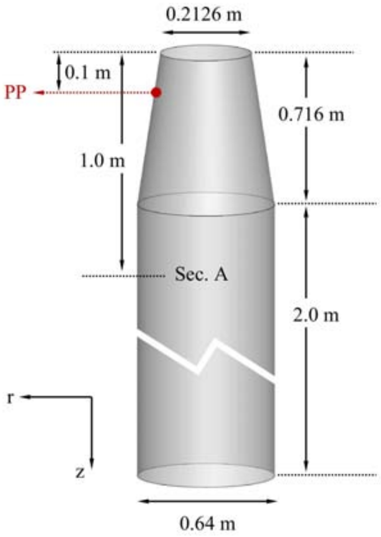

Figure 7.1: Computational domain for the simplified draft tube used in investigations of the vortex rope control technique. Wall pressure is monitored at point PP, with results being shown in Fig. 7.8.

As a result, the jet velocity depends on the turbine head which is constant for both investigated cases

$$V_{\mathrm{jet}} \approx \sqrt{2g\,(H-h_l)} = \zeta\sqrt{2gH} \tag{7.1}$$

where h_l represents the hydraulic losses through the penstock and bypass line and ζ is the total loss coefficient of the tube supplying the jet. For penstock length less than three times the head, the total hydraulic losses (including those of the trash rack, intake, and bend losses) do not exceed 1% of the turbine head [167]. The total losses in the bypass line including major losses in the pipeline system and minor losses within the nozzle, bends, and a regulating valve are estimated to be around 10% of the turbine head H, assuming a rational configuration for the bypass line. Therefore, the loss coefficient is assumed to be $\zeta \approx \sqrt{0.89} = 0.94$. It should be noted that jet velocity exiting the nozzle does not depend on the flow rate through the turbine, but only on the turbine head. Therefore, the jet discharge (flow rate) can be adjusted by changing the jet radius (i.e., by using a needle-controlled nozzle) since

$$Q_{\mathrm{jet}} = \pi R_{\mathrm{jet}}^2 V_{\mathrm{jet}} \tag{7.2}$$

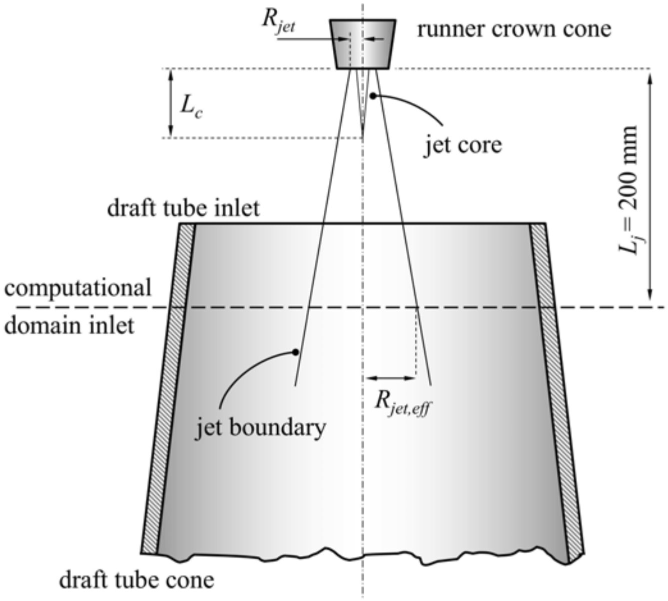

Figure 7.2: Water jet injection from the runner crown cone into the draft tube.

Several jet radius values are considered in the range of 3 mm to 9 mm for case C and 10 mm to 17 mm for case D. Jet radii are chosen to be in the range of 0.1 to 0.5 times the runner crown tip radius of 34 mm.

Knowing the radius and velocity of the jet injected from the runner crown cone, jet velocity profiles at the inlet to the computational domain located 200 mm downstream (see Fig. 7.2) are estimated based on the correlations presented by Rajaratnam [168]. As shown in Fig. 7.2, one can divide the jet flow into two distinct regions: a region of undiminished mean velocity close to the nozzle, known as the jet potential core, and a surrounding mixing layer developing radially along the axis. Farther downstream, the mixing region penetrates towards the axis, and the potential core disappears. The distance between the nozzle and the point where the potential core vanishes is known as the jet core length, which is given by [168]

$$L_c \approx 10.5 R_{\text{jet}} \tag{7.3}$$

Therefore, the longest jet core length corresponds to the maximum considered jet radius ($R_{\text{jet}} = 17$ mm), which is $L_c \approx 178.5$ mm. This length is still smaller than the distance between the nozzle and the inlet section, i.e., $L_j = 200$ mm. Hence, the jet flow is considered to be fully developed for all conditions investigated in this paper.

Nevertheless, assuming that the jet is discharged from a "long" supply pipe, the potential core would have disappeared and the exiting flow can be considered as fully developed. The fully developed jet extends radially, following a linear correlation [168]

$$R_{\text{jet},z} = \left[1.04 + 0.16\frac{z}{R_{\text{jet}}}\right] R_{\text{jet}} \tag{7.4}$$

Therefore the effective jet radius at the inlet section to the computational domain ($z = L_j$) can be expressed as

$$R_{\text{jet,eff}} = \left[1.04 + \frac{32}{R_{\text{jet}}}\right] R_{\text{jet}}\,(\text{mm}) \tag{7.5}$$

The radial distribution of the axial jet effective velocity for a fully developed jet (outside the potential core) is approximated by [168]

$$\frac{V_{\text{jet,eff}}(r)}{V_m} = \begin{cases} \frac{1}{2}\left[1 + \cos\left(\frac{\pi r}{R_{\text{jet,eff}}}\right)\right] & r < R_{\text{jet,eff}} \\ 0 & r \geq R_{\text{jet,eff}} \end{cases} \tag{7.6}$$

where V_m is the maximum velocity at the jet axis, which initially remains constant within the potential core then decreases as [168]

$$V_m = V_{\text{jet}}\frac{L_c}{z}, \quad (z \geq L_c) \tag{7.7}$$

The modified axial velocity profile, including the effects of jet injection, is obtained by adding the jet effective velocity profile $V_{\text{jet,eff}}$ to the main axial velocity without jet injection. However, the effect of jet entrainment should also be taken into account, which decreases the main axial velocity. Therefore, the modified axial velocity is approximated by [168]

$$V_{z,\text{mod}}(r) = V_z(r)\left[1 - (\alpha - 1)\frac{Q_{\text{jet}}}{Q}\right] + V_{\text{jet,eff}}(r) \tag{7.8}$$

where $V_z(r)$ is the axial velocity profile without jet injection and α is the ratio between the jet flow rate calculated by integrating Eq.(7.6), and the correct jet flow rate (Eq.(7.2)) and is called the jet entrainment coefficient [168]

$$\alpha = \frac{1}{2}\left(1 - \frac{4}{\pi^2}\right)\left(\frac{V_m}{V_{\text{jet}}}\right)\left(\frac{R_{\text{jet,eff}}}{R_{\text{jet}}}\right)^2 \tag{7.9}$$

Therefore, the total discharge associated with the modified axial velocity profile (Eq.(7.8)) is equal to $Q + Q_{\text{jet}}$ and is independent of the location of the nozzle.

Figure 7.3 compares the axial velocity profiles at the inlet section for cases C and D with and without water jet injection. Velocity profiles at three different jet radius values (3, 6, and 9 mm for case C, and 10, 15, and 17 mm for case D) are compared. It can be seen that the main effect of the jet is to increase the velocity near the centerline and reduce the wake of the crown cone. Away from the centerline the cases with jet injection show a little lower axial velocity. As discussed above, this is due to the fact that the jet entrains the surrounding fluid as it travels forward, which in turn slows down the outer main flow [168]. All simulations are performed with the same circumferential velocity profiles (identical to one without jet injection).

7.3 Results and Discussion

Steady axisymmetric simulations are performed in order to investigate the effects of jet injection on stagnant region and draft tube performance. The two-equation standard k-ε turbulence model with two-layer zonal model for near wall treatment is used in steady simulations. Unsteady, 3D simulations are also performed with the objective of studying water jet injection effects on the vortex rope formation and its unsteady behavior. As shown in chapter 4, URANS models cannot predict the unsteady features of the vortex rope correctly. Therefore, in this section, detached eddy simulation (DES) model [83] is used for unsteady simulations.

7.3.1 Steady Axisymmetric Simulations

Figure 7.4 shows the streamline patterns in the meridian half-plane obtained from steady axisymmetric simulations with different jet radius values for both case C and D. As discussed in Sec. 4.2, the stagnant region at the center of the draft tube visualized by streamlines represents the formation of the vortex rope. This region is developed as a result of the flow deceleration along the axis and its size indicates the vortex rope size and strength [12]. It is seen that applying the water jet increases the axial flow momentum at the center and removes the stagnant and reverse flow region in both cases. This, in practice, can result in vortex rope elimination and flow stability. Obviously larger jet radii are associated with higher jet discharge and more reduction in the reverse flow region. Furthermore, higher jet discharges are required for case D which is farther away

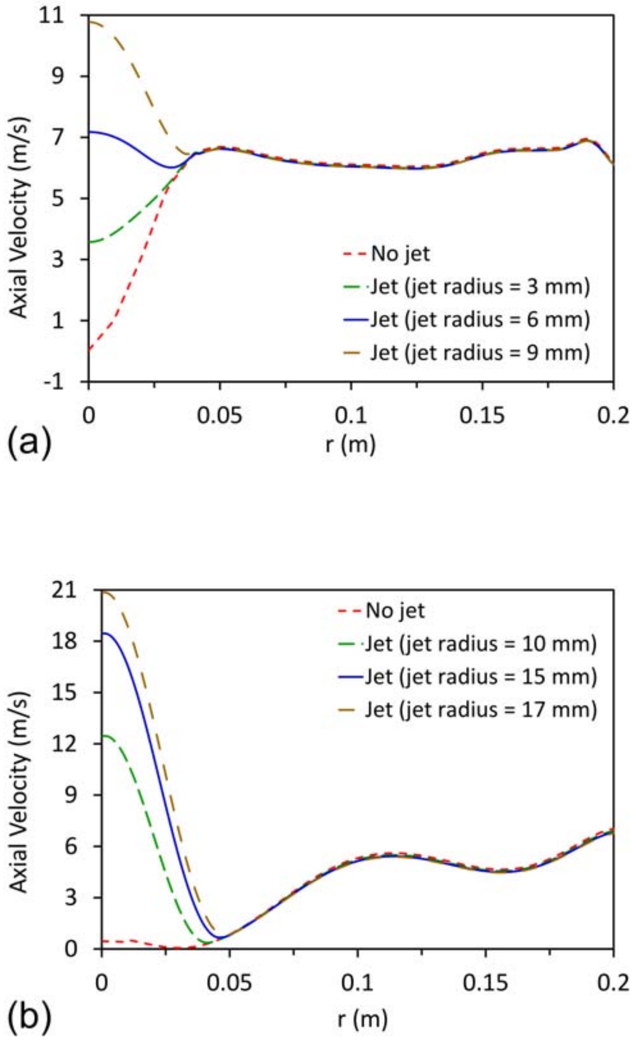

Figure 7.3: Axial velocity profiles at the inlet section to the draft tube for (a) case C and (b) case D, effect of jet injection.

from the BEP. The jet radius needed for fully eliminating the stagnant region in case D (70% of the BEP flow rate) is almost twice the one in case C (91% of the BEP flow rate).

The effect of water jet injection is also investigated quantitatively. Table 7.1 shows the draft tube performance parameters, introduced in Sec 4.2. These parameters are calculated between the inlet section and a section 1 m downstream (section A in Fig. 7.1) in the draft tube. For case C, increasing the jet radius (i.e., the jet flow rate) increases the

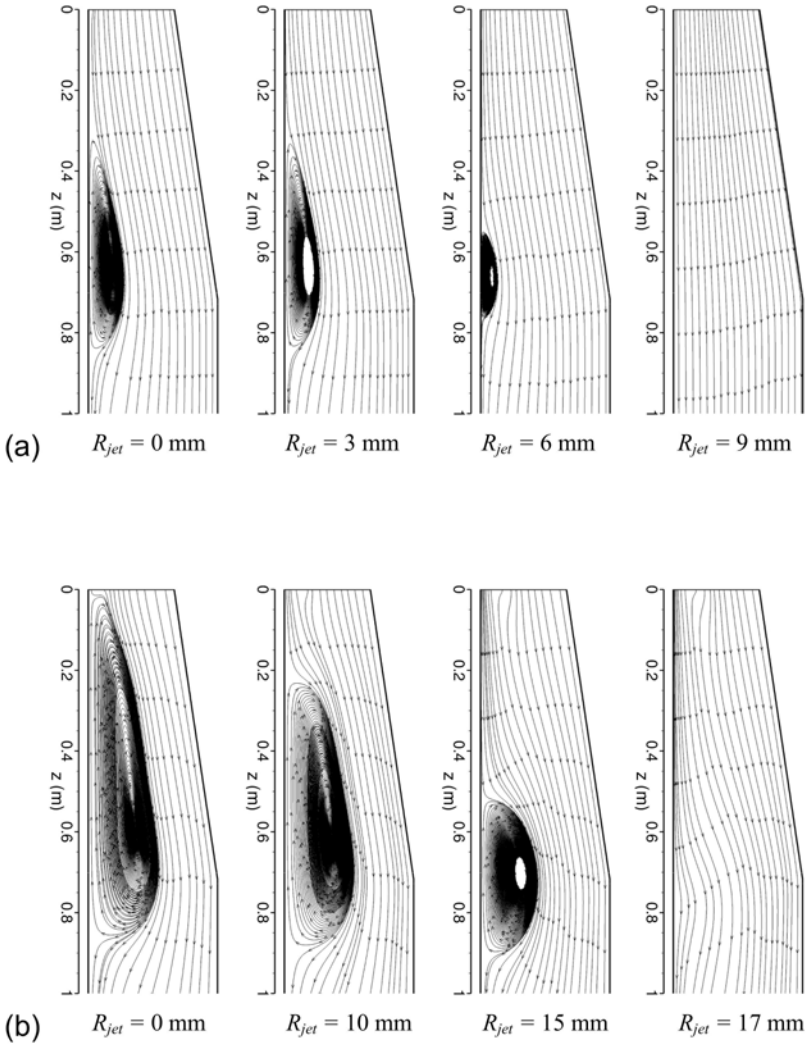

Figure 7.4: Streamline patterns for the steady axisymmetric simulation of flow in the simplified draft tube, effect of water jet injection (a) case C (91% of BEP flow rate), and (b) case D (70% of BEP flow rate).

kinetic energy and pressure recovery coefficients monotonically. This results in improving the kinetic energy-to-pressure conversion coefficient C_{cr} and reduction of the draft tube losses C_l, hence the higher efficiency. For the highest flow rate, $R_{\text{jet}} = 9$ mm, C_{cr} increases by 5%, while C_l decreases by 50%. Also it is interesting to note that even the highest jet flow rate is still less than 1% of the draft tube flow rate for this case. Case D, however, shows a different behavior due to a considerably larger stagnant region developed in the draft tube. Low jet discharges have negligible or even reverse effects on the kinetic energy and pressure recovery coefficients. It can be seen that a water jet with at least 15 mm radius is needed to obtain an improvement in the kinetic energy-to-pressure conversion coefficient. For the highest flow rate, $R_{\text{jet}} = 17$ mm, C_{cr} shows as much as 11% improvement, while C_l decreases by 14%.

Table 7.1: Draft tube performance parameters calculated between inlet section and a section 1 m downstream (Section A in Fig. 7.1). The effect of jet injection is studied by changing the jet radius. Maximum possible jet radius, i.e., the runner crown tip radius, is 34 mm.

Case C				
	No jet	R_{jet}=3 mm	R_{jet}=6 mm	R_{jet}=9 mm
$Q_{jet}/Q(\%)$	0	0.072	0.288	0.648
C_{kr}	0.7114	0.7114	0.7329	0.7668
C_{pr}	0.6465	0.6502	0.6922	0.7342
C_{cr}	0.9088	0.9140	0.9444	0.9575
C_l	0.0649	0.0612	0.0407	0.0326

Case D				
	No jet	R_{jet}=10 mm	R_{jet}=15 mm	R_{jet}=17 mm
$Q_{jet}/Q(\%)$	0	1.044	2.349	3.017
C_{kr}	0.6747	0.6561	0.6435	0.6614
C_{pr}	0.3481	0.3358	0.3589	0.3801
C_{cr}	0.5159	0.5118	0.5577	0.5747
C_l	0.3266	0.3203	0.2846	0.2813

As discussed above, no extra pump is used in this method for injecting water. Therefore, no input work to a pump, which should be considered as a loss, is needed. From the exergy viewpoint, however, the water behind the dam has the potential to flow through the turbine and generate electricity. So for power generation, the flux used for injection is an exergy loss since it is bypassed and injected in the draft tube instead of being allowed to flow through the turbine. Figure 7.5 shows these losses for case C and D. For each case the draft tube hydraulic losses are the difference between total mechanical energy of the flow in the draft tube ($\Delta E = E(z) - E(0)$), and the losses of exergy are equal to the power associated with the water jet ($P_{\text{jet}} = \rho g H Q_{\text{jet}}$). The total losses are the summation of these two losses. All these parameters in Fig. 7.5 are normalized by the turbine power ($\rho g H Q$). As shown in Fig. 7.5(a) for case C (91% of BEP flow rate), the draft tube hydraulic losses decreases with increasing jet radius due to elimination of the vortex rope. On the other hand, the losses in exergy increase since the flow rate (and, hence, power) associated with the water jet increases by increasing the jet radius. As a result, the summation of these two, the total losses, reaches a minimum value which occurs at around $R_{\text{jet}} = 6.5$ mm in this case. Total losses for this condition are about 13% lower than the case with no jet injection. Therefore, the optimum jet radius, associated with the minimum total losses, is found to be 6.5 mm for case C with 91% of BEP flow rate. The fraction of water used for injection in this case is only about 0.3% of the total flow rate. Results for case D (70% of BEP flow rate) are shown in Fig. 7.5(b). The maximum reduction, about 5%, in draft tube losses are achieved by R_{jet} = 15 mm, while higher jet flow rates show inverse effects and result in increasing losses. In order to eliminate the considerably larger stagnant region in case D, higher jet flow rates are required, which in turn increase the losses in exergy significantly more than case C, as shown in Fig. 7.5(b). Therefore, total losses in this case do not show a minimum value, as in case C. It should be noted, however, that in the case with 70% of BEP flow rate, a large vortex rope develops in the draft tube and severe pressure fluctuations and structural vibrations occur. Therefore, the first priority in this case is to suppress these fluctuations.

7.3.2 Unsteady 3D Simulations

Unsteady, three-dimensional simulations are performed using DES turbulence model and R_{jet} = 6.5 mm and 10 mm for case C and case D respectively. As discussed above, R_{jet} = 6.5 mm is associated with minimum total losses in draft tube for case C. No such optimum jet radius is found for case D, therefore, the minimum jet radius required to mitigate the vortex rope pressure fluctuations is chosen (R_{jet} = 10 mm). This value corresponds to the jet-to-turbine flow rate of about 1% (see Table 7.1).

Figure 7.6 shows the instantaneous axial velocity contours on the meridian plane in draft tube with and without jet injection. It is seen that for cases without jet injection a relatively large region of reverse flow (dark region) develops within the center of the draft tube. The stagnant region visualized by flow streamlines in Fig. 7.6 resembles the mean, circumferentially-averaged location of these reverse flow regions in time. Obviously case D has relatively larger reverse flow region due to lower flow rate and higher swirl resulting in a stronger shear layer. In cases with water jet injection, axial momentum of flow is increased at the center and this region is reduced in size considerably. The effectiveness of this control technique becomes more obvious by comparing isopressure surfaces in the draft tube. As discussed in Sec. 4.4, these surfaces can represent the vortex rope in the draft tube. Figure 7.7 includes a sequence of figures showing the isopressure surfaces in the draft tube as well as the axial velocity contours (the darker the color, the higher the axial velocity) on the meridian plane. The sequence starts at the onset of jet injection (top left) and continues to the final frame (bottom right) where the water jet is

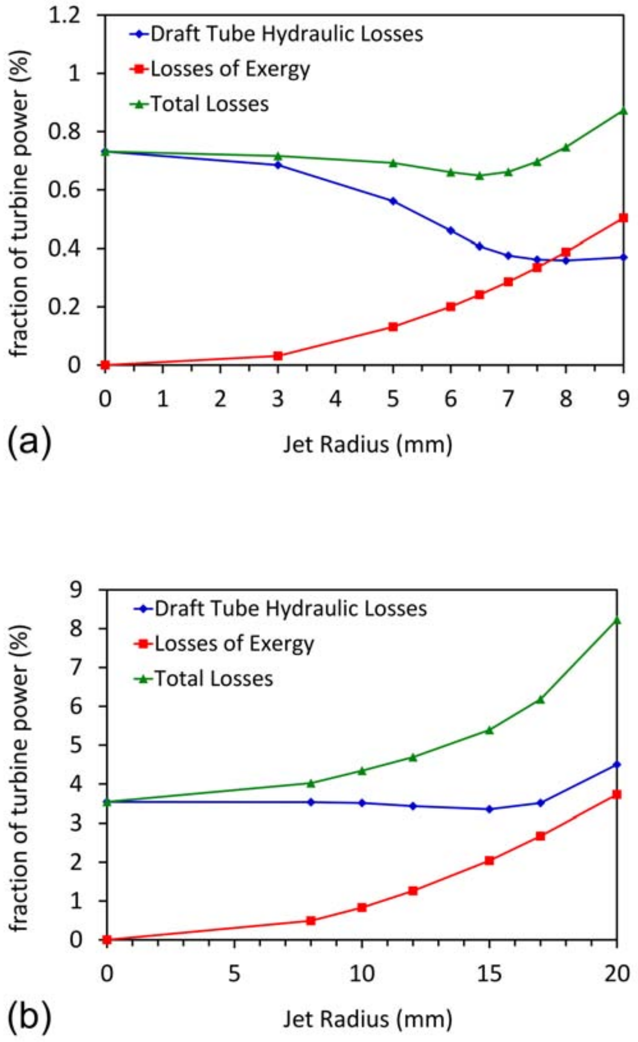

Figure 7.5: Losses in the draft tube for (a) case C and (b) case D as a function of the jet radius.

completely developed. The time between each frame is 0.083 s. It is seen that without jet injection a relatively large vortex rope exists in the draft tube wrapped around a low axial velocity (light color) region. When the water jet is applied, the axial velocity (flow momentum) within the center of the draft tube increases (see the darker color at the center), therefore, the velocity gradients within the free shear layer between the stagnant region and outer flow decrease. This reduces the potential that the shear layer would roll up and form the vortex rope; hence, the vortex strength is weakened and the rope is practically eliminated. However, some low pressure pockets are still seen in the flow.

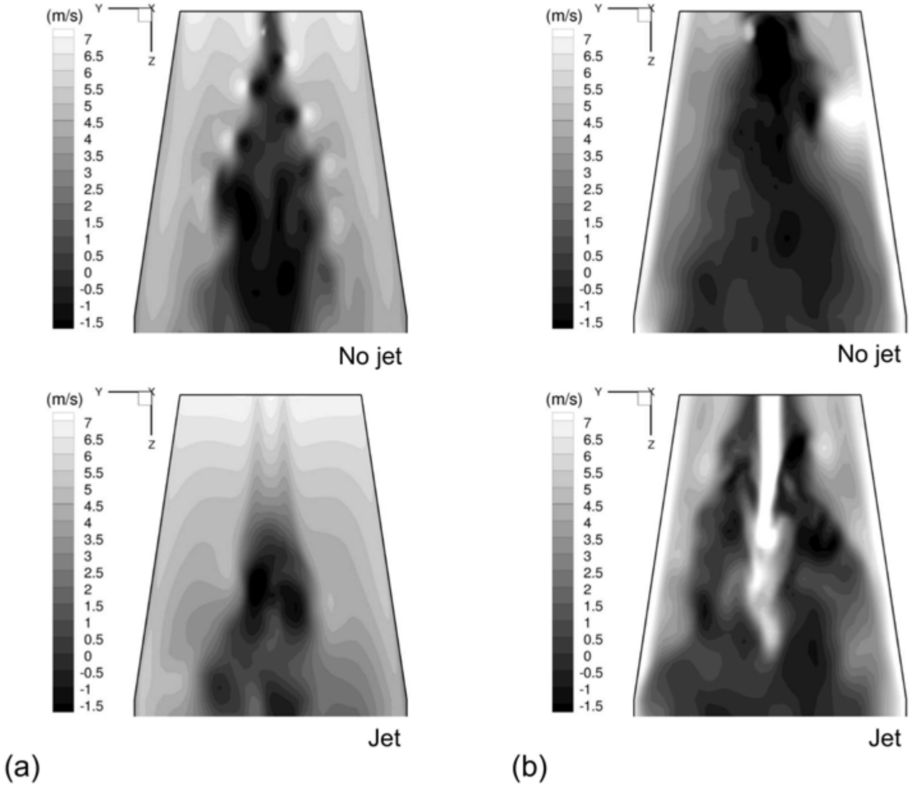

Figure 7.6: Contours of instantaneous axial velocity showing the stagnant region and vortex rope for (a) case C (91% of BEP flow rate), and (b) case D (70% of BEP flow rate) with and without water jet injection.

The effect of water jet injection on the pressure fluctuations in the draft tube (point PP in Fig. 7.1) is investigated by unsteady simulations of case D and results are shown in Fig. 7.8. As discussed previously in Sec. 4.4, vortex rope formation results in low frequency, high amplitude pressure fluctuations. By applying a water jet one can eliminate the vortex rope and, thus, significantly reduce the pressure fluctuations amplitude as seen in Fig. 7.8. The peak-to-peak amplitude of pressure fluctuations decreases from about 9,000 Pa to about 3,000 Pa in this case. Furthermore, the dominant frequency of fluctuations is altered. It is specifically important to move the dominant frequency of the pressure fluctuations far away from the natural frequency of the power-plant structure.

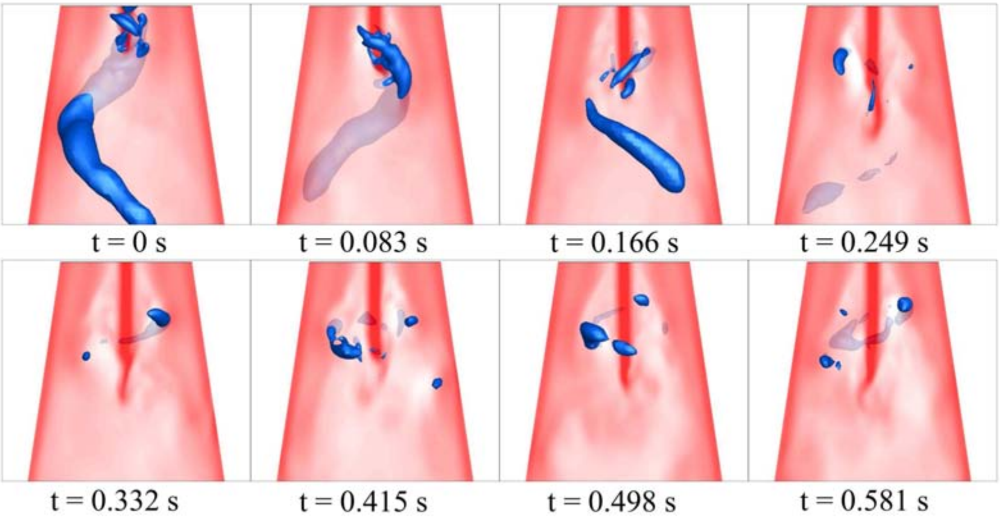

Figure 7.7: Time evolution of the controlled draft tube flow by water jet injection showing the reduction and elimination of the vortex rope (top left to bottom right).

7.4 Summary

Numerical simulations and investigation of a method for mitigation of the vortex rope formation in draft tubes are discussed in this chapter. As shown in the previous chapters, formation of the vortex rope is associated with a large stagnant region at the center of the draft tube. Therefore, it is concluded that a successful control technique should focus on the elimination of this region. In practice, this can be performed by axially injecting a small fraction (few percent of the total flow rate) of water into the draft tube. The water jet is supplied from the high pressure flow upstream of the turbine spiral case by a bypass line; thus, no extra pump is needed in this method. It is shown that this method is very effective in elimination of the stagnant region in a simplified draft tube operating at two part-load conditions, i.e., at 91% and 70% of the BEP flow rate. This results in improvement of the draft tube performance and reduction of hydraulic losses. The loss coefficient is reduced by as much as 50% for the case with 91% of BEP flow rate and 14% for the case with 70% of BEP flow rate. Unsteady 3D simulations show that the jet increases the axial momentum of flow at the center of the draft tube and decreases the wake of the crown cone, and thereby decreases the shear at the interface of the stagnant region and high velocity outer flow, which ultimately results in mitigation of the vortex rope. Furthermore, reduction (by about 1/3 in the case with 70% of BEP flow rate) of strong pressure fluctuations leads to reliable operation of the turbine.

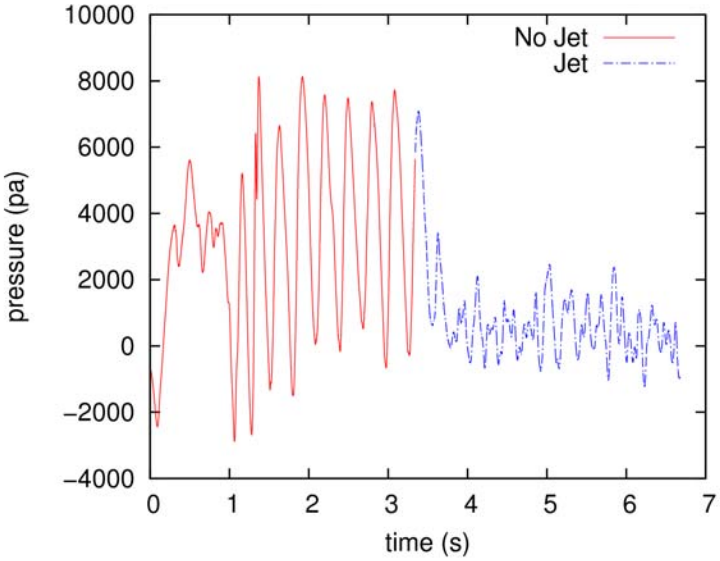

Figure 7.8: Unsteady pressure on the draft tube wall for case D, effect of water jet injection.

Chapter 8

Summary and Conclusions

"If you can't explain it simply, you don't understand it well enough." - Albert Einstein

8.1 Highlights

The core contributions and findings of the present study are as follows

- Simulation and analysis of the vortex rope formation is performed, and the physics behind it is understood.
- High fidelity numerical simulations are carried out using a wide range of turbulence models in the framework of RANS, URANS, and hybrid RANS/LES modeling.
- Three widely used RANS turbulence models, namely the standard and realizable k-ε, and the SST k-ω model are shown to be insufficient for modeling the vortex rope behavior, specially at lower flow rates.
- Turbulent kinetic energy production and diffusion is underpredicted by the above-mentioned RANS models when a strong vortex rope is formed in the draft tube.
- A new RANS turbulence model including the extra production and diffusion of the turbulent kinetic energy is developed, that can successfully model the mean flow in the draft tube when the vortex rope is formed.
- URANS models are generally not capable of resolving the self-induced unsteadiness associated with the vortex rope, therefore, hybrid RANS/LES models should be used.

- A new hybrid RANS/LES model in the framework of partially-averaged Navier-Stokes (PANS) modeling is developed for the unsteady simulation of the vortex rope.
- The new PANS model uses a new relation for the unresolved-to-total turbulent kinetic energy ratio developed in this work for the first time.
- The newly developed PANS model is validated against experimental data in a benchmark test case, namely swirling flow through a sudden expansion, and is shown to give accurate results.
- The new PANS model is used in unsteady simulations of the flow in a complete draft tube (FLINDT draft tube) for four operating conditions ranging from 70% to 110% of the BEP flow rate.
- The geometry of the FLINDT draft tube is regenerated based on data from several resources and is presented for the first time in this study.
- The PANS model developed in this study successfully predicts various draft tube flow parameters including the pressure recovery factor, mean velocity and pressure profiles, vortex rope frequency, and unsteady pressure fluctuations.
- Investigations of the wall unsteady pressure reveals that the critical region in the draft tube with the highest pressure fluctuations is located at the inner side of the elbow.
- The formation of the vortex rope is shown to be attributed to the formation of a stagnant region at the center of the draft tube; therefore, it is proposed that a vortex rope control technique should target this region.
- Centrally injecting water to the draft tube inlet is shown to be an effective method in mitigating the vortex rope formation, and in reducing hydraulic losses and pressure fluctuations due to the formation of the vortex rope.

8.2 Summary

Simulation, physical understanding, and analysis of vortex rope formation in Francis turbine draft tubes were addressed in this study using high fidelity CFD. The vortex rope is a complex three-dimensional unsteady turbulent phenomenon occurring when a hydraulic turbine operates under off-design conditions. Previous experimental and numerical studies reviewed in this dissertation have shown that formation of the vortex rope is associated with severe pressure fluctuations and even structural vibrations. The vortex rope is recognized as the main cause of flow instabilities, draft tube surge, and efficiency drop, affecting the performance of the whole hydropower plant. Therefore, its understanding and mitigation are of industrial interest. Investigations of vortex rope formation and mitigation were carried out using high fidelity numerical simulations in the present study. Specifically a vortex rope control technique, which includes injection of water from the crown tip (nose cone) to the inlet of the draft tube, was studied. Furthermore, detailed features of the vortex rope formation are shown to be difficult to predict with numerical computations, which are still widely based on the traditional RANS turbulence models. The turbulence models' limitations, however, are not well known. Hence, another objective of the present work was to understand the fundamental processes governing the formation of a vortex rope and investigating, understanding, and defining the predictive capability of the models and developing turbulence models for better prediction of vortex rope behavior.

A step-by-step systematic approach was considered in this study starting from the simplest and advancing towards the most complicated flow structure. Firstly, simulations and analysis of vortex rope formation in a simplified draft tube of a model Francis turbine operating at partial load were performed. Steady and unsteady simulations were then carried out using 2D axisymmetric and 3D computational domains for an axisymmetric geometry. Several turbulence models were used, namely standard and realizable k-ε, SST k-ω, and DES. In the case of the simplified draft tube, two part-load operating conditions with the same head and different flow rates were considered. The flow rates for these two operating points correspond to 91% of the flow rate at best efficiency point (case C) and 70% of the flow rate at best efficiency point (case D). Although they cannot capture the vortex rope, steady, 2D axisymmetric simulations can predict the occurrence and development of vortex breakdown with a central stagnant region in the draft tube. It was shown that, moving farther from the best efficiency point, the size of this stagnant region increases, which results in flow blockage and reduction of the pressure recovery coefficient. The kinetic energy recovery coefficient, pressure recovery coefficient, and kinetic energy-to-pressure conversion coefficient are reduced by 5%, 46%, and 43%, respectively, by decreasing the flow rate from case C to case D, while the loss coefficient becomes five times larger. It was shown that steady simulations for 3D and 2D axisymmetric flow geometries give identical results, underpredicting axial velocity and turbulent kinetic energy near the center of the draft tube by at least 14% and 40% for case C, respectively. Farther from the BEP, i.e., for case D, this deviation increases considerably. No considerable improvement in predictions was seen applying different turbulence models. Unsteady, three-dimensional simulations were performed in the case of the simplified draft tube in order to capture the vortex rope. It was seen that the unsteadiness of the vortex rope cannot be modeled by the URANS approach resulting in steady, symmetric solutions, while applying hybrid RANS/LES models (DES in this case), vortex rope unsteady behavior can be captured sufficiently. Using the DES turbulence model, the overall shape of the vortex rope agrees well with the experimental visualizations for the cases considered. The vortex rope frequency was found to be about 0.318 of the runner rotation frequency which shows only 6% difference compared to the experimental data.

Attention was then focused on developing a new steady RANS turbulence model in order to correctly predict the mean flow field in a draft tube operating under partial load using an axisymmetric model. The goal was to provide designers with a simulation tool (a new k-ε RANS model) that does not take too much time and storage to run, but lets them evaluate the draft tube performance. It was argued in detail that steady RANS models underpredict the turbulent kinetic energy (TKE) production and diffusion in regions of the flow where the vortex rope forms. Therefore, a new model taking into account the extra production and diffusion of TKE due to coherent structures was developed. Predictions of this new RANS model are in much closer agreement with the experimental data compared to those using the traditional RANS models.

Nevertheless, as discussed above, hybrid RANS/LES models should be used when unsteady features of the draft tube flow, such as pressure fluctuations and vortex rope frequency, are of interest. Considering this requirement, a new hybrid RANS/LES model in the framework of partially-averaged Navier-Stokes (PANS) modeling was developed. This is one the main contributions of the present study. The present model was formulated based on the extended k-ε turbulence model of Chen and Kim [133] by employing the PANS methodology. The main distinctive feature of the present model is to incorporate a newly developed relation for the unresolved-to-total turbulent kinetic energy ratio f_k, using partial integration of the complete turbulence energy spectrum. The new expression overcomes the problem of overestimating f_k and damping turbulent motions where the grid cut-off wave number is below the inertial range. It was clearly shown that the new formulation improves the predictions compared to the previously used expression for f_k. The case of a turbulent swirling flow through a sudden expansion was used to validate the results of this model. Predictions of the present PANS model were in very good agreement with experimental data, while improvements were seen comparing to the results of DDES and URANS (SST k-ω) models. Specifically, mean and rms axial and circumferential velocity profiles, as well as the reattachment length were accurately predicted. Although the DDES model also performs quite well, it overpredicts the velocity values around the reattachment point resulting in a 16% overprediction of the reattachment length. The present model predicts the reattachment length by only 1.6% error.

As the ultimate case, this newly developed PANS model was used in unsteady numerical simulations of flow in a complex elbow draft tube. The draft tube of a model Francis turbine investigated in the FLINDT project [29] was chosen for numerical studies due to the availability of accurate and detailed measured data. The geometry of the draft tube, however, was not available. Therefore, the FLINDT draft tube was reconstructed in this study compiling data from several previously published papers. To the best of author's knowledge, this is the first attempt at regenerating the FLINDT draft tube and making it available in the open literature, hence, it should be considered as one of the important contributions of this research study. In the case of the complete FLINDT draft tube, four operating conditions ranging from 110% to 70% of the BEP flow rate were considered and several parameters including the pressure recovery coefficient, mean velocity, and wall pressure obtained from the present PANS simulations were compared with those from the experimental measurements as well as those obtained from the RANS k-ε simulations. It was shown that RANS and PANS both can predict the flow behavior close to the BEP operating condition. However, RANS results deviate considerably from the experimental data as the operating condition moves away from the BEP. The pressure recovery factor predicted by the RANS k-ε model showed more than 13% overprediction for case C with 91% of BEP flow rate, while axial velocity was underpredicted by more than 64% near the centerline. In case D, with even lower flow rate (70% of BEP), the k-ε model substantially failed in predicting mean axial velocity while more than 58% difference was seen in the prediction of the recovery factor. Predictions can be improved dramatically using the present unsteady PANS simulations. Specifically, the pressure recovery factor was predicted to less than 4% deviation and mean axial velocity was calculated to less than 17% difference compared to experimental data for case C. Even for case D, with a strong vortex rope forming in the draft tube and flow being very unstable, the pressure recovery factor was predicted to only 6% difference compared to data, while considerable improvement was seen in comparison to the RANS results, although still notable underprediction was seen near the center of the draft tube. Furthermore, details of the unsteady flow field, including the unstable shear layer, the stagnant region, and the precessing helical vortex rope were captured using the unsteady PANS simulations. The vortex rope frequency was obtained by monitoring wall pressure fluctuations, and it was found to be about 0.308 of the runner rotation frequency which shows only 2.7% difference compared to the experimental data. It was shown that the formation of the vortex rope under partial load conditions results in severe pressure fluctuations with the peak-to-peak amplitude as high as 14,000 Pa. The oscillatory forces exerted on the draft tube by these fluctuations may result in structural damage. Investigations of the unsteady wall pressure revealed that the critical region in the draft tube with highest pressure fluctuations is located at the inner side of the elbow.

Using high fidelity numerical simulations results, the physical mechanism causing the formation of a vortex rope was analyzed. It was confirmed in this study that the development of the vortex rope is associated with formation of a low-velocity region at the center of the draft tube. The vortex rope forms at the shear layer between this low-velocity inner region and the swirling outer flow. Therefore, a vortex rope control technique was numerically studied, in which a small fraction of water is bypassed from upstream of the turbine spiral case and axially injected through the runner crown cone into the draft tube. The main benefits of this method are that no extra pump is needed for injecting water, and the jet flow rate can be adjusted for different operating conditions (active control). In the present study, simulations were performed in the case of the simplified draft tube for two operating conditions at partial load (cases C and D). Both steady (using a 2D axisymmetric grid) and unsteady (using a 3D grid) simulations are carried out. It was shown that applying a water jet increases the axial flow momentum at the center and removes the stagnant region in both cases, while the loss coefficient is reduced by as much as 50% for case C and 14% for case D. Several jet radii were investigated considering the total losses including draft tube hydraulic losses and the losses in exergy. An optimum jet radius corresponding to minimum total loss was found for case C. This optimized jet decreases the total losses by 13% for case C in comparison with the no jet condition. The fraction of water used for the optimum jet was less than 0.3% of the turbine discharge. Monitoring the unsteady wall pressure for case D showed that the amplitude of pressure fluctuations in the draft tube is reduced by about 1/3 by applying a water jet which eliminates the vortex rope and stabilizes the flow.

As a closing comment, the primary merit of the present study is to demonstrate how a complex, industrially interesting, and real-life problem can be studied using a systematic approach. In this approach, a complementary knowledge of fluid dynamics, turbulence physics and modeling, and numerical simulation was used to investigate the problem. The insight gained from these detailed fundamental investigations were shown to be beneficial in mitigating the problem of the vortex rope, and that is the ultimate goal from an engineering perspective.

8.3 Recommendations for Future Studies

The present study tries to address several issues related to vortex rope formation in draft tubes. In the course of this study, however, it was found that a number of other issues deserve additional investigation. In this study, only cavitation-free operating conditions are considered, and therefore, single-phase numerical simulations of the vortex rope are performed. To continue this work, multiphase simulations incorporating the effects of cavitation should be considered. These simulations should be able to show the dependence of the vortex rope frequency and pressure fluctuation amplitude on the volume of the vapor generated due to the cavitation. Numerical simulation of multiphase flows, however, poses far greater difficulties than that of single-phase flows due to interfaces between phases, and large or discontinuous property variations across these interfaces. Particularly, application of hybrid RANS/LES turbulence models in the case of a multiphase flow is challenging.

Another research orientation should concern further investigation and application of the partially-averaged Navier-Stokes (PANS) model developed in this study. The present PANS model is developed as a generic hybrid RANS/LES model; therefore, its application is not limited to the draft tube or hydroturbine simulations. Several numerical simulations for various test cases and computational grids should be performed to demonstrate the capabilities and limitations of the present model in detail.

From a more general perspective, providing more detailed publicly available experimental data should be considered. These data help in understanding the behavior of vortex rope and vortex breakdown at different operating points of the turbine, and thus, help in controlling its formation and effects. Furthermore, they are necessary to validate models and simulations. An important set of measurements are related to the inlet conditions to the draft tube. Numerical simulations of vortex rope formation usually include the draft tube with prescribed inlet boundary conditions; however, not all of the quantities at the inlet are available. Therefore, it is inevitable to have to “assume” some of these quantities (specially those related to turbulence) which would affect the solution. Detailed measurements will improve numerical simulations by eliminating these non-realistic assumptions.

Appendix A

Videos

A.1 Vortex Rope Formation Inside the FLINDT Draft Tube

This video shows the formation of a vortex rope inside the FLINDT draft tube. Iso-pressure surfaces are chosen to illustrate the vortex rope. As shown in this video, the tail of the vortex rope may impact the inner side of the elbow wall. This impact, called the "shock phenomenon", induces strong acoustic noise, pressure fluctuations, and even structural vibrations. The flow rate is 70% of the flow rate at BEP.
Note: Adobe Acrobat 6, or later, is required to play the video.

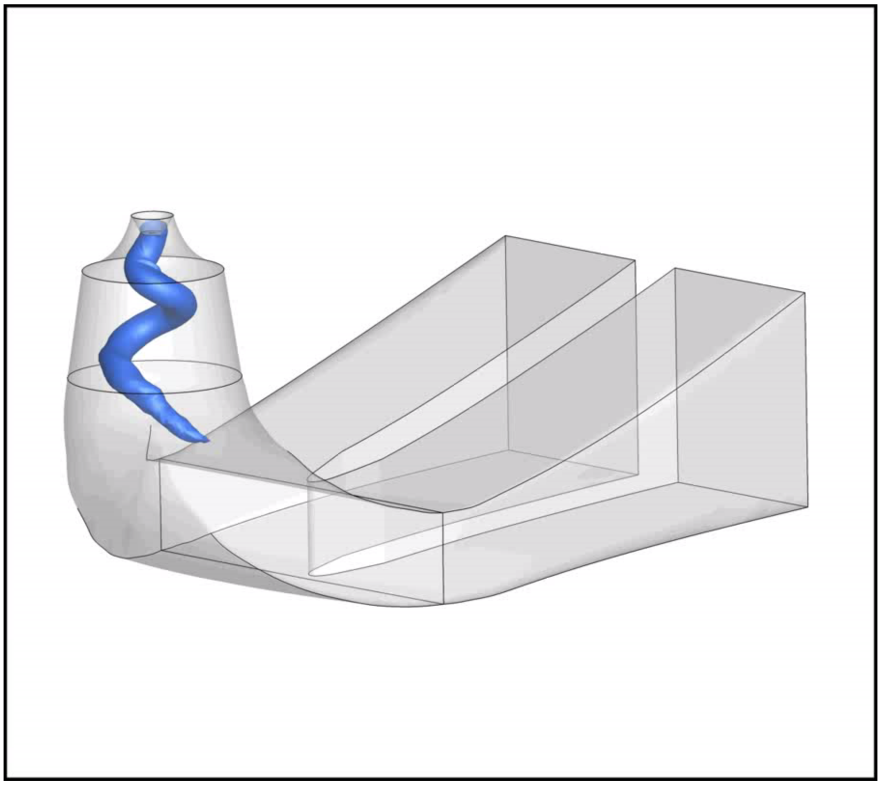

A.2 Mitigation of the Vortex Rope by Water Jet Injection

The video shows the isopressure surfaces representing the vortex rope in the draft tube (blue), as well as the axial velocity contours (red) on the meridian plane (the darker the red color, the higher the axial velocity). It is clearly seen how a water jet can eliminate the stagnant region at the center of the draft tube, and thereby control the vortex rope formation. The flow rate is 70% of the flow rate at BEP, and the jet flow rate is only about 1% of the total flow rate.

Note: Adobe Acrobat 6, or later, is required to play the video.

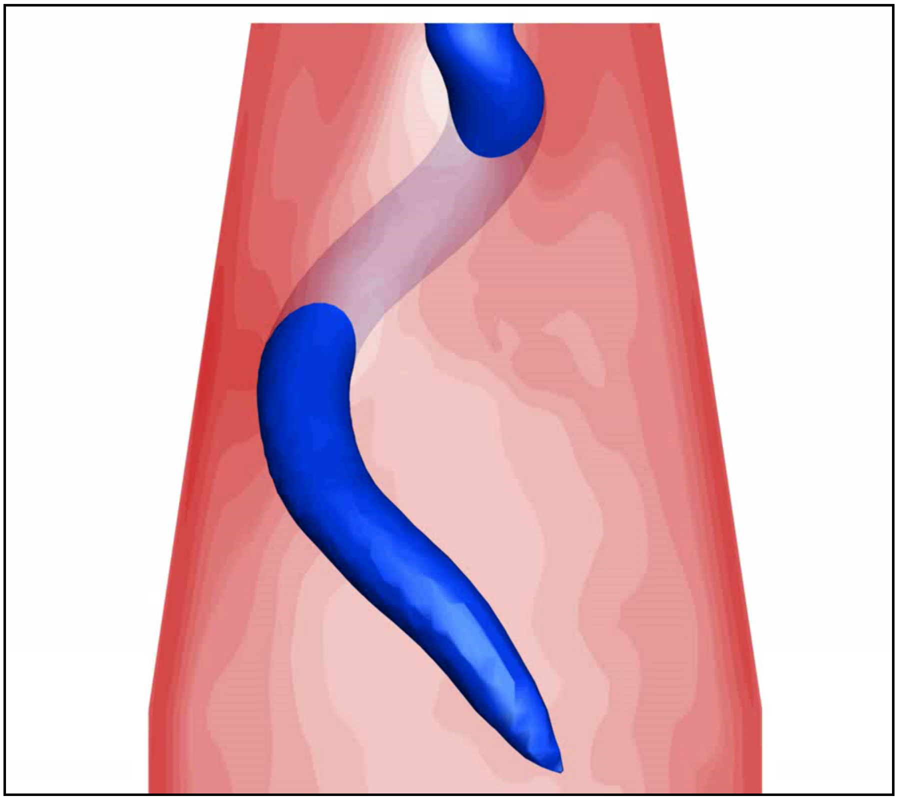

Appendix B

Publications Related to this Dissertation

The following publications are available at the time of writing this dissertation.

1. Foroutan, H. and Yavuzkurt, S., 2014, “A partially-averaged Navier-Stokes model for the simulation of turbulent swirling flow with vortex breakdown,” International Journal of Heat and Fluid Flow, Vol. 50, pp. 402-416.
2. Foroutan, H. and Yavuzkurt, S., 2014, “Flow in the simplified draft tube of a Francis turbine operating at partial load - Part I: Simulation of the vortex rope,” ASME J. Applied Mechanics, Vol. 81(6), p. 061010.
3. Foroutan, H. and Yavuzkurt, S., 2014, “Flow in the simplified draft tube of a Francis turbine operating at partial load - Part II: Control of the vortex rope,” ASME J. Applied Mechanics., Vol. 81(6), p. 061011.
4. Foroutan, H. and Yavuzkurt, S., 2012, “Simulation of flow in a simplified draft tube: turbulence closure considerations,” IOP Conf. Ser.: Earth and Environmental Science, Vol. 15, p. 022020.
5. Foroutan, H. and Yavuzkurt, S., 2013, “Partially-averaged Navier-Stokes modeling of turbulent swirling flow,” 66th Annual Meeting of the APS Division of Fluid Dynamics, Pittsburgh, PA, USA. In: Bulletin of the American Physical Society, Vol. 58, No. 18.
6. Foroutan, H. and Yavuzkurt, S., 2012, “Analysis and prevention of vortex rope

formation in the draft tube cone of a hydraulic turbine," ASME 2012 International Mechanical Engineering Congress and Exposition, Houston, TX, USA.

7. Dhiman, S., Foroutan, H., and Yavuzkurt, S., 2011, "Simulation of flow through conical diffusers with and without inlet swirl using CFD," Proceedings of ASME-JSME-KSME Joint Fluids Engineering Conference 2011, 11th Symposium on Applications in Computational Fluid Dynamics, Hamamatsu, Japan.

8. Foroutan, H. and Yavuzkurt, S., 2011, "Two applications of OpenFOAM: evaluation of k-ε models in boundary layer predictions under high free stream turbulence and simulation of the flow in simplified draft tube of a Francis turbine," 6th OpenFOAM Workshop, The Pennsylvania State University, University park, PA, USA.

Bibliography

[1] U.S. Energy Information Administration (2013) *International energy outlook 2013 (IEO2013)*, *Tech. rep.*, Office of Energy Analysis, U.S. Department of Energy.

[2] REN21 (2013) *Renewables 2013 global status report*, *Tech. rep.*, Renewable Energy Policy Network for the 21st Century.

[3] British Petroleum (2013) *BP statistical review of world energy 2013*, *Tech. rep.*, BP p.l.c.

[4] International Hydropower Association (2010) *Activity report 2010*, *Tech. rep.*

[5] Franc, J., F. Avellan, B. Belahadji, J. Billard, L. Briançon-Marjollet, D. Fréchou, D. Fruman, A. Karimi, J. Kueny, and J. Michel (1995) “La cavitation,” *Mécanismes physiques et aspects industriels. Presses Universitaires de Grenoble, Grenoble.*

[6] Subramanya, K. (2013) *Hydraulic Machines*, Tata McGraw-Hill Education.

[7] Wagner, H.-J. and J. Mathur (2011) “Introduction and Status of Hydropower,” in *Introduction to Hydro Energy Systems*, Green Energy and Technology, Springer Berlin Heidelberg, pp. 1–20.

[8] Henry, P. (1992) *Turbomachines hydrauliques: choix illustré de réalisations marquantes*, PPUR presses polytechniques.

[9] Zobeiri, A. (2009) *Investigations of time dependent flow phenomena in a turbine and a pump-turbine of Francis type: rotor-stator interactions and precessing vortex rope*, Ph.D. thesis, École Polytechnique Fédérale de Lausanne.

[10] Allligné, S. (2011) *Forced and Self Oscillations of Hydraulic Systems Induced by Cavitation Vortex Rope of Francis Turbines*, Ph.D. thesis, École Polytechnique Fédérale de Lausanne.

[11] Mauri, S. (2002) *Numerical simulation and flow analysis of an elbow diffuser*, Ph.D. thesis, École Polytechnique Fédérale de Lausanne.

[12] Susan-Resiga, R., S. Muntean, V. Hasmatuchi, I. Anton, and F. Avellan (2010) "Analysis and prevention of vortex breakdown in the simplified discharge cone of a francis turbine," *Journal of Fluids Engineering*, **132**(5), p. 051102.

[13] Dörfler, P., M. Sick, and A. Coutu (2013) *Flow-Induced Pulsation and Vibration in Hydroelectric Machinery*, Springer.

[14] Palde, U. (1972) *Influence of draft tube Shape on Surging Characteristics of Reaction Turbines*, *Tech. Rep. REC-ERC-72-24*, Hydraulics Branch, Division of General Research, Engineering and Research Center, US Department of the Interior, Bureau of Reclamation.

[15] Hall, M. (1972) "Vortex breakdown," *Annual Review of Fluid Mechanics*, **4**(1), pp. 195–218.

[16] Sarpkaya, T. (1971) "On stationary and travelling vortex breakdowns," *Journal of Fluid Mechanics*, **45**(03), pp. 545–559.

[17] Harvey, J. (1962) "Some observations of the vortex breakdown phenomenon," *Journal of Fluid Mechanics*, **14**(04), pp. 585–592.

[18] Cassidy, J. J. and H. T. Falvey (1970) "Observations of unsteady flow arising after vortex breakdown," *Journal of Fluid Mechanics*, **41**(04), pp. 727–736.

[19] Faler, J. H. and S. Leibovich (1977) "Disrupted states of vortex flow and vortex breakdown," *Physics of Fluids*, **20**, pp. 1385–1400.

[20] Brücker, C. and W. Althaus (1992) "Study of vortex breakdown by particle tracking velocimetry (PTV)," *Experiments in Fluids*, **13**(5), pp. 339–349.

[21] Benjamin, T. B. (1962) "Theory of the vortex breakdown phenomenon," *Journal of Fluid Mechanics*, **14**(04), pp. 593–629.

[22] Hall, M. (1967) "A new approach to vortex breakdown," in *Proceedings of Heat Transfer Fluid Mech. Inst*, pp. 319–340.

[23] Prenat, J. E., T. Jacob, and G. Angelico (1994) "Unstable part-load operation of a model Francis turbine: evaluation of disturbance magnitude," in *Proceedings of the 17th IAHR Symposium on Hydraulic Machinery and System (Beijing, China)*, pp. 933–942.

[24] Susan-Resiga, R., G. D. Ciocan, I. Anton, and F. Avellan (2006) "Analysis of the swirling flow downstream a Francis turbine runner," *Journal of Fluids Engineering*, **128**(1), pp. 177–189.

[25] Kuibin, P., V. Okulov, R. Susan-Resiga, and S. Muntean (2010) "Validation of mathematical models for predicting the swirling flow and the vortex rope in a Francis turbine operated at partial discharge," in *IOP Conference Series: Earth and Environmental Science*, vol. 12, p. 012051.

[26] Susan-Resiga, R., S. Muntean, F. Avellan, and I. Anton (2011) "Mathematical modelling of swirling flow in hydraulic turbines for the full operating range," *Applied Mathematical Modelling*, **35**(10), pp. 4759–4773.

[27] Nishi, M., S. Matsunaga, T. Kubota, and Y. Senoo (1982) "Flow regimes in an elbow-type draft tube," in *Proceedings of the 11th IAHR Symposium on Hydraulic Machinery and System (Amsterdam, Netherlands)*, pp. 1–13.

[28] ——— (1984) "Surging characteristics of conical and elbow type draft tubes," in *Proceedings of the 12th IAHR Symposium on Hydraulic Machinery and System (Stirling, Scotland)*, pp. 272–283.

[29] Avellan, F. (2000) "Flow investigation in a Francis draft tube: the FLINDT project," in *Proceedings of the 20th IAHR Symposium on Hydraulic Machinery and System (Charlotte, NC, USA)*.

[30] Arpe, J., C. Nicolet, and F. Avellan (2009) "Experimental evidence of hydroacoustic pressure waves in a Francis turbine elbow draft tube for low discharge conditions," *Journal of Fluids Engineering*, **131**(8), p. 081102.

[31] Ciocan, G. D., F. Avellan, and J.-L. Kueny (2000) "Optical measurement techniques for experimental analysis of hydraulic turbines rotor-stator interaction," in *Proceedings of the ASME Fluids Engineering Division Summer 2000 Meeting (Boston, MA, USA)*.

[32] Iliescu, M. S., G. D. Ciocan, and F. Avellan (2008) "Analysis of the cavitating draft tube vortex in a Francis turbine using particle image velocimetry measurements in two-phase flow," *Journal of Fluids Engineering*, **130**(2), p. 021105.

[33] Nishi, M. and S. Liu (2013) "An Outlook on the Draft-Tube-Surge Study," *International Journal of Fluid Machinery and Systems*, **6**(1), pp. 33–48.

[34] Miyagawa, K., K. Tsuji, J. Yahara, and Y. Nombra (2002) "Flow instability in an elbow draft tube for a Francis pump-turbine," in *Proceedings of the 21st IAHR Symposium on Hydraulic Machinery and Systems (Lausane, Switzerland)*, pp. 277–286.

[35] Sick, M., P. Doerfler, W. Michler, M. Sallaberger, and A. Lohmberg (2004) "Investigation of the draft tube vortex in a pump-turbine," in *Proceedings of the 22nd IAHR Symposium on Hydraulic Machinery and Systems (Stockholm, Sweden)*.

[36] Ciocan, G. D., T. C. Vu, F. Avellan, B. Nennemann, and M. S. Iliescu (2007) "Experimental study and numerical simulation of the FLINDT draft tube rotating vortex," *Journal of Fluids Engineering*, **129**(2), pp. 146–158.

[37] Wu, J.-Z., S.-Y. Chen, Y.-L. Wu, R.-k. Zhang, F. Mao, and S.-H. Liu (2009) "Characteristics and control of the draft-tube flow in part-load Francis turbine," *Journal of Fluids Engineering*, **131**(2), p. 021101.

[38] Vu, T., C. Devals, Y. Zhang, B. Nennemann, and F. Guibault (2011) "Steady and unsteady flow computation in an elbow dr aft tube with experimental validation," *International Journal of Fluid Machinery and Systems*, **4**(1), pp. 85–96.

[39] Yaras, M. and A. Grosvenor (2003) "Evaluation of one-and two-equation low-Re turbulence models. Part IAxisymmetric separating and swirling flows," *International Journal for Numerical Methods in Fluids*, **42**(12), pp. 1293–1319.

[40] Ware, A. (1999) *Evaluation of computational fluid dynamics codes and turbulence models for draft tubes*, Master's thesis, The Pennsylvania State University.

[41] Skotak, A. (2000) "Of the helical vortex in the turbine draft tube modeling," in *Proceedings of the 20th IAHR Symposium on Hydraulic Machinery and System (Charlotte, NC, USA)*.

[42] Ruprecht, A., T. Helmrich, T. Aschenbrenner, and T. Scherer (2002) "Simulation of vortex rope in a turbine draft tube," in *Proceedings of the 21st IAHR Symposium on Hydraulic Machinery and Systems (Lausane, Switzerland)*, pp. 259–266.

[43] Paik, J., F. Sotiropoulos, and M. J. Sale (2005) "Numerical simulation of swirling flow in complex hydroturbine draft tube using unsteady statistical turbulence models," *Journal of Hydraulic Engineering*, **131**(6), pp. 441–456.

[44] Gyllenram, W. and H. Nilsson (2008) "Design and validation of a scale-adaptive filtering technique for LRN turbulence modeling of unsteady flow," *Journal of Fluids Engineering*, **130**(5), p. 051401.

[45] Jošt, D. and A. Lipej (2011) "Numerical prediction of non-cavitating and cavitating vortex rope in a Francis turbine draft tube," *Strojniski Vestnik/Journal of Mechanical Engineering*, **57**(6).

[46] Jester-Zuerker, R., A. Jung, and M. Maiwald (2012) "Evaluation of a Francis turbine draft tube flow at part load using hybrid RANS-LES turbulence modelling," in *IOP Conference Series: Earth and Environmental Science*, vol. 15, p. 062010.

[47] Brennen, C. E. (1995) *Cavitation and Bubble Dynamics*, Cambridge University Press.
URL `http://authors.library.caltech.edu/25017/4/chap7.htm`

[48] Vu, T. C., M. Koller, M. Gauthier, and C. Deschênes (2010) "Flow simulation and efficiency hill chart prediction for a Propeller turbine," in *IOP Conference Series: Earth and Environmental Science*, vol. 12, p. 012040.

[49] Falvey, H. (1989) "The anatomy of a steady oscillatory flow problem," in *4th meeting of the IAHR of the work group on the behavior of hydraulic machinery under steady oscillatory conditions (Fort Collins, CO, USA)*.

[50] Speziale, C. (1998) "Turbulence modeling for time-dependent RANS and VLES: a review," *AIAA Journal*, **36**(2), pp. 173–184.

[51] Germano, M. (1992) "Turbulence: the filtering approach," *Journal of Fluid Mechanics*, **238**, pp. 325–336.

[52] ANSYS Inc. (2010) *ANSYS FLUENT 13.0 User's Guide*.

[53] Silicon Graphics International Corp. (2004) *OpenFOAM: The open source computational fluid dynamics (CFD) toolbox*.
URL `http://www.openfoam.com`

[54] Smagorinsky, J. (1963) "General circulation experiments with the primitive equations," *Monthly Weather Review*, **91**, pp. 99–164.

[55] Menter, F. (2012) *Best practice: Scale-resolving simulations in ANSYS CFD*, *Tech. rep.*, ANSYS Germany GmbH.

[56] Fröhlich, J. and D. von Terzi (2008) "Hybrid LES/RANS methods for the simulation of turbulent flows," *Progress in Aerospace Sciences*, **44**(5), pp. 349–377.

[57] Balaras, E., C. Benocci, and U. Piomelli (1996) "Two-layer approximate boundary conditions for large-eddy simulations," *AIAA Journal*, **34**(6), pp. 1111–1119.

[58] Wang, M. and P. Moin (2002) "Dynamic wall modeling for large-eddy simulation of complex turbulent flows," *Physics of Fluids*, **14**(7), pp. 2043–2051.

[59] Kawai, S. and J. Larsson (2013) "Dynamic non-equilibrium wall-modeling for large eddy simulation at high Reynolds numbers," *Physics of Fluids*, **25**(1), p. 015105.

[60] Kawai, S. and K. Asada (2013) "Wall-modeled large-eddy simulation of high Reynolds number flow around an airfoil near stall condition," *Computers & Fluids*, **85**, pp. 105–113.

[61] Sagaut, P., S. Deck, and M. Terracol (2006) *Multiscale and multiresolution approaches in turbulence*, Imperial College Press.

[62] Piomelli, U. and E. Balaras (2002) "Wall-layer models for large-eddy simulations," *Annual Review of Fluid Mechanics*, **34**(1), pp. 349–374.

[63] Mathey, F., D. Cokljat, J.-P. Bertoglio, and E. Sergent (2006) "Specification of LES inlet boundary condition using vortex method," *Progress in Computational Fluid Dynamics*, **6**, pp. 58–67.

[64] Wilcox, D. C. (2006) *Turbulence Modeling for CFD*, DCW industries.

[65] Rumsey, C., "NASA Langley Research Center, Turbulence Modeling Resource," Available at `http://turbmodels.larc.nasa.gov` (11/12/2014).

[66] Haase, W., M. Braza, and A. Revell (2009) *DESider–A European Effort on Hybrid RANS-LES Modelling: Results of the European-Union Funded Project, 2004-2007*, vol. 103, Springer.

[67] Launder, B. E. and N. D. Sandham (2002) *Closure Strategies for Turbulent and Transitional Flows*, Cambridge University Press.

[68] Shih, T.-H., W. W. Liou, A. Shabbir, Z. Yang, and J. Zhu (1995) "A new $k - \varepsilon$ eddy viscosity model for high reynolds number turbulent flows," *Computers & Fluids*, **24**(3), pp. 227–238.

[69] Wilcox, D. C. (1988) "Reassessment of the scale-determining equation for advanced turbulence models," *AIAA Journal*, **26**(11), pp. 1299–1310.

[70] Menter, F. R. (1994) "Two-equation eddy-viscosity turbulence models for engineering applications," *AIAA Journal*, **32**(8), pp. 1598–1605.

[71] Launder, B. E. and D. Spalding (1974) "The numerical computation of turbulent flows," *Computer Methods in Applied Mechanics and Engineering*, **3**(2), pp. 269–289.

[72] Patel, V. C., W. Rodi, and G. Scheuerer (1985) "Turbulence models for near-wall and low Reynolds number flows-a review," *AIAA Journal*, **23**(9), pp. 1308–1319.

[73] Chen, H. and V. Patel (1988) "Near-wall turbulence models for complex flows including separation," *AIAA Journal*, **26**(6), pp. 641–648.

[74] Schmidt, T., C. Mockett, and F. Thiele (2009) "Adaptive wall function for the prediction of turbulent flows," in *MEGADESIGN and MegaOpt–German Initiatives for Aerodynamic Simulation and Optimization in Aircraft Design*, Springer, pp. 21–33.

[75] Spalart, P. R. (2009) "Detached-eddy simulation," *Annual Review of Fluid Mechanics*, **41**, pp. 181–202.

[76] Kok, J., H. Dol, B. Oskam, and H. van der Ven (2004) "Extra-large eddy simulation of massively separated flows," *AIAA paper 264*.

[77] Chaouat, B. and R. Schiestel (2005) "A new partially integrated transport model for subgrid-scale stresses and dissipation rate for turbulent developing flows," *Physics of Fluids*, **17**(6), p. 065106.

[78] Girimaji, S. S. (2006) "Partially-averaged Navier-Stokes model for turbulence: A Reynolds-averaged Navier-Stokes to direct numerical simulation bridging method," *Journal of Applied Mechanics*, **73**(3), pp. 413–421.

[79] Menter, F. and Y. Egorov (2006) "SAS turbulence modelling of technical flows," in *Direct and Large-Eddy Simulation VI*, Springer, pp. 687–694.

[80] Travin, A., M. Shur, M. Strelets, and P. Spalart (2002) "Physical and numerical upgrades in the detached-eddy simulation of complex turbulent flows," in *Advances in LES of complex flows*, Springer, pp. 239–254.

[81] Shur, M., P. Spalart, M. Strelets, and A. Travin (1999) "Detached-eddy simulation of an airfoil at high angle of attack," in *Proceedings of the 4th International Symposium On Engineering Turbulence Modeling and Measurements (Corsica, France)*.

[82] Spalart, P., W. Jou, M. Strelets, and S. Allmaras (1997) "Comments on the feasibility of LES for wings, and on a hybrid RANS/LES approach," in *Advances in DNS/LES*, Greyden Press Columbus, pp. 137–148.

[83] Menter, F., M. Kuntz, and R. Langtry (2003) "Ten years of industrial experience with the SST turbulence model," in *Turbulence, heat and mass transfer 4*, Begell House Inc., pp. 625–632.

[84] Mockett, C. (2009) *A Comprehensive Study of Detached Eddy Simulation*, Ph.D. thesis, Technische Universitt Berlin.

[85] ANSYS Inc. (2011) *ANSYS FLUENT 14.0 Theory Guide*.

[86] Spalart, P. R., S. Deck, M. Shur, K. Squires, M. K. Strelets, and A. Travin (2006) "A new version of detached-eddy simulation, resistant to ambiguous grid densities," *Theoretical and computational fluid dynamics*, **20**(3), pp. 181–195.

[87] Ferziger, J. H. and M. Perić (2002) *Computational Methods for Fluid Dynamics*, vol. 3, Springer.

[88] Patankar, S. (1980) *Numerical Heat Transfer and Fluid Flow*, Hemisphere Publishing Corporation.

[89] Jasak, H., H. Weller, and A. Gosman (1999) "High resolution NVD differencing scheme for arbitrarily unstructured meshes," *International Journal for Numerical Methods in Fluids*, **31**(2), pp. 431–449.

[90] Gaskell, P. and A. Lau (1988) "Curvature-compensated convective transport: SMART, A new boundedness-preserving transport algorithm," *International Journal for Numerical Methods in Fluids*, **8**(6), pp. 617–641.

[91] Park, N., J. Y. Yoo, and H. Choi (2004) "Discretization errors in large eddy simulation: on the suitability of centered and upwind-biased compact difference schemes," *Journal of Computational Physics*, **198**(2), pp. 580–616.

[92] Adedoyin, A. A., D. K. Walters, and S. Bhushan (2006) "Assesment of Modeling and Discretization Error in Finite-Volume Large Eddy Simulations," in *Proceedings of the ASME 2006 International Mechanical Engineering Congress and Exposition (Chicago, IL, USA)*, pp. 379–388.

[93] ANSYS Inc. (2010) *ANSYS FLUENT 13.0 UDF Manual.*

[94] Petit, O. (2012) *Towards full predictions of the unsteady incompressible flow in rotating machines using OpenFOAM*, Ph.D. thesis, Chalmers University of Technology.

[95] Lewis, B. (2014) *Improving unsteady hydroturbine performance during off-design operation by injecting water from the trailing edge of the wicket gates*, Ph.D. thesis, The Pennsylvania State University.

[96] Spalart, P. (2001) *Young-person's guide to detached-eddy simulation grids*, *Tech. Rep. CR-2001-211032*, NASA.

[97] Nicolet, C. (2007) *Hydroacoustic modelling and numerical simulation of unsteady operation of hydroelectric systems*, Ph.D. thesis, École Polytechnique Fédérale de Lausanne.

[98] Arpe, J. (2003) *Analyse du champ de pression pariétale dun diffuseur coudé de turbine Francis*, Ph.D. thesis, École Polytechnique Fédérale de Lausanne.

[99] Ciocan, G. and M. Iliescu (2007) "Vortex rope investigation by 3D-PIV method," in *Proceedings of the 2nd IAHR International Meeting of the Workgroup on Cavitation and Dynamic Problems in Hydraulic Machinery and Systems (Timisoara, Romania). Scientific Bulletin of the Politehnica University of Timisoara, Transactions on Mechanics*, vol. 52, pp. 159–172.

[100] Rudolf, P. (2009) "Connection between inlet velocity field and diffuser flow instability," *Applied and Computational Mechanics*, **3**, pp. 177–184.

[101] Susan-Resiga, R., S. Muntean, P. Stein, and F. Avellan (2009) "Axisymmetric swirling flow simulation of the draft tube vortex in Francis turbines at partial discharge," *International Journal of Fluid Machinery and Systems*, **2**(4), pp. 295–302.

[102] Kalitzin, G., G. Medic, G. Iaccarino, and P. Durbin (2005) "Near-wall behavior of RANS turbulence models and implications for wall functions," *Journal of Computational Physics*, **204**(1), pp. 265–291.

[103] Cervantes, M., T. Engström, and L. Gustavsson (eds.) (2005) *Third IAHR/ERCOFTAC workshop on draft tube flows.*

[104] Jacob, T. (1993) *Evaluation sur modèle réduit et prédiction de la stabilité de fonctionnement des turbines Francis*, Ph.D. thesis, École Polytechnique Fédérale de Lausanne.

[105] Ulith, P., E. Jaeger, and M. Strscheletzky (1974) "Contribution to clarifying the inception of nonstationary flow phenomena in the draft tube of high specific speed Francis turbines operating at part load," in *Proceedings of the 7th IAHR Symposium on Hydraulic Machinery and Systems (Vienna, Austria)*.

[106] Rheingans, W. (1940) "Power swings in hydroelectric power plants," *Trans. ASME*, **62**, pp. 171–184.

[107] Hosoi, Y. (1965) "Experimental investigations of pressure surge in draft tubes of Francis water turbine," *Hitachi Review*, **14**(12), pp. 1–12.

[108] Cassidy, J. J. (1969) *Experimental study and analysis of sraft-tube surging*, *Tech. Rep. HYD-591*, US Department of the Interior, Bureau of Reclamation.

[109] Falvey, H. and J. Cassidy (1970) "Frequency and amplitude of pressure surges generated by swirling flow," in *Proceedings of the 5th IAHR Symposium on Hydraulic Machinery and Systems (Stockholm, Sweden)*.

[110] Wahl, T. L. (1990) *Draft tube surging hydraulic model study*, Master's thesis, Colorado State University.

[111] EPRI (2000) *Hydro life extension modernization guides: Volume 2 hydromechanical equipment*, *Tech. Rep. TR-112350-V2*, Electric Power Research Institute, Inc.

[112] Kirschner, O., S. Muntean, R. Susan-Resiga, and A. Ruprecht (2007) "Swirling flow in a straight cone draft tube: Axi-symmetric flow analysis and comparison with circumferentially averaged PIV measurements," in *Proceedings of the 2nd IAHR International Meeting of the Workgroup on Cavitation and Dynamic Problems in Hydraulic Machinery and Systems (Timisoara, Romania)*.

[113] Bosioc, A., C. Tanasa, S. Muntean, and R. Susan-Resiga (2009) "2D LDV measurements and comparison with axisymmetric flow analysis of swirling flow in a simplified draft tube," in *Proceedings of the 3rd IAHR International Meeting of the Workgroup on Cavitation and Dynamic Problems in Hydraulic Machinery and Systems (Brno, Czech Republic)*, pp. 551–560.

[114] Scarano, F., C. Benocci, and M. Riethmuller (1999) "Pattern recognition analysis of the turbulent flow past a backward facing step," *Physics of Fluids*, **11**(12), pp. 3808–3818.

[115] Matsumoto, Y. and M. Hoshino (2004) "Onset of turbulence induced by a Kelvin-Helmholtz vortex," *Geophysical Research Letters*, **31**(2).

[116] Brede, M. (2004) "Measurement of turbulence production in the cylinder separated shear-layer using event-triggered Laser-Doppler anemometry," *Experiments in Fluids*, **36**(6), pp. 860–866.

[117] Leschziner, M. and S. Hogg (1989) "Computation of highly swirling confined flow with a Reynolds stress turbulence model," *AIAA Journal*, **27**(1), pp. 57–63.

[118] Xia, J., G. Yadigaroglu, Y. Liu, J. Schmidli, and B. Smith (1998) "Numerical and experimental study of swirling flow in a model combustor," *International Journal of Heat and Mass Transfer*, **41**(11), pp. 1485–1497.

[119] Fu, S., P. Huang, B. Launder, and M. Leschziner (1988) "A comparison of algebraic and differential second-moment closures for axisymmetric turbulent shear flows with and without swirl," *Journal of Fluids Engineering*, **110**(2), pp. 216–221.

[120] Lu, P. and V. Semiao (2003) "A new second-moment closure approach for turbulent swirling confined flows," *International Journal for Numerical Methods in Fluids*, **41**(2), pp. 133–150.

[121] Schlüter, J., H. Pitsch, and P. Moin (2004) "Large-eddy simulation inflow conditions for coupling with Reynolds-averaged flow solvers," *AIAA Journal*, **42**(3), pp. 478–484.

[122] Sagaut, P. (2002) *Large Eddy Simulation for Incompressible Flows*, Springer.

[123] Jeong, E. and S. S. Girimaji (2010) "Partially-averaged Navier-Stokes (PANS) method for turbulence simulationsFlow past a square cylinder," *Journal of Fluids Engineering*, **132**(12), p. 121203.

[124] Lakshmipathy, S. and S. S. Girimaji (2010) "Partially-averaged Navier–Stokes (PANS) method for turbulence simulations: Flow past a circular cylinder," *Journal of Fluids Engineering*, **132**(12), p. 121202.

[125] Frendi, A., A. Tosh, and S. Girimaji (2006) "Flow past a backward-facing step: comparison of PANS, DES and URANS results with experiments," *International Journal for Computational Methods in Engineering Science and Mechanics*, **8**(1), pp. 23–38.

[126] Han, X., S. Krajnović, and B. Basara (2013) "Study of active flow control for a simplified vehicle model using the PANS method," *International Journal of Heat and Fluid Flow*, **42**, pp. 139–150.

[127] Krajnović, S., R. Lárusson, and B. Basara (2012) "Superiority of PANS compared to LES in predicting a rudimentary landing gear flow with affordable meshes," *International Journal of Heat and Fluid Flow*, **37**, pp. 109–122.

[128] Speziale, C. G. (1997) "Computing non-equilibrium turbulent flows with time-dependent RANS and VLES," in *15th International Conference on Numerical Methods in Fluid Dynamics*, Springer, pp. 123–129.

[129] Lakshmipathy, S. and S. S. Girimaji (2006) "Partially-averaged Navier-Stokes method for turbulent flows: $k-\omega$ model implementation," *AIAA paper 119*.

[130] Basara, B., S. Krajnovic, S. Girimaji, and Z. Pavlovic (2011) "Near-wall formulation of the partially averaged Navier-Stokes turbulence model," *AIAA Journal*, **49**(12), pp. 2627–2636.

[131] Ma, J., S.-H. Peng, L. Davidson, and F. Wang (2011) “A low Reynolds number variant of partially-averaged Navier-Stokes model for turbulence,” *International Journal of Heat and Fluid Flow*, **32**(3), pp. 652–669.

[132] Abe, K., T. Kondoh, and Y. Nagano (1994) “A new turbulence model for predicting fluid flow and heat transfer in separating and reattaching flows–I. Flow field calculations,” *International Journal of Heat and Mass Transfer*, **37**(1), pp. 139–151.

[133] Chen, Y.-S. and S.-W. Kim (1987) *Computation of turbulent flows using an extended $k-\varepsilon$ turbulence closure model*, *Tech. Rep. CR-179204*, NASA.

[134] Monson, D., H. Seegmiller, and P. McConnaughey (1990) “Comparison of experiment with calculations using curvature-corrected zero and two equation turbulence models for a two-dimensional U-duct,” *AIAA paper 1484*.

[135] Lam, C. and K. Bremhorst (1981) “A modified form of the $k-\varepsilon$ model for predicting wall turbulence,” *Journal of Fluids Engineering*, **103**(3), pp. 456–460.

[136] Girimaji, S. S. and K. S. Abdol-Hamid (2005) “Partially averaged Navier-Stokes model for turbulence: Implementation and validation,” *AIAA paper 502*.

[137] Basara, B., S. Krajnovic, and S. Girimaji (2008) “PANS vs. LES for computations of the flow around a 3D bluff body,” in *Proceedings of ERCOFTAC 7th Int. Symp.–ETMM7 (Lymassol, Cyprus)*.

[138] Davidson, L. (2014) “The PANS $k-\varepsilon$ model in a zonal hybrid RANS–LES formulation,” *International Journal of Heat and Fluid Flow*, **46**, pp. 112–126.

[139] Fadai-Ghotbi, A., C. Friess, R. Manceau, and J. Borée (2010) “A seamless hybrid RANS-LES model based on transport equations for the subgrid stresses and elliptic blending,” *Physics of Fluids*, **22**(5), p. 055104.

[140] Lesieur, M. (2008) *Turbulence in Fluids*, Springer.

[141] Schiestel, R. and A. Dejoan (2005) “Towards a new partially integrated transport model for coarse grid and unsteady turbulent flow simulations,” *Theoretical and Computational Fluid Dynamics*, **18**(6), pp. 443–468.

[142] Pope, S. B. (2000) *Turbulent Flows*, Cambridge university press.

[143] Dellenback, P., D. Metzger, and G. Neitzel (1988) “Measurements in turbulent swirling flow through an abrupt axisymmetric expansion,” *AIAA Journal*, **26**(6), pp. 669–681.

[144] Paik, J. and F. Sotiropoulos (2010) “Numerical simulation of strongly swirling turbulent flows through an abrupt expansion,” *International Journal of Heat and Fluid Flow*, **31**(3), pp. 390–400.

[145] Chong, M., A. E. Perry, and B. Cantwell (1990) “A general classification of three-dimensional flow fields,” *Physics of Fluids*, **2**(5), pp. 765–777.

[146] Kubacki, S., J. Rokicki, and E. Dick (2013) "Hybrid RANS/LES computations of plane impinging jets with DES and PANS models," *International Journal of Heat and Fluid Flow*, **44**, pp. 596–609.

[147] Stein, P., M. Sick, P. Dörfler, P. White, and A. Braune (2006) "Numerical simulation of the cavitating draft tube vortex in a Francis turbine," in *Proceedings of the 23rd IAHR Symposium on Hydraulic Machinery and Systems (Yokohama, Japan)*.

[148] Avellan, F. (2004) "Introduction to cavitation in hydraulic machinery," in *Proceedings of the 6th International Conference on Hydraulic Machinery and Hydrodynamics (Timisoara, Romania)*.

[149] Mauri, S., J.-L. Kueny, and F. Avellan (2000) "Numerical prediction of the flow in a turbine draft tube: Influence of the boundary conditions," in *Proceedings of the ASME Fluids Engineering Division Summer 2000 Meeting (Boston, MA, USA)*.

[150] ANSYS Inc. (2011) *ANSYS FLUENT 14.0 User's Guide*.

[151] Dörfler, P. (1994) "Observation of pressure pulsations on a Francis model turbine with high specific speed," *International Journal of Hydropower and Dams*, **1**, pp. 21–26.

[152] Hydropower Task Committee of American Society of Civil Engineers (2007) *Civil Works for Hydroelectric Facilities: Guidelines for Life Extension and Upgrade*, ASCE Publications.

[153] Bhan, S., J. Codrington, and H. Mieke (1988) "Reduction of Francis turbine draft tube surges," in *Proceedings of the 5th International Symposium on Hydro Power Fluid Machinery (Chicago, IL, USA)*.

[154] Nishi, M., X. Wang, K. Yoshida, T. Takahashi, and T. Tsukamoto (1996) "An experimental study on fins, their role in control of the draft tube surging," in *Hydraulic Machinery and Cavitation* (E. Cabrera, V. Espert, and F. Martinez, eds.), Kluwer Academic Publishers, pp. 905–914.

[155] Falvey, H. T. (1971) *Draft tube surges–a review of present knowledge and an annotated bibliography*, *Tech. Rep. REC-ERC-71-42*, US Department of the Interior, Bureau of Reclamation.

[156] Vekve, T. (2004) *An experimental investigation of draft tube flow*, Ph.D. thesis, Norwegian University of Science and Technology.

[157] Sano, T., M. Maekawa, N. Okamoto, H. Yano, and K. Miyagawa (2012) "Investigation of flow pattern downstream of spiral grooved runner cone in pump-turbine," in *IOP Conference Series: Earth and Environmental Science*, vol. 15, p. 022019.

[158] Qian, Z., W. Li, W. Huai, and Y. Wu (2012) "The effect of runner cone design on pressure oscillation characteristics in a Francis hydraulic turbine," *Proceedings of the Institution of Mechanical Engineers, Part A: Journal of Power and Energy*, **226**(1), pp. 137–150.

[159] Papillon, B., M. Sabourin, M. Couston, and C. Deschenes (2002) "Methods for air admission in hydro turbines," in *Proceedings of the 21st IAHR Symposium on Hydraulic Machinery and Systems (Lausanne, Switzerland)*.

[160] Ulith, P. (1968) "A contribution to influencing the part-load behavior of Francis turbines by aeration and σ-value," in *Proceedings of the 4th IAHR Symposium for Hydraulic Machinery Equipment and Cavitation (Lausanne, Switzerland)*.

[161] Isaev, I. M. (1968) *Influence of a method of air admission on pressure surges in draft tube models of axial hydro-turbines*, *Tech. Rep. Translation No. 756*, US Department of the Interior, Bureau of Reclamation.

[162] Nukunishi, K. and T. Uedo (1964) "Air supply into draft tube of Francis turbine," *Fuji Electric Review*, **10**(3), pp. 81–91.

[163] Grein, H. (1980) "Vibration phenomena in Francis turbines: their causes and prevention," in *Proceedings of the 10th IAHR Symposium on Hydraulic Machinery Equipment and Cavitation (Tokyo, Japan)*.

[164] Susan-Resiga, R., T. C. Vu, S. Muntean, G. D. Ciocan, and B. Nennemann (2006) "Jet control of the draft tube vortex rope in Francis turbines at partial discharge," in *Proceedings of the 23rd IAHR Symposium on Hydraulic Machinery and Systems (Yokohama, Japan)*.

[165] Bosioc, A. I., R. Susan-Resiga, S. Muntean, and C. Tanasa (2012) "Unsteady pressure analysis of a swirling flow with vortex rope and axial water injection in a discharge cone," *Journal of Fluids Engineering*, **134**(8), p. 081104.

[166] Tănasă, C., R. Susan-Resiga, S. Muntean, and A. I. Bosioc (2013) "Flow-feedback method for mitigating the vortex rope in decelerated swirling flows," *Journal of Fluids Engineering*, **135**(6), p. 061304.

[167] Krueger, R. E. (1976) *Selecting hydraulic reaction turbines*, *Tech. Rep. Engineering Monograph No. 20*, US Department of the Interior, Bureau of Reclamation.

[168] Rajaratnam, N. (1976) *Turbulent Jets*, Elsevier.

Vita

Hosein Foroutan

Hosein Foroutan joined The Pennsylvania State University in 2009, to pursue a doctoral degree in Mechanical Engineering. Prior to that, he received his Master's and Bachelor's degrees in Mechanical Engineering both as "first-in-class" (highest GPA) from Iran University of Science and Technology in Tehran, Iran. Hosein's current publishing credits include 15 peer reviewed papers. He also has presented at several professional meetings, including conferences and workshops.

Hosein's areas of interest include Fluid Mechanics, Heat Transfer, Turbulent Flows, and Numerical Modeling. Specifically, he is interested in using numerical techniques to study problems related to energy and the environment. He is also very interested in teaching. After completing his studies, Hosein plans to seek a faculty position and perform teaching and research activities. His long-term goal is to help developing more efficient renewable energy sources, protecting the environment, and increasing the general awareness of these topics.

Honors and Awards

1. Hydro Research Foundation (HRF) Fellowship, 2013.
2. Iranian-American Academics and Professionals (IAAP) Scholarship Award, 2013.
3. ASME-IGTI Heat Transfer Committee Best Technical Paper Award, 2012.
4. Best Graduate Poster, 9th Annual College of Engineering Research Symposium, College of Engineering, The Pennsylvania State University, 2012.

Selected Publications

1. Foroutan, H. and Yavuzkurt, S., 2015, "Numerical simulations of the near-field region of film cooling jets under high free stream turbulence: Application of RANS and hybrid URANS/LES models," J. Heat Transfer, Vol. 137(1), p. 011701.
2. Foroutan, H. and Yavuzkurt, S., 2014, "A partially-averaged Navier-Stokes model for the simulation of turbulent swirling flow with vortex breakdown," International Journal of Heat and Fluid Flow, Vol. 50, pp. 402-416.
3. Foroutan, H. and Yavuzkurt, S., 2014, "Flow in the simplified draft tube of a Francis turbine operating at partial loadPart I: Simulation of the vortex rope," ASME J. Applied Mechanics, Vol. 81(6), p. 061010.
4. Foroutan, H. and Yavuzkurt, S., 2014, "Flow in the simplified draft tube of a Francis turbine operating at partial loadPart II: Control of the vortex rope," ASME J. Applied Mechanics., Vol. 81(6), p. 061011.
5. Foroutan, H. and Yavuzkurt, S., 2013, "A model for simulation of turbulent flow with high free stream turbulence implemented in OpenFOAM," J. Turbomachinery, Vol. 135(3), p. 031022 (ASME-IGTI Best Technical Paper Award).